GAS JET ASSISTED VAPOR DEPOSITION ON COMPLEX SHAPED SURFACES

A Dissertation
Presented to
the faculty of the School of Engineering and Applied Science
University of Virginia

In partial fulfillment
of the requirements for the Degree
of Doctor of Philosophy in Engineering Physics
by

Theron M. Rodgers

August
2015

APPROVAL SHEET

The dissertation is submitted in partial fulfillment of the requirements for the degree of
Doctor of Philosophy in Engineering Physics

Theron M. Rodgers

AUTHOR

This dissertation has been read and approved by the examining Committee:

Haydn Wadley

Dissertation Advisor

Petra Reinke

Hossein Haj-Hariri

Harsha Chelliah

Joseph Poon

Accepted for the School of Engineering and Applied Science:

James H. Aylor

Dean, School of Engineering and Applied Science

August 2015

Executive Summary

The need to apply coatings to components with complex surface geometries, such as the blades and guide vanes in gas turbine engines, has stimulated significant interest in the development of vapor deposition techniques capable of depositing uniform coatings on such surfaces. Conventional high vacuum physical vapor deposition techniques use low deposition chamber pressures to avoid gas phase collisions, and enable vapor to reach the substrate. As a consequence, they are only able to deposit coatings on substrate surfaces that are in the line-of-sight of the vapor source. However, many of the components used in gas turbine engines contain regions that cannot be seen by such a vapor source. Recently, gas jet assisted vapor deposition techniques that utilize vapor-phase scattering collisions to transport the evaporant to a components have shown promise for enabling deposition on flux-shadowed (non-line-of-sight) regions. This dissertation has investigated the deposition of a simple nickel coating onto both single and doublet airfoil substrates that have non-line-of-sight surface regions. It has utilized multiscale Monte Carlo simulations of the coating process that are validated against experimental depositions. The study explores the viability of gas jet assisted deposition methods, and investigates the mechanisms that control atomic deposition on surfaces hidden from view of the vapor source including those found of the interior channels between closely spaced pairs of airfoils.

Coating deposition was simulated using direct simulation Monte Carlo simulations to model the vapor transport within the deposition chamber. This simulation method enabled the local flux incident on the substrate surface to be determined. It also enabled the incident angle of the vapor with the substrate to be ascertained. These two quantities were then used to simulate coating growth as a function of location on the substrate surface with a kinetic Monte Carlo simulation method. Combining the two techniques has allowed the simulation of coating thickness uniformity and microstructural development along the entirety of the substrate surface, with only the deposition configuration parameters required as input. The simulations were then used to study deposition at varying deposition chamber pressures and gas flow velocities with both stationary and rotated substrate configurations.

The incident flux over the surface of a stationary single airfoil substrate was found to depend primarily on the mean free path between vapor and carrier gas atom collisions in the vapor transporting gas jet, and the average momentum of the vapor atoms within the jet. During deposition on a single, stationary airfoil substrate, the most uniform incident flux profiles were found with a mean free path of approximately 1/10th the maximum dimension of the airfoil (3-5 mm) and low vapor atom momentum, conditions that occur at low chamber pressures and gas jet velocities. Stationary deposition resulted in substantially lower thickness coatings on non-line-of-sight regions. The coatings also had a columnar microstructure but with significant variations in columnar growth angle, thickness, and porosity around the surface of the substrate.

Rotation of the single airfoil substrates greatly improved coating thickness uniformity. During substrate rotation, the majority of flux onto a surface region was deposited while it was in the vapor source's line-of-sight. The best coating thickness uniformity was then found to occur for a process operating at a low-pressure (0.015 Pa) where gas phase scattering did not occur. However, significant variations in the coatings columnar growth angle and pore fraction were observed in the low-pressure simulated coatings, and the fraction of the evaporated atoms that condense on the substrate was low. Deposition at higher chamber pressures resulted in more uniform microstructures, and significantly improved total deposition efficiency (which was maximized at a chamber pressure near 10 Pa). However, the introduction of a inert gas jet created a non-uniform thickness profile along the convex and concave surface and resulted in the deposition of a coating whose thickness on the convex surface was 1.2 to 3 times thicker than on the concave side. An optimization method was developed to investigate non-uniform substrate rotation and source material evaporation rate variations to overcome the non-uniformity in coating thickness. Coatings simulated using an optimized rotation and evaporation rate patterns exhibited a thickness variation of 10% or less between the convex and concave surfaces.

Deposition onto a rotated double airfoil geometry substrate introduced additional complications with deposition behavior since some regions on the interior surface were never in the line-of-sight of the vapor source. Deposition onto the outer doublet surfaces closely matched that on single airfoil substrates. However deposition to the interior surfaces relied on the scattering of vapor atoms from carrier gas streamlines that flowed through the inter-airfoil channel. Optimum deposition conditions were found where the vapor was fully depleted from the flow (and deposited onto the substrate's interior surfaces) just as the flow exited channel's rear opening. The coating thickness on the interior surfaces was found to depend on the chamber pressure and carrier gas velocity. Increasing the chamber pressure decreased the vapor's diffusion distance transverse to the carrier gas stream flow direction and allowed vapor to propagate further through the channel before deposition. At the highest chamber pressures investigated (100 Pa), most of the vapor traveled through the interior channel without depositing. The maximum deposition efficiency on the interior surfaces was found to occur at chamber pressures near 30 Pa and with high gas flow velocity. The use of higher velocity flows also improved the deposition uniformity, but had a smaller influence than variation of the chamber pressure. These observations were effected by the substrate geometry. Along the inner substrate surfaces, coatings with reasonable thickness uniformity were only possible when the mean free path was significantly smaller than the width of the channel opening. When the mean free path was of similar magnitude or greater than the channel width, deposition occurred only from line-of-sight trajectories. This prevented significant coating deposition near the inner surface midpoints.

Acknowledgments

This dissertation was a labor of love. Here I would like to thank just a few individuals who were instrumental in its completion.

First, thanks to my committee. Your insights and discussion have helped shaped this project and suggest new directions of investigation for me to pursue.

I am appreciative of various staff members of the MSE department for their assistance during my carrier. Kim Fitzhugh-Higgins, Sherri Sullivan, and Vickie Thomas all provided welcome relief from the minutiae of grad school.

Petra Reinke, who has been a chair of the EP program my entire graduate career was instrumental in me achieving my degree. Her guidance and assistance, especially during my difficult first year was truly irreplaceable.

I would also like to acknowledge the many friends I have met during my time at UVa. Brad Gelfand, Irwin Reyes, Lissa Anderson, LaToya Roker, Zack Knoll, and other members of the First Harmonics allowed me to find an outlet for my creative energies with little disruption to my graduate studies. Justin Erwin, Ryan Comes, and Sarah O'Donnell helped me push through quantum mechanics and have been great friends ever since. Toni Kember, Brad Richards, Mark O'Masta, and other members of the IPM group provided great assistance and were always there to help. Matt Steiner and Kirsten Andersen provided many social opportunities to escape work for a bit.

I have endless admiration for Dr. Hengbei Zhao for his assistance in performing the experimental work of this study. His tireless work ethic allowed me to focus on computational work and prevented near-certain injury that would've resulted from my clumsiness in the lab.

I would also like to extend a special thank you to my advisor Haydn Wadley. It has been a pleasure to work with and learn from you over the years. Many times our discussions solved my confusions and provided a spark of inspiration.

I would also like to think my parents and family for their encouragement, patience, and love.

Finally, I give endless praise to my wife Karen. You provide the meaning in my life and the motivation to pursue it.

Contents

List of Figures

List of Tables

Chapter 1

Introduction

Our civilization is a function of the degree of vacuum man can produce industrially.
-Peter Schlumbohm, Inventor of the Chemex coffee maker

1.1 Vapor deposition

Vapor deposition refers to the process by which a material is condensed from its vapor phase upon a substrate by an atom-by-atom (or molecule-by-molecule) manner. An investigation of vapor deposition was first reported in the 1649 by the German pharmacist Johann Schroeder [1]. Over the next 200 years, thin film and coating growth via the vapor phase was the subject of great scientific interest. Depositions were often (but not always) performed at low pressures, to enable the vapor to reach a substrate, to reduce impurities in the resulting coatings and to avoid gas phase cluster formation [2, 3]. However, practical applications were limited until improvements in vacuum pumps, gauges, and power supplies were made beginning in the mid-to-late 1800's. During the 20th century, both the number of applications and the variety of methods used for vapor deposition increased rapidly. Today vapor deposition underpins many industries including microelectronics[4, 5], medical devices[6, 7], gas turbine engines[8, 9] and many others [10–13].

These diverse applications have driven the invention of a broad range of deposition techniques; many specifically tuned for the material system of interest. These methods have varied the deposition chamber pressure, the initial form of the input source material, formation of the vapor via thermal evaporation or ion impact methods [14], and the mechanism of deposition onto the substrate surface. Deposition chamber pressures have ranged from atmospheric pressure (101,325 Pa) to ultra-high vacuum (below 10^{-7} Pa) [15, 16]. Methods have used solid[17, 18], and gaseous feedstocks [12]. Thermal evaporation methods have exploited resistive heating [19], electron beam methods [20, 21] and pulsed laser excitation [22]. Deposition mechanisms can either be entirely physical, or be dependent on chemical reactions. The translational (kinetic) energy of the atoms during deposition can also be high[5]-or-low[23]. The rate of vapor deposition and coating growth can also vary. Extremely low deposition rate (MBE)[24] is used to deposit thin, sometimes epitaxial coatings, while very high deposition rates provide an economical route for the application of thick coatings [25].

1.2 Non-line-of-sight (NLS) deposition

Many industrial coating applications require coatings to be applied to non-planar substrates that contain regions of the surface that are not in line-of-sight of the vapor source. Examples include the application of thermal barrier coatings to gas turbine airfoil shaped components [26–31], wear-resistant coatings applied to cutting tools [32], and bio-compatible coatings on medical implants [6, 7]. These applications sometimes require relatively thick (1-100 μm thick) coatings, which necessitate use of high deposition rate methods [2]. These requirements have led to the development of numerous, sometimes novel growth techniques with many exploiting complicated rotation or other manipulation of the substrate. Some are chemical reaction based [33, 34] while others exploit purely physical mechanisms [35, 36].

Numerous vapor-phase deposition methods have been used to create many categories of coating [33, 37–39]. These coating methods are valued for their high deposition rates, good coating quality, and low impurity concentrations. However, they use low deposition chamber pressures to prevent particle formation and ensure atom-by-atom coating growth. At these low pressures, vapor species travel in free (straight line) flight without undergoing interparticle collisions from the evaporation source to the substrate. Even though the vapor travels in straight lines, high-vacuum (low pressure) physical vapor deposition techniques such as electron beam physical vapor deposition (EB-PVD) [17] can deposit coatings on many complex substrate shapes by careful control of substrate motion and source material emission rate [40–42]. However, substrates with interior surfaces, such as doublet guide vanes used to control gas flow in gas turbine engines [43, 44], have regions that are hidden from sight of the vapor source at every substrate orientation. A schematic of a model doublet substrate that contains such regions is shown in Figure 1.1.

In order for vapor molecules to access NLS regions during PVD, the mean free

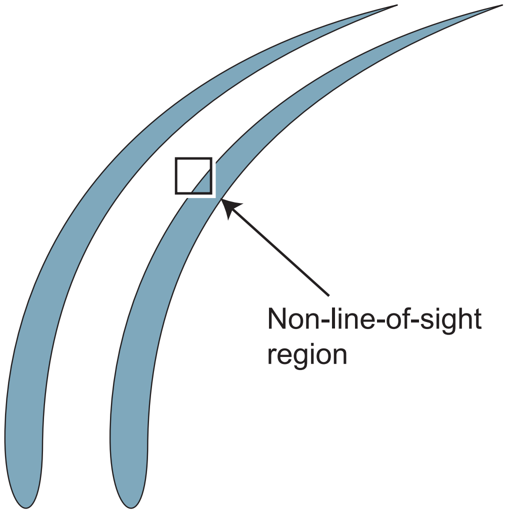

Figure 1.1: Schematic of model doublet guide vane substrate.

path (MFP) between vapor and background gas collisions must be smaller than the length of the opening to the inner substrate surfaces. The variation of MFP with pressure for helium at 300 K can be calculated from kinetic theory for an ideal gas [45], and is shown in Figure 1.2 together with characteristic lengths for several substrate feature types and the operating pressure ranges of several deposition methods.

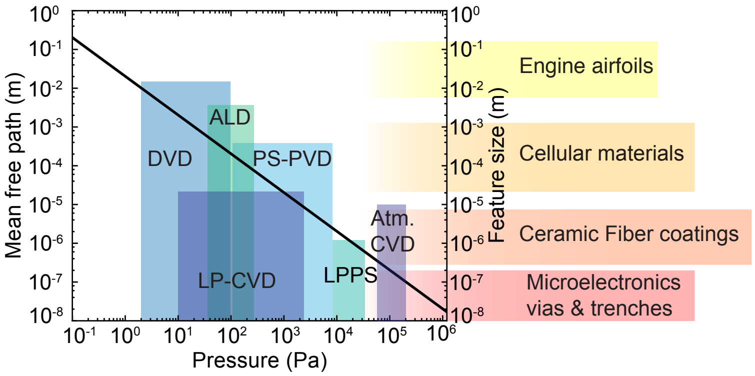

Figure 1.2: Calculated variation of mean free path between binary collisions with helium pressure at 300 K from kinetic theory for an ideal gas. The pressure ranges of several deposition methods are indicated, along with approximate characteristic length scales of several substrate classes.

Chemical-reaction based methods, including chemical vapor deposition (CVD) or atomic layer deposition (ALD), can be used when the MFP is significantly larger than the substrate's characteristic length due to the low sticking coefficient of the vapor on the substrate surface [12, 46, 47]. In these methods, vapor molecules can collide with the substrate surface many times before depositing [11]. Vapor can propagate into non-line-of-sight (NLS) regions by multiple reflections off of the substrate surface without gas-phase collisions (ballistic transport) [48]. Due to the low sticking coefficient, deposition rates are typically low for these methods. In ALD, the molecular precursor is heated to decompose the molecule and release the coating atom. Since only a monolayer is typically physisorbed coatings grow at a rate of $\sim$ 0.1 nm per deposition and heating cycle, each of which takes several seconds, precluding its economical use for thick coatings. In many cases, the complexity of the coating composition or required structure also preclude the use of chemical vapor deposition approaches.

Gas jet assisted PVD methods offer the possibility of non-line-of-sight deposition while retaining the high deposition rates achievable with electron beam or sputter evaporation methods [35, 49, 50]. However, these processes require careful manipulation of deposition parameters to ensure acceptable coating properties and to prevent gas-phase vapor cluster formation which increases rapidly at pressures above 60 Pa [2]. Vapor atoms that condense onto the partially coated substrate surface bind to the dangling bonds of those atoms already there. Unlike CVD methods, the sticking coefficient of thermalized vapor in PVD deposition methods is therefore close to unity. No multi-step chemical reactions are required to incorporate the adatoms. This results in rapid vapor depletion near the substrate surfaces, and presents a significant challenge to NLS deposition. Conformal (uniform thickness) coating during CVD deposition can be achieved only under conditions that permit significant vapor penetration into all substrate surface regions. Conformal NLS deposition via PVD similarly requires that significant vapor penetration into shadowed regions *without contacting any intervening substrate surface*. This has stimulated the development of PVD methods that operate at higher chamber pressures (1 Pa) and incorporate an inert carrier gas to transport an evaporant towards and around/through substrates with NLS regions [51–54].

1.3 Gas turbines and thermal barrier coatings

Gas turbine engines are widely used for aircraft and ship propulsion, as well as electrical power generation [8, 29]. Figure 1.3 shows the basic design of a high-bypass turbofan turbine along with a high-pressure turbine blade and applied thermal barrier coating (TBC). The TBC is a multi-layer system comprised of an alumina-forming bond coat, thermally grown oxide (TGO), and ceramic topcoat. The performance of these engines has been significantly improved through increases in the gas temperature at the inlet to the turbine section of the engine [55]. In this region of the engine, the momentum of the high temperature combustion gases is partially converted to rotation of a disk by interaction with a set of turbine blades (airfoils) attached to the periphery of the disk. These turbine airfoils are subjected to one of the most extreme thermo-mechanical and chemically aggressive environments encountered by a materials system, and their durability in this environment paces many future advances in engine performance.

Gas turbine airfoils are currently made from superalloys. Those in the hottest locations are cast in single crystal form to reduce creep deformation rates under

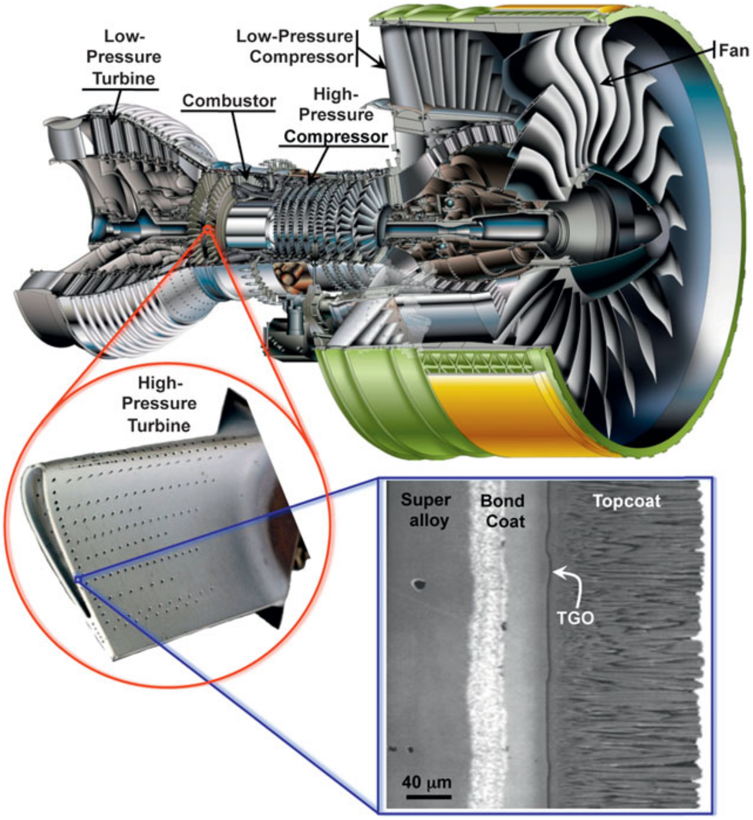

Figure 1.3: Schematic of a high-bypass turbofan turbine. From [8].

the severe centrifugally created stresses associated with engine operation [56–58]. The airfoil interiors are hollow, and the thin metal wall is penetrated by many small holes so that cold compressed air can be used to reduce the airfoil's temperature and rate of degradation. To further protect the superalloy airfoils, they are coated with a metallic bond coat whose composition is optimized to reduce the rates of both oxidation and hot corrosion (usually at the expense of bond coat creep resistance). Further durability is achieved by depositing a TBC on the bond coat. Its purpose is to thermally insulate the bond coat, thereby reducing its temperature and thermal degradation rate. The most commonly used thermal barrier is a 100-150 μm thick layer of low thermal conductivity zirconia stabilized with 7 wt. % yttria. Such coatings reduce the bond coat surface temperature of internally cooled components by 100-200 °C [25, 28, 29]. Other ceramic TBCs containing additional rare earth dopants are also being developed with even lower thermal conductivity[30, 59].

The thermal protection provided by ceramic coatings, and their durability in the engine environment, are both greatly influenced by the thickness and structure of the coating [8, 26]. In a ceramic layer deposited by PVD, the coating thickness, pore volume fraction (porosity) and inclination of the growth columns (and pores) govern the thermal resistance. Coatings applied by one of the PVD methods are usually used for components subjected to severe thermal cycling, since they have a columnar structure leading to a low in-plane modulus (a consequence of the many intercolumnar pores oriented perpendicular to the substrate surface), and increased delamination resistance [60–62]. Their expansion and contraction partially accommodates the substantial thermal strain during thermal cycling without creating stored (elastic) strain energy sufficient to drive delamination cracks. While thicker coatings could give increased thermal protection, the stored elastic strain energy in a coating is proportional to its thickness [56, 57, 63], and so thick coatings are subject to an increased risk of delamination. It is therefore important to balance the coating's thickness to achieve the required temperature drop without overly increasing the risk of delamination. Achieving a balance of coating thickness, pore volume fraction, and pore morphology is therefore essential to fully realize the potential of this airfoil protection strategy.

Numerous methods have been proposed for the deposition of these coatings including liquid droplet processes such as air or vacuum plasma spray (APS) [64], and electron beam-physical vapor deposition (EB-PVD) [8] concepts that create an atomically dispersed vapor plume which is condensed on the substrate surface. More recently hybrid techniques have been also proposed including Plasma Spray-

PVD (PS-PVD) [27, 36, 65] which uses a high power plasma to evaporate liquid droplets in a high-pressure gas jet, and electron beam-directed vapor deposition (EB-DVD) [25, 66] in which an electron beam is used to evaporate a source material located in the throat of a helium gas jet forming nozzle.

Vapor condensation onto a non-planar substrate geometry affects both coating growth behavior during deposition and in-service performance of the ensuing coating. For example, the delamination resistance of a TBC appears to depend on the curvature of the substrate to which it is applied. Steinbrech et. al. [61] have shown that the lifetime of coatings applied to the outer surface of cylindrical tubes increased with the cylindrical substrate's radius. Other investigations of the failure modes of coated airfoils removed from gas turbine engines have shown the failure mode to vary with location on the airfoil surface [26]. This arises from a complex combination of factors including; spatial variations of both the temperature and thermal stress experienced by the coating, the local substrate curvature, and the probability of impact by small or larger particles leading to erosion or foreign object damage.

The pore structures in TBCs deposited by EB-PVD (and its higher-pressure, EB-DVD counterpart) occur on several length-scales: large intercolumnar pores surround typically ~10 μm diameter growth columns, while smaller micron-scale pores, and isolated nano-scale pores exist within the columns [25, 67]. While the large intercolumnar pores reduce coating strain energy by accommodating mismatches in thermal expansion [68], the micron-scale pores provide a significant reduction in coating thermal conductivity in the heat-flux propagation direction [25, 69]. Nano-scale pores in many "as-deposited" coatings also reduce coating conductivity by increasing phonon scattering, but are quickly removed by sintering during operation of the engine [8, 70, 71].

1.4 Dissertation objective

The objective of this dissertation is to advance a fundamental understanding of non-line-of-sight physical vapor deposition. It seeks to understand the gas-phase mechanisms controlling NLS deposition, as well as their effects on coating microstructure. This objective is achieved by the pursuit of four inter-related goals. The first seeks to develop a simulation methodology that can relate the atom-by-atom assembly of a nickel coating on a model, airfoil-shaped substrate in a gas jet assisted deposition environment. When held stationary above a vapor source, such a substrate has NLS regions on its surface, and deposition into these regions will be studied. This is achieved through both computational and experimental studies which analyze the coating structure and thickness by studies of gas phase scattering and surface assembly mechanisms. The second goal seeks to understand the influence of substrate rotation upon the coating that would be deposited during gas jet assisted vapor deposition processes. The third goal extends those of the first two and investigates the NLS deposition of coatings upon substrates with internal confined channels like those encountered during the coating of doublet guide vane airfoils, Figure 1.1. The fourth goal of the dissertation is to explore the feasibility of controlling (optimizing) the thickness and microstructure of coatings on airfoil shaped substrates to meet a surface location specified balance of properties.

1.5 Dissertation outline

The dissertation is organized into this introductory chapter, followed by Chapter 2 which provides a background to the development of the DVD method and its previous use for NLS deposition. Chapter 3 introduces DSMC and kMC simulation methods used here. It also discusses other NLS-capable deposition methods, their deposition mechanisms, abilities, and limitations. Chapter 4 presents experimental and simulated DSMC results on a stationary airfoil substrate. Chapter 5 discusses the deposition behavior on a rotated single airfoil substrate. It studies both deposition efficiency variation (using the DSMC method) and microstructural variation (using a combined kMC/DSMC approach).

Chapter 6 examines the deposition efficiency profiles around the substrate surfaces as well as the deposition conditions that most effect deposition behavior. Chapter 7 focuses on the coating microstructure along the inner doublet surfaces. It also presents an optimization method to minimize coating variation between the inner and outer surfaces. Chapter 8 presents a discussion and Chapter 9 the key conclusions.

Chapter 2

Directed Vapor Deposition

Gas jet assisted processes such as EB-DVD uses an inert gas (typically He or Ar) jet to entrain evaporated atoms or molecules and redirect them towards a substrate [66, 68, 69]. The vapor molecules in this process undergo many collisions before reaching the substrate, and deposition occurs by scattering from the jet flow streamlines. As a result, deposition onto any surface over which a stream flows (including non-line-of-sight regions) is potentially viable, and has been experimentally demonstrated by uniformly coating a non-rotated cylindrical substrate oriented transversely to the gas jet [35]. To ensure source material evaporation by the electron beam in the low vacuum environment (where a portion of beam energy is dissipated by electronically exciting and partially ionizing the carrier gas) of the EB-PVD process, a high voltage (70 kV) electron beam gun is used, as the scattering cross section of electrons with background gasses decreases with increasing electron accelerating voltage [69, 72].

A critical challenge posed by the use any of the PVD methods for TBC deposition is the requirement to deposit coatings onto complex shaped engine components such as turbine blades, vanes and nozzles. Uniform deposition with the low-pressure EB-PVD method is not possible on substrates with non-planar surfaces unless they are rotated or otherwise manipulated during deposition [50]. Sophisticated substrate translation and rotation schemes have been designed to improve the coating thickness uniformity on these components [40, 73]. The EB-DVD process utilizes a higher deposition chamber pressure (typically 1 - 45 Pa) and a gas jet to partially overcome this limitation by enabling the incident vapor to flow over the entire substrate surface; eliminating sharp coating thickness discontinuities in line-of-sight limited, low-pressure EB-PVD coatings. The EB-DVD method has been used to deposit coatings on several non-line-of-sight substrates including fibers [35], polymer foam templates [49], and stationary airfoil shaped substrates [50]. A similar capability has been reported for the PS-PVD method, which operates with chamber pressures in the 100 - 1,000 Pa range [27, 36, 65].

The DVD technique is a modification of traditional low-pressure Electron Beam-Physical Vapor Deposition (EB-PVD). The DVD method inherits the high evaporation rate and purity of electron beam evaporation, while adding a carrier gas jet and higher chamber pressure to allow for deposition into non-line-of-sight substrate regions. A simplified schematic of the DVD chamber is shown in Figure 2.1. The DVD method has undergone twenty years of development since its first incarnation in the 1990's [74]. In this time, significant advances have been made in both system design and deposition performance.

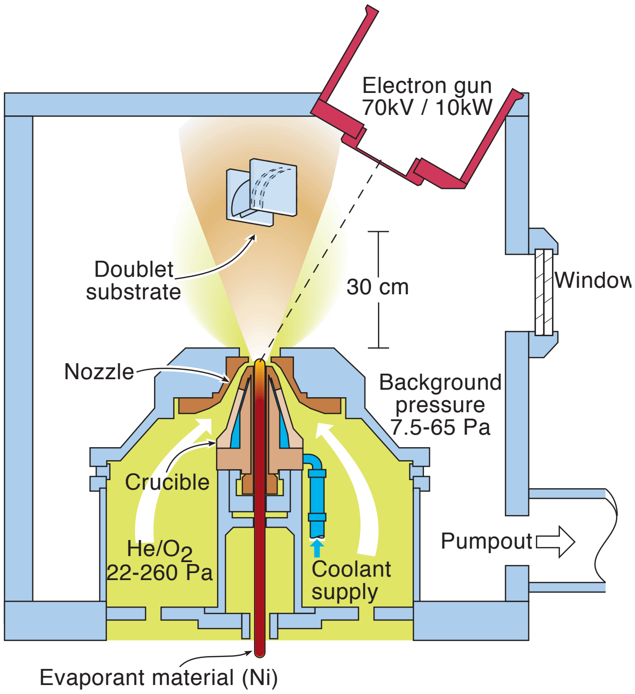

Figure 2.1: A schematic of the DVD chamber configuration during deposition onto a doublet guide vane substrate.

2.1 DVD Development History

There have been several major modifications to DVD system design. The initial version of DVD, DVD I, utilized a separated gas inlet nozzle and source evaporation geometry, as shown in Figure 2.2. In this configuration, the carrier gas jet flows horizontally across the source rod surface and redirects the evaporant towards the substrate. This configuration ensures the electron beam only travels a minimum distance through the deposition chamber, which reduces the amount of beam energy absorbed by the background gas. However, it was determined through computer simulations that the momentum required to bend the vapor 90° resulted in a significant portion of the evaporant failing to be entrained in the gas jet and missing the substrate surface [69]. A resistive substrate heater was typically used, to enhance diffusion in the film.

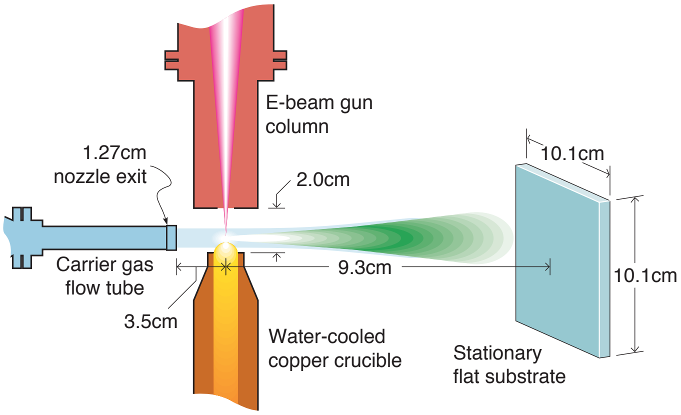

Figure 2.2: Schematic of the original DVD configuration. The gas nozzle and source rod configuration reduced deposition efficiency.

The second generation of DVD (DVD II) was developed in the early 2000's to counteract the efficiency problems of DVD I. This system employs a coaxial vapor source and carrier gas inlet design, as shown in Figure 2.1. This configuration allows for greatly enhanced entrainment of the evaporated source material into the vapor plume [75]. By employing electron beam acceleration voltages in the range of 70 kV, the beam is ensured to travel > 1 meter at DVD operating pressures [74]. Along with the redesigned source configuration, the deposition chamber was augmented with a hollow cathode plasma system to allow for plasma-assisted vapor deposition [76, 77]. A schematic of the DVD II system with plasma system is shown in Figure 2.3. The plasma system increases vapor-atom energy and allows for the deposition of dense coatings without the need for a substrate heater. However, the transverse orientation of the system reduces the materials usage efficiency due to broadening of the vapor plume, similar to the entrainment issues with DVD I.

In order to counteract the reduce deposition efficiency, the DVD system has been redesigned to incorporate a coaxial plasma system, as shown in Figure 2.4. This configuration allows for the enhancements of the plasma activation while reducing

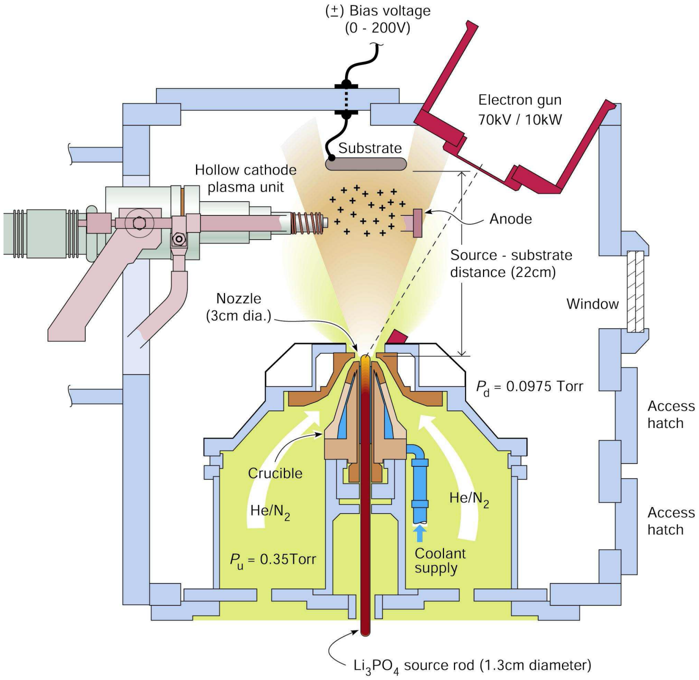

Figure 2.3: Schematic of DVD II chamber with plasma-activation system. The plasma system enhances vapor energy, but reduces the overall deposition efficiency due to its transverse orientation to the vapor plume.

the efficiency losses caused by transverse plasma alignment.

2.2 DVD Application History

2.2.1 Deposition Materials

The DVD method has been used to deposit many materials on several substrate configurations. During DVD development, work focused on the deposition of simple, metal coatings [66]. It was soon realized that the high-pressure environment of the DVD system is ideal for reactive vapor deposition, such as oxide materials used in thermal barrier coatings and solid oxide fuel cells. This has led to the most

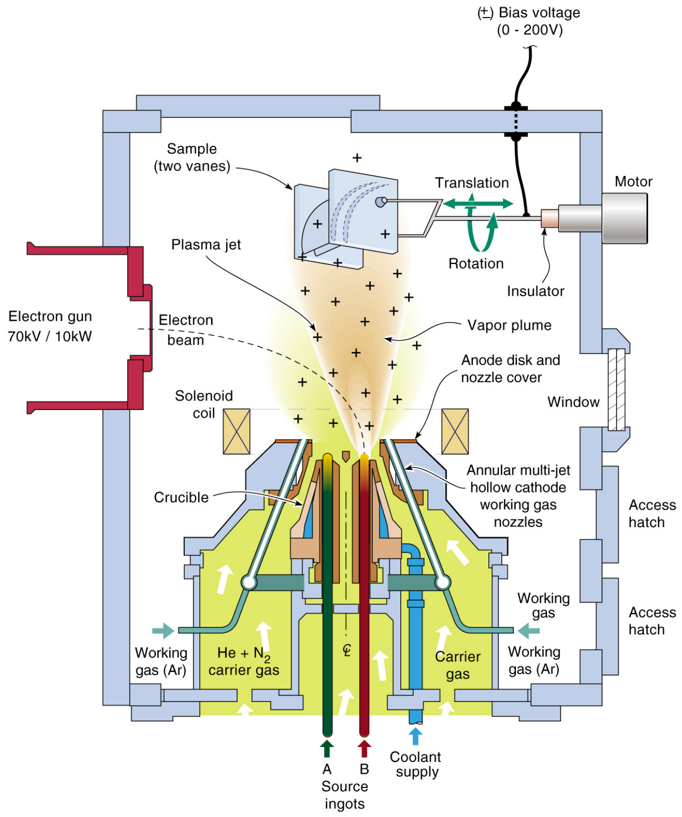

Figure 2.4: Schematic of DVD II system with coaxial plasma-activation system.

widespread use of the DVD system in the deposition of thermal barrier coatings (TBC) [68]. The DVD technique is extremely well suited for TBC deposition due to its high deposition, enhanced coating porosity, and non-line of sight capabilities [2, 50]. Several TBC candidate materials have been deposited via DVD, including industry standard 7% yttria stabilized zirconia (YSZ) [67] and samarium zirconate [30]. Additionally, multi-component coatings consisting of YSZ and platinum layers have been deposited [57, 78]. DVD has also deposited NiAl and NiAlPt bond coats that are used when applying TBCs to nickel superalloy substrates [79, 80].

In addition to material variation, the processing parameters for TBC growth have been varied extensively. The porosity variation with deposition conditions has been studied extensively [81]. Novel, zig-zag microstructures have also been deposited, resulting entirely from modifying the substrate's rotation pattern [23, 25]. These microstructures have extremely low thermal conductivities (~0.8 W/mK) due to their long thermal diffusion paths, but retain the good strain tolerance of PVD coatings.

Additional oxide materials have been deposited, including Lithium Manganese Oxide and Lithium Phosphorous Oxynitride (Lipon) films with potential applications in thin film batteries [75–77]. The Lipon films were deposited with the plasma assisted method discussed earlier.

2.2.2 Non-line-of-sight Capabilities

Non-line-of-sight deposition has been an important advantage of the DVD method over traditional low-pressure deposition systems. However, the difficulty of describing behavior over the wide variety of non-line-of-sight substrates has prevented the development of a general treatment. One of the earliest non-line-of-sight substrates studied with the DVD method was fibers used in MMC applications [35, 74]. The DVD method has also been used to created open-cell metal foams [49]. The foams were deposited onto a polymer foam template, which was then removed by thermal decomposition after deposition. Both of these non-line-of-sight applications are small-scale (~100 μm) and present a much different configuration than millimeter scale non-line-of-sight objects studied here.

Chapter 3

Simulation Methods

Vapor deposition techniques have been the subject of many simulation studies [37, 82, 83]. The multi-phase and complex nature of the deposition process requires a multi-scale simulation approach to model the entire deposition process. Typically gas phase behavior and film growth kinetics are simulated with separate methods. Gas phase behavior can be simulated with computational fluid dynamics (CFD), the lattice Boltzmann method, ray tracing, or direct simulation Monte Carlo (DSMC). The exact method used depends on the chamber pressure, simulation volume size, and species studied. An even greater variety of techniques have been used to simulate coating growth, including level-set, molecular dynamics (MD), kinetic Monte Carlo (kMC), and even density functional theory (DFT). Important variables for film kinetics code selection include the presence/absence of chemical reactions, crystal structure of film, and size of simulation grid.

A numerical simulation of coating deposition provides an efficient means of exploring the relationships between the local coating thickness, its structure and the conditions used for its deposition. In principle, molecular dynamics provides a means for this [84, 85], but the computational expense is prohibitive for coatings that are typically 100 μm thick and deposited at rates of a few microns per minute. The alternatives are more computationally efficient (but more approximate) atomistic kMC techniques [23, 82], continuum-based methods such as the level-set method [86], or finite element based methods [87, 88]. Of these, only the kMC technique can address structure at both the atomic and coating thickness scales. Advanced kMC methods have been developed with built in controllers to manipulate surface roughness and site occupancy [89, 90], and even account for material elasticity [91, 92]. An overview of the kMC method has been recently published in [93].

We chose to implement the DSMC method [94] for gas phase simulations and the kMC [93, 95, 96] method for film kinetics. We selected the DSMC method due to its ability to simulate gas behavior under a wide range of pressures, ranging from near-continuum to free molecular flow. This is important for the wide range of degrees of rarefaction found in the DVD chamber. The kMC method was select due to its ability to simulate large grids with low computational demands. Both methods use atomistic-scale simulations which facilities simple results/input passing between them.

DSMC is a statistical simulation method developed to analyze rarified gas environments for which continuum computational fluid dynamics methods are difficult to apply [94]. It has been widely used to study conventional physical [97–100] and chemical vapor deposition processes [101–104], and has been employed to better understand the EB-DVD coating process [2, 25, 35, 75, 81]. DSMC uses a subset of test particles within a grid to simulate the behavior of a much larger number of real gas particles (on the order of 1 test atom per billion real atoms). The simulation atoms interact with each other through binary collisions. Between collisions they can interact with electromagnetic fields and can be deposited by collisions with surfaces [105].

The kMC method utilized was based on the work of Yang [96], but shares no code in common and includes several enhancements. These include the ability to simulate substrate rotation during coating growth, along with the use of an incident angle distribution for adatom trajectories determined by DSMC simulations. Advancements in computational power since the code's initial creation allow for efficient modeling of much larger substrate regions and allow for simulation along the surface of an entire macroscopic substrate.

3.1 Direct Simulation Monte Carlo

DSMC is an atomistic method that models rarefied gas dynamics via direct simulation of the Boltzmann equation [94]. The method uses a subset of virtual "test" molecules to model the behavior of the full ensemble of real molecules. Flow behavior is determined through a cyclic procedure of independent interatomic collision and collision-free propagation time steps. Icarus uses the variable hard sphere (VHS) molecular collision model, which simulates gas molecules as hard spheres with velocity dependent radii [98–100]. The DSMC simulation method and its application to the simulation of vapor deposition has been described in detail elsewhere [35, 67].

The DSMC program Icarus developed by T.J. Bartel at Sandia National Lab was used for gas phase simulation [105]. It is a two-dimensional code capable of simulations on either axisymmetric or Cartesian coordinate meshes. Icarus uses the variable hard sphere (VHS) approximation to model particle-particle interactions [94]. The DSMC technique is a stochastic simulation method that uses a subset of test particles to simulate a real ensemble of molecules. It has been used to simulate many rarefied gas environments including atmospheric reentry, planetary atmospheres, and vapor deposition. The DSMC method uses alternating steps of free-molecular movement and atomic collisions to simulate gas dynamics. The time step must be chosen as a small fraction of the molecular collision frequency (a timestep of 10^{-7}s was used in this study). During the free movement step, atoms propagate through the simulation grid, pass over grid connecting boundaries, and bounce off of or absorb onto solid surfaces. After a timestep has passed, binary collisions are performed by randomly selecting pairs of molecules from the local grid cell. The probability of atom collision is defined based on the molecular radii and intersection of the molecule's paths. Then, another Monte Carlo selection is made to determine if the collision should be performed. If so, new trajectories for the pair are calculated using one of several force models (hard sphere, variable hard sphere, variable soft sphere, etc). After the specific number of collisions have been performed, another timestep is performed. The cycle continues until a specific number of timesteps have occurred. A schematic of the simulation procedure within a single grid cell is shown in Figure 3.1.

A typical simulation in this study consisted of a total of 325,000 timesteps. For each simulation, a certain number of unsteady timesteps, where the flow field is iterated until reaching a steady state, must first be performed. For our simulations this was generally set to 75,000. Afterwards, steady timesteps are used, during which statistics are continuously collected. Statistical noise is reduced by increasing

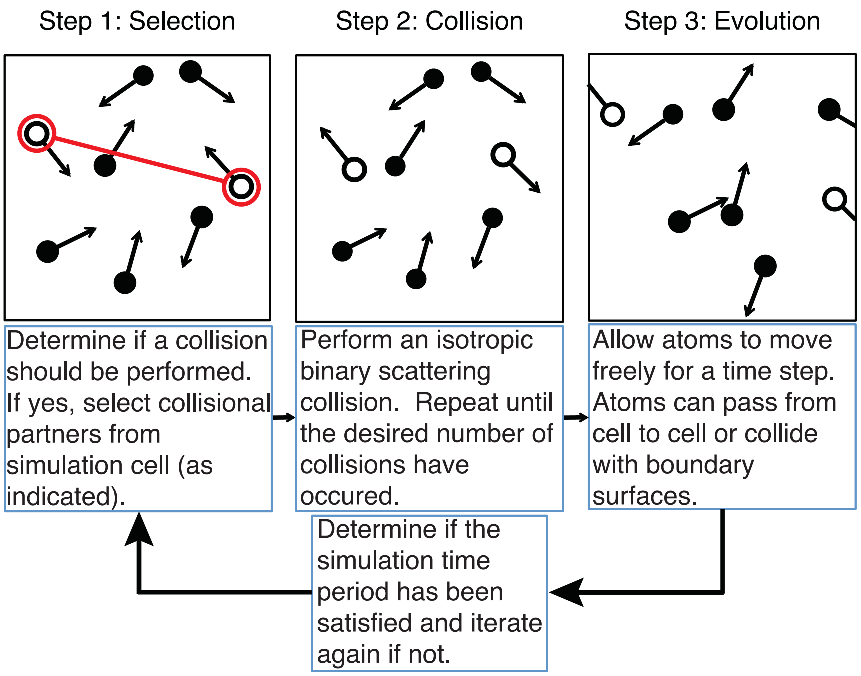

Figure 3.1: A schematic of the DSMC simulation procedure.

the number of timesteps.

The major limitation of the use of DSMC to simulate ceramic coating deposition is the lack of vapor-phase information for ceramic materials. Due to the high melting and vapor points of the materials (which also makes them useful in their applications), there exists virtually no experimental information about their viscosity or molecular diameters. Similar difficulties exist with metal vapor species, although several approximations have been investigated [98–100]. However, the importance of metallic vapor deposition has encouraged several approximation methods.

Fan et al. [98] were the first to determine VHS parameters for metal vapors. They used theoretical data at 700 and 2000 K to determine collision cross sections and coefficients of viscosity for sodium and cesium. They then generalized their results to other metals by assuming all elements in a periodic table row shared similar values. Although this is a crude assumption, they make the important note that metal atom collisional cross sections are much larger than atomic gas species, which in turn will encourage much higher collision rates. This becomes important and will negatively affect simulations at very dense vapor concentrations. Venkattraman and Alexeenko [99, 100] created an improved model that adapts the Lennard-Jones interatomic potential parameters for each metal species to VHS parameters. This approach offers greater accuracy for all species of metal atoms. The work in Chapter 4 uses Fan's method to calculate parameters for Zr atoms, while the work in the remaining chapters utilizes Venkattraman and Alexeenko's approach to calculate Ni atom parameters.

3.2 Kinetic Monte Carlo

The kMC technique is a stochastic technique that simulates vapor deposition in a time-accurate manner. During a kMC simulation, vapor atom deposition rates are linked with diffusional atomic jump rates determined from molecular statics [95, 121]. A schematic of the simulation scheme is shown in Figure 3.2. As with DSMC studies, the lack of ceramic material parameters is a major limitation for the kMC simulations. Due to this, the studies presented here used Ni atoms during simulation.

The kMC method is well suited for simulation of the vapor deposition of a coating since it is sufficiently computational efficient to permit prediction of the thickness and microstructure of a coating grown at realistic deposition rates, angle of atom impacts and substrate temperatures. The relationship between deposition

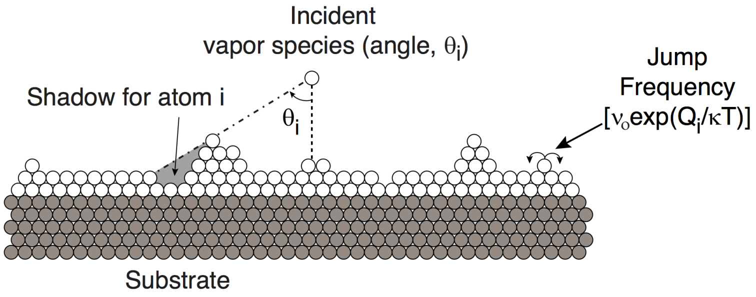

Figure 3.2: A schematic of the 2D kMC simulation scheme.

rate and surface diffusion is determined by linking the sum of all single atom diffusional jump probabilities with the vapor atom arrival rate obtained from the DSMC simulation. The probability of a diffusional jump occurring is determined by the jump attempt frequency, the activation energy of the jump and the temperature. For a jump over a barrier with activation energy E_i, the successful probability is given by;

$$P_i = \nu_o e^{(-E_i/kT)} \tag{3.1}$$

where ν_o is the effective vibrational frequency of atoms in the solid (fixed at $5x10^{12}s^{-1}$ in this study), E_i is the activation barrier for the specific jump i in eV (tabulated in 3.3), k is Boltzmann's constant in eV/K, and T is the absolute temperature in kelvin. The simulation advances by adding $(\sum P_i)^{-1}$ to the simulation time after each jump is performed. When the elapsed simulation time is greater than the time interval between vapor atom arrivals (the inverse of the deposition rate), an additional vapor atom is added to the simulation and the cycle repeats until the desired number of atoms have been deposited.

During a simulation each occupied lattice site can possess several activation energies (and thus jump probabilities) corresponding to the different (atomic configuration dependent) diffusional pathways available to it. The number of pathways in the full 3D problem is dramatically increased and requires the use of parallelized simulation methods [106, 107]. However, the kMC method is an inherently serial algorithm and parallelization requires the careful division of the simulation volume into individual sub-domains, which communicate through shared boundary regions. Thus for simplicity, a 2D kMC scheme was implemented.

The diffusional pathway tables used for the kMC simulations are shown in Figure 3.3. All possible pathways for a given 2D lattice configuration are stored in memory, and a Monte Carlo algorithm is used to select a specific jump. The energy barrier values are stored in a binary tree to minimize computational effort when selecting a jump and updating the grid afterwards. A comprehensive discussion of the kMC procedure used here can be found in Yang [96]. The 2D nature of the kMC lattice requires the use of 2D energy barriers (calculated here using the 2D embedded atom method) and scaling of the simulation temperature. The simulation temperature is determined by scaling the homologous melting temperature, T/T_m, for the reduced degrees of freedom. Here, T_m is the 2D melting temperature (1150 K for nickel), which is approximated as 2/3 of the 3D nickel melting temperature.

Important input parameters for kMC simulations of vapor deposition include the vapor atom deposition rate, substrate temperature, vapor atom incidence angle distribution (IAD), and total deposition time. All these parameters can either be defined externally by the user or linked to the surface flux information of gas-phase simulations. In our DVD modeling approach, the vapor atom deposition rate and IAD are read in from corresponding DSMC simulations, while the other parameters are specified depending on the situation simulated.

The kMC method can simulate both rotated and stationary deposition. This is

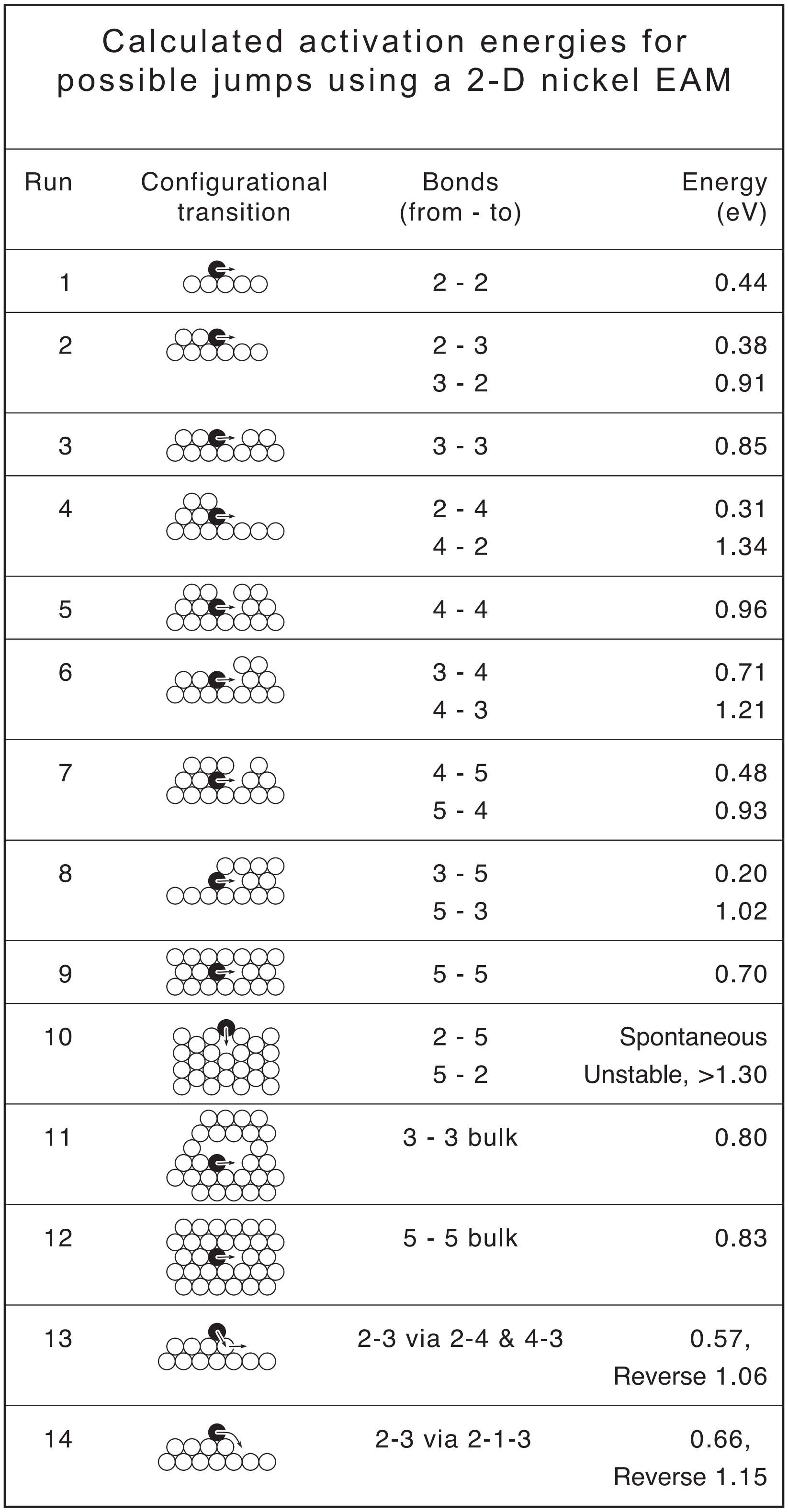

Calculated activation energies for possible jumps using a 2-D nickel EAM

Run	Configurational transition	Bonds (from - to)	Energy (eV)
1		2 - 2	0.44
2		2 - 3 3 - 2	0.38 0.91
3		3 - 3	0.85
4		2 - 4 4 - 2	0.31 1.34
5		4 - 4	0.96
6		3 - 4 4 - 3	0.71 1.21
7		4 - 5 5 - 4	0.48 0.93
8		3 - 5 5 - 3	0.20 1.02
9		5 - 5	0.70
10		2 - 5 5 - 2	Spontaneous Unstable, >1.30
11		3 - 3 bulk	0.80
12		5 - 5 bulk	0.83
13		2-3 via 2-4 & 4-3	0.57, Reverse 1.06
14		2-3 via 2-1-3	0.66, Reverse 1.15

Figure 3.3: Table of Ni atom jump pathways and their respective activation energies [96].

done by specifying the number of substrate rotations and the number of atoms deposited per position in the input file. While simulating rotation, the deposition rate and IAD can be adjusted for each orientation. The substrate rotation simulation procedure is further discussed in Chapter 5.

Chapter 4

Simulations of deposition on a stationary airfoil[1]

4.1 Synopsis

The uniform coating of a complex shaped substrate, such as a gas turbine airfoil, by collisionless physical vapor deposition processes requires rotation/translation of the substrate or sources and is inconceivable for regions on the substrate that are never in the line-of-sight of the vapor source. Recently developed directed vapor deposition processes use electron beam evaporation and inert gas jets to entrain, transport, and deposit metal oxide vapor in an environment where many vapor atom collisions occur prior to deposition. Direct simulation Monte Carlo simulations and experimental depositions of a rare earth modified thermal barrier coating are used to investigate fundamental aspects of the deposition process,

---

[1] Adapted from a peer reviewed article published in the *Journal of Vacuum Science and Technology A*[50].

including coating thickness and column orientation, over the surface of a non-rotated model airfoil substrate with substantial non-line-of-sight regions. The coating thickness uniformity was found to depend on the deposition chamber pressure and the pressure ratio between the low-pressure deposition chamber and high-pressure reservoir upstream of the gas jet forming nozzle. Under slow flow conditions, significant coating of the non-line-of-sight regions was possible. The growth column orientation is found to also vary over the substrate surface due to changes in the local incidence angle distribution of depositing vapor atoms. The variation in growth column orientation is not predictable by the Tangent rule widely used for predicting columnar growth orientation in physical vapor deposition processes.

4.2 Introduction

Thermal barrier coatings are often deposited on gas turbine airfoils using an electron beam-physical vapor deposition (EB-PVD) process [8, 26, 108]. In the traditional EB-PVD method, an intense electron beam is used to melt and evaporate a ceramic source material. The evaporated molecules travel to, and condense on the airfoil, in a high vacuum in which few gas phase collisions occur. The molecules therefore travel in essentially a straight line from the source to the airfoil, and only regions on the airfoil that are visible from the source are coated. Substrate rotation is required to coat the non-planar airfoils (blades and vanes) of interest here [40]. Some complex shaped turbine components, such as doublet guide vanes, have regions on their gas flow path surfaces that are never in the line-of-sight of the vapor source regardless of the manner of substrate rotation. These components are therefore impossible to uniformly coat using the EB-PVD approach. Several groups are exploring alternative methods of coating deposition on complex substrates including plasma spray [52, 53, 109, 110] and sputtering processes [51, 111].

In this chapter, the DSMC technique is used to investigate some of the factors controlling coating thickness uniformity over the surface of a model, non-rotated airfoil undergoing DVD coating. Some regions on the airfoil we investigate are never in line-of-sight of the vapor source. We explore the effects of process conditions including the deposition chamber pressure (which controls the inter-collision mean free path) and the pressure ratio upstream and downstream of the gas jet forming nozzle, which governs jet speed. The validity of the simulation approach is assessed by comparison of the predicted and experimentally deposited coating thickness distributions on the model airfoil. The predicted coating thickness distributions for the EB-DVD and EB-PVD processes are also compared, and the factors controlling coating uniformity identified. The experimental coatings contained through thickness, inter growth-column pores whose orientation to the airfoil surface varied along the airfoil. The columnar growth angles are compared with results obtained from the Tangent Rule [112, 113], which describes the correlation between vapor atom incident angle and resulting columnar growth angle. The rule was found to be an unreliable prediction tool for DVD as the incident flux strikes the surface with a broad distribution of angles, instead of the sharply defined single value assumed in the Tangent Rule. However, insight into the columnar growth process can be gained through computed incidence angle distributions (IAD) of the vapor atom flux along the airfoil surface.

4.3 Simulation Methodology

In the EB-DVD process, a gas jet is established by allowing gas from a high-pressure reservoir to flow through a nozzle into a chamber maintained at a lower pressure [35, 69]. The nozzle is arranged so that it surrounds a water-cooled crucible containing an evaporation source, Figure 4.1. Evaporation occurs by impingement of a high power electron beam on to the surface of the source material. By arranging for evaporation to occur in the throat of a nozzle, the gas expansion process entrains the evaporant in a trans-sonic jet that travels towards the airfoil substrate.

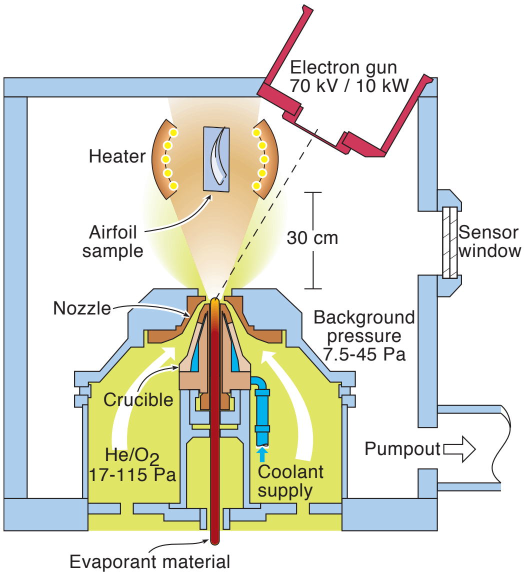

Figure 4.1: Schematic illustration of a directed vapor deposition process showing the electron beam evaporated vapor plume and model air- foil sample geometry. A mixture of 90% He and 10% O2 was used for experimental studies.

A model turbine blade airfoil was designed for both numerical simulations and experimental depositions in the EB-DVD process environment, Figure 4.2. It was attached to a thin back-plate to facilitate mounting in the deposition chamber during experimental depositions. The airfoil's shape varied in only two dimensions (it had no twist) to simplify the simulations. The airfoil's convex and concave surfaces were defined by quadratic functions of the y-coordinate to simplify simulation grid design and test piece manufacture. The airfoils were oriented with the y-axis aligned with the central axes of both the jet flow and evaporation source. The y-coordinate origin was placed closest to the source.

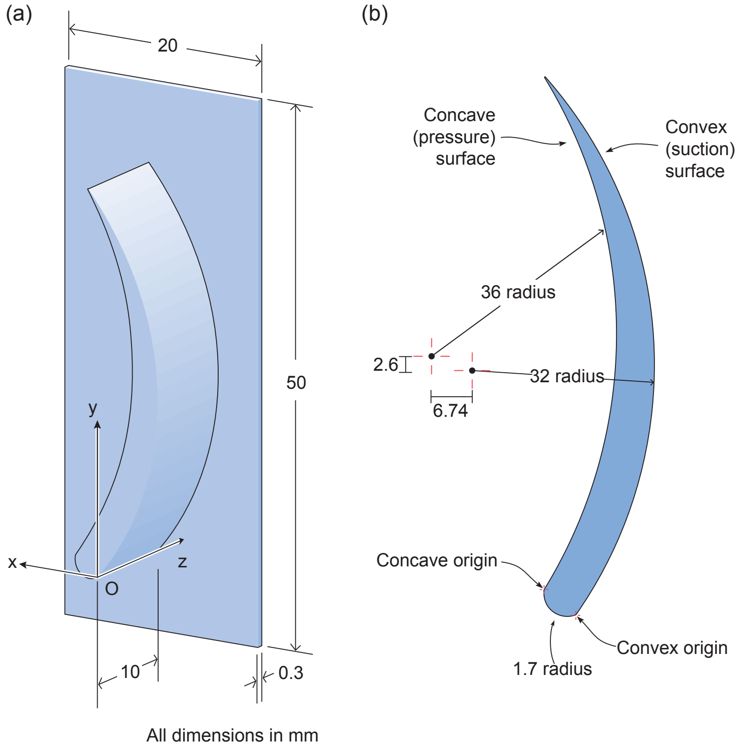

Figure 4.2: Geometry, dimensions, and coordinate system of the model airfoil and substrate to which it was attached.

The DSMC simulations were performed using a gas jet mixture consisting of 90 at. % helium and 10 at. % oxygen (identical to that used in subsequent experiments). Reflections from solid surfaces were modeled as fully diffuse [94]. Elemental Zr atoms were used as the simulated vapor species as parameters for the rare earth metals and the metal oxide molecules also present in the experimental vapor plumes were not available. The Zr parameters were deduced from experimental measurements on vapors of alkali group metals using a procedure proposed by

Fan [98]. A recent evaluation of the approximation procedure for PVD simulations found that it uniformly underestimated the mass flux at the substrate, but closely matched experimental results when normalized with the maximum incident flux [99]. The DSMC calculations proceeded in time steps of 10^{-7} seconds each of which included a free propagation and a collision step [94, 105].

The mesh developed to simulate the EB-DVD process with a stationary airfoil substrate is shown in Figure 4.3. The cell size in a DSMC mesh must be smaller than the local mean free path (MFP) between collisions to properly resolve flow gradients [114]. The simulated zone grid was optimized by performing numerous trials until converged results were attained at minimized computational cost. The grid used here consisted of 28 regions with differing grid size to account for variations in the MFP. The grid spacing was optimized to reduce computational time following the suggestions of Kannenberg and Boyd [114], and a species-weighting scheme was used to enhance the number of zirconium atoms in critical regions [115]. Due to the 2D planar simulation geometry, the circular annulus nozzle used in the experimental chamber must be modeled as a linear double slit. To verify the accuracy of the simulation geometry, cylindrical axisymmetric and planar XY simulations with a simple flat disk substrate geometry were performed and showed qualitatively similar flow fields.

Simulation flow parameters were calculated to closely model the conditions used in the experiments described later. The chamber pressure was fixed at the external grid boundaries. The upstream/downstream pressure ratio was set by the inlet carrier gas flow rate, which was adjusted through trial and error until the desired value was reached. The vapor flux emitted by the source was held constant for all the simulations at 8.8×10^{20} atoms $m^{-2}s^{-1}$. The simulations were executed

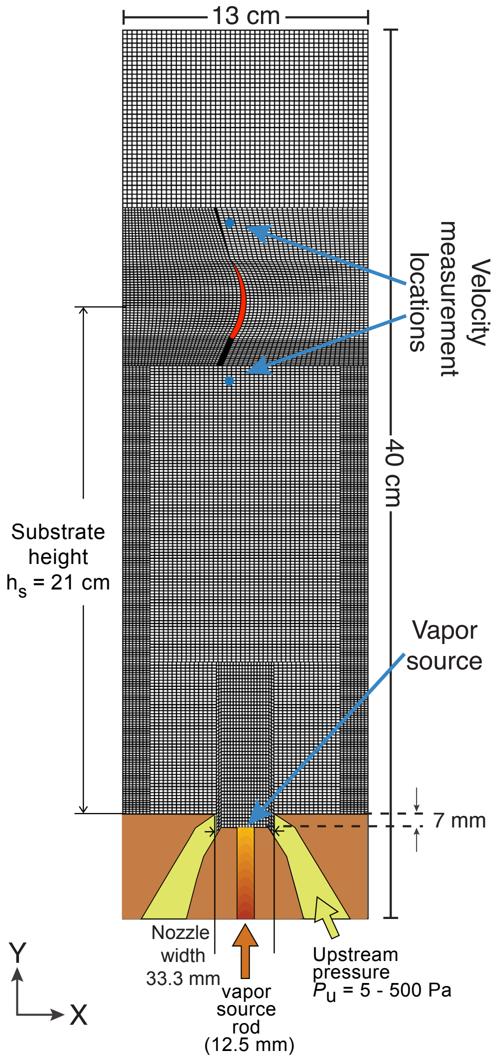

Figure 4.3: Schematic of DSMC simulation mesh containing 17217 cells. The cells immediately above the (green) vapor source have lengths of 2.52 μm.

for 325,000 time iterations to reduce statistical scatter. Between 1 and 10 million particles of He, O_2, and Zr were simulated to ensure adequate populations of trace deposition atoms. The simulations were performed on a 16-core Linux cluster with Intel E5000 series processors and ran for approximately 40 hours each.

4.4 Relationship of flow velocity and pressure ratio

The velocity of the under-expanded gas jet is controlled by the pressure ratio upstream and downstream of the gas inlet nozzle. Larger pressure ratios result in higher jet velocities [35, 116, 117]. The maximum jet velocity is given by the equations for isentropic flow of a compressible fluid through a choked nozzle [69];

$$\frac{p_u}{p_d} = \left[1 + \frac{\gamma - 1}{2} M^2\right]^{\frac{\gamma}{\gamma-1}} \tag{4.1}$$

$$\frac{T_u}{T_d} = 1 + \frac{\gamma - 1}{2} M^2 \tag{4.2}$$

where γ is the ratio of specific heats (5/3 for helium), M is the Mach number, P_u is the upstream pressure, P_d is the downstream chamber pressure, T_u is the upstream temperature in K, and T_d is the downstream temperature in K,. For an ideal gas, velocity, U, is related to M by;

$$U = M\sqrt{\gamma R_s T} \tag{4.3}$$

where R_s is the gas constant (2077 J/(kg K) for helium) and T is the absolute temperature in K. These equations can be combined to determine the maximum velocity downstream of the nozzle;

$$U_{max} = \sqrt{\gamma R_s T_d}\sqrt{\frac{2}{\gamma - 1}\left(\left(\frac{P_u}{P_d}\right)^{\frac{\gamma-1}{\gamma}} - 1\right)} \tag{4.4}$$

Flow velocities calculated with Equation 4.4 and measured from DSMC simulations at several pressure ratios are shown in Table 4.1. The DSMC simulations

Pressure ratio	Calculated U_{max} (m/s)	Simulated U_{max} (m/s)	U at 17 cm downstream of nozzle (m/s)
3	1048	960	170
5	1207	1045	345
7.5	1301	1294	519
10	1355	1406	589
13	1397	1501	613

Table 4.1: Comparison of calculated and simulated gas jet velocities at several pressure ratios. Simulations were performed at a chamber pressure of 45 Pa without the presence of a vapor species.

were performed at 45 Pa and used the simulation grid shown in Figure 4.3. Only carrier gas atoms were present in the simulations; no vapor was emitted from the source. The maximum velocities show good agreement between the calculated and simulated values. The simulated velocities on the flow axis 17 cm downstream of the inlet nozzle are also shown in Table 4.1 and demonstrate a significant reduction from the maximum jet velocity. These downstream velocities are more representative of flow conditions near the substrates.

4.5 Simulation Results

4.5.1 Flow Fields

If the nozzle design, upstream gas temperature and composition, and pressure within the deposition chamber are held constant, the flow field is controlled only by the ratio of pressures before and after the expansion nozzle [118]. The relationship between the gas velocity, measured at test locations 15 mm up- and downstream of the substrate (see Figure 4.3), is shown for four nozzle pressure ratios in Table 4.2.

Pressure ratio	Velocity upstream of substrate (m/s)	Velocity downstream of substrate
2.0	288	88
3.0	363	104
4.5	452	125
7.0	553	158

Table 4.2: He jet velocities upstream and downstream of the substrate with various pressure ratios. at a chamber pressure of 16 Pa.

The velocities increase with pressure ratio and are much higher upstream of the substrate indicating a significant flow resistance created by the substrate. The Zr vapor atom concentration in the gas jet is also influenced by the pressure ratio. The steady state vapor concentration distributions for three pressure ratios are shown in Figure 4.4. The overall vapor concentration decreases with increasing pressure ratio due to the reduced residence time in the jet as velocity increases. Increasing pressure ratio also leads to a narrowing of the gas jet. This results from the higher axial jet velocity and vapor atom momentum, which reduces the transverse scattering effects of collisions with background gas atoms. A large vapor depleted (dark blue) region surrounds the substrate. This depleted region is a result of vapor atoms scattering from the gas jet onto the substrate surface where they are allowed to stick and are then removed from the simulation. As the pressure ratio was increased, the depleted region behind the substrate dramatically increased in area due to the higher jet momentum. However, at low jet speeds, transverse diffusion of the vapor had begun to significantly reduce the non-uniformity in evaporant concentration.

When the nozzle pressure ratio was held constant, the flow field was dependent only upon the deposition chamber pressure. Increasing the chamber pressure reduced the jet velocities both before and after the substrate, as indicated in Table 4.3. The velocity downstream of the substrate was again always much lower than

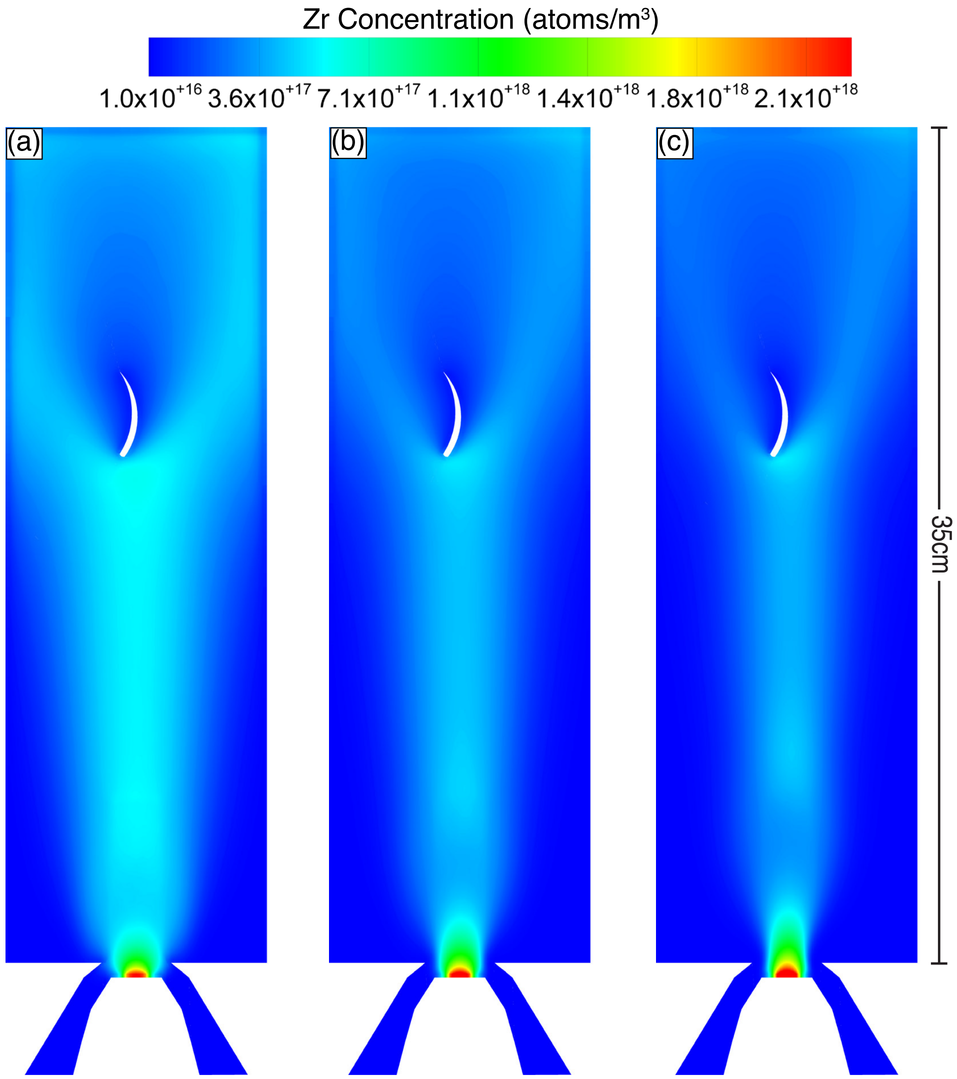

Figure 4.4: Contour plots of Zr vapor atom concentration for a chamber pressure of 16 Pa and three nozzle pressure ratios: (a) 2.0, (b) 4.5, and (c) 7.5.

that found upstream; especially at high chamber pressures. The effects of changing the chamber pressure on vapor concentration within a jet plume are shown in Figure 4.5. As the pressure increased, the vapor in these slow jets became much more concentrated on the center-line of the carrier gas jet, and the vapor depleted region behind the substrate decreased in area due to the decrease in the axial velocity component of the jet. The slow jet's increased vapor atom concentration was a

Chamber pressure (Pa)	Velocity upstream of substrate (m/s)	Velocity downstream of substrate
7.5	317	166
16	288	88
30	264	50
45	231	35

Table 4.3: He jet velocities upstream and downstream of the substrate at various chamber pressures for a fixed pressure ratio of 2.0. The velocity decreases with increasing chamber pressure.

consequence of the increased residence time of vapor atoms in the jet plume, while the increased chamber pressure (smaller mean free path) confined the vapor to the center of the jet by reducing the rate of lateral diffusion.

4.5.2 Atom Trajectories

To gain better insight into the scattering processes responsible for vapor depletion near the substrate, we calculated the He jet streamlines in the vicinity of the substrate by determining the average trajectories along the simulation grid. Those for a representative deposition configuration (a chamber pressure of 16 Pa and a pressure ratio of 2) are shown in Figure 4.6 overlaying the local pressure distribution. The streamlines (the time averaged helium atom trajectories) generally curve towards regions of lower pressure and away from those of higher pressure. There are regions of high pressure at the airfoil's leading edge and along its concave surface. Along the concave side, the streamlines are initially deflected towards the surface, and later bend away from the substrate. Along the convex surface, the local pressure was reduced and the collisional mean free path increased. As a result, fewer scattering collisions occur and the He atoms travel a straighter path.

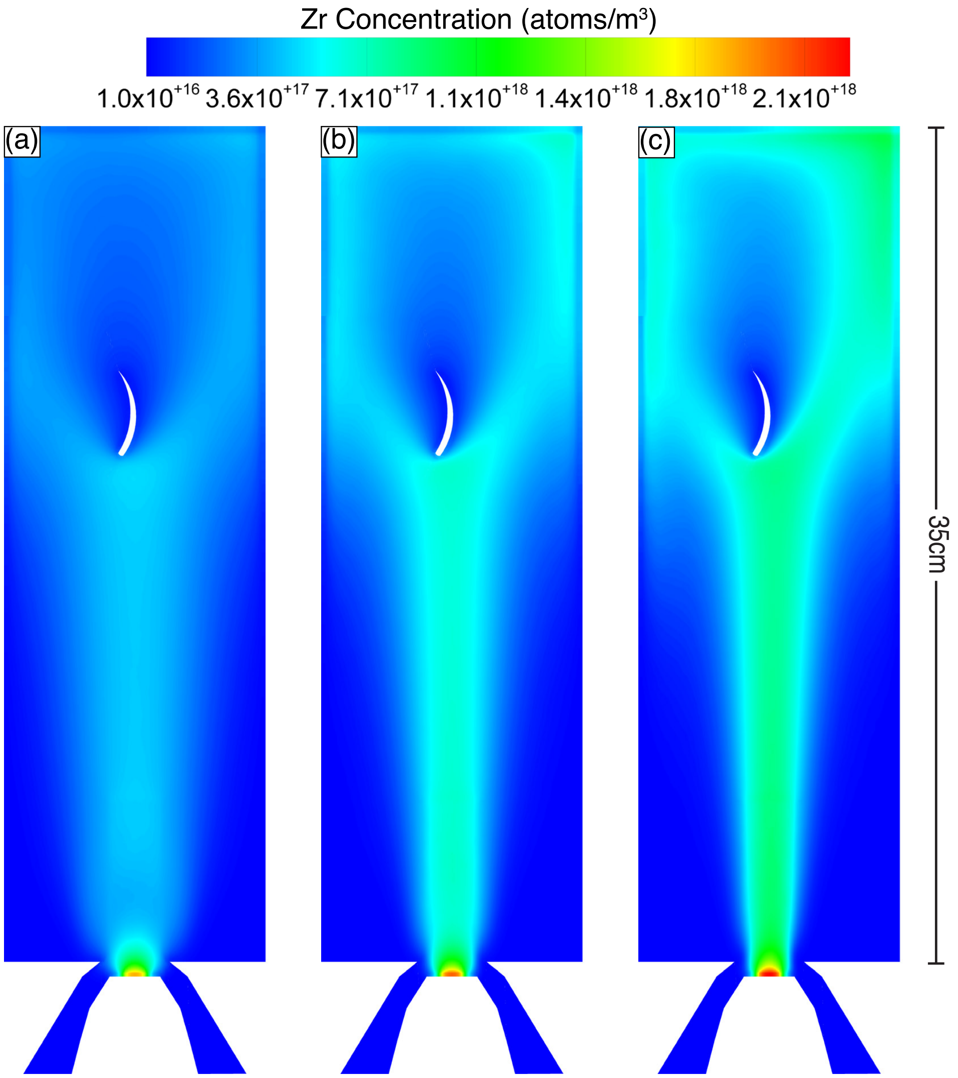

Figure 4.5: Contour plots of Zr concentration at a nozzle pressure ratio of 2.0 and chamber pressures of (a) 16 Pa, (b) 30 Pa, and (c) 45 Pa.

The vapor atom streamlines at the above conditions were also determined and are shown, along with the trajectories of three hypothetical Zr atom classes that impact the airfoil, in Figure 4.7. Each solid circle represents a collision between a vapor atom and an atom in the jet flow. The dashed lines indicate the vapor atom's trajectory between collisions. The mean free path between collisions for this example was 3-4 mm near the substrate, but varies with pressure within the

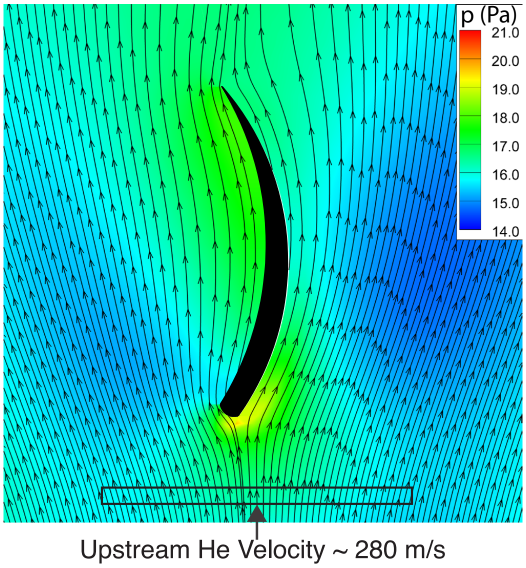

Figure 4.6: He streamlines and pressure contours near the substrate at a chamber pressure of 16 Pa and nozzle pressure ratio of 2.0.

deposition chamber. The three paths shown in Figure 4.7 exemplify three classes of condensation. The center path results in deposition onto the leading edge of the airfoil at near normal incidence to the surface and with little deviation from the original direction of the jet. The atoms in the outer paths are knocked randomly left and right by collisions. In the gas jet far from the substrate, there are an equal number of scattering collisions to the left and right. However near the substrate surface, a collision can scatter a vapor atom towards, and onto the substrate. This destroys the directional balance that exists far from the substrate, and results in more vapor atoms traveling towards the substrate than away from it. As a result, the vapor streamlines bend towards the substrate as shown in the figure. In both cases, atoms are deposited from streamlines onto surface regions that are not in the line-of-sight of the vapor source and enables the possibility of non-line-of-sight (NLS) deposition.

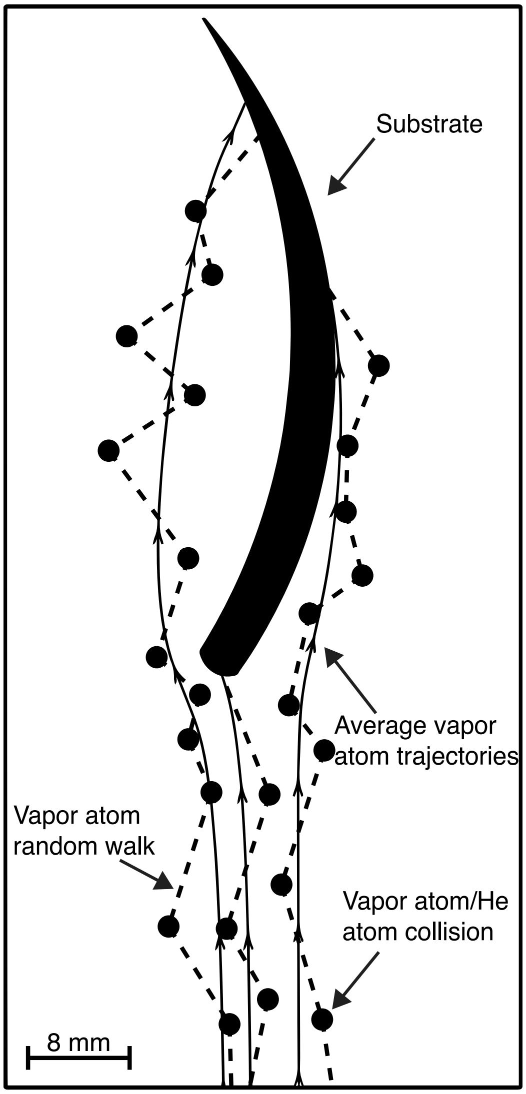

Figure 4.7: Schematic illustration demonstrating the paths of vapor atoms that deposit on the concave surface, leading edge, and convex surface. The random walk path of a hypothetical individual atom is overlaid with the average trajectory of vapor atoms in the region.

To investigate the effect of pressure ratio variation (at a fixed chamber pressure of 16 Pa) upon the deposition process, vapor atom streamlines for pressure ratios of 2, 4.5, and 7 are shown in Figure 4.8. We define the capture width as the cross-section of the vapor jet that is eventually deposited on the substrate surface. The capture width is defined 13.5 mm upstream of the substrate's leading edge, before the jet is significantly influenced by the substrate. The capture width is asymmetric around the center line of the airfoil with the majority of the included streamlines terminating on the convex substrate surface. A large capture width increases the vapor flux incident upon the substrate surface and the deposition efficiency (the ratio of deposited atoms to atoms emitted by the source). The simulations show that vapor atom streamlines nearest to the substrate's centerline result in deposition at the front of the airfoil, while atoms in streamlines further from the centerline are more likely to deposit near the tail. The capture width in Figure 4.8 decreases with increased pressure ratio due to the greater momentum of the vapor atoms. Fast moving vapor atoms are deflected less towards the substrate by scattering collisions than slower ones found at lower pressure ratios, resulting in fewer streamlines terminating on the substrate surface.

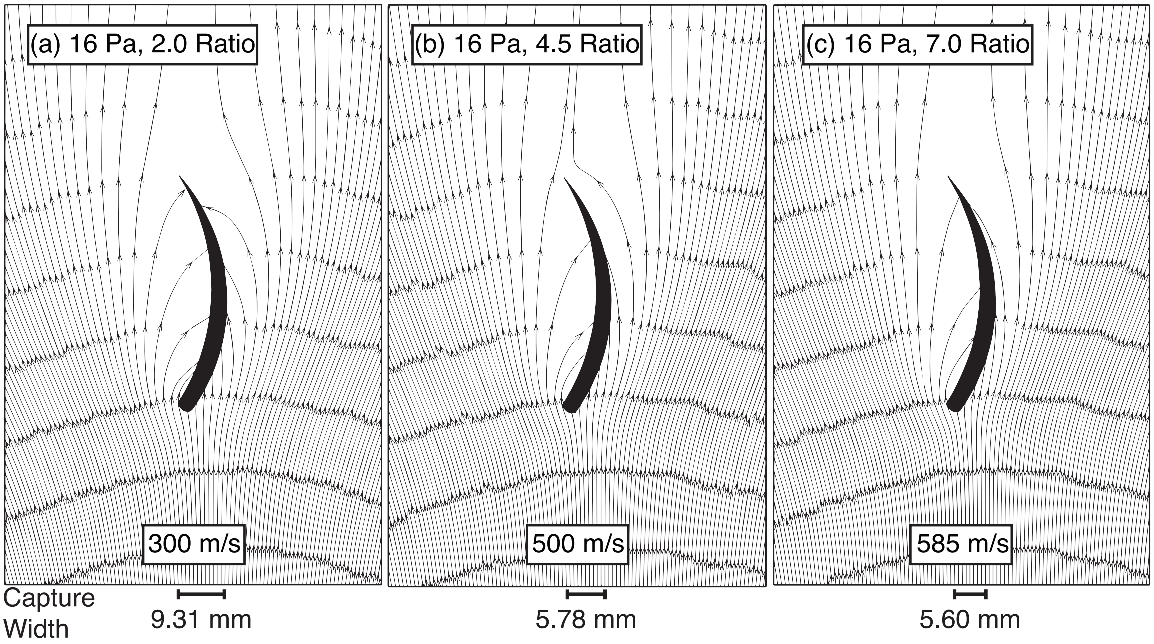

Figure 4.8: Zr vapor atom streamlines for at a fixed chamber pressure and pressure ratios of (a) 2.0, (b) 4.5, and (c) 7.0. The vapor atom capture distance is noted on each flow field. The capture distance decreases with increasing pressure ratio (jet speed), resulting in a reduction of deposited flux onto the substrate surface.

The effect of changing the deposition chamber pressure (at a fixed pressure ratio of 2.0) on the vapor atom trajectories is shown in Figure 4.9. As the chamber pressure was increased from 7.5 to 45 Pa, the capture width decreased from 12.5 to 5.8 mm. At high pressures (i.e. shorter mean free path and lower jet velocity), the majority of the substrate intersecting streamlines end near the leading edge. Streamlines outside of this region are curved away from the substrate by the high pressure regions surrounding it. Although the carrier jet is moving slowly, the streamlines must make a large divergence from the jet axis. At lower chamber pressures, the mean free path is greater, and the capture distance is larger with streamlines intersecting the substrate uniformly. The reduced rate of scattering collisions results in vapor streamlines with more gradual curvature. The streamlines that do not terminate at the substrate are much less perturbed than those at higher pressures indicating a reduced influence of the substrate on the carrier gas jet.

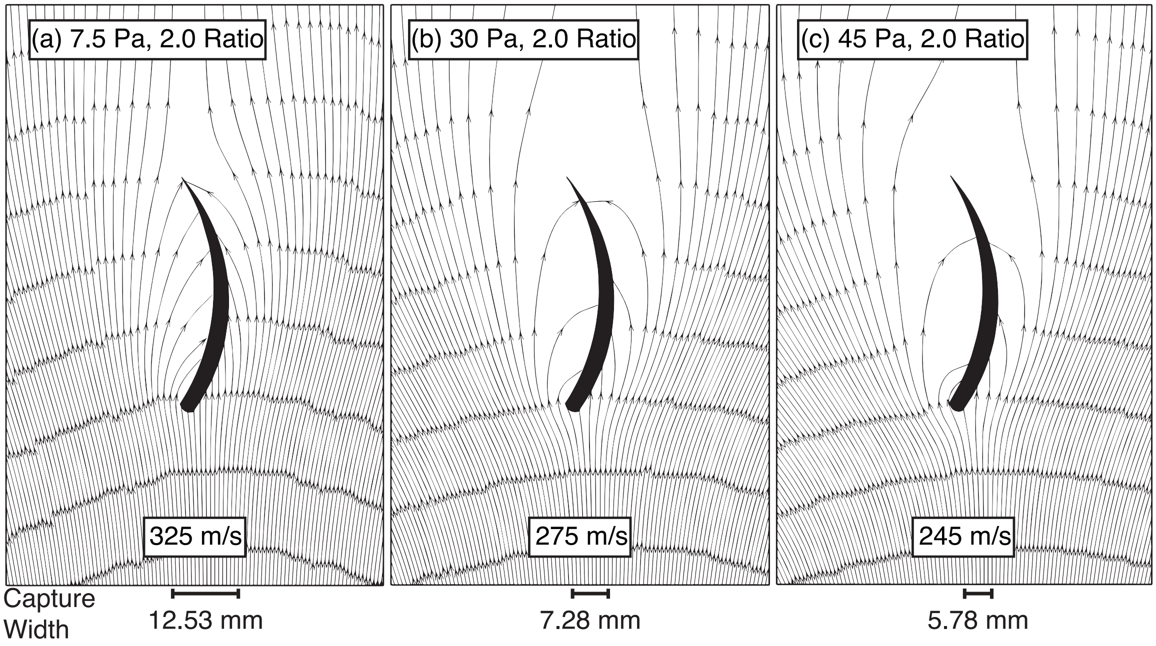

Figure 4.9: Zr vapor atom streamlines at a fixed pressure ratio of 2.0 and chamber pressures of (a) 7.5 Pa, (b) 30 Pa, and (c) 45 Pa. The capture distance decreases with increasing chamber pressure.

It is interesting to note that while a larger capture width is correlated with a larger fraction (width) of the vapor plume impacting the substrate surface; it doesn't correlate with the largest vapor flux impacting the airfoil surface. This disparity arises because of the dependence of vapor concentration in the jet with flow conditions as discussed in Section 4.5.1. The condition with the largest capture widths in Figures 4.8 and 4.9 (7.5 Pa and pressure ratio of 2) has the lowest vapor density. Thus, although it captures a larger volume fraction of the vapor, the lower vapor concentration results in a smaller total flux. The consequences of this will be discussed below.

4.5.3 Coating Thickness

By assuming a sticking factor of unity, the local flux deposited on the substrate surface can be determined from the DSMC simulations. If the deposited coating's density does not change with position on the airfoil surface, this flux is then proportional to coating thickness. To deduce the vapor flux profile on the airfoil, the concave and convex sides of the simulation substrate were each divided into 40 surface elements that corresponded to the surrounding DSMC simulation grid, and the flux incident to each region was then calculated. Incident flux profiles for the concave and convex surfaces of the airfoil are shown for several pressure ratios (at a fixed chamber pressure of 16 Pa) in Figure 4.10. Along the convex surface (Figure 4.10(a)), the flux near the leading edge of the airfoil decreases with increasing pressure ratio. This decrease indicates that larger areas of the substrate become shadowed from the vapor in the jet due to increased vapor atom velocity. This is also observable in Figure 8 where depositing streamlines at high pressure ratios gradually deflect towards the substrate. The flux profiles along the convex surface

(Figure 4.10(b)) show a much reduced dependence on the pressure ratio. For all ratios, the flux maximum is located at the leading edge of the airfoil. This results from the region near the leading edge being in the line-of-sight of the vapor source. The largest flux is recorded at the highest pressure ratio of 7.0. This arises because the vapor is highly collimated, and does not need to undergo scattering collisions to be deposited on the leading edge.

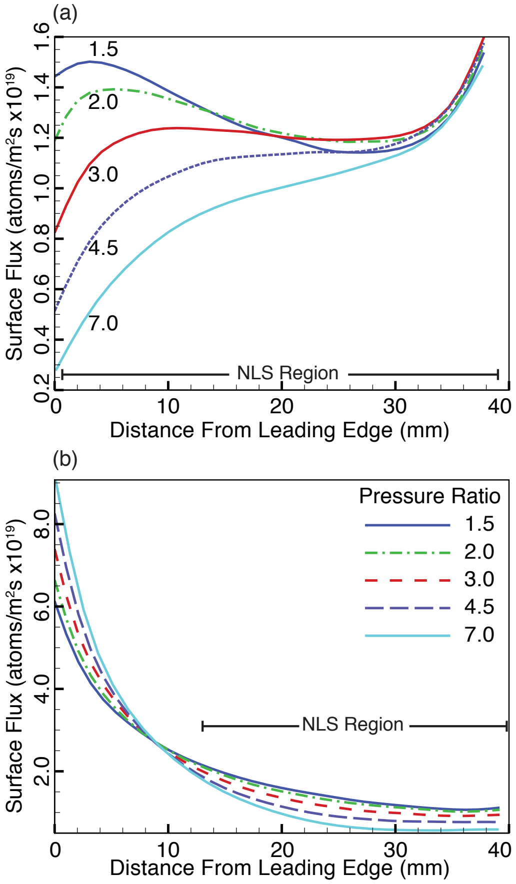

Figure 4.10: Flux profiles along the (a) concave and (b) convex airfoil surfaces at a fixed chamber pressure of 16 Pa and varying pressure ratio. Regions on the substrate not within the line-of-sight of the vapor source are indicated on the plots as "NLS Region."

The flux profiles also vary with the chamber pressure. The profiles for several chamber pressures (at a fixed pressure ratio of 2.0) are shown in Figure 4.11. At the lowest chamber pressure, the concave surface flux, Figure 4.11(a), is lowest at the leading edge and gradually increases towards the tail. At this chamber pressure, the mean free path is large (5 mm at 7.5 Pa), and the vapor atoms travel a significant distance along the substrate before scattering onto the surface. The vapor atom concentration in the jet is only slowly depleted due to the infrequent scattering, and additional deposition occurs due to the reduced diffusion distance needed to impact the protruding tail. As the chamber pressure rises, the location of highest flux on the concave side moves from the tail to the tip of the airfoil. The most uniform concave surface deposition (at a pressure ratio of 2) occurs at an intermediate pressure of 16 Pa. Along the convex surface (Figure 4.11(a)) the flux profiles show little dependence upon the chamber pressure as in Figure 4.10(b).

Examination of Figures 4.10 and 4.11 reveals that the best coating uniformity occurs at moderate chamber pressures and pressure ratios. These slow flow conditions provide an optimum balance between mean free path and vapor velocity. Higher chamber pressures result in shorter mean free paths, and atoms experience more collisions which direct them towards the substrate. However, the atoms also move with lower momentum, which allows scattering collisions to rapidly direct the atoms to the substrate. Lower pressures result in longer mean free paths, and atoms can travel greater distances without depositing onto the substrate. Changing the pressure ratio influenced the flux profile by controlling the momentum of the incident vapor atoms. At high pressure ratios the vapor atoms had large momentums, which increased the distance atoms travelled before depositing onto the substrate. A very small pressure ratio (~1.5) resulted in atoms depositing quickly, near the leading edge of the substrate.

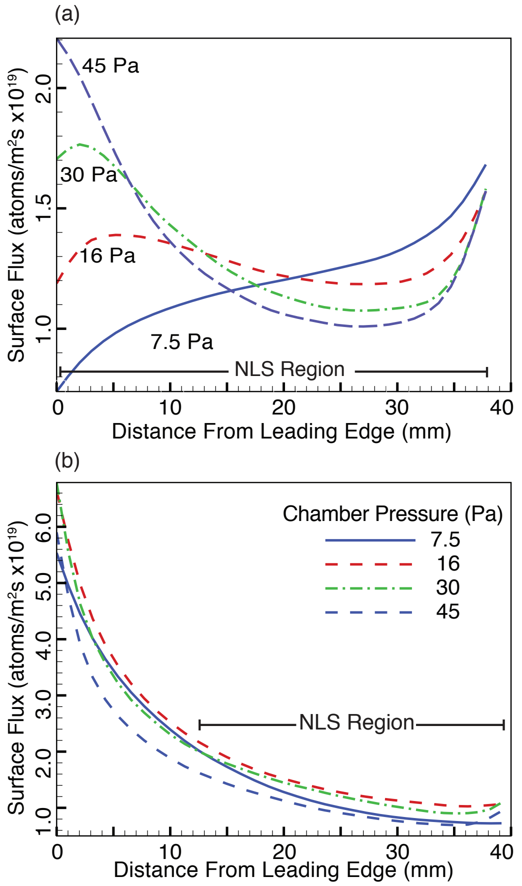

Figure 4.11: Flux profiles along the (a) concave and (b) convex airfoil surfaces for a pressure ratio of 2.0 and varying chamber pressures.

4.6 Experimental Comparisons

To evaluate the validity of the coating flux and thickness predictions above, thermal barrier coatings were experimentally deposited upon identical airfoil substrates to those used in the simulations. The vapor source was a 1.25 cm diameter zirconia rod triply doped with yttria, gadolinia, and samaria obtained from TCI ceramics, Inc. (Bethlehem, PA). The surface of the source rod was evaporated using a 70 kV/2.45 kW electron gun in the EB-DVD system schematically illustrated in Figure 4.1. Model airfoil-shaped substrates were milled from 303 grade stainless steel plates, grit blasted and cleaned prior to deposition of the ceramic coating. No bond coat was used since we were not evaluating the durability of the coating. The substrates were first heated to 500 °C at 16 Pa for 30 minutes to clean the surface and then heated to 1000 °C during deposition. During depositions the substrate was held at a fixed orientation (no rotation) with the airfoil leading edge nearest to the source as shown in Figure 4.1. Coatings were deposited at a chamber pressure of 16 Pa using an upstream/downstream nozzle pressure ratio of 3.5. The carrier gas flow rate was set to 9.0 slm of helium, and 1.0 slm of oxygen. After deposition, the samples were sectioned and the thickness and microstructure of the coating examined at various positions using a scanning electron microscope.

4.6.1 Experimental Results

The experimentally measured coating thickness (normalized by the maximum value on each side) for the convex and concave airfoil surfaces is compared with simulation results in Figure 4.12. SEM images of the coating at several locations around the substrate are shown in Figure 4.13 for an experimental deposition performed at 16 Pa and a pressure ratio of 3.5. The coating was thickest on the airfoil's leading edge, while the thinnest region was near the trailing edge. The experimental and simulated thickness profiles are very similar on both surfaces. On the convex surface, the trends were quite similar to those found in Figures 4.10(b) and 4.11(b). Along the concave surface, the experimental profile was sensitive to the precise point on the leading edge where the first thickness measurement was recorded. Near the front of the airfoil, in the region that is within the line-of-sight to the source, the coating is thick. However, this thickness quickly decreases with increasing distance along the airfoil. The non-line-of-sight region that occupies most of the airfoils concave surface has a fairly uniform thickness coating that slowly increases down the length of the substrate. The profile demonstrates the vapor flux variation between line-of-sight and non-line-of-sight deposition.

(a) concave surface

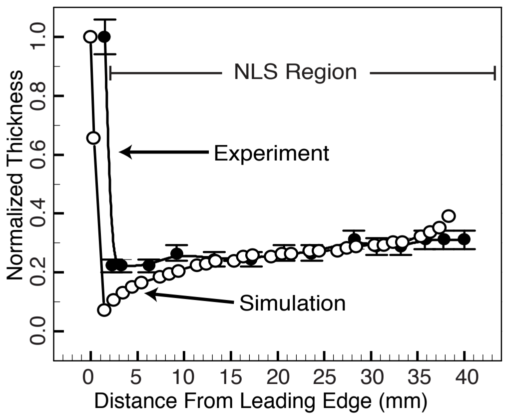

(b) convex surface

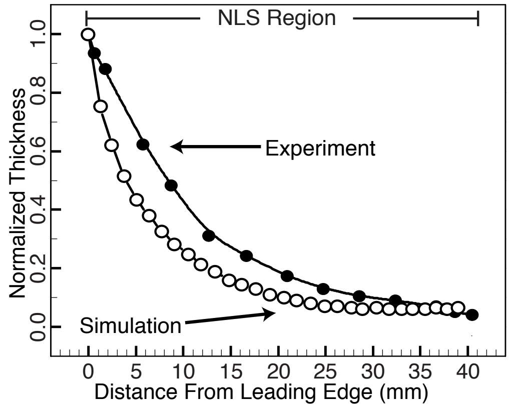

Figure 4.12: Comparison of experimental and simulated thickness profiles along (a) concave and (b) convex surfaces. The experiment and simulation were both conducted at a chamber pressure of 16 Pa and pressure ratio of 3.5.

The microstructure of the coating was also found to vary along the substrate (Figure 4.13). At the leading edge, the columns are oriented with angles approximately equal to the local substrate surface normal. Along the convex and concave surfaces, the growth angles tilt away from the surface normal and towards the incident gas jet. This column orientation variation is usually thought to be governed by the incidence angle of the vapor with respect to the local surface normal [23, 82].

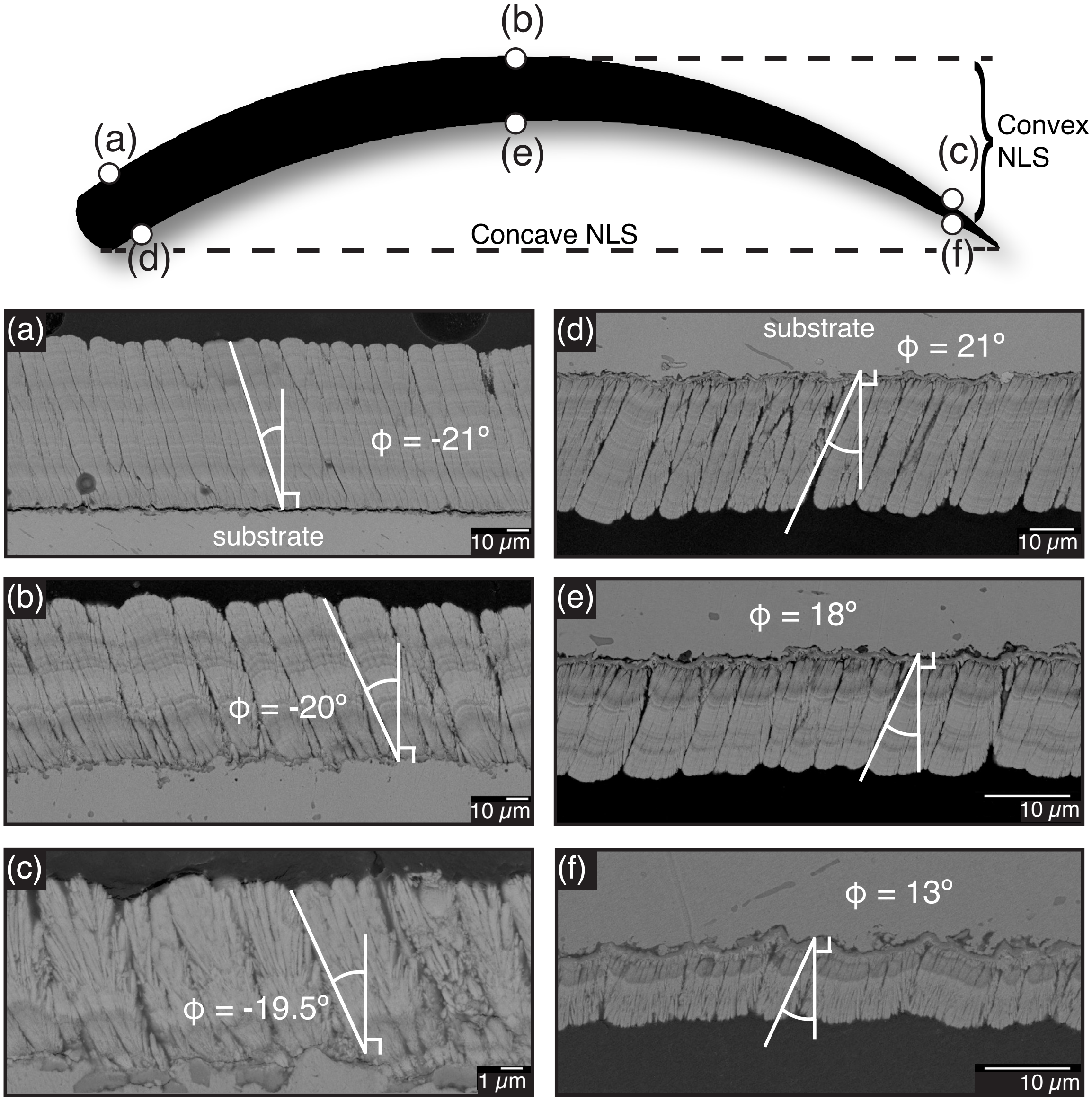

Figure 4.13: SEM images of the coating at various locations on the airfoil substrate with the average columnar growth angle indicated. Note the differences in magnification between images.

4.6.2 Incidence Angle Distribution (IAD)

The incident angle distributions (IAD) for a simulation corresponding to the experiment were determined from the DSMC results and were found to vary greatly along the airfoil, as shown in Figure 4.14, which shows results at the same locations as

Figure 4.13. On the leading edge of the airfoil (not shown), the IAD was narrowly distributed around normal incidence, indicating that the vapor atoms were impacting the surface with minimal scattering from the main plume. In the less shadowed regions, (Figure 4.14(a, b, and d)) the IADs were also narrow, but now skewed away from normal incidence. The broadest IADs (Figure 4.14(c, e, and f)) were found in shadowed regions along the convex and concave sides. The broad IADs in these regions result from the scattering collisions the vapor must experience to deposit in these regions.

The IADs are also modified by the chamber pressure and pressure ratio. The effects of these variations are shown in Figure 4.15 using the IAD experienced by the surface on the center of the concave side (point b in Figures 4.13 and 4.14). Increasing the chamber pressure causes a broadening of the IAD in shadowed regions (due to increased scattering). The peak of the IAD moves away from the surface normal with decreasing chamber pressure. An extreme case is shown for a simulation using conventional PVD conditions (pressure of 0.02 Pa) in Figure 4.15(b). The PVD angle of incidence is sharply peaked at an angle far from the local surface normal.

4.6.3 PVD Versus DVD

All of the configurations of the DVD environment provided greatly improved coating uniformity compared to PVD. To demonstrate the improvement, simulations were conducted using an identical simulation grid, but with PVD-like deposition conditions. The chamber pressure was held at 0.02 Pa, while the carrier gas jet was turned off. The vapor evaporation rate was set identical to the DVD simulations.

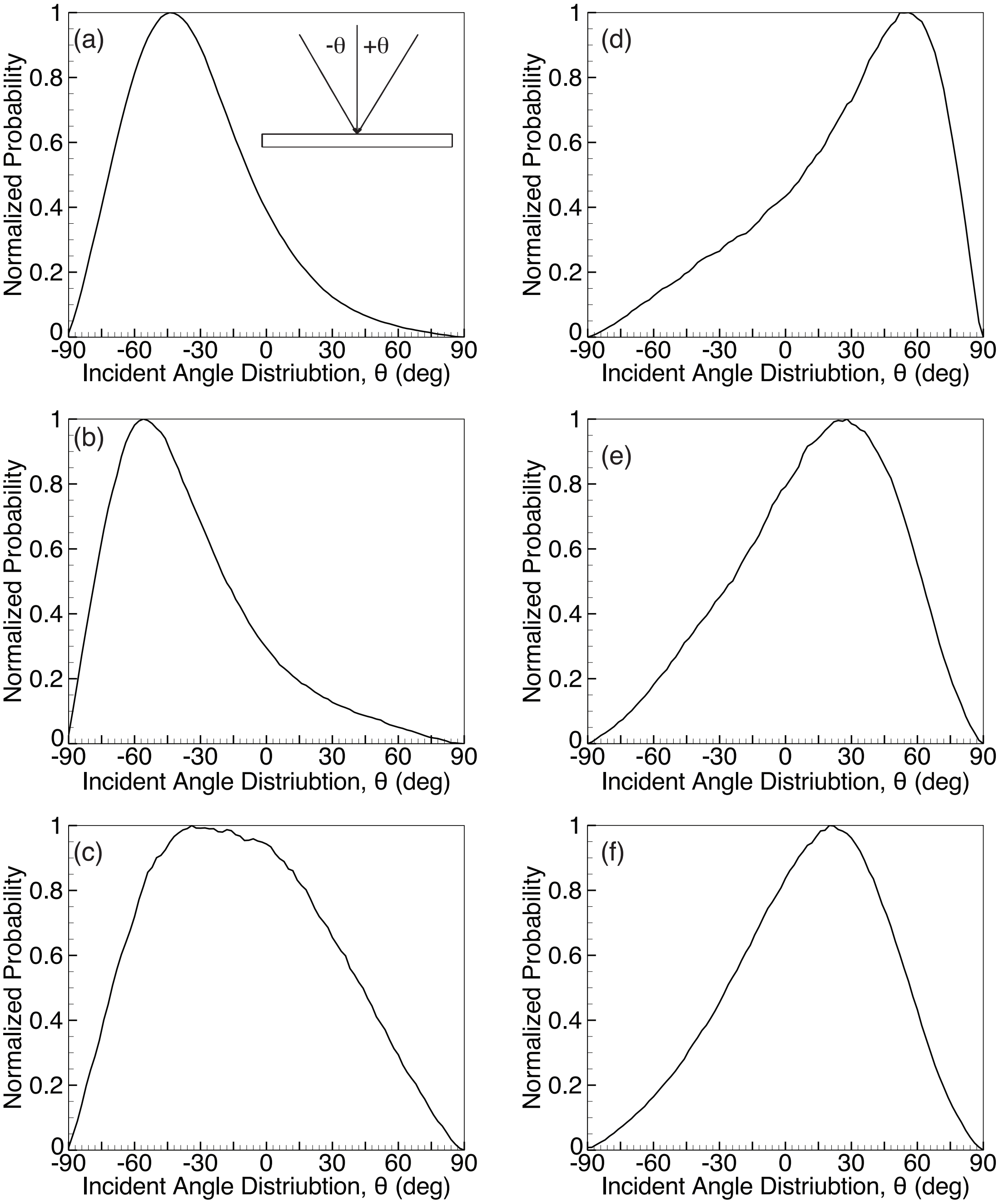

Figure 4.14: Incident angle distribution at the six substrate surface locations defined in Fig. 4.13 for a simulation at 16 Pa and pressure ratio of 3.5. The IAD is defined with the local surface normal at $\theta = 0$ as shown at the top of the figure.

(a) Pressure ratio effect

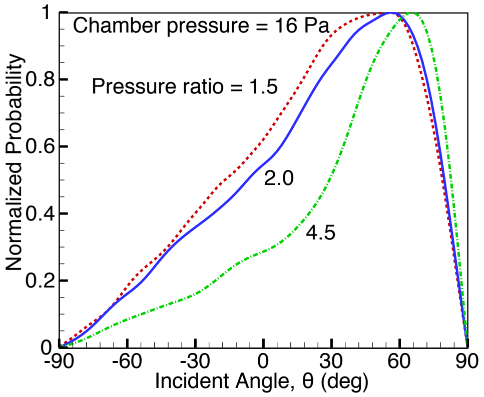

(b) Chamber pressure effect

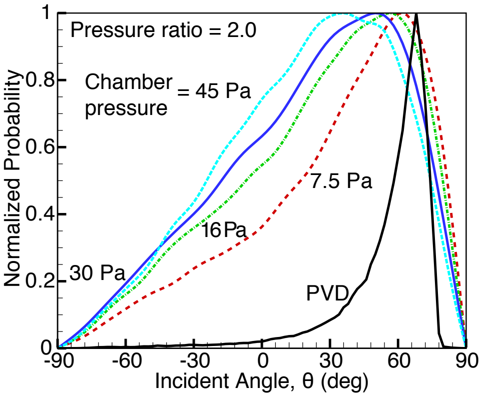

Figure 4.15: IAD at center of concave surface (location e in Fig. 4.13) showing the effects of varying (a) the nozzle pressure ratio and (b) the chamber pressure. The result for a conventional (low pressure) PVD simulation is also shown on (b).

Figure 4.16 shows the flux along the concave surface for PVD and DVD simulations where the DVD simulation was performed with a 16 Pa chamber pressure and a 3.0 pressure ratio. The flux impacting the airfoil surface was generally one to two orders of magnitude higher under DVD conditions than PVD. The mean free path under PVD conditions was approximately 0.5 m. This distance is greater than the length of the simulation domain (0.4 m) and thus the average vapor particle experienced no collisions during its flight. The lack of scattering is reflected on the plot of IADs at different chamber pressures in Figure 4.15. The PVD conditions result in the narrowest distribution with a maximum far from the local substrate normal. The peak in the angular distribution is very close to the angle the substrate surface makes to the incident vapor rays.

(a) concave surface

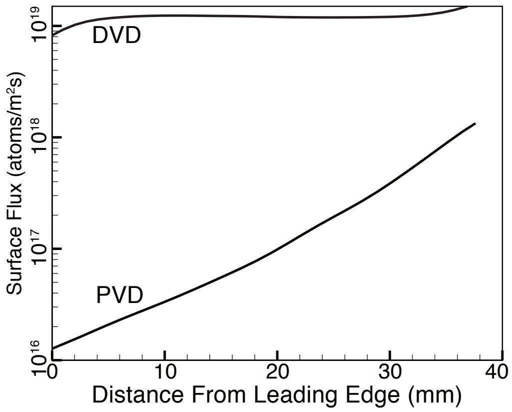

(b) convex surface

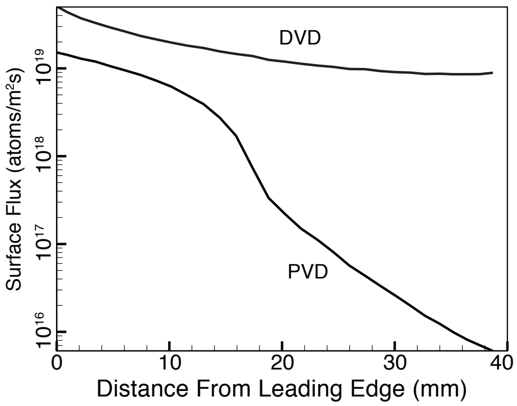

Figure 4.16: Comparison of PVD and DVD flux profiles along (a) concave and (b) convex substrate surfaces. The DVD simulation was conducted at a chamber pressure of 16 Pa and pressure ratio of 2.0. The PVD simulation was conducted at a chamber pressure of 0.02 Pa.

4.7 Discussion

Coating uniformity is determined by the binary scattering conditions in chamber regions near the substrate surface. The uniformity is controlled through both the rate of scattering collisions near the substrate and the momentum imparted from the collisions. In the substrate-adjacent regions, an incident vapor atom has the possibility of undergoing collisions with three classes of carrier gas atoms:

- Type I: The vapor atom collides with a carrier gas atom from the main jet column. These collisions serve to knock the atom further away from the source and in a random direction perpendicular to the gas jet axis.
- Type II: The vapor atom collides with a carrier gas atom that has struck and randomly scattered from the substrate surface. These collisions decrease the likelihood that a vapor atom will eventually reach the substrate surface by imparting momentum away from the substrate. These types of collisions are prevalent near the leading edge and along the convex surface of the airfoil (Figure 4.6). Many carrier gas atoms strike this surface region and reflect with high velocities. These reflected atoms collide with the incident vapor atoms and deflect their trajectories away from the substrate surface.
- Type III: The atom collides with a background atom of the carrier gas. These background atoms have random motions, but their collisions will generally push the vapor atom towards the center of the carrier gas plume. Background gas atoms must travel through the the midpoint of the vapor plume's cross section before they will scatter vapor atoms away from the substrate.

Type I and III collisions can be considered as enabling deposition near the collision location, while type II collisions knock the vapor atoms away from the local substrate surface. The influence of type II collisions can be seen in the streamlines at different chamber pressures shown in Figure 4.9. As the chamber pressure increases, the number of atoms scattering from the substrate surface also grows, which increases the number of type II collisions and causes the vapor atom streamlines to deflect farther from the substrate surface. As a result, vapor atoms either impact near the leading edge, or are likely to travel past the substrate.

The three classes of collisions can be manipulated with the chamber pressure and the pressure ratio. Modifying the chamber pressure does little to change the momentum imparted during the collisions, but it does adjust the frequency of collisions. Modifying the pressure ratio doesn't change the rate of collisions, but alters the momentum of the carrier gas jet. The higher jet momentum causes the atoms to travel further in the axial direction between collisions, and results in the vapor atoms experiencing fewer collisions as they travel past the substrate.

The results above show the importance of two fundamental quantities that determine coating uniformity: the vapor atom concentration and mean free path. Vapor atom concentration is of great importance for deposition onto macroscopic, non-line-of-sight substrates. Although the carrier gas may flow along the entire surface of a substrate, depletion of vapor atoms can prevent deposition onto a non-line-of-sight region. This vapor depletion can be controlled via the mean-free path near the substrate. With larger mean free paths, scattering collisions are less frequent, allowing the vapor atoms to travel further in a straight line. A large mean free path will allow deep penetration into a non-line-of-sight region, but may prevent the necessary collisions for eventual deposition onto the surface. Thus, ideal deposition conditions are found through balancing these two parameters, which occurs at moderately low pressure ratios (2-3) and moderate chamber pressures (~16 Pa) where the jet flows are slow.

The paths of three individual vapor atoms along with the average streamline trajectories in their vicinity are shown in Figure 4.7. The mean free path distance that atoms travel between collisions varies along the streamline path. Each collision with the carrier gas knocks the vapor atom along the streamline, but also introduces random movement perpendicular to the carrier gas axis. Far away from the substrate the mean free path is large (several mm) but generally becomes shorter closer to the substrate due to the increasing local pressure. The mean free path remains comparably large compared to the substrate dimensions, which maintains the importance of the random motion imparted by collisions with the background gas. The random collisions cause incident atoms to impact the substrate at random angles and results in a broad IAD. The schematic in Figure 4.7 also shows how a broad IAD is created through scattering collisions. The random direction of motion allowed between collisions enabled individual atom trajectories to deviate substantially from the average ones represented by the streamlines.

Further insight into the coating process can be obtained by comparing the measured angles of the growth columns with the Tangent Rule using the simulated IADs. Nieuwenhuizen and Haanstra first proposed the Tangent Rule for predicting the inclination angle of growth columns deposited from a mono-angle incident flux in 1966 [112]. By measuring the growth angle of the deposited columns, one can determine the angle of incidence through the relationship;

$$2tan(\phi) = tan(\theta) \tag{4.5}$$

where θ is the flux angle, and ϕ is the columnar growth angle (both measured from the local surface normal). To test its validity with non-line-of-sight deposition, the rule was evaluated at locations around the substrate to determine its applicability

Measurement region	Peak vapor atom incident angle (θ) (deg)	Predicted columnar growth angle (ϕ_p) (deg)	Measured columnar growth angle (ϕ_m) (deg)	Percent difference with simulation (%)
Leading edge	3	1.5	2	7
Center of convex surface	-64	-45.7	-22	70
Center of concave surface	28	15	21	33

Table 4.4: Comparison of columnar growth angles predicted by the Tangent rule, and measured from experiments.

in non-line-of-sight regions. Table 4.4 shows the results of applying the tangent rule at various points on the substrate surface. The rule is accurate at locations in line-of-sight regions, but performs poorly in non-line-of-sight regions. This is not unexpected, as the Tangent Rule was not designed to evaluate coatings deposited from vapor fluxes with a wide IAD. Clearly alternative methods are necessary to predict columnar growth characteristics in regions where condensation occurs with a broad IAD.

4.8 Summary and Conclusions

Coatings have been deposited onto a stationary airfoil substrate using a gas-jet assisted DVD technique. Complete coverage of the substrate was achieved, which is impossible using traditional PVD. DSMC simulations were found to accurately predict coating thickness trends with both substrate surface location and deposition conditions. The thickness uniformity and coating porosity were found to be sensitive to the deposition chamber pressure and gas jet velocity, both of which manipulate the mean free path of the vapor atoms. The optimum conditions for creating uniform thickness distributions have been identified.

Chapter 5

Microstructure of Vapor Deposited Coatings on Curved Substrates[1]

5.1 Synopsis

Thermal barrier coating systems consisting of a metallic bond coat and ceramic over layer are widely used to extend the life of gas turbine engine components. They are applied using either high-vacuum physical vapor deposition techniques in which vapor atoms rarely experience scattering collisions during propagation to a substrate, or by gas jet assisted (low-vacuum) vapor deposition techniques that utilize scattering from streamlines to enable non-line-of-sight deposition. Both approaches require substrate motion to coat a substrate of complex shape. Here, direct simulation Monte Carlo and kinetic Monte Carlo simulation methods are combined to simulate the deposition of a nickel coating over the concave and convex

---

[1] Adapted from a technical article submitted to the *Journal of Vacuum Science and Technology A*[119].

surfaces of a model airfoil, and the simulation results are compared with those from experimental depositions. The simulation method successfully predicted variations in coating thickness, columnar growth angle, and porosity during both stationary and substrate rotated deposition. It was then used to investigate a wide range of vapor deposition conditions spanning high-vacuum physical vapor deposition to low-vacuum gas jet assisted vapor deposition. The average coating thickness was found to increase initially with gas pressure reaching a maximum at a chamber pressure of 8-10 Pa, but the most uniform coating thickness was achieved under high vacuum deposition conditions. However, high vacuum conditions increased the variation in the coatings pore volume fraction over the surface of the airfoil. The simulation approach was combined with an optimization algorithm and used to investigate novel deposition concepts to locally tailor the coating thickness.

5.2 Introduction

In this chapter we use a combination of kMC modeling for simulating atomic assembly and a direct simulation Monte Carlo (DSMC) technique for vapor transport to investigate the deposition of a coating on a model airfoil-shaped substrate. Deposition onto both stationary and rotated substrates is investigated as the background pressure, gas jet velocity (via the changes to the pressure ratio across the nozzle used for its formation) and the homologous coating temperature are varied. Experimental coatings on both stationary and rotated airfoils are also deposited to assess the validity of the modeling approach. The dependence of the local coating thickness, columnar growth angle and porosity are reported as a function of the deposition conditions, and opportunities to control the spatial variation of these parameters are discussed.

5.3 Methods

The airfoil substrate used for experimental and simulated depositions is shown in Figure 5.1. The airfoil's exterior surface shape was defined by three quadratic surfaces with varying radii and centers of curvature. To allow for the use of two-dimensional simulations, the airfoil's cross-section remained constant through its thickness (it had no twist). Simulation airfoils were considered perfectly two-dimensional, while experimental airfoils had a width of 12.7 mm and were mounted to a thin backing plate during deposition. During stationary deposition, the substrate was aligned with the airfoil's chord parallel to the gas jet flow direction, and oriented with the leading edge nearest to the vapor source, as shown in Figure 5.1.

A schematic of the deposition geometry is shown in Figure 5.2. The substrate was positioned in the vacuum chamber with the center of rotation located 21 cm above the center of the 12.5 mm wide vapor source. The evaporation rate of a model nickel source was set at 8.8 x 10^{20} atoms $m^{-2}s^{-1}$ for all simulations. A coaxial gas jet was formed around the vapor source by expansion of a 90 at. % He and 10 at. % O_2 gas mixture through a choked nozzle, Figure 5.2. The velocity of the rarefied gas jet was governed by the ratio of the gas pressure up and downstream of the nozzle, the ratio of specific heats of the gas, and its initial temperature (taken to be 300 K here) [69, 120].

5.3.1 Simulation Methods

A two-step simulation method was used to encompass the range of length and time scales relevant to the deposition process. First, the rarefied gas dynamics within

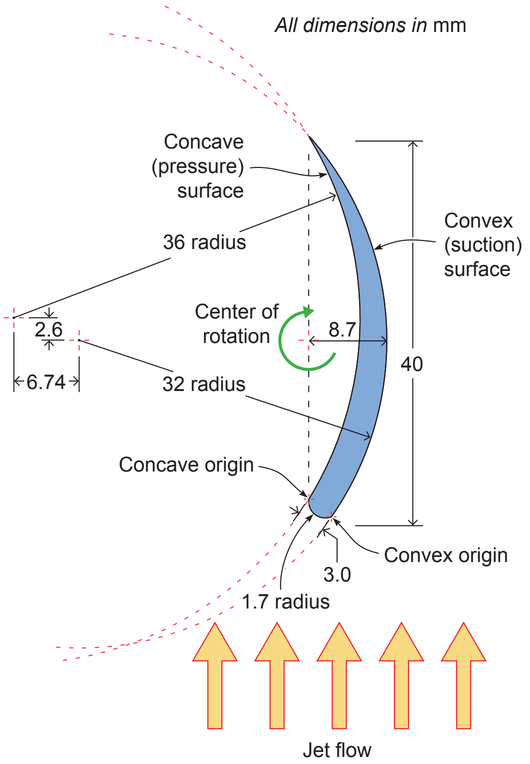

Figure 5.1: Schematic illustration of the model 2D airfoil substrate and the axis of rotation used for simulations and deposition experiments. During stationary deposition, the airfoil was aligned with the gas jet flow direction and for the other simulations and experiments it was rotated clockwise about the center of rotation. (All dimensions are in mm).

a deposition chamber was simulated with a DSMC method described in Section 3.1 [50, 94]. The vapor species was taken to be nickel with scattering parameters calculated using the method of Venkattraman [100]. The local nickel atom flux incident on a surface, and its incidence angle distribution (IAD) obtained from these simulations were used as the input to a 2D on-lattice kMC method, which simulated atomic assembly and growth of the coating. The kMC method used here has been previously used to simulate the vapor deposition of porous coatings [23, 81, 82] and microelectronic trench filling [5]. The method simulates the deposition of individual vapor atoms on the substrate surface and links the deposition rate to single-atom diffusional jumps between lattice sites within, or on the surface of the

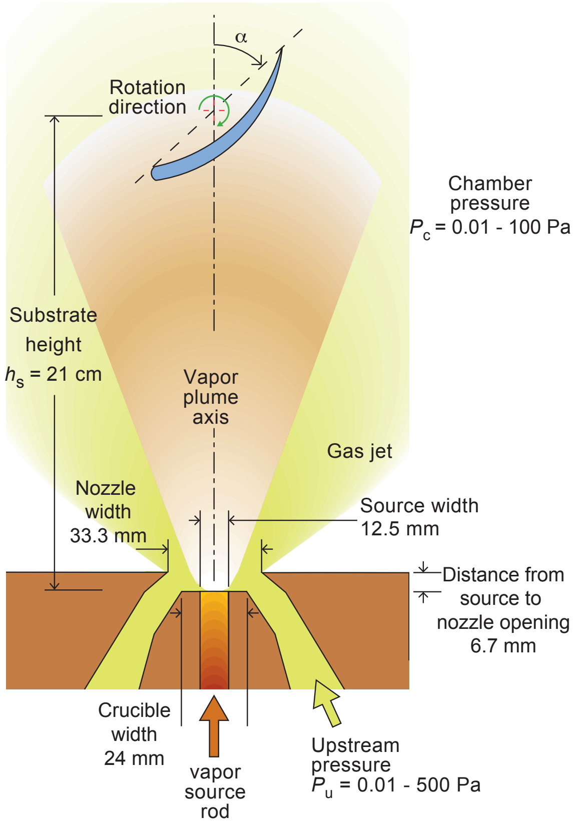

Figure 5.2: Schematic illustration of the deposition configuration used for simulations and experiments.

existing coating. The energy barriers used to determine diffusion kinetics of nickel were pre-calculated using the embedded atom method [121] and are tabulated in Hass [81].

The convex and concave surfaces of the airfoil were divided into 40 independent kMC simulation regions to allow for microstructure simulation along the entire substrate surface. Each simulation region was separated from the next by a distance of 1.13 mm along the convex surface and 1.07 mm along the (shorter) concave surface. These kMC regions corresponded to the substrate surface elements used in the input DSMC simulations. Each kMC region was assigned a width of 4,000 virtual lattice sites (∼1 μm wide). To reduce variability in columnar growth, an initial substrate roughness was used for the simulations [23]. The effects of surface asperity size, shape, and spacing on simulated coating microstructure have been quantified in previous studies [81, 122]. The roughness used here consisted of flat-topped pyramidal asperities with a base width of 100 atoms, a height of 75 atoms, and a spacing of 256 lattice sites between asperity midpoints.

The DSMC simulations yielded two variables that subsequently govern the thickness and structure variation across the substrate: the local deposition rate and IAD of the vapor atoms. The deposition rate influences the number of diffusional jumps possible between vapor atom arrivals and the final thickness of a coating deposited in a fixed time. The IAD specifies the likelihood that an incident vapor atom impacts a substrate at a specific incidence angle, θ, measured from the local surface normal, Figure 5.3(a). Angles oriented towards the airfoil's leading edge were taken as positive, while those oriented towards the trailing edge were negative. Atoms arriving with similar trajectories that impact opposite sides of the substrate (convex or concave) will have θ values of identical sign. Oblique atom arrivals are susceptible to shadowing by growth surface protuberances, leading to the eventual formation of pores under conditions of insufficient thermally activated surface diffusion [81, 82].

Simulations of deposition on rotated substrates were performed by sequentially combining data from a set of stationary DSMC simulations with substrate orientation specified by the angle α, as shown in Figure 5.3(b). Eight stationary DSMC simulations, each separated by 45° of rotation, were used as input for each rotated kMC simulation. Substrate rotation was simulated by depositing a specified number of atoms (determined by the orientation-specific local deposition rate) from the IAD of each orientation. The eight orientations were cycled through until the desired total number of atoms had been deposited.

a) Definition of vapor incidence angle (θ)

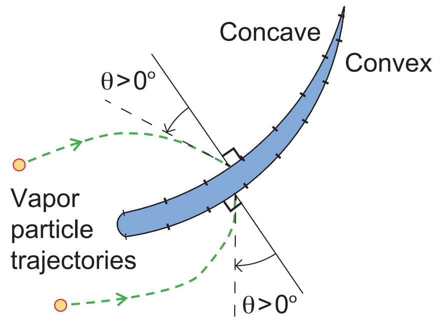

b) Definition of substrate orientation angle (α)

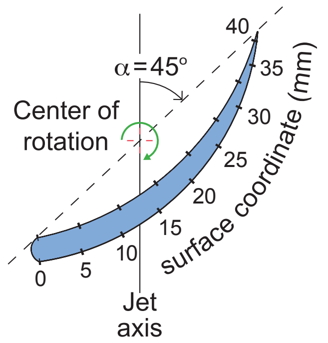

c) Vapor incident angle distribution

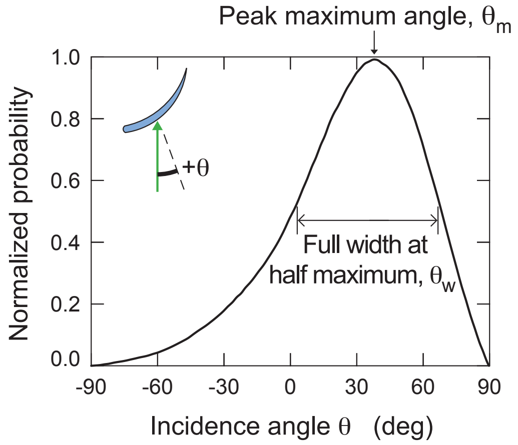

Figure 5.3: Definition of (a) the incidence angle, θ of a vapor atom relative to the local surface normal, and (b) the orientation of the airfoil substrate, α relative to the jet flow axis. (c) Shows an example of an incident vapor atom angle probability distribution ($\theta_m = 20°$, $\theta_w = 87°$) calculated by simulating jet flow near a tilted substrate ($\alpha = 45°$) at a chamber pressure of 22 Pa and a pressure ratio of 5.45. The distribution was recorded at a location 15 mm along the convex side of the airfoil.

The kMC deposition rate was determined by assuming a maximum deposition rate of $D_{max} = 4.3\mu\text{m/min}$ [123] at the surface region with the highest deposition flux as calculated by DSMC. The deposition rate, D at each surface region along the remainder of the substrate was determined by normalizing the DSMC calculated fluxes by the maximum value;

$$D = D_{max}(f/f_{max}) \tag{5.1}$$

where f is the DSMC determined vapor flux at a surface region and f_{max} is the maximum vapor flux at each orientation. When rotated deposition was simulated, D was calculated at each orientation. The total number of atoms deposited in each simulation region, N, was also scaled by the total DSMC flux;

$$N = N_{max}(f/f_{max}) \tag{5.2}$$

where $N_{max} = 9,000,000$. During rotated deposition, f and f_{max} were determined by summation of DSMC fluxes from all orientations.

The simulations were performed first using baseline DVD conditions consisting of a chamber pressure of 22 Pa, a pressure ratio of 5.45 and a substrate homologous temperature $T/T_m = 0.243$ (where T_m is the absolute melting temperature of the deposited material, in this case nickel). The effects of varying these three baseline parameters were then systematically explored. When substrate rotation was modeled, the incident atom flux was scaled to simulate a rotation rate of 6 rpm. This was achieved by using the input variables from each orientation for a simulation time of 1.25 seconds and then advancing to the next orientation. Once simulations were completed, the columnar growth angles were measured by applying a Hough transformation [124] to renderings of the simulation microstructure. The pore volume fraction was determined by measuring the fraction of occupied lattice sites in the inner 80% of the coating's thickness. The outer boundary was excluded to avoid spurious porosity from column tip roughness.

5.3.2 Deposition experiments

To test the validity of the simulation approach, experimental depositions were performed using the EB-DVD method using a He carrier gas [25, 28]. Nickel coatings were deposited onto grade 303 stainless steel substrates shaped by wire-cut electric discharge machining. The substrates surface was roughened before deposition by grit blasting. Both rotated and stationary depositions were performed for approximately 70 minutes. Rotated substrate depositions were performed at 6 rpm. The coatings were deposited without substrate heating. However, heat radiated from the electron beam's interaction with the vapor source resulted in a substrate temperature of 150 °C, which corresponds to a homologous temperature, $T/T_m = 0.243$; the same as that used during simulations. After deposition, the samples were cross-section, polished, and imaged in a scanning electron microscope (SEM) to determine their thickness and local columnar growth angle.

5.4 Simulation and experimental results

5.4.1 Coatings from stationary deposition

As indicated in Figure 5.3(c), two key parameters of an IAD are the location of the distribution's maximum (θ_m) and the distribution's full width at half maximum (θ_w). The variation of both parameters for deposition using the baseline EB-DVD conditions (a chamber pressure of 22 Pa, a pressure ratio of 5.45 and a substrate temperature $T/T_m = 0.243$) is shown in Figure 5.4. The variation in maximum angle along the concave and convex surfaces is shown in Figure 5.4 (a) and (b) respectively. The change in full width at half maximum along the concave and convex surfaces is shown in subplots (c) and (d) respectively. The plots show that the IAD varied significantly between line-of-sight regions near the airfoil's leading edge and the highly shadowed regions found closer to the trailing edge. In near line-of-sight regions (distance from leading edge < 20 mm), the IAD was narrow with θ_m close to the incident angle of the carrier gas flow. Deposition in these regions was highly influenced by the carrier gas flow field.

In highly shadowed regions (substrate distance > 20 mm on both surfaces), the IAD was broad with a maximum angle close to the local surface normal. Vapor atoms deposited in this region had undergone multiple scattering collisions with the background gas and made impact with the substrate from a wide range of incident angles, including from directions that were opposite to the flow direction of the carrier gas. Deposition in these regions was weakly correlated with the local carrier gas flow properties. These non-line-of-sight (NLS) substrate regions had much lower deposition rates than the line-of-sight areas, with vapor atom arrivals

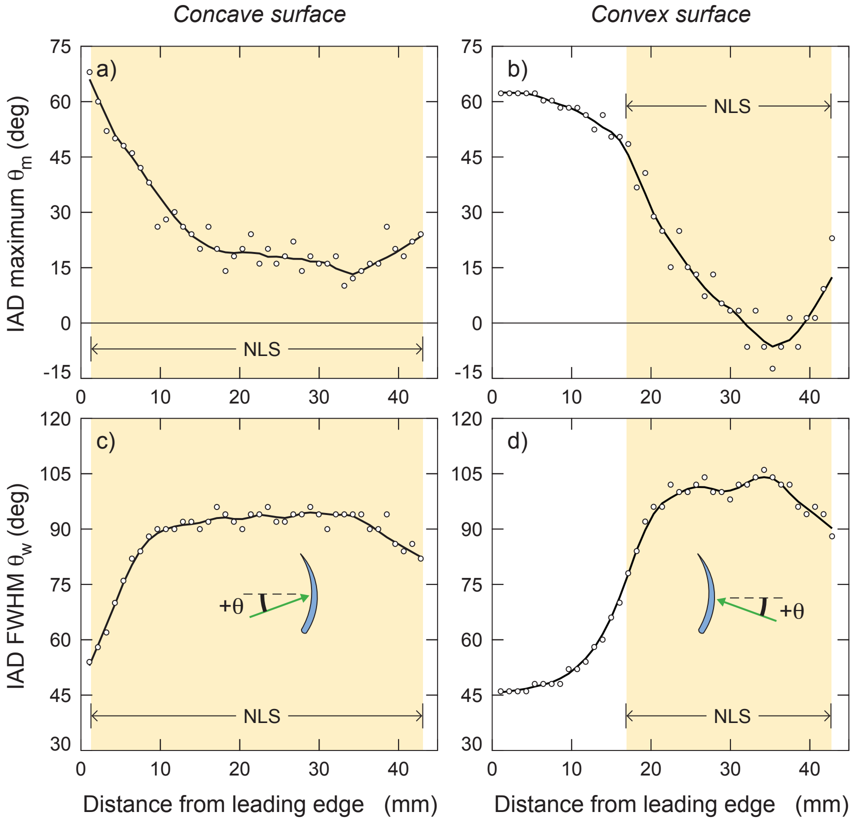

Figure 5.4: DSMC predicted parameters of the IAD along both surfaces of a stationary airfoil oriented at $\alpha = 0°$. Results were calculated for a chamber pressure of 22 Pa and pressure ratio of 5.45. The shaded regions were not in the line-of-sight of the vapor source.

the result of substantial gas phase diffusion transverse to the flow direction.

The kMC simulations were initially performed for a stationary substrate oriented at $\alpha = 0°$, using the baseline deposition conditions. Figure 5.5 shows the thickness and structure of coatings that were deposited at six representative locations on the airfoil under these conditions. It is evident that the coating had a significant variation in both its thickness and structure along each surface. Reduced, but significant vapor deposition occurred on NLS regions as shown in Chapter 4.

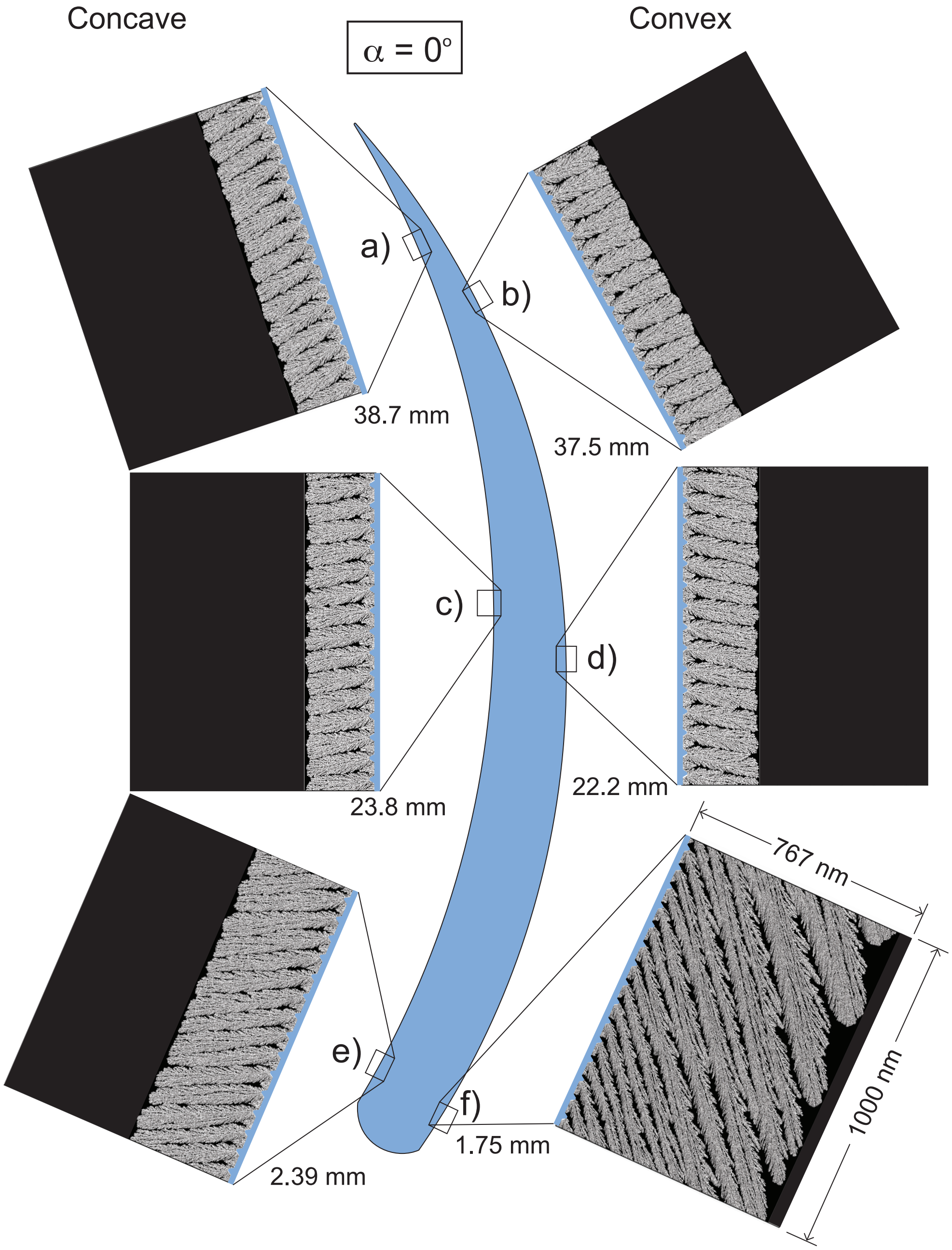

Figure 5.5: Simulated coating microstructures at six locations on a stationary airfoil substrate. The chamber pressure was 22 Pa, the pressure ratio was 5.45, and the source evaporation rate was 8.8 x 10^{20} atoms $m^{-2}s^{-1}$. The substrate's homologous temperature, $T/T_m = 0.243$, and the highest deposition rate shown (at the subplot f location) was 2.5 x 10^{20} atoms $m^{-2}s^{-1}$.

The simulated and experimental coating thickness, columnar growth angle, and pore volume fraction along the entire substrate surface are shown in Figure 5.6 for the concave (left column) and convex (right column) surfaces of a stationary airfoil. The variation in simulated and experimental thickness along the concave and convex surfaces of the airfoil are shown in Figures 5.6(a) and (b). The thickest coating on each surface was formed at the leading edge, as vapor was quickly depleted (by deposition) from the carrier gas streamlines that traveled closest to the stationary substrate surfaces. The concave surface shows an increased thickness near the trailing edge; a consequence of this section of substrate curving back into less vapor depleted regions of the carrier gas jet stream.

The simulated and experimental columnar growth angles, ϕ, are plotted versus position on the airfoil in Figure 5.6(c) and (d) for both surfaces. Near the leading edge of both surfaces, the coating had a feathery appearance due to nucleation of secondary growth columns, Figure 5.5(e) and (f). The primary intercolumnar pores at these leading edge locations were oriented towards the leading edge. However, the magnitude of this angle gradually decreased along the surface, and eventually approached the local surface normal. In NLS regions such as (a-d) in Figure 5.5, the columnar growth angles were smaller as the highly scattered vapor atoms were deposited with a broad range of incident angles.

Measurement of the columnar growth angle in experimentally deposited coatings gave orientation results with significant scatter; a consequence of the substrate's long wavelength surface roughness which caused local variation of the surface normal. The estimated standard deviation of the measured angle was 5°. Examination of Figure 5.6 shows that the simulation predicted column angles agreed reasonably with experimental values (to within ~10° on the concave surface), Figure 5.6(c),

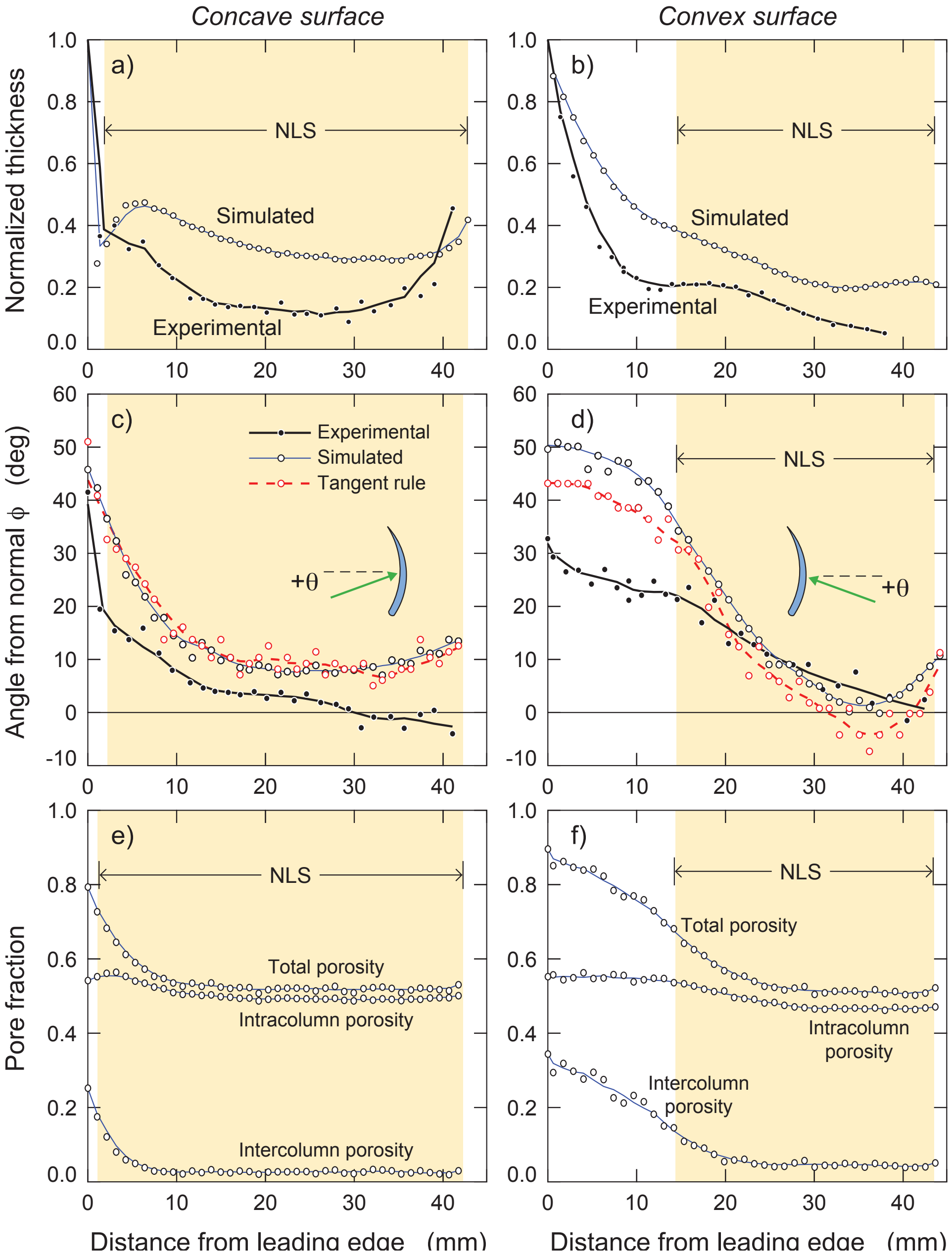

Figure 5.6: Comparison between experimental and simulation results for a stationary airfoil ($\alpha = 0°$). Subplots a) and b) show the simulated and experimental thickness profiles (normalized by the thickness at the origin of the concave surface). Subplots c) and d) show the columnar growth angles along with those predicted by the Tangent rule. Subplots e) and f) show the simulated total pore volume fraction together with the intracolumnar and intercolumnar components of the total porosity.

and beyond a distance of ∼15 mm from the leading edge, Figure 5.6(d). However, the simulated growth angles were ∼20° higher than the experimentally measured values on the convex surface near the airfoil's leading edge. Recent work has shown that for highly-inclined incident angles, the instantaneous IAD experienced at the coating surface after formation of the feathery structure is significantly different to that experienced at the substrate surface during initial deposition [125]. Improved simulation accuracy might be obtained in future simulations by using an IAD defined by the angle with the instantaneous column surface as the coating develops. Fortunately, these large growth angles do not develop on rotated substrates, and as shown below, the simulations were then better behaved.

The columnar inclination angle, ϕ, formed on flat substrates by condensation of a collimated, mono-angular flux with an incident angle, θ, can often be well fitted by a Tangent rule [113] given by;

$$2tan(\phi) = tan(\theta) \tag{5.3}$$

Using the IAD peak angle, θ_m, for θ, the Tangent rule prediction has been plotted on Figures 5.6(c) and (d), and correctly predicts that growth columns are tilted in the direction of the incident flux but with a columnar growth angle of smaller magnitude than the incidence angle. The Tangent rule growth column angle was found to agree reasonably with kMC simulations. It has been found that the predictive accuracy of the Tangent rule also decreases as the magnitude of the incidence angle increases beyond 70° [126–128]. Several more complex empirical and semi-empirical approaches have been attempted [125, 129–131], but no universal empirical approach has been successfully proposed for high incident angle fluxes.

The coating porosity was determined from the kMC simulations as function of location along the substrate surfaces, Figure 5.6(e) and (f). The plots show the total pore fraction, the small length scale intracolumnar porosity and larger intercolumnar porosity. Along both surfaces, porosity is greatest at the leading edge and gradually decreases along the surface before reaching near-constant values in NLS surface regions. The total porosity variation results from changes to the intercolumnar porosity, as the width of the intercolumnar pores decreased with distance along the substrate surfaces. To understand these observations, it is helpful to examine the jet flow and vapor atom concentrations near the airfoil.

The flow field behavior, as characterized by the carrier gas streamlines and contours of pressure for this stationary simulated deposition condition is shown in Figure 5.7(a). Figure 5.8(a) shows the corresponding vapor streamlines and concentration contours. The highest density of vapor particle streamlines terminated near the leading edge of convex side of the airfoil substrate, consistent with the thickness profile predicted by the simulation methodology. This region of highest deposition rate was within the line of sight of the vapor source and depleted the concentration of vapor in the gas jet flow that subsequently passed close to the airfoil surface. However, binary collisions between the vapor and gas jet atoms were able to scatter vapor atoms towards the substrate, resulting in significant (diffusive) coating of the NLS regions of the stationary airfoil.

5.4.2 Rotated substrate deposition

The results above indicate that it is not possible to deposit a uniformly thick coating over all surfaces of a stationary airfoil substrate. Even though gas jet assisted deposition processes result in some deposition onto NLS surfaces, the thickest coatings form on regions within sight of the vapor source. However, rotation of such a substrate during deposition allows all areas of the substrate to spend some time within the line of sight of the vapor source, and results in improved coating uniformity.

The behavior of the gas jet near the substrate varies significantly during substrate rotation. This variation is shown by the carrier gas streamlines and pressure contour plots in Figure 5.7 for the baseline DVD simulation conditions. The figure shows that flow remains laminar for all orientations. At orientations where the airfoil's chord was roughly parallel to the flow direction ($\alpha = 0°$ and $180°$), Figure 5.7(a) and (e), the streamlines flow past the substrate with modest perturbation. However, isolated regions of stagnation that resulted in an elevated pressure (~1.3 times the background) above the airfoil surface nearest to the vapor source. Greater increases in pressure (up to 1.5 times background) over larger areas of the airfoil's primary surfaces were observed when the airfoils were oriented at $\alpha = 90°$ and $270°$ to the jet flow axis, Figure 5.7(c) and (g). This again is a manifestation of stagnation against the airfoil surface. Intermediate orientations exhibited a transition between these two limiting scenarios.

The variation of gas flow near the airfoil shown in Figure 5.7 greatly affected the vapor atom streamlines near the substrate. The average vapor atom trajectories and contour plots of the vapor atom concentration are shown in Figure 5.8 for each simulated orientation. The results were also calculated at baseline simulation conditions. When the substrate was oriented in-line with the jet axis ($\alpha = 0°$ and $180°$), Figure 5.8(a) and (e), both the convex and concave surfaces received a significant vapor flux. Surface regions closest to the vapor source (the leading

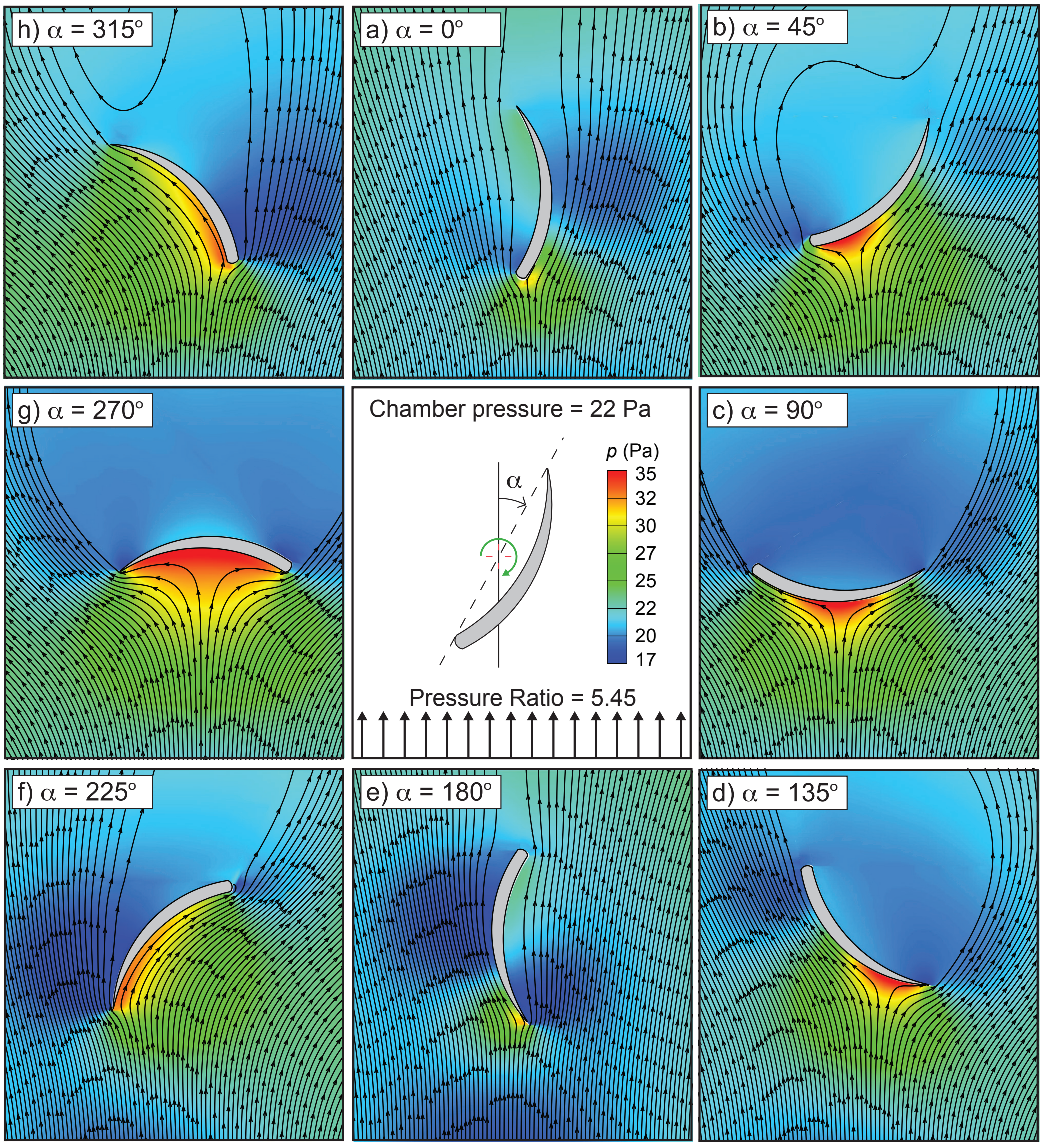

Figure 5.7: Helium gas jet streamlines and pressure contours at the eight orientations used to simulate deposition onto a rotated substrate. Simulations were performed at a chamber pressure of 22 Pa and pressure ratio of 5.45.

edge at $\alpha = 0°$ and trailing edge at $\alpha = 180°$) received the highest vapor fluxes. Airfoil regions downstream from the leading or trailing edge received a reduced flux because of earlier depletion from the gas jet streamlines by condensation onto the leading or trailing edges [50]. When the substrate was oriented perpendicular to the jet axis ($\alpha = 90°$ and $270°$), Figure 5.8(c) and (g) the surface facing the vapor source received a much higher vapor flux compared to that on the shadowed surface. At other intermediate substrate orientations, Figure 5.8(b), (d), (f) and (h), significant parts of one surface were in the line-of-sight of the vapor source while others were shadowed resulting in a strong spatial variation in the local flux incident upon the surface.

The orientation of the substrate also affected the IAD at all locations on the substrate. For example, Figure 5.9 shows the IAD at the midpoint of the concave surface for each angle of rotation. When the midpoint of the concave surface was in the line-of-sight of the gas jet origin, Figure 5.9(f), (g) and (h), the distribution maximum angle was closely correlated with the angle between the local surface normal and the gas jet axis. However, when this midpoint location was in a NLS position, the IAD received a much more isotropic flux, Figure 5.9(b) and (e), though in some cases with a still substantial shift in θ_m from zero, Figure 5.9(a).

The kMC simulated coatings at six locations on the substrate (the same locations used for stationary deposition in Figure 5.5) using baseline deposition conditions are shown in Figure 5.10. The variations with location of the coating thickness, the columnar growth angle and the porosity were much reduced compared to the stationary case. As with coatings created by stationary deposition, each protuberance on the substrate acted as a nucleation site for columnar growth. On the concave surface, the growth columns typically extended through the entire coating

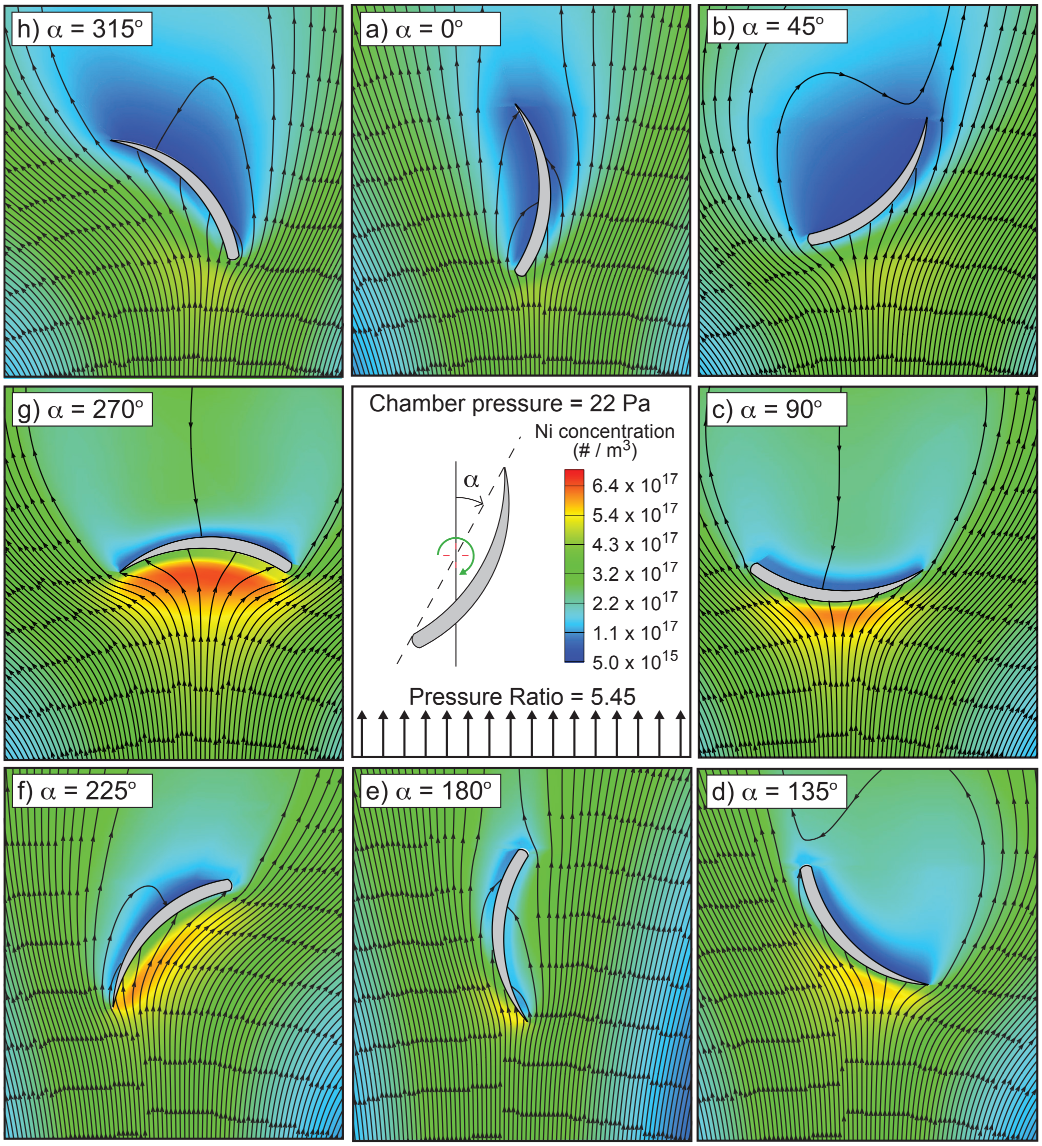

Figure 5.8: Nickel vapor atom streamlines and concentration contour plots at the eight orientations used to simulate deposition on a rotated substrate. Simulations were preformed at a chamber pressure of 22 Pa and pressure ratio of 5.45.

thickness, and the number density of column tips on the coating's exterior surface was similar to the density of nucleation sites. Along the convex surface, the coating microstructure was comprised of wedge-shaped columns that increase in width as they grew out from the substrate surface. Many columns intersected with each

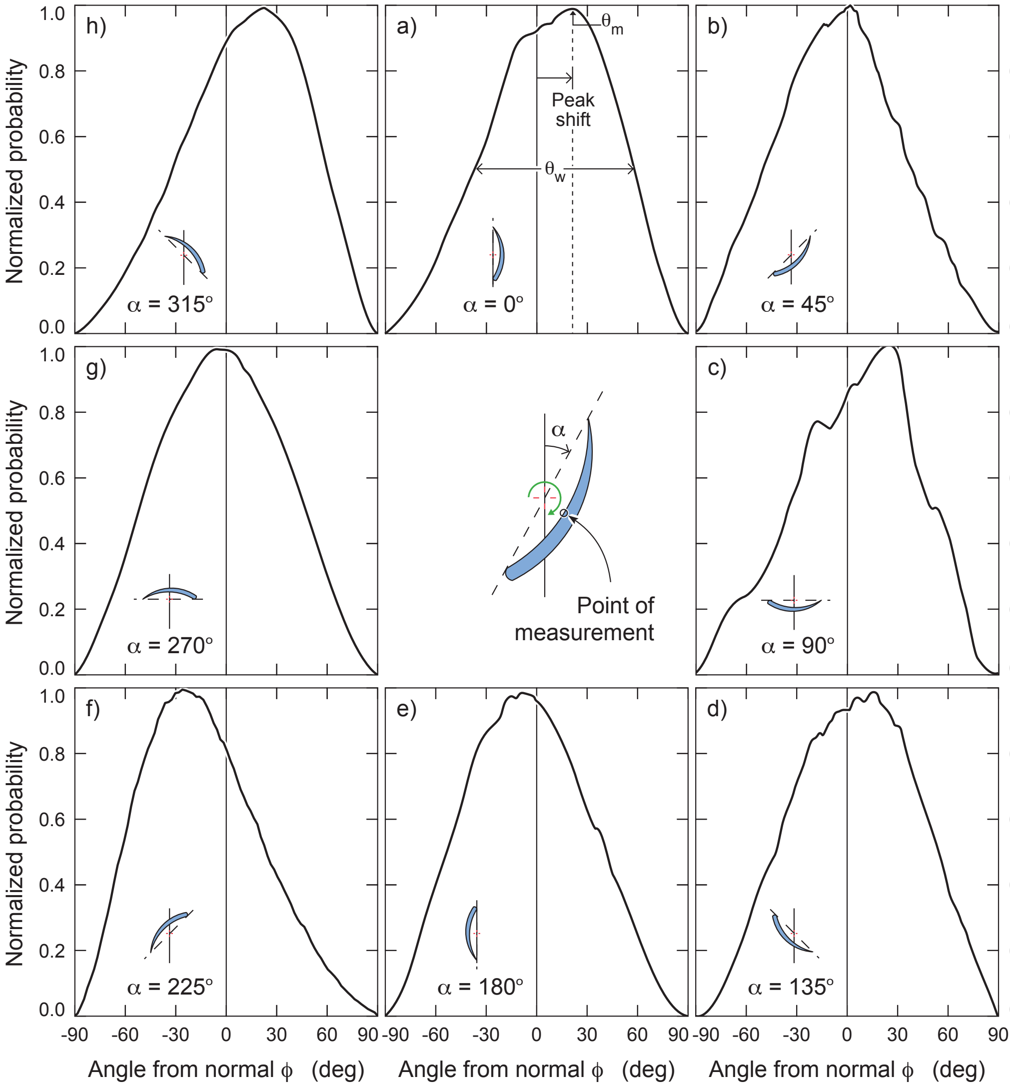

Figure 5.9: Nickel vapor particle incidence angle distributions used to simulate rotated deposition at the center of the concave side of the airfoil. Simulations were preformed at a chamber pressure of 22 Pa and pressure ratio of 5.45.

other during this competitive growth process, and as a result, the coating surface was composed of fewer, wider column tips, each covering several nucleation sites.

SEM micrographs of a nickel coating deposited on a rotated airfoil substrate using a chamber pressure of 22 Pa, a pressure ratio of 5.45 and a substrate temperature $T/T_m = 0.243$ (the same as the simulations above) are shown in Figure 5.11 for

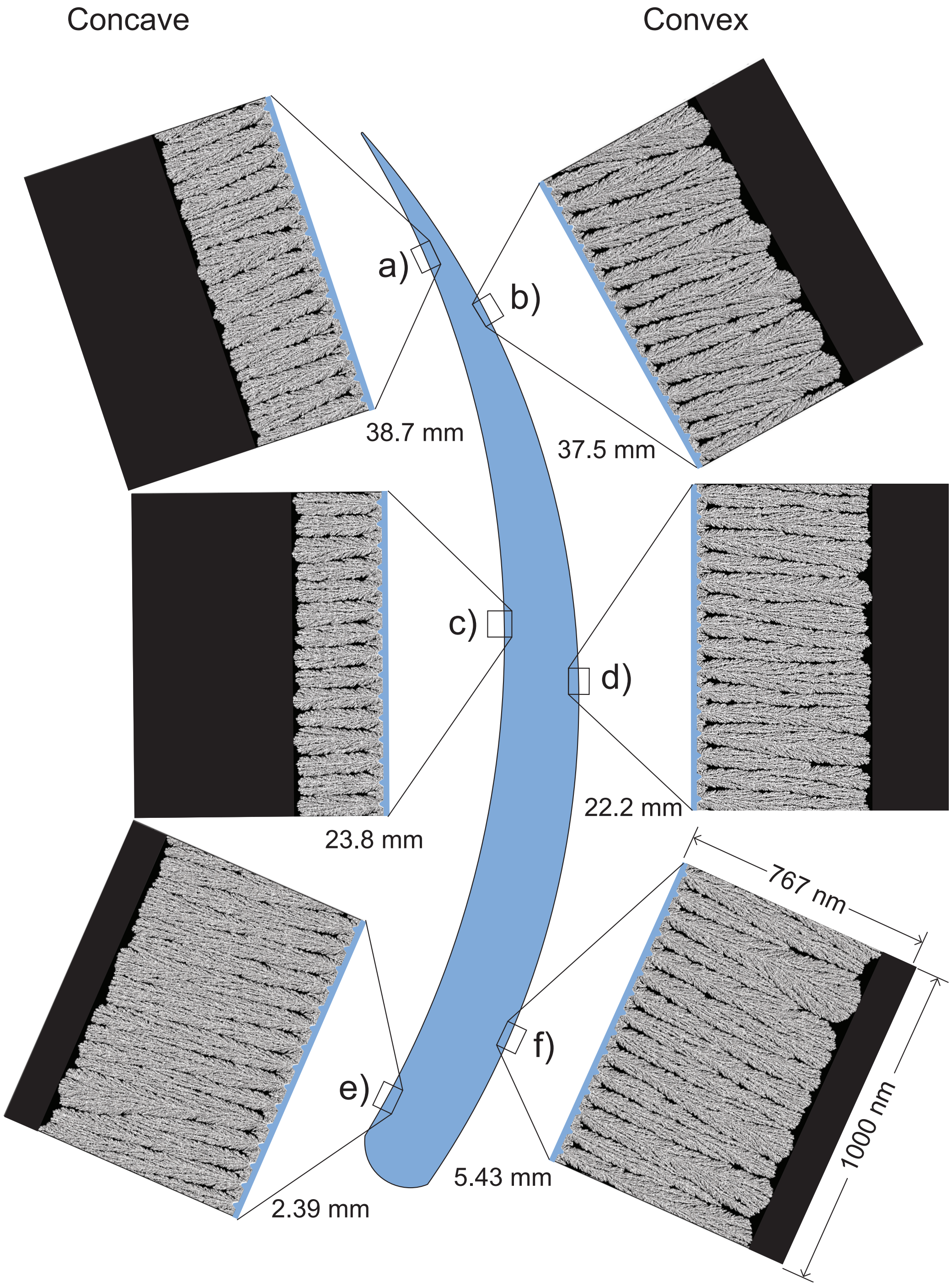

Figure 5.10: Simulated coating microstructures at six locations on the surface of a rotated substrate. Simulations were performed at a rotation rate of 6 rpm, a chamber pressure of 22 Pa, a pressure ratio of 5.45, a substrate temperature $T/T_m = 0.243$, and an evaporation rate of 8.8 x 10^{20} atoms $m^{-2}s^{-1}$ (baseline DVD conditions).

similar locations to those shown in Figure 5.10. The experimental coatings exhibited generally similar trends in coating thickness, and columnar growth angle as the simulations. The experimental coatings also had similar variations of surface morphology to those found on the simulated coatings. Along the concave surface, the growth columns were narrower and neighboring columns typically grew parallel to each other with vertical sides. Along the convex surface, columns were often wider and more fan-like, with neighboring columns often intersecting each other during growth.

Rotation of the substrate greatly improved the uniformity of coating thickness along the concave, Figure 5.12(a), and the convex, Figure 5.12(b) surfaces compared to stationary deposition, Figure 5.6(a) and (b). The experimental coating thickness is also plotted on Figure 5.12(a) and (b) and was in reasonable agreement with that simulated. Once again, the thickness profiles on both sides were normalized by the thickness at the convex surface's origin at the leading edge as shown in Figure 5.3. The coatings located near the leading and trailing edges were thicker than at the center of the substrate surfaces. It is also evident that the coating on the concave side of the airfoil was thinner than that on the convex surface.

The growth column angle variation with location along the concave and convex substrate surfaces can be seen in Figure 5.12(c) and (d). Comparison with Figure 5.6(c) and (d) for the stationary case, shows that substrate rotation greatly reduced the average growth angle and angle variation along both surfaces. For much of the substrate, the rotated coating's growth columns were almost normal to the local substrate surface. The most significant deviations (of 5° to 15°) from normal were confined to locations near the leading and trailing edges of the substrate. Agreement between simulated and experimental growth angles was also much improved.

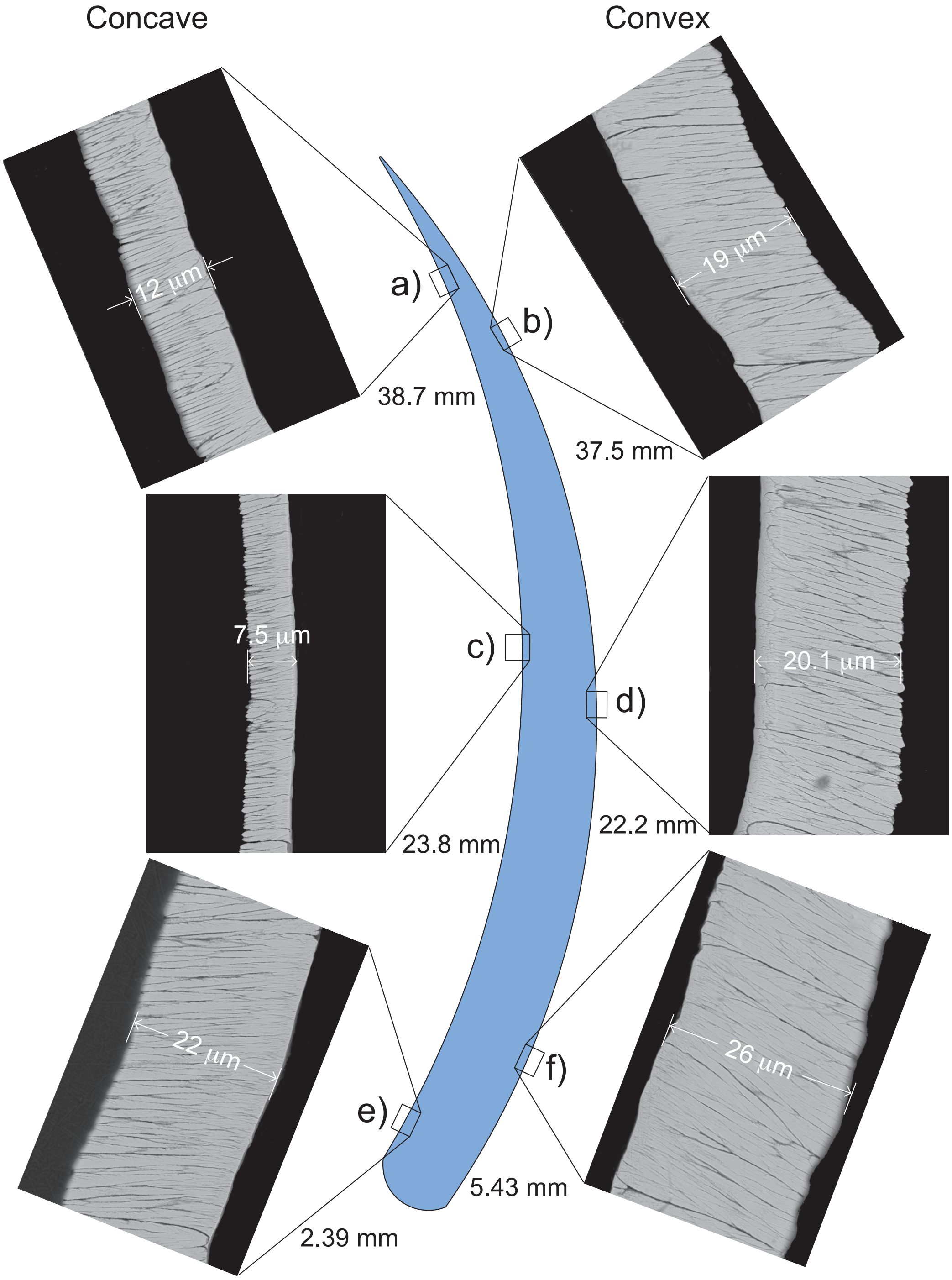

Figure 5.11: SEM images of experimentally deposited nickel coatings at various locations on a rotated substrate. Coatings were deposited using a rotation rate of 6 rpm, a chamber pressure of 22 Pa, a pressure ratio of 5.45, and a substrate homologous temperature $T/T_m = 0.243$. The 12.5 mm diameter source rod was evaporated at a rate of approximately 0.1 μm/min, which corresponds to an atomic evaporation rate of approximately 7.48 x 10^{19} atoms $m^{-2}s^{-1}$

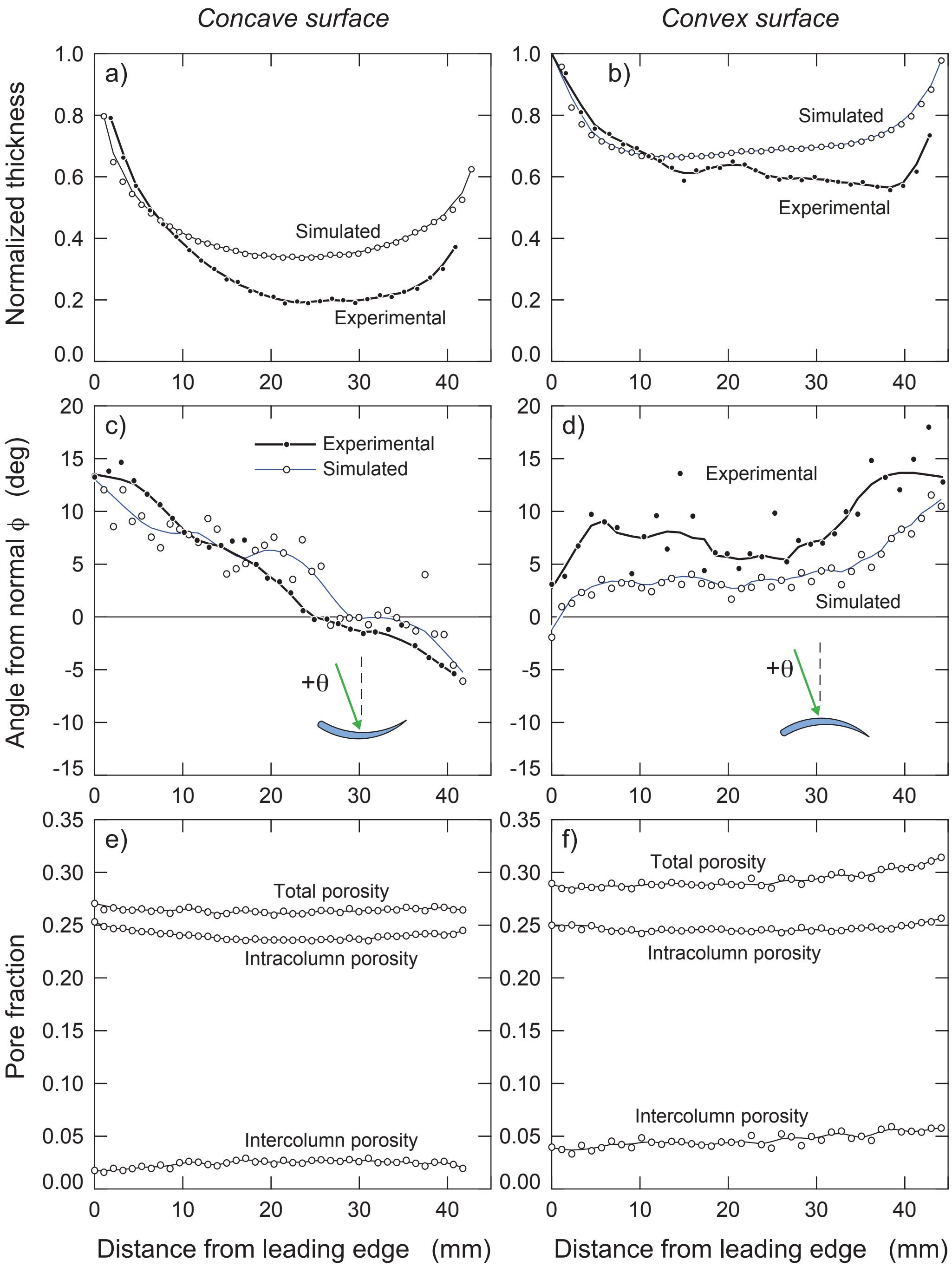

Figure 5.12: Comparison between experimental and simulation results for deposition of nickel on a rotated substrate. Subplots a) and b) show the simulated and experimental thickness profiles (normalized by the thickness at the origin of the convex surface). Subplots c) and d) show the columnar growth angles. Subplots e) and f) show the simulated porosity along the surfaces, including intracolumnar and intercolumnar components of the total porosity. The simulated coatings were deposited under baseline DVD conditions.

5.4.3 Porosity

The intracolumnar pores in the experimentally grown coatings were ~10-100 nm in length while those between the growth columns had widths (intercolumnar gaps) of ~1 μm and a length comparable (in some cases equal) to the coating thickness. The volume fraction of intracolumnar pores was typically independent of the initial roughness of the substrate, whereas the intercolumnar pore volume fraction was very sensitive to the surface topology of the substrate [81]; especially during early stages of deposition when the gap width depended sensitively upon the surface asperity spacing.

The total porosity (and its two constituent types) of a coating simulated using the baseline DVD conditions is shown as a function of location along the concave and convex surfaces of a rotated airfoil in Figure 5.12(e) and (f). Examination of the figure shows that the total, and two components of the pore volume fraction (for a rotated deposition using the baseline conditions) were approximately independent of position along the airfoil surface. However, while the intracolumnar porosity was approximately the same on both the concave and convex surfaces (with a pore fraction of ~0.25), the intercolumnar component of porosity on the convex surface was almost twice that of the concave surface coating. By comparing Figures 5.10(c) and (d), it can be seen that this difference resulted from the formation of wider intercolumnar pores on the convex surface of the rotated airfoil. This occurred because of the increased fraction of oblique atom trajectories that impact the convex surface. On the concave surface, the airfoil's leading edge and trailing end shadowed many of the atoms traveling along these highly inclined trajectories.

Porosity evolution during vapor deposition resulted from flux shadowing in combination with insufficient surface diffusion to replace the local adatom deficit. The surface roughness, and therefore pore fraction of a coating, is consequently temperature and deposition rate dependent since the rate of (thermally activated) surface diffusion is sensitive to the substrate's temperature during the deposition process. The porosity increased with deposition rate, due to the reduced interval of time available for surface diffusion between atom arrivals. However, coating porosity was less sensitive to deposition rate than to temperature since it has a linear effect on the degree of surface diffusion, while the temperature dependence is exponential (Equation 3.1. Simulations were performed at homologous temperatures, T/T_m from 0.2 to 0.515 to investigate the effects of temperature on the two components of the total porosity. The simulations were again performed using baseline DVD parameters for a rotated airfoil.

The pore volume fractions midway along the convex airfoil surface are shown in Figure 5.13(a) (the trend at the midpoint of the concave surface was nearly identical and therefore not shown). Increasing the substrates temperature resulted in a rapid densification of the growth columns, Figure 5.13(b). The intracolumnar pore fraction decreased from ~0.27 at $T/T_m = 0.206$ to approximately 0.12 at $T/T_m = 0.515$, consistent with increased surface diffusion during the deposition process. However, the intercolumnar porosity at first increased with increasing temperature before reaching a maximum at $T/T_m = 0.36$ and then decreasing at higher temperatures. This was a result of a gradual increase in the width of the intercolumnar pores until $T/T_m = 0.36$, Figure 5.13(c). Further increases in temperature resulted in more surface diffusion, the sintering of some growth columns and a reduction in the width of intercolumnar pores along the substrate surface, Figure 5.13(d).

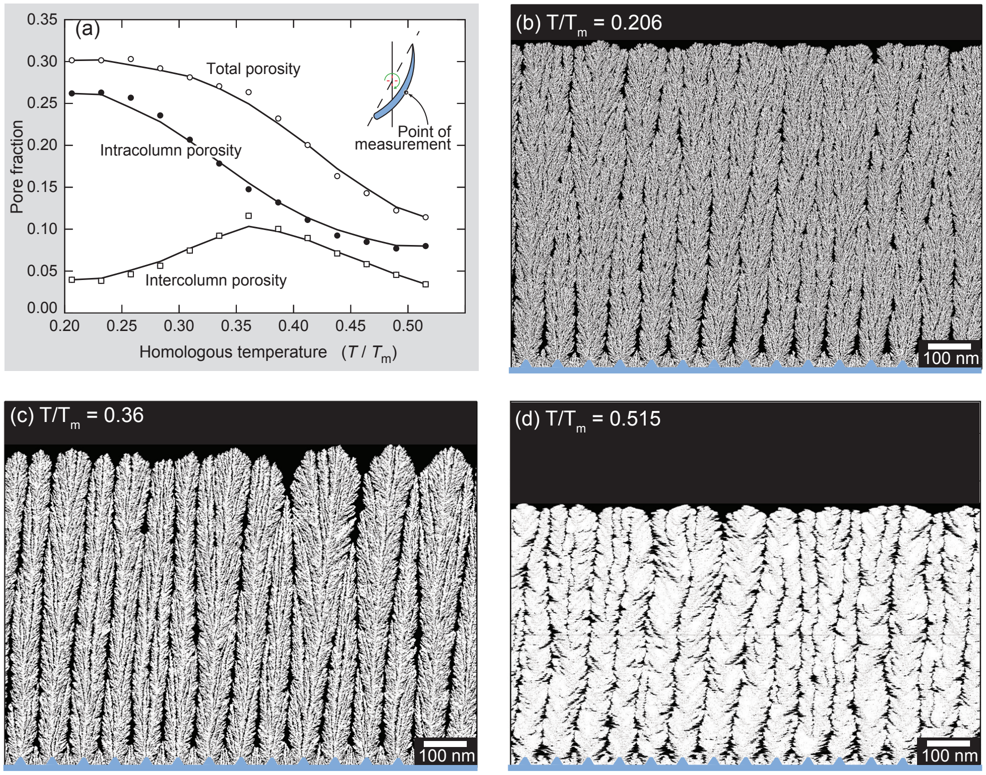

Figure 5.13: Simulated variation of coating porosity with substrate temperature for a rotated deposition (a) along with simulated microstructures at three temperatures (b-d). Depositions were performed using a chamber pressure of 22 Pa and a pressure ratio of 5.45. The data was calculated at the midpoint of the convex surface. An almost identical trend was found at the midpoint of the concave surface.

5.5 Pressure and jet flow effects

The results above show that the local thickness, growth column inclination and pore volume fraction within a coating deposited on a rotated, airfoil shaped substrate are controlled by many parameters. The deposition temperature, vapor atom IAD (determined by vapor phase scattering, which in turn depends upon the pressure, flow field and scattering coefficients of colliding species), and deposition rate all significantly influence the structure, and therefore thermophysical and mechanical properties of the coatings. In order to investigate the effects of process conditions, simulations were performed at a broad range of conditions including a low chamber pressure of 0.015 Pa and a pressure ratio of unity (typical of an EB-PVD coating process). Additional simulations at chamber pressures of 1, 16 and 45 Pa (using a pressure ratio of 5.) typically accessible by an EB-DVD process were performed. Simulations using the much higher chamber pressure (of 100 Pa with a pressure ratio of 5) typical of a PS-PVD process were also performed. A substrate temperature, $T/T_m = 0.243$ an evaporation rate of 8.8 x 10^{20} atoms $m^{-2}s^{-1}$ and a rotation rate of 6 rpm was used for all simulations. The effect of the chamber pressure upon the incident vapor flux (closely related to local coating thickness), growth column orientation and pore volume fraction were all investigated.

Simulated microstructures calculated for EB-PVD conditions are shown in Figure 5.14 at identical locations to those in similar figures above. They show that the coating thickness uniformity was significantly better than for the high-pressure EB-DVD conditions. However, increased variation of coating porosity was evident around the substrate. The porosity was highest in regions that received a significant amount of flux from oblique incident angles, Figure 5.14(b, d, e, and f). In these regions, the intercolumnar gaps were wide, and competitive growth between neighboring columns was found. In the regions near the trailing edge on the concave surface, Figure 5.14(a) and (c), the microstructures were much denser with narrow intercolumnar pores. In these regions, oblique incident atom trajectories were shadowed by the airfoil's edges and most atoms were deposited from trajectories oriented near the surface normal.

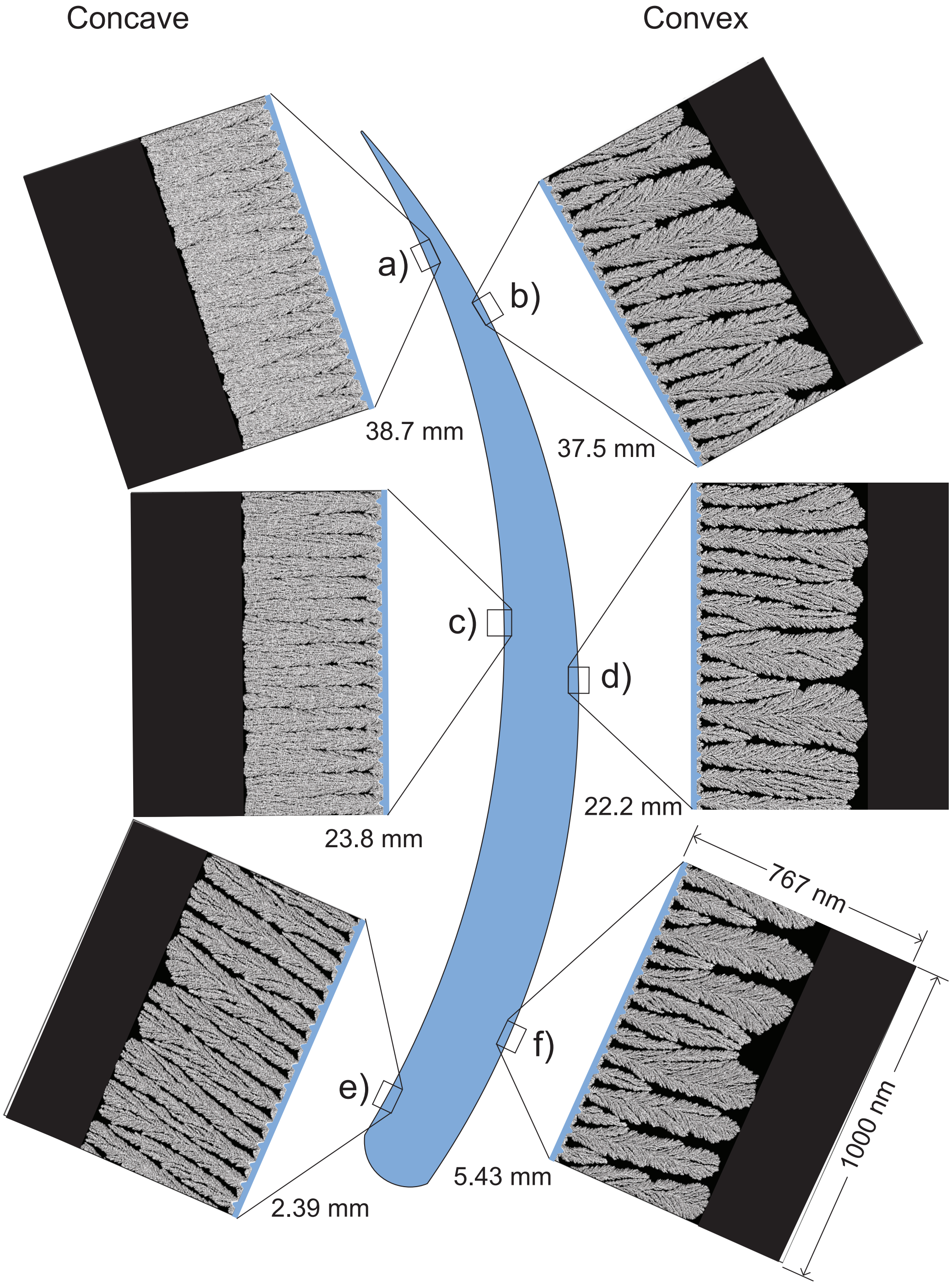

Figure 5.14: Simulated microstructure for rotated deposition under PVD like conditions (a chamber pressure of 0.015 Pa, a pressure ratio of 1.0, a substrate temperature $T/T_m = 0.243$, and an evaporation rate of 8.8 x 10^{20} atoms $m^{-2}s^{-1}$.

5.5.1 Coating thickness variations

The ratio of the number of vapor atoms deposited in each (∼1 mm wide) simulation region to the total number of evaporated atoms (the deposition efficiency) is a key factor contributing to the local thickness of a coating. This local deposition efficiency is plotted as a function of the position on the two surfaces of a rotated airfoil in Figure 5.15(a) and (b), and used as a surrogate for normalized coating thickness. Deposition under the lowest pressure (EB-PVD) conditions resulted in coatings of an almost constant thickness along each surface. Comparison of Figures 5.15(a) and (b) for this case also shows that the local deposition efficiencies on the convex and concave sides were also identical, and varied little with position. However, the vapor flux incident on each 1 mm wide region was slightly less than 10^{-3} of the emitted vapor. When integrated over the 40, 1 mm-wide regions, this resulted in a deposition efficiency of 0.034 for the concave surface and 0.039 for the convex side. This deposition efficiency of ∼4% of the evaporated flux was due to lateral expansion of the vapor plume during propagation from the source, and would decrease further with increasing source to airfoil (standoff) distance.

Increasing the chamber pressure to 1 Pa began to laterally confine the vapor plume, and increased the fraction of flux deposited on both surfaces, but with that deposited on the convex surface rising more rapidly. As the pressure was further increased, the deposition efficiency at first increased on both sides of the airfoil, but then reached a maximum before falling with further pressure increases. This drop in local efficiency was most dramatic on the concave surface, where the flux eventually decreased below that of the lowest pressure depositions. This phenomenon contributed to the development of a substantial difference in coating thicknesses on the two surfaces. Increasing the chamber pressure also increased the variation in deposited flux with location along each surface; the maxima in incident flux occurred at the ends of the airfoil, and increased relative to the minima at midpoint locations.

The effects of the chamber pressure and pressure ratio on the fraction of vapor that was deposited at the midpoints of the concave and convex surfaces can be seen in Figures 5.16(a) and (b). An increase in pressure to 10 Pa was accompanied by a substantial increase in the fraction of the evaporated flux that condensed on the substrate. This increase in local deposition efficiency reached a maximum at a chamber pressure of ∼5 Pa, and was relatively insensitive to the pressure ratio. Figure 5.16(c) shows the variation of the ratio of the concave to convex surface midpoint coating thicknesses for the same conditions. The asymmetry in coating thickness between concave and convex surfaces was small while the chamber pressure remained below about 1 Pa. Above this pressure, the thickness ratio dropped rapidly as the pressure was increased. Beyond a chamber pressure of 10 Pa, the deposition efficiency began to decrease, and both the deposition efficiency and concave/convex thickness ratio quickly decreased.

The trend in local deposition efficiency at the surface midpoints was quite similar to that for the overall deposition efficiency determined by integration of the local efficiency distribution over the entire substrate surface. Table 5.1 shows the ratio of the number of deposited atoms to the number evaporated along the concave, convex, leading edge, and entire substrate surface at several chamber pressures all at a pressure ratio of 5. Deposition efficiency along all of the surfaces increased with chamber pressure until it reached a maximum at 10 Pa of about 18.3% (compared with 7.6% at a pressure of 0.01 Pa). The total deposition efficiencies at 0.01 and 100 Pa were quite similar. While the 0.01 Pa efficiency was low due gas phase spreading,

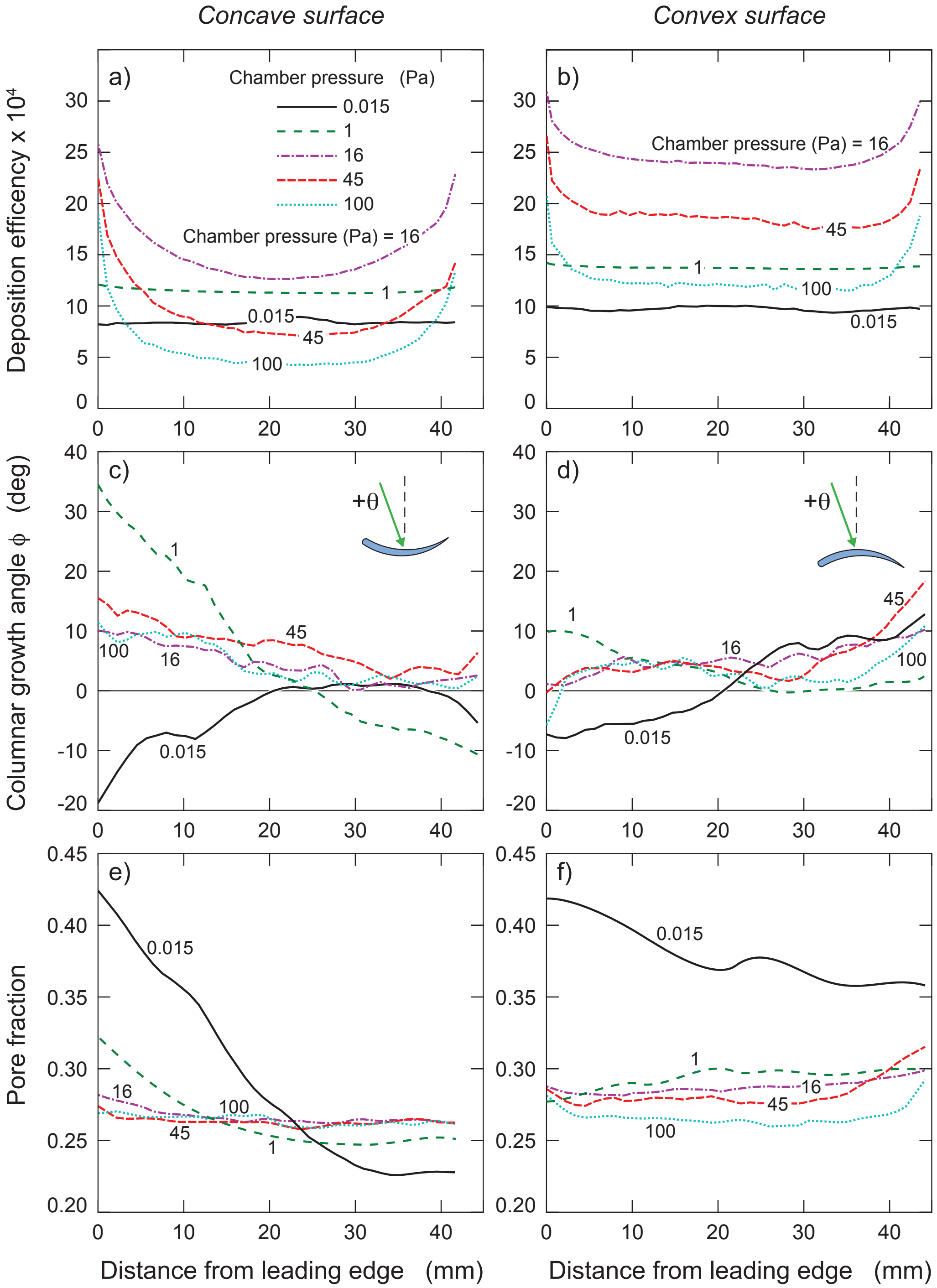

Figure 5.15: Variation of deposition efficiency profiles (a, and b), columnar growth angle (c, and d), and pore fraction (e, and f) along the convex (left column) and concave (right column) surfaces of the airfoil for several chamber pressure conditions using a pressure ratio of 5.0. Coating depositions were simulated at a homologous temperature $T/T_m = 0.243$ and a substrate rotation rate of 6 rpm.

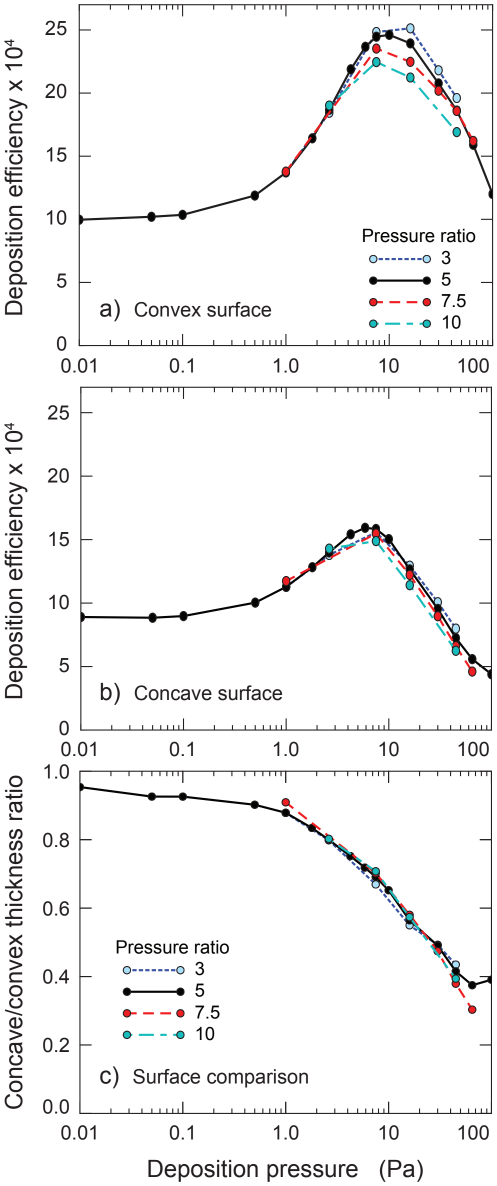

Figure 5.16: Plot of deposition efficiency at the mid-point locations on (a) the convex and (b) concave surfaces of the airfoil (atoms deposited divided by atoms evaporated). The figures show that coating deposition rate at the substrate midpoints was maximized at a chamber pressure of 8 - 10 Pa. The upstream/downstream pressure ratio only slightly influenced the amount of vapor flux received at these locations. Subplot c) shows the ratio of the deposition efficiency (thickness) at the midpoint of the concave and convex surfaces. The coating thickness ratio decreased from unity with increasing chamber pressure.

	Deposition efficiency			
Chamber pressure (Pa)	Concave surface	Convex surface	Leading edge	All surfaces
0.01	0.034	0.039	0.003	0.076
1	0.046	0.055	0.004	0.105
10	0.069	0.104	0.010	0.183
100	0.025	0.051	0.011	0.087

Table 5.1: Ratio of the number of deposited to evaporated atoms on the concave, convex, leading edge and entire airfoil surface for rotated deposition at a pressure ratio of 5.0 and a standoff distance of 21 cm.

at high pressures, the low efficiency resulted from short diffusion distances of the vapor transverse to the vapor streamlines. This slow transverse diffusion resulted in many vapor atoms flowing past the substrate without impacting and condensing upon its surface.

Coatings deposited at a chamber pressure typical of EB-DVD conditions possessed thickness variations over the airfoil surface quite different to those deposited under EB-PVD-like conditions (Figures 5.15 and 5.16). The differences were a result of two effects of the carrier gas jet: Deposition from gas streamlines close to a substrate edge and the creation of a wall jet for substrate orientations perpendicular to the gas jet. The influence of both effects increased with chamber pressure. Deposition from gas flow around a substrate edge was most significant when the airfoil was oriented with the leading edge nearest the vapor source, but slight inclined, as in Figure 5.8(f). Under low-pressure (0.015 Pa) conditions, no vapor was deposited onto the shadowed surface region (in this case, the convex surface). Although there is a significant concentration of vapor just above this surface region, no scattering collisions occurred to knock atoms from their straight-line trajectories, and onto the substrate surface. However, these collisions were present during DVD-like deposition, and significant amounts of vapor were deposited from the gas jet flow around the airfoil's edges. This contributed to thicker coatings near the airfoil edges under DVD conditions. The frequency of these collisions increased with chamber pressure, resulting in a higher deposition rate onto the shadowed surface.

Deposition onto the substrate ends was also enhanced when the substrate was oriented transverse to the gas jet ($\alpha = 0°$ and $90°$). At higher chamber pressures, the gas jet sensed the substrate and flowed around it. This created a wall jet [2] that transported incident vapor parallel to the substrate surface, decreasing the amount that reached the substrate's midpoint, and increasing the amount able to impact near the substrates ends. As the chamber pressure increased, multiple scattering collisions in the boundary flow made it increasingly less likely for vapor to reach the substrate surface, and the overall deposition efficiency decreased. The low-pressure used in PVD deposition, resulted in the incident vapor plume being uninfluenced by the substrate's orientation, resulting in a uniform deposition rate along the entire line-of-sight region of surface. The PVD profiles have slight rises near the center of each surface, as these regions remain in the line-of-sight of the vapor source for a longer duration during rotated substrate deposition.

5.5.2 Growth column orientation

The variation in columnar growth angle, ϕ, along the convex and concave surfaces is shown in Figure 5.15(c) and (d). Deposition at the lowest chamber pressure (0.015 Pa) resulted in a substantial ($\sim 20°$) variation of the growth column orientation angle along the concave and convex surfaces. Figure 5.15(d) shows that on the concave surface, columns grown near the leading edge at a pressure of 0.015 Pa were oriented away from the leading edge and gradually transitioned to perpendicular growth with increase in distance from the leading edge. On the convex surface near the leading edge, the 0.015 Pa growth column orientation angle was about 7° away from the leading edge, Figure 5.15(d), similar to that reported for EB-PVD coatings by Darolia [26]. At the trailing end of the convex surface coating, the growth column angle was ∼12°, with the columns sloped towards the leading edge. Under the lowest pressure deposition condition, the column angle on the convex surface changed progressively between these two limits so that near the mid-point of the coating, the columns were oriented normal to the local substrate surface.

The use of a gas jet with chamber pressures up to 100 Pa led to significant changes to the angle of the growth columns. On the convex surface, coatings grown at higher pressures, Figure 5.15(d), formed columns that were oriented very nearly perpendicular to the surface except for regions within ∼5 mm of the convex origin and ∼10 mm of the trailing end. Between ∼5 and 35 mm from the convex origin, the columns were only slightly tilted (by about 5°) towards the leading edge. Near the trailing edge, the growth angle was more severely tilted towards the leading edge, reaching maximum angle of 10 to 20°. On the concave surface, Figure 5.15(c), the use of a higher chamber pressure resulted in column growth in the opposite orientation from those grown at 0.015 Pa between the leading edge and surface midpoint (i.e. they oriented towards the leading edge). From the midpoint to trailing edge, the coatings grew at an angle within 5° of the local surface. Columns grown at 1 Pa show a different pattern to those deposited at other conditions. These columns tended to point towards the nearest substrate edge. Unlike the lowest pressure (0.015 Pa) case, vapor experiences scattering collisions at this pressure. However, their frequency is insufficient to cause significant diffusion transverse to, or against the direction of the gas jet. Atoms therefore arrive at the surface from trajectories closely aligned to the local gas jet flow.

The columnar growth angle was significantly affected by the introduction of a gas jet into the deposition process. For EB-PVD conditions, growth angles were aligned to the least-shadowed directions, while the introduction of a carrier gas causes the columns to tilt towards the directions with the most incident gas flow. This is most apparent near the leading edge along the concave surface (Figure 5.15(c)). Under EB-PVD-like conditions, this surface area is shadowed by the leading edge at many orientations. Thus, the majority of vapor arrives from the trailing edge direction, and the columns were tilted towards it. With introduction of a carrier gas, a significant amount of vapor flows around the leading edge and deposits on the nearby substrate surface. Vapor arriving from the trailing edge's direction must first flow along the concave surface, and is likely to deposit before reaching the leading edge. This resulted in columns that were oriented towards the leading edge.

5.5.3 Porosity

The coating porosity is shown for both airfoil surfaces in Figure 5.15 (e) and (f). Deposition at the lowest pressure led to a pore volume fraction of ∼0.4 at the leading edge of both the convex and concave surfaces. This then progressively decreased towards the trailing edge of the coatings. This decrease occurred more rapidly with distance along the concave surface, and fell to a lower value (∼0.2) than on the convex side. Coatings deposited at chamber pressures of 16 Pa and above had a nearly uniform pore volume fraction of ∼0.27 on both sides of the airfoil. The porosity varied little with position along either airfoil surface. The porosity near the leading edge of the concave side initially decreased rapidly with pressure, but for pressures above 1 Pa, was independent of pressure. However, beyond a distance of the ∼25 mm from the leading edge, the porosity of the EB-PVD condition coating decreased below that of the high-pressure coatings. On the convex surface, increasing the pressure above 0.015 Pa resulted in a decrease in porosity. Above 1 Pa, the porosity continued to decrease with increasing pressure, but at a much slower rate. In this higher-pressure regime, the porosity was substantially less than that of an EB-PVD pressure coating.

5.6 Local coating optimization

The simulations above have revealed that the thickness of a coating and its microstructure vary with position on an airfoil surface in a manner that is sensitive to the deposition conditions. Usually these deposition conditions are fixed during the application of the coating. However, modifying the evaporation rate (by modulating the electron beam power), the dwell time at each airfoil orientation (with a variable rotation rate), or the standoff distance (by eccentric substrate rotation), could enable the deposition of coatings whose thickness and microstructure were locally controlled. This might provide a means to form coatings that provided protection against the most life limiting threat to each specific region of the substrate's surface. Rapidly varied parameters of the jet flow (pressure ratio or gas composition) could also be used for a similar purpose.

To investigate such an optimization, the dwell time at specific angles of airfoil rotation were varied with the objective of eliminating the difference in coating thickness between the concave and convex surfaces of an airfoil substrate. The simulated incident vapor fluxes at the eight stationary orientations used to simulate a rotation were each assigned a variable weight coefficient. The total flux incident on each surface region, j, was then given by;

$$j = \sum_{m=1}^{8} a_m f_m \tag{5.4}$$

where f_m is the incident flux at each orientation, and a_m is the orientation coefficient to be determined. The minimize function in the Scipy Python suite was then used to determine the a_m resulting in the minimum total flux difference between the two airfoil surfaces expressed by;

$$\Delta j = \sum_{n=1}^{40} |j_{1,n} - j_{2,n}| \tag{5.5}$$

where $j_{1,n}$ and $j_{2,n}$ are the total flux at each of the n substrate regions along the concave and convex surfaces($n = 1 - 40$ surface regions). The summation began at the convex and concave surface origins (near the leading edge) and proceeded along each surface towards the trailing edge (increasing n). The coefficients were constrained so that each deposition had a maximum/minimum rotation rate ratio of 8 (the maximum allowable dwell coefficient was eight times larger than the minimum).

The resulting coatings obtained using the optimized rotation coefficients exhibited less than a 10% difference in flux (and thickness for a non-varying porosity) between the midpoint on their concave and convex surfaces, and combinations of coefficients could be found at all chamber pressures that maintained this level of resulting uniformity. The optimized coefficients are presented in Table 5.2 for depositions at 0.01, 2.625, 16, 45 and 100 Pa using a pressure ratio of 5 (except at

Dwell orientation, α (deg)	Dwell fraction during a rotation, a_m 0.01 Pa	2.625 Pa	16 Pa	45 Pa	100 Pa
0	0.104	0.149	0.267	0.345	0.222
45	0.104	0.116	0.122	0.043	0.042
90	0.135	0.120	0.033	0.043	0.042
135	0.135	0.074	0.033	0.043	0.042
180	0.116	0.130	0.135	0.043	0.042
225	0.113	0.139	0.125	0.079	0.042
270	0.133	0.113	0.178	0.059	0.227
315	0.161	0.160	0.106	0.344	0.339

Table 5.2: Dwell fraction during a rotation to ensure identical coating thickness on concave and convex surface mid-points for deposition at various pressures. A constant rotation rate had a dwell fraction of 0.125 of the rotation period. The dwell fraction was bounded so that the maximum rotation rate was up to 8 times the minimum at each deposition.

0.01 Pa where the ratio was 1). At the two lowest pressures, the coefficients varied only slightly from the coefficient for constant rotation (of 0.125). However, as the chamber pressure was increased, less uniform rotation patterns were required to achieve uniformity.

The total amount of flux incident on a substrate at each orientation can also be manipulated by adjusting the evaporation rate of the material source. In the current optimization design, this is mathematically equivalent to varying the rotation rate. In either case, a coefficient is used to adjust the deposition rate along the entire substrate surface. Optimizations in which both rotation and the evaporation rate are simultaneously adjusted can be implemented by using two, independent coefficients for each airfoil orientation. In that case Equation 5.4 is rewritten as;

$$j = \sum_{m=1}^{8} a_m b_m f_m \tag{5.6}$$

where a_m is the dwell coefficient for variable rotation and b_m is the coefficient for variable evaporation rate. The flux variation between the convex and concave surface can then be minimized by again using Equation 5.5. When the coefficients are unbounded, they can be represented by a single value. However, experimental depositions have a limited range of rotation rate and evaporation rate adjustment, and the use of both coefficients improved optimization.

The design of deposition strategies resulting in potentially beneficial, non-uniform thickness profiles can also be identified by this approach. For example, a thicker coating might be applied in regions prone to erosion or that require a larger drop in temperature across the coating to slow the growth rate of the bond coat's thermally grown oxide [26].

As an example, suppose the coating along the leading edge and concave (pressure) surfaces of an airfoil were designed to be thicker than that on the convex surface. The combined rotation/evaporation optimization method can be used to find a deposition sequence that achieves this. A target coating thickness profile that has a maximum at the leading edge and tapers to zero along the surfaces of the airfoil is schematically illustrated shown in Figure 5.17(a). For simplicity of presentation, the coating profile was defined so that the flux to the leading edge (defined between the concave and convex surface origins) had a constant value of unity and the target flux profile along the concave side was defined as;

$$j_{1T}(x) = 1 - 0.027x \tag{5.7}$$

Along the convex surface it was defined as;

$$j_{2T}(x) = \begin{cases} 1 - 0.041x, x \leqslant 27 \\ 0.1, x > 27 \end{cases} \tag{5.8}$$

where x was the distance from each surface origin in mm. The difference between the target and simulated flux profiles was then minimized using;

$$\Delta J = |j_{Leading} - 1| + \sum_{n=1}^{40} (|j_{1,n} - j_{1T}(\Delta xn)| + |j_{2,n} - j_{2T}(\Delta xn)|) \tag{5.9}$$

where Δx is the distance between simulation surface regions (1.13 mm and 1.07 mm for the convex and concave surfaces respectively) and $j_{Leading}$ is j at the single leading edge surface region. During optimization the rotation rate was bounded between 0.5 and 10 times the constant rotation rate value, while the normalized evaporation rate was allowed to vary by no more than a factor of 5 (from 0.2 to 1.0), consistent with experimental observations [67]. The optimization was performed at a chamber pressure of 0.015 (PVD-like conditions).

The resulting optimized flux profiles are shown in Figure 5.17(b) along with their respective target flux profiles. The optimized profiles achieved the flux objectives fairly well, especially near the leading edge. However, both surfaces exceeded the thickness objective as the trailing edge was approached. The rotation pattern and evaporation rate variation used to obtain the optimized coating are shown in Figure 5.17(d). Wider bars indicate a larger dwell fraction, while taller bars indicate a higher evaporation rate. The plot shows that the majority of deposition flux was concentrated at 45 and 225° orientations. Significant additional deposition occurred at the 0° orientation. Both the evaporation rate and the dwell fraction

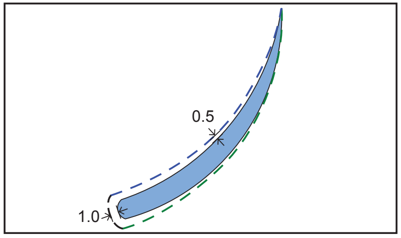

(a) Flux profile schematic

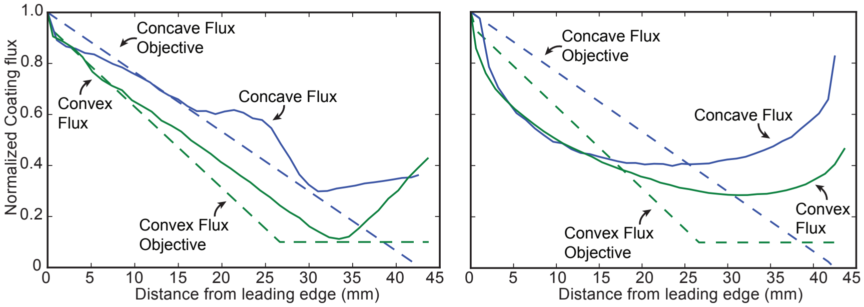

(b) 0.015 Pa target and optimized flux profiles

(C) 22 Pa target and optimized flux profiles

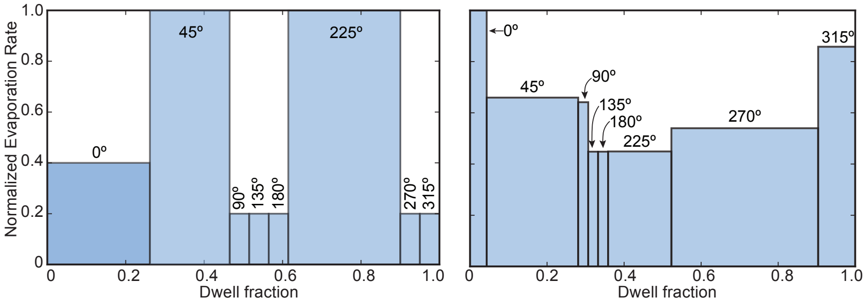

(c) 0.015 Pa optimized rotation pattern and evaporation rate

(d) 22 Pa optimized rotation pattern and evaporation rate

Figure 5.17: Optimization-generated thickness profiles at two deposition conditions. (b and c) Show the objective and optimization procedure generated flux profiles incident upon the convex and concave surfaces. (d and e) Show the dwell fraction and evaporation rate sequences that came closest to achieving the objective profiles. A chamber pressure of 0.015 Pa and pressure ratio of 1.0 was used in subplots (b) and (e) while a chamber pressure of 22 Pa and pressure ratio of 5.45 was used for subplots (c) and (e). The ability to match the desired flux profile decreased with increasing chamber pressure.

were minimized for all other orientations. Finally, it is noted that the ability of the optimization process to meet this thickness objective gradually decreased with increasing chamber pressure. This is shown in Figure 5.17(c and e) for chamber pressures of 22 Pa and pressure ratio of 5.45. The resulting flux profiles poorly matched the objective profiles due to a rapid decrease in flux from the leading edge and an increased flux near the trailing edge on both surfaces. The use of more simulated substrate orientations (beyond the eight used here) might improve the optimization at high pressures by providing additional variable coefficients.

5.7 Concluding remarks

The combination of DSMC simulations to analyze vapor phase transport in a rarefied, gas jet assisted deposition process has been combined with a kMC method to enable prediction of the thickness and structure of a porous coating applied to an airfoil. Coatings applied to substrates that were not rotated during deposition were found to have non-uniform thickness and contained acute growth column inclination angles. Rotation of the substrate was found to result in uniform thickness coatings grown under EB-PVD like conditions, but the coating microstructure varied substantially with location. Introducing a gas jet and raising the pressure during deposition led to the growth of coatings whose growth columns were almost all oriented perpendicular to the airfoil surface. However, under constant rate rotation, the thickness of the coating on the concave surface was only a half that on the convex surface. The simulation method has shown that by modulating the rate of evaporation, it is possible to deposit coatings with both uniform thickness and the majority of the growth columns oriented normal to the local airfoil surface.

Dynamic modulation of deposition also offers opportunities to “tune” the local coating thickness and structure to potentially better resist the damage mechanisms associated with specific locations on the airfoil surface.

Chapter 6

Physical Vapor Deposition on Doublet Airfoil Substrates: Controlling the Coating Thickness[1]

6.1 Synopsis

The previous two chapters have shown that attempts to use physical vapor deposition to uniformly coat shaped substrates require complex substrate manipulation schemes, but did not investigate deposition on surfaces that are never visible to the source. Gas jet assisted deposition techniques that operate at higher chamber pressures offer the promise of non-line-of-sight (NLS) deposition into such regions. A combined simulation and experimental approach is used to investigate vapor deposition onto model doublet guide vane substrates found in gas turbine

---

[1] Adapted from a technical article in preparation [132].

engines. Particular attention is given to coatings on interior surfaces, which are only accessible through the leading and trailing openings of the doublet airfoil substrate. Deposition of nickel is simulated for several flow conditions and vane separation widths, using a direct simulation Monte Carlo method. The simulated coating thickness results are then verified with experimental depositions of nickel coatings. Coating uniformity along interior surfaces was found to be highly sensitive to deposition conditions and to the separation width between the pair of airfoils. Coating thickness on these surfaces was also found to vary with the ratio of laminar flow distance through the inter-airfoil channel to the transverse diffusion (across the channel gap) distance; a parameter which can be used to guide to coating of any size channel-like substrate.

6.2 Introduction

Here we apply the previously developed atomistic simulation method to investigate the use of a directed vapor deposition approach for depositing columnar coatings on the surfaces of doublet guide vane substrates containing regions that are never in line of sight of the vapor source. The study focuses upon the thickness uniformity over these surfaces and its variation with deposition conditions including the pressure at which deposition is conducted. The study first examines the gas-phase environment near the substrate and its variation with both substrate orientation and deposition conditions. It then simulates the deposition of coatings under several conditions and compares their thickness distributions to experimental results for coatings deposited with the same conditions. Finally, the uniformity in coating thickness is investigated as the process environment is systematically changed from conditions found in high vacuum EB-PVD to high pressure PS-PVD.

6.3 Methods

A doublet guide vane substrate geometry was designed for use in both experiments and simulations. Each airfoil was identical in design to that used in the earlier studies of deposition on single airfoil substrates (Chapters 4 and 5). A general schematic of a doublet guide vane substrate is shown in Figure 6.1. The geometry and dimensions of the 2D doublet substrate are shown in Figure 6.2. The airfoils were placed parallel to each other and attached to flat mounting plates along their sides during experimental depositions. The channel width between the airfoils was defined as the distance between the inner convex and concave surface origins (indicated on the schematic). The width was varied between 8, 12 and 16 mm. The local channel width varied slightly along the channel due to the differing radii of the convex and concave surfaces. During deposition, the substrate was rotated clockwise around the center of rotation, defined as the center of the rectangle that completely encompassed the airfoil pair. A rotation angle α was defined between the center of the gas jet and airfoil axis (both pass through the center of rotation) defined as shown in Figure 6.2(a). At $\alpha = 0°$ the two axes are coincident.

Surface regions along the interior of the doublet substrate experience a significant portion of the deposition process out of the line-of-sight of the vapor source. The degree of shadowing experienced by these regions varies significantly with the channel width of the substrate. The strictest definition of a NLS region is a surface area that is inaccessible to any vector originating outside of the substrate's volume. The only substrate configuration studied here that meets this criteria is the 8 mm channel width, which has a permanently NLS area approximately 1 mm in width. However, the inner channel regions at all channel widths are shadowed from

a) Model doublet guide vane

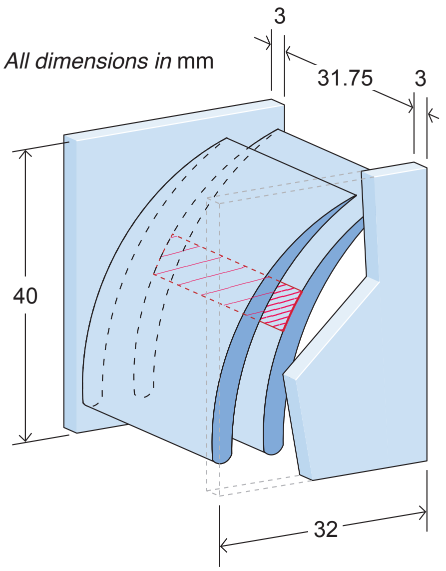

b) 2D cross section

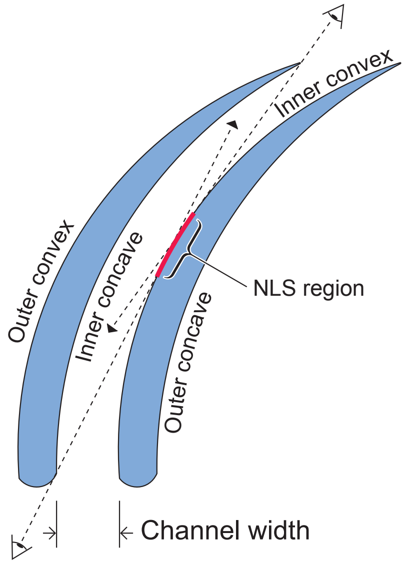

Figure 6.1: (a) Schematic illustration of a model doublet guide vane substrate used for simulations and experiments. (b) Definition of the channel width separating the two airfoils and the non-line of sight (NLS) region created on the inner convex surface. All dimensions are in mm.

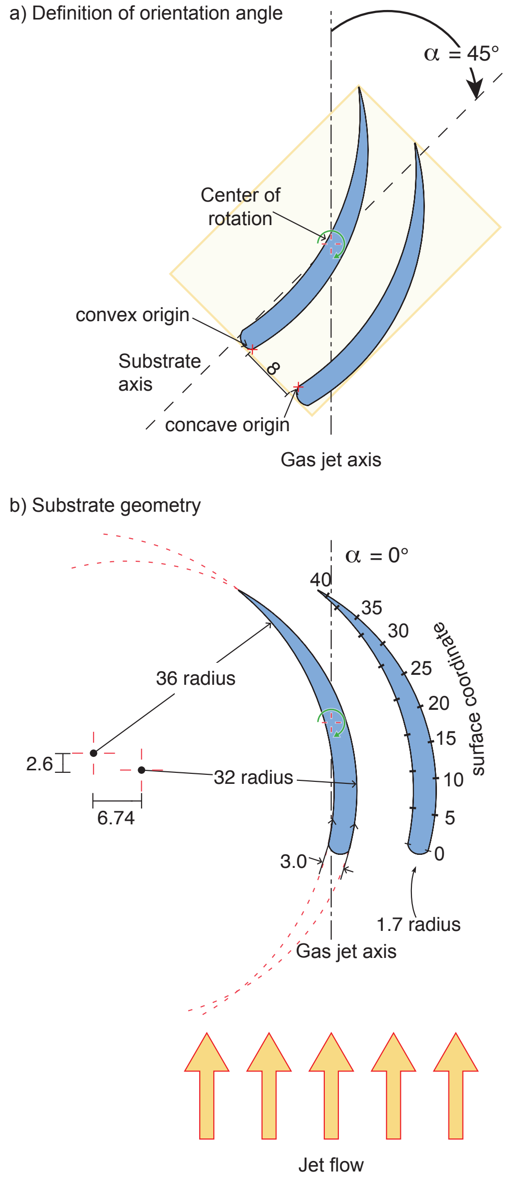

Figure 6.2: Schematic illustration of the doublet airfoil substrate geometry used in experiments and simulations. The center of its rotation was the geometric center of the encompassing rectangle that contained the doublet substrate. (b) Definition of the orientation angle, α, between the substrate axis and gas jet centerline. All dimensions are in mm.

the material source for most of a rotation cycle. These “near-non-line-of-sight” conditions appear more common in doublet vane geometries [36, 44]. When the gas phase MFP is significantly smaller than the substrate’s characteristic length (e.g., the channel width in this study), deposition into NLS regions is controlled by the dynamics of the flow.

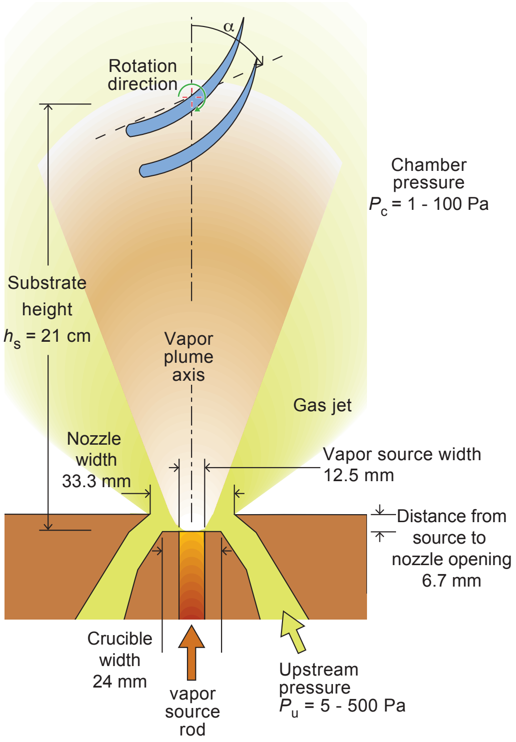

Figure 6.3: Schematic illustration of the source and substrate configuration used for simulation and experiment.

6.3.1 Simulation Method

The direct simulation Monte Carlo (DSMC) code Icarus developed by T. J. Bartel was used for the deposition simulations [105]. A simulation grid for the $\alpha = 0°$ substrate orientation is shown in Figure 6.4. The gas jet was formed by inserting gas molecules from the lower grid boundary into the high-pressure inlet region.

These then entered the lower pressure deposition chamber through a choked nozzle. The vapor species were nickel atoms and were input as a constant flux of 8.8 x 10^{20} atoms $m^{-2}s^{-1}$ from the 12.5 mm wide solid grid boundary labeled as "vapor emitting surface" near the exit of the gas inlet nozzle. The parameters for the Ni atoms were again determined from their Lennard-Jones potential parameters using the procedure of Venkattraman [100]. Chamber pressure was set by applying freestream boundary conditions along the vertical and upper grid boundaries. A two-dimensional Cartesian X-Y grid was used to model the doublet substrates.

During analysis of the simulation results, each convex and concave substrate surface was again divided into forty grid regions. Each region on the concave surfaces had a width of 1.07 mm. The regions on the (longer) convex surface were 1.14 mm wide. As a surrogate for coating thickness, a local deposition efficiency for each surface region was determined. The local deposition efficiency was calculated as the number of atoms deposited in each region divided by the total number of atoms emitted from the vapor source. Summation of the deposition efficiency along the entire substrate results in the total fraction of emitted vapor that was deposited on the substrate.

Deposition onto rotating substrates was simulated by performing independent simulations at eight stationary substrate orientations (each separated by 45° of rotation). The resulting coating properties were then determined by summing the results from each orientation with equal weighting; equivalent to assuming a constant rotation rate. Simulations were performed for 75,000 unsteady time steps to reach steady-state conditions and then an additional 250,000 to accumulate flow statistics. They were performed on a Linux cluster and required approximately 24 hours of wall time using 16 Intel Xeon processor cores.

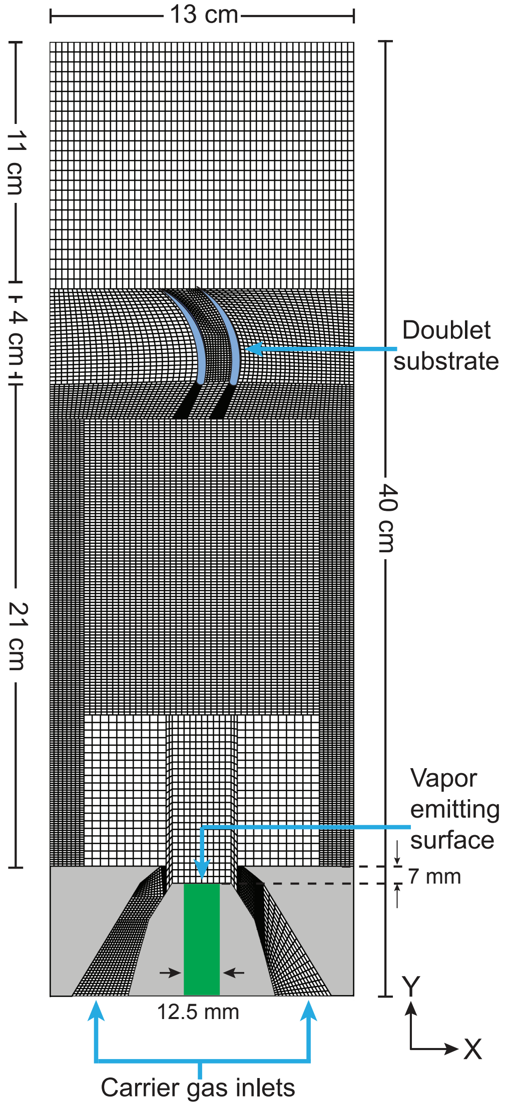

Figure 6.4: Grid used for DSMC simulations with a substrate orientation $\alpha = 0°$. The inlet pressure ratio was defined as the ratio of the gas inlet pressure upstream of the nozzle to that within the chamber. The cell size was iteratively refined until convergence of the jet flow was achieved.α

6.3.2 Experimental Methods

To verify simulation results, nickel coatings were deposited onto grade 303 stainless steel doublet airfoil using the EB-DVD technique [28, 66]. Experimental deposition conditions were quite similar to those used for deposition on a single airfoil [119].

A 70kV/2.45kW electron beam was used for all depositions. A channel width of 16 mm was used, and substrates were rotated at 6 rpm. This rate was determined to be high enough to create a columnar microstructure with a constant morphology through the thickness of the coating [23, 28, 82]. After deposition, the substrates were cross-sectioned, polished and examined in a scanning electron microscope (SEM).

The experimental substrate incorporated a pair of mounting plates to hold the airfoils in place and restrict access to the substrate channel only through the two ends of the doublet pair. These plates are neglected in the DSMC simulations, due to the two-dimensionality of the simulations. However, these plates will provide an additional vapor-sink in experimental depositions, resulting in less vapor depositing on the inner channel surfaces than predicted by the 2D simulations. To minimize this effect, the airfoil thickness (and spacing between mounting plates) was set at 31.75 mm; significantly larger than the inter-airfoil channel width, and the coating thickness was measured at the midline between mounting plates.

6.4 Results

6.4.1 Simulated Flow fields

Figure 6.5 shows DSMC calculated pressure contours and streamlines for the carrier gas jet near the substrate at the eight orientations used to simulate rotated deposition at a chamber pressure of 22 Pa, an upstream/downstream pressure ratio of 5.45, and channel width of 16 mm. The pressure contours show that the local pressure was slightly increased in the inter-airfoil region for those orientations that allowed significant flow through the channel. The in-channel pressure decreased significantly at orientations where the channel was perpendicular to the flow direction ($\alpha = 90°$ and $270°$). At these orientations, the highest pressure was observed at the outer substrate surface nearest the nozzle. In these regions, the flow stagnated against the substrate surface and led to an increase in local pressure. This dependence of the pressure near the external surfaces of the airfoils is very similar to that recently observed during deposition on a single airfoil substrate (5).

Figure 6.5 also shows streamlines corresponding to locally averaged carrier gas atom trajectories. Streamlines were calculated with an initially uniform spacing of 0.96 mm along a line perpendicular to the gas jet located 50 mm upstream of the substrate's leading edge. The streamlines show that laminar flow was maintained around the doublet at all orientations, even when the flow met a nearly perpendicular substrate surface, Figure 6.5(c) and (g). At these orientations, there is very little flow into the inner channel region of the substrate. In addition, the chamber region immediately downstream of the substrate is shadowed from the gas jet at all orientations, and gas flow in this region is reduced. At locations where a channel opening faces the gas jet (as in $\alpha = 315°$), there is significant flow through the channel. Upon exiting the channel, the gas continues to flow primarily along the jet's axis.

Contour plots of the vapor concentration at the eight substrate orientations are shown in Figure 6.6 for the same deposition conditions used for Figure 6.5. Significant penetration of vapor into the channel occurred at $\alpha = 0$, 45, 180, 225, and 315° orientations. At these orientations, the vapor concentration was highest at the channel opening. The vapor concentration gradually decreased with distance along the channel's length as vapor was depleted by condensation onto the inner

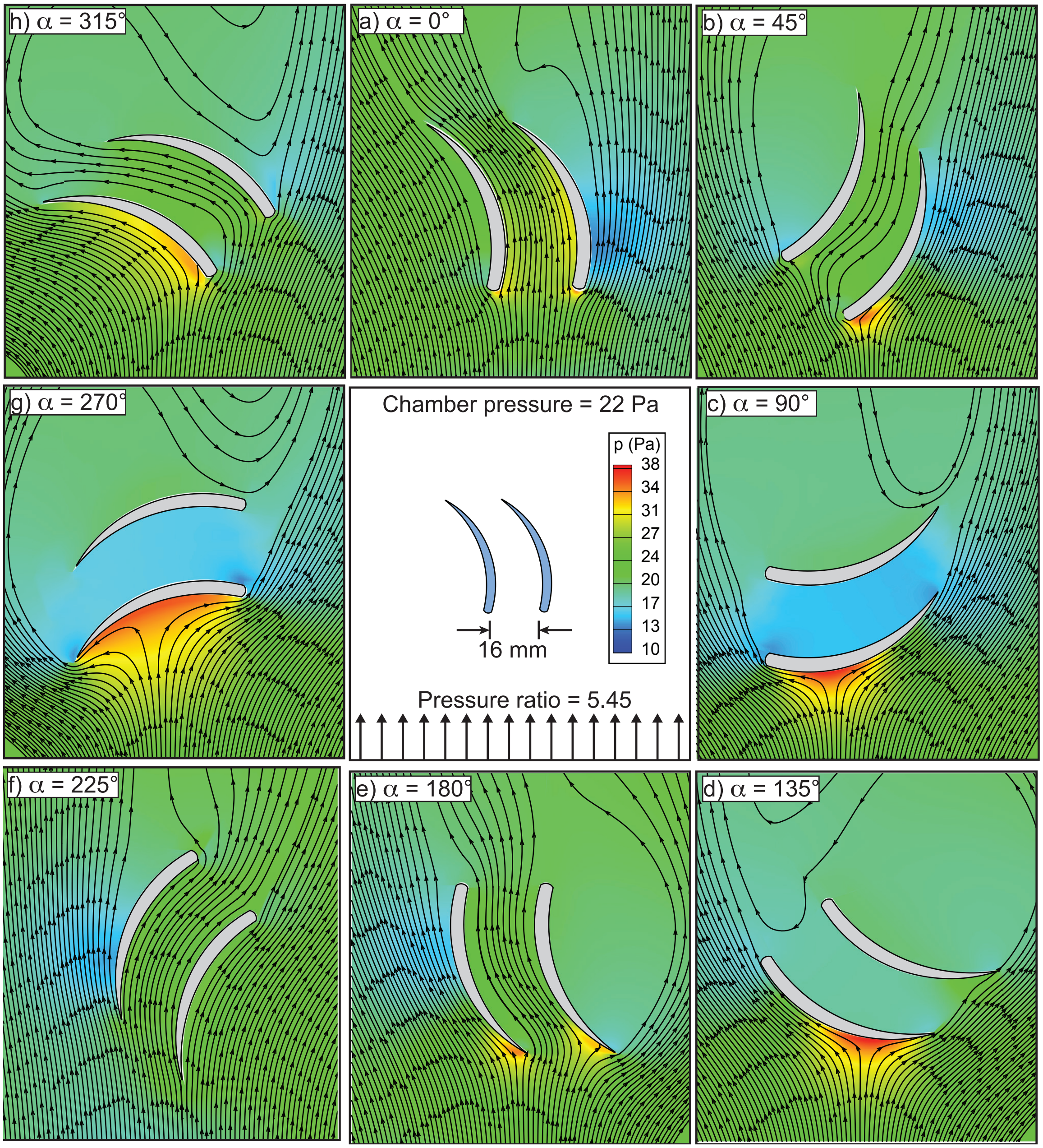

Figure 6.5: Chamber pressure contour plots near the substrate with helium gas jet streamlines overlaid for a channel width of 16 mm, a chamber pressure of 22 Pa, and pressure ratio of 5.45. The gas entering the inlet nozzle had an initial temperature of 300 K. Laminar flow was maintained around the airfoils at all orientations.

surfaces of the substrate. At the other orientations (α = 90, 135, and 270°), line-of-sight deposition onto the exterior surfaces was dominant, with very little vapor entered the inter-channel region. Note that in all cases, a steep gradient in vapor concentration existed near the substrate surface.

Vapor atom streamlines representing locally averaged trajectories of vapor atoms are also shown on Figure 6.6. The streamlines show that the vapor travels along laminar flow lines before depositing onto the substrate surface. In many cases, a significant amount of the vapor plume travelled beyond the substrate without depositing. Several streamlines also travel through the entire inter-airfoil channel without being deposited. At orientations where the channel was transversely aligned to the gas jet (α = 90, 135 and 270°), very few vapor atom streamlines were present in the inter-airfoil channel region.

The variation in vapor atom concentration with deposition conditions is shown in Figure 6.7 for the $\alpha = 0°$ orientation case. The figure shows the effects of chamber pressure (which increases from the top to bottom) and pressure ratio (which increases from left to right). The concentration contours show that vapor penetration into the channel increased with both increasing pressure and pressure ratio. However, significant vapor concentration remains in the flow at the airfoil exit for the highest combinations of these variables, Figure 6.7(i).

Vapor atom streamlines are also shown in Figure 6.7. At the lowest pressure ratio and chamber pressure, Figure 6.7(a), few if any streamlines travelled the entire interior channel length, indicating rapid depletion of the vapor by condensation onto the interior airfoil surfaces. At high-pressure ratios, Figure 6.7(c), more of the vapor streamlines traveled through the channel, indicating some vapor was

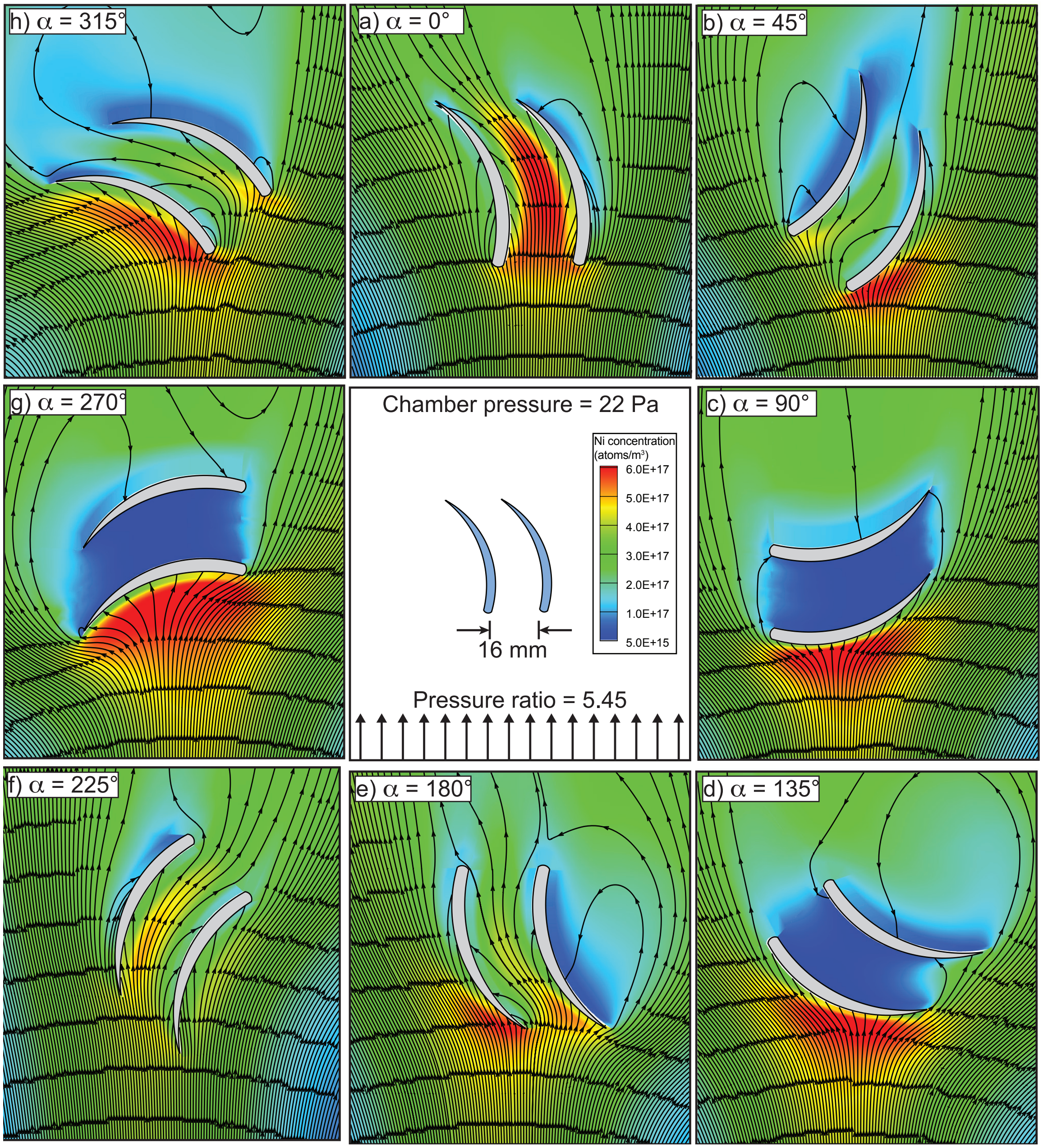

Figure 6.6: Vapor atom streamlines and concentration contour plots for a substrate with a 12 mm channel width, using a chamber pressure of 22 Pa and a pressure ratio of 5.45.

not deposited on the interior walls. For high chamber pressures and low-pressure ratios, Figure 6.7(g), significant vapor concentration existed through most of the channel, while little vapor travelled through the channel without condensing upon the interior surfaces of the doublet substrate.

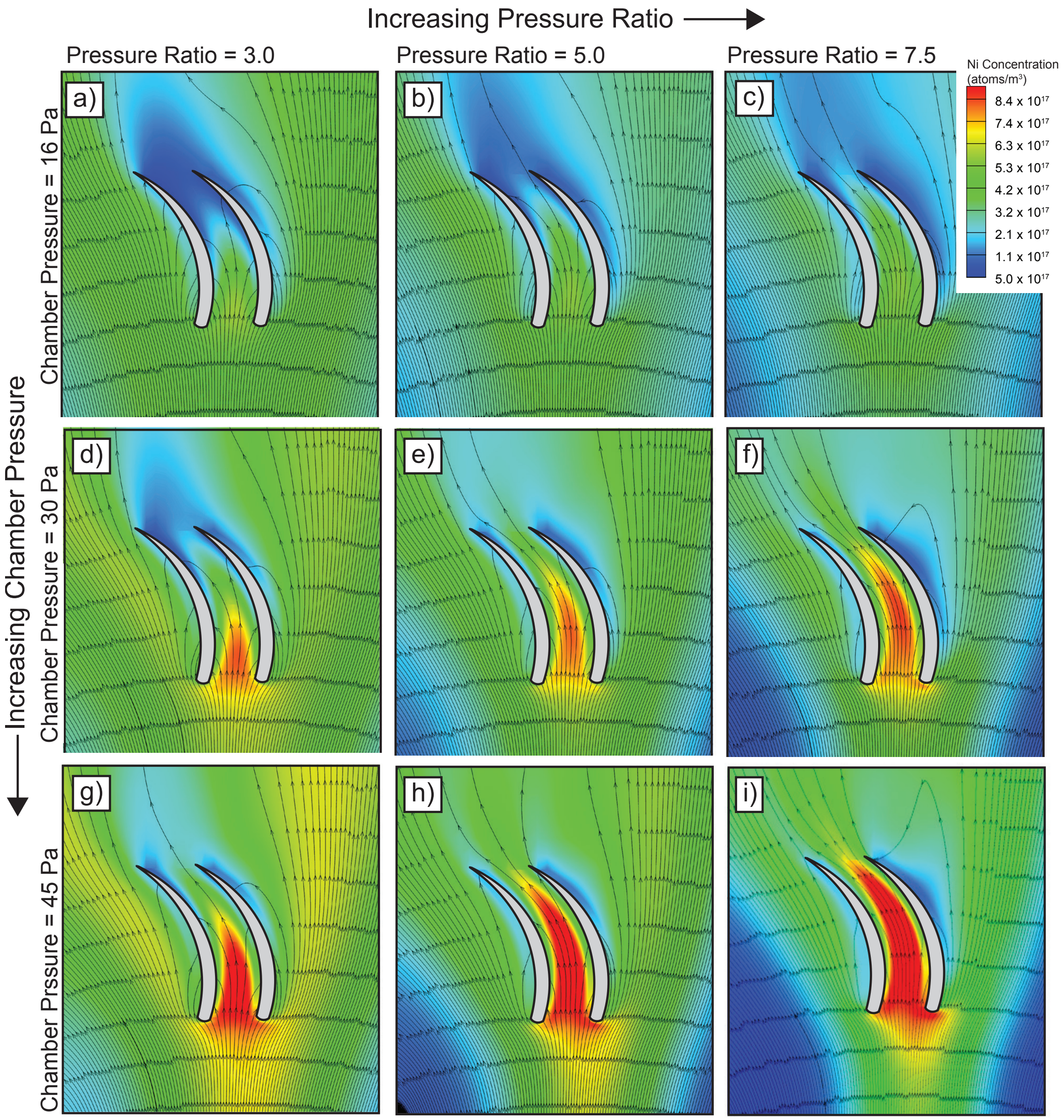

Figure 6.7: Vapor atom streamlines and concentration contour plots for a substrate orientation $\alpha = 0°$ as the pressure ratio (rows) and chamber pressure (columns) were independently varied.

Variation of the inter-airfoil channel width also resulted in significant changes to the vapor flow. The vapor concentration contours and streamlines at channel widths of 8, 12 and 16 mm are shown in Figure 6.8. A pressure ratio of 3 and chamber pressure of 16 Pa was used for all simulations. At a width of 8 mm, the vapor concentration in the inter-airfoil region is quickly depleted onto the inner surfaces. As the channel width increased, vapor traveled further along the channel. At a width of 16 mm, some vapor streamlines traveled through the entire channel without depositing on the substrate surface.

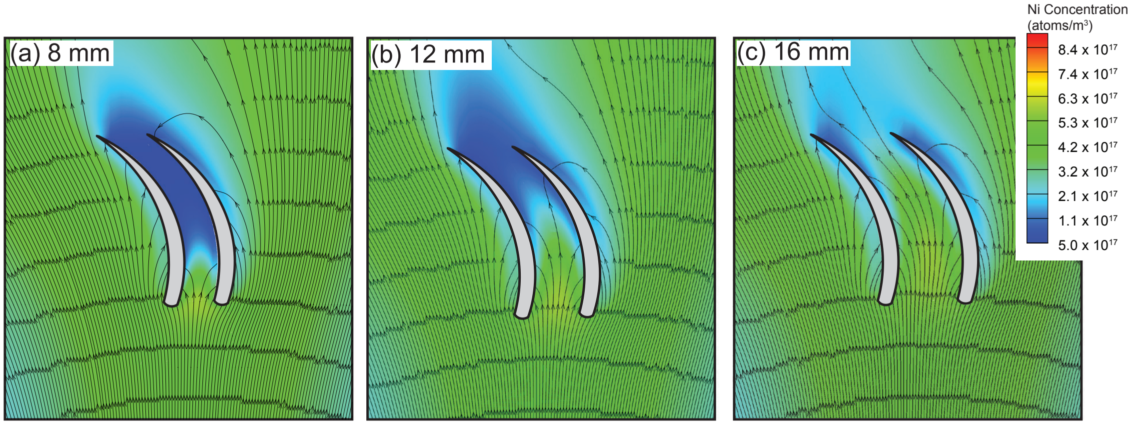

Figure 6.8: Vapor atom streamlines and concentration contour plots for a substrate orientation $\alpha = 0°$ as the channel width was varied. Simulations were performed at a chamber pressure of 16 Pa and pressure ratio of 3.

Figure 6.7 indicated that greater vapor penetration into the channel occurs at increased chamber pressures and pressure ratios. Figure 6.9 shows the variation of vapor concentration contours and streamlines with channel width at a pressure ratio of 5 and chamber pressure of 45 Pa. At a channel width of 8 mm, vapor penetration is significantly improved over the 16 Pa conditions used in Figure 6.8. As in Figure 6.8, as channel width increased vapor propagated further down the channel. At the 16 mm channel width, a large fraction of the vapor in the inter-airfoil region travels through the channel without depositing.

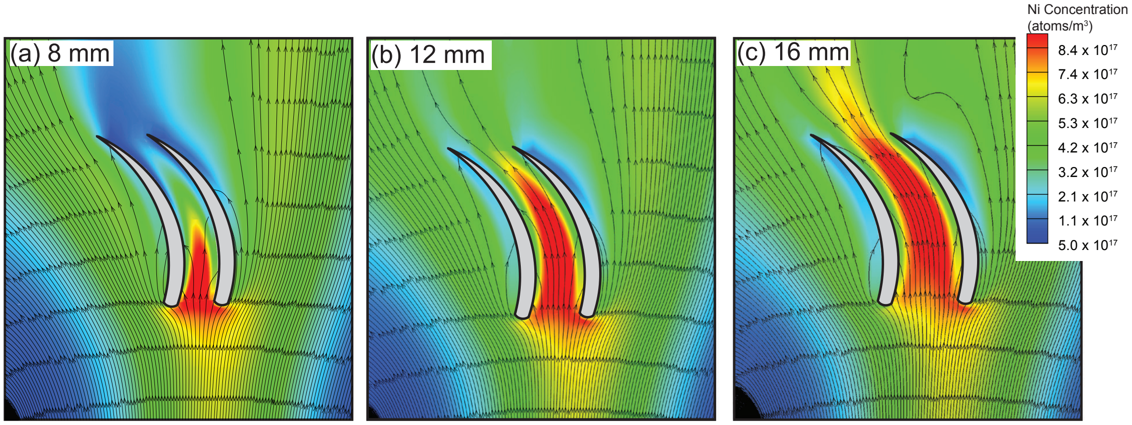

Figure 6.9: Vapor atom streamlines and concentration contour plots for a substrate orientation $\alpha = 0°$ as the channel width was varied. Simulations were performed at a chamber pressure of 45 Pa and pressure ratio of 5.

6.4.2 Experimental depositions and comparison

Experimental thickness profiles are shown in Figure 6.10. Depositions were performed at two conditions: a chamber pressure of 22 Pa and pressure ratio of 5.45, and a chamber pressure of 43 Pa and pressure ratio of 4.19. Both depositions used a substrate with a 16 mm channel width, a rotation rate of 6 rpm, and were performed for ~70 minutes. Both depositions resulted in a PVD-like columnar microstructure around the entire substrate surface. Deposition at 43 Pa resulted in a higher average coating thickness. The ratio of minimum coating thickness (found at the inner convex and concave surface midpoints) to maximum thickness (found at the surface ends) was also greater. The coating thickness along the outer surfaces was typically greater than that on the inner. However, the maximum thicknesses at the entry and exit ends of the doublet were comparable.

Along the outer surfaces, Figure 6.10(a) and (b), the thickness quickly (within 5 mm of the surface endpoints) decreased from the thickness maximums and then remained largely uniform for the remainder of the surface. This also occurred on

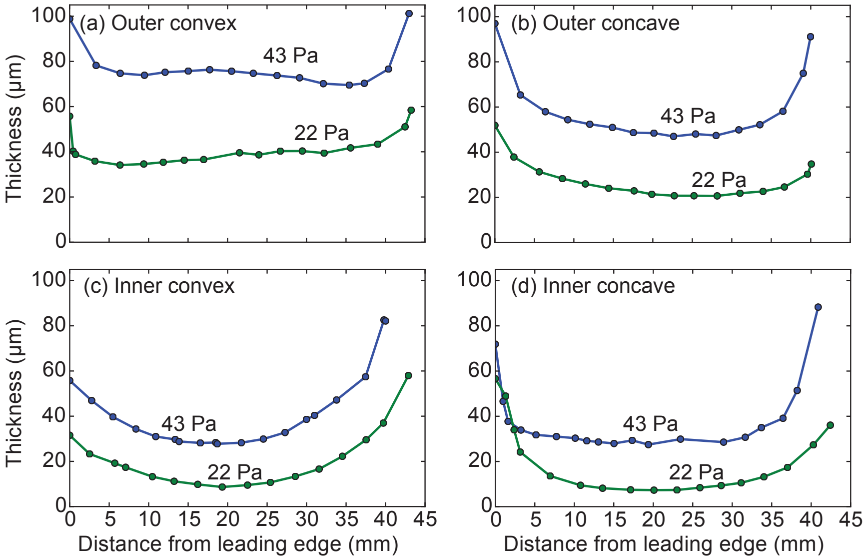

Figure 6.10: Measured coating thickness profiles for experimental depositions performed at a chamber pressure 22 Pa using a pressure ratio of 5.5, and at a chamber pressure of 43 Pa and pressure ratio of 4.5. The airfoil separation gap for both cases was 16 mm, and the substrate was rotated at 6 rpm.

the inner concave surface, Figure 6.10(d), where the coating thickness was quite uniform for much of the surface (from 5 to 35 mm from the leading edge). Along the inner convex surface, Figure 6.10(c), the coating thickness smoothly decreased until reaching a minimum value near the surface midpoint.

Experimental and DSMC simulation results can be compared by normalizing the experimental thickness and simulated deposition flux profiles by a thickness at the leading edge. All values along the surfaces were normalized by the maximum thickness value at the outer convex surface's trailing edge (found at the upper right hand corner of Figure 6.11(a)). The normalized profiles on the four coated surfaces for a deposition performed at a chamber pressure of 22 Pa with a 5.45 pressure ratio and doublet separation distance of 16 mm are shown in Figure 6.11(a and b), while normalized profiles simulated and measured at a chamber pressure of 43

Pa and pressure ratio of 4.5 are shown in Figure 6.11(c and d). The experimental and simulated profiles are in reasonable agreement, including the shape differences between the inner surfaces mentioned above.

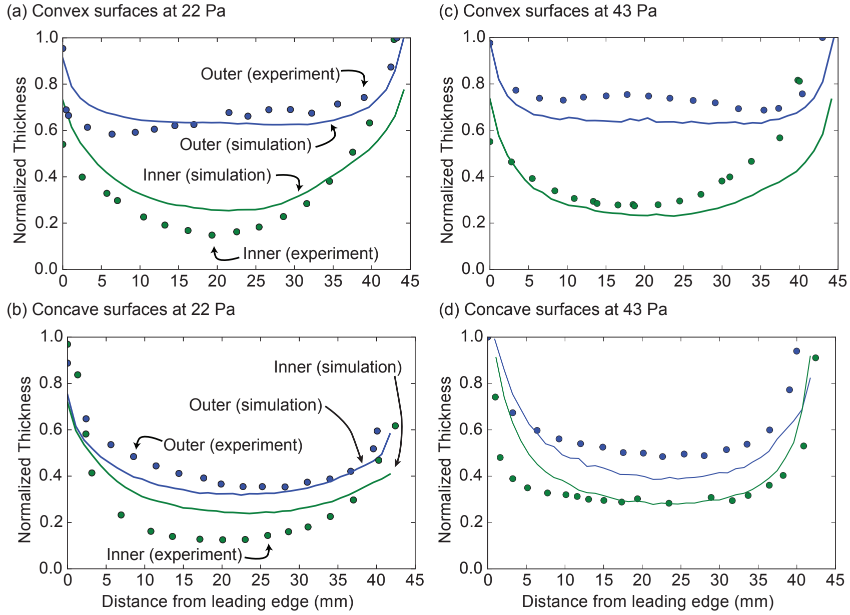

Figure 6.11: Comparison of normalized experimental and simulation thickness profiles along the convex and concave airfoil surfaces with a channel width of 16 mm. The chamber pressure was 22 Pa and the pressure ratio was 5.45 in (a) and (b), while (c) and (d) used a chamber pressure of 43 Pa and pressure ratio of 4.5. The substrates were rotated at a rate of 6 rpm.

Each surface has a thickness - position profile with a minimum value near the surface's midpoint and a maximum value at either the trailing or leading edge of the airfoil. The profiles on the exterior substrate surfaces have a higher average deposition efficiency and are more uniform than those along the interior surfaces. Deposition on these external surfaces is dominated by line-of-sight deposition. The coating thickness profiles on these surfaces are similar to those deposited on rotated single airfoils; especially when the channel width was small. Along the interior surfaces, the profiles have similar shapes but with much larger variation between minimum and maximum values. The inner concave surface has a maximum near the leading edge, while the inner convex surface has a maximum near the trailing edge. This surface region experiences an extended period of rotation in the line-of-sight of the vapor source. The minimum deposition efficiencies along the interior surfaces are nearly equal, as they occur in NLS regions where diffusion is the dominant deposition mechanism.

6.4.3 Simulated deposition efficiency profiles

The three variables that most affected deposition uniformity were the channel width, pressure ratio, and chamber pressure. The local vapor deposition efficiency variation with position along each doublet substrate surface for three channel widths is shown in Figure 6.12 for deposition into a chamber at a pressure of 16 Pa at a pressure ratio of 5.0. The profiles along the outer surfaces, Figure 6.12 (a) and (b), varied little as the channel width was changed. The efficiency profiles on these surfaces are quite similar to those along a single airfoil and remain as such until the substrate width that of the impinging vapor plume. Along the inner substrate surfaces, Figure 6.12(c) and (d), the deposition efficiency profiles are more significantly affected by channel width. The lowest deposition efficiency on each inner surface was located near the midpoint of the surface. This local deposition efficiency minimum exhibited a nearly tenfold increase as the airfoil separation width increased from 8 to 16 mm, while the maximum deposition efficiencies on the inner surfaces (near the surface endpoints) remained similar for all channel widths.

The effects of varying the upstream/downstream pressure ratio upon the local deposition efficiency along both the inner and outer surfaces of a doublet substrate with a fixed 12 mm channel width and chamber pressure of 16 Pa are shown in

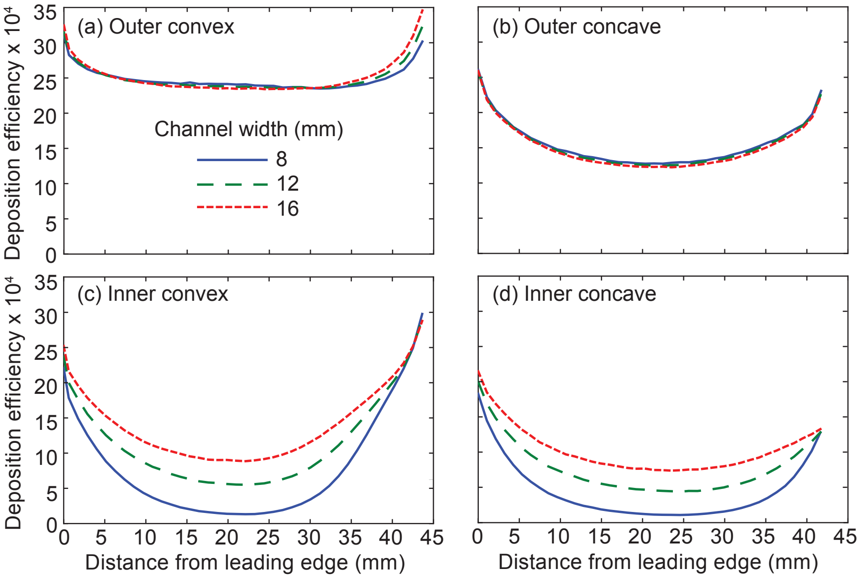

Figure 6.12: Predicted local deposition efficiency (coating thickness) profiles along the 4 substrate surfaces of doublet airfoil substrates with channel widths of 8, 12 and 16 mm. Depositions were performed for a chamber pressure of 16 Pa and pressure ratio of 5.0.

Figure 6.13. Along the exterior surfaces, Figures 6.13(a) and (b), the fraction of vapor that condensed upon the surfaces decreased with increasing pressure ratio. However, along the inner surfaces, Figure 6.13(c) and (d), the fraction of vapor that condensed near the surface midpoint increased with pressure ratio. Increasing the pressure ratio increased the jet velocity, Equation 4.4, enabled deeper penetration of the vapor plume into the channel, while simultaneously increasing the fraction of vapor that flowed past the external doublet surfaces without condensing.

The effect of chamber pressure upon the local deposition efficiency is shown in Figure 6.14 for a fixed channel width of 12 mm and pressure ratio of 5.0. The chamber pressure controls the rate of diffusion of the vapor atoms in the gas flow, and has a large effect on both the magnitude and shape of the local deposition efficiency profile on all of the surfaces. Figure 6.14 shows that the most uniform deposition profiles on all surfaces occur at the lowest chamber pressure of 1 Pa.

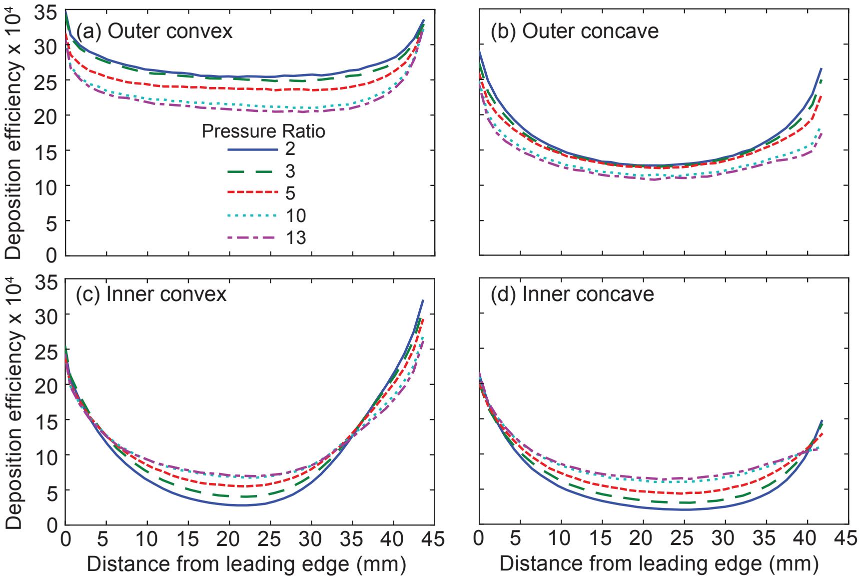

Figure 6.13: The effect of pressure ratio upon the simulated local deposition efficiency profiles along the 4 substrate surfaces. Depositions were performed at a chamber pressure of 16 Pa and for a channel width of 12 mm.

However, the deposition efficiency along the inner surface was extremely small compared to that on the external surfaces and virtually no vapor was deposited near the midpoint of the inner convex surface, Figure 6.14(c).

Increasing the pressure resulted in a peak in deposition efficiency on all surfaces at a pressure of 10 Pa. This also coincided in a decrease in the local deposition efficiency variation along each surface, resulting in more uniformity of coating thickness on each surface. As the pressure was increased towards 30 Pa, the exterior surface deposition efficiency decreased, but the inner surface minima efficiency slightly increased. At 100 Pa, the surface deposition efficiency was greatly reduced on all surfaces. The average vapor deposition efficiency is much lower than the other profiles along the outer concave surface, and is quite similar to the 1 Pa results along the other surfaces. This high pressure simulation neglects gas-phase cluster formation, which can be a significant factor as the chamber pressure rises [2].

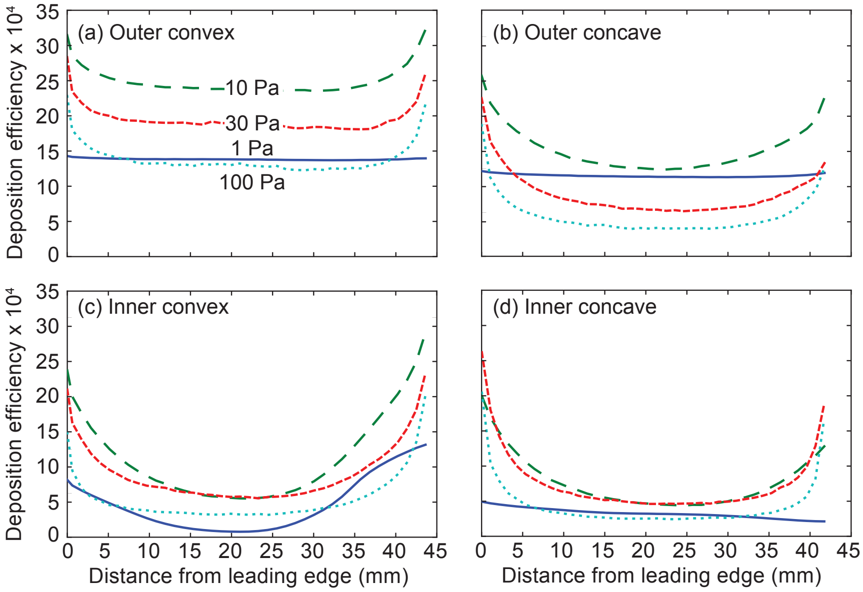

Figure 6.14: Simulated deposition efficiency profiles along the 4 substrate surfaces for several chamber pressures. Depositions were performed at a pressure ratio of 5.0 and channel width of 12 mm.

To more deeply investigate the effect of chamber pressure and pressure ratio upon a coating's thickness uniformity, the local deposition efficiency has been determined midway along the two the inner surfaces of the doublet substrate. The midpoint deposition efficiency was calculated by dividing the number of simulated vapor atoms that deposit in the midpoint surface region by the total number of atoms evaporated from the source. This is shown as a function of chamber pressure (from 0.01 to 100 Pa) in Figure 6.15 (a) and (b) for the inner concave and inner convex surfaces. The pressure ratio was also varied from 3 to 10 for each of the chamber pressures while the channel width was held constant at 12 mm.

The midpoint deposition efficiency on the inner concave surface, Figure 6.15 (a), varied between 2.5 and 6 $x10^{-4}$. At the lowest PVD-like chamber pressure (0.01 Pa), 0.027% of the total evaporated vapor was condensed upon the 1.07 mm-wide midpoint surface region. This efficiency improved with increasing chamber

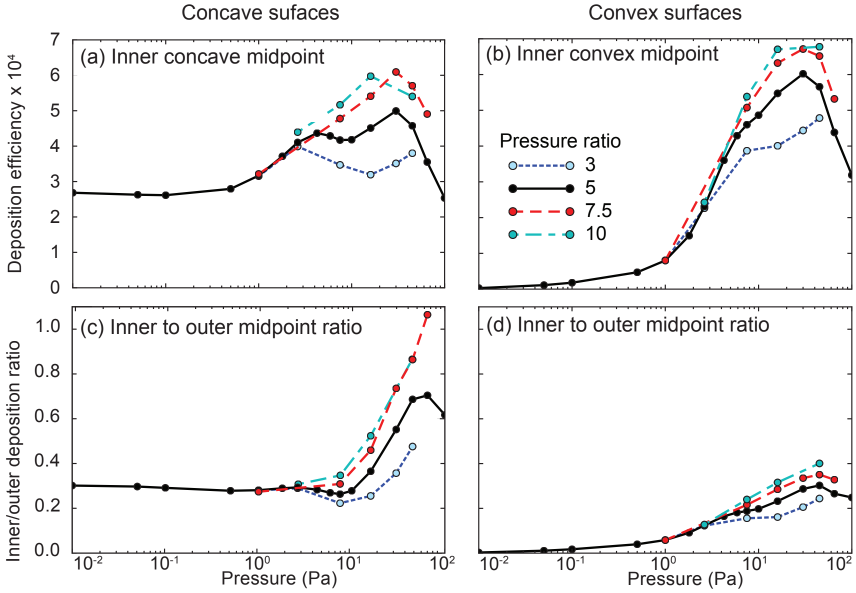

Figure 6.15: Variation of vapor deposition efficiencies at the midpoints of substrate surfaces with chamber pressure and pressure ratio. Subplots (a) and (b) show the deposition efficiency at the inner surface midpoints. Subplots (c) and (d) show the ratio of deposition efficiencies at the inner and outer surface midpoints. All simulations were performed with a channel width of 12 mm.

pressure, reaching the maximum close to a chamber pressure of 40 Pa before decreasing rapidly with further increase in pressure. The deposition efficiency also increased with increases in the pressure ratio for pressures near that where the peak in deposition efficiency occurred.

The variation of the midpoint deposition efficiency on the inner convex surface exhibited a much larger variation. This surface contained a region that was only very briefly in the line of sight of the vapor source during rotation. At the lowest pressure, the midpoint deposition efficiency was very close to zero, with almost no atoms reaching this surface region. The deposition efficiency then increased, at first slowly with chamber pressure before rapidly increasing between a pressure of 1 and 10 Pa. The deposition efficiency reached a maximum ~40 Pa, before rapidly decreasing at higher pressures. Near the pressure of maximum efficiency, the midpoint deposition efficiency increased with pressure ratio and exceeded that on the inner concave surface.

Ideally, the ratio of surface midpoint deposition efficiency for the inner and outer convex (or concave) surfaces should also be as close to unity as possible for this application. These ratios are shown in Figure 6.15 (c) and (d) for the two concave and two convex surfaces. The figures show that this ratio is also highly sensitive to deposition conditions. On the concave surfaces, deposition efficiency is largely constant until a chamber pressure of ∼7 Pa is reached. Above this pressure, the ratio rapidly increases due to a much faster increase in deposition efficiency on the inner surface than on the exterior. The deposition efficiency ratio shows a greater sensitivity to pressure ratio. The deposition efficiency ratio is much less sensitive to deposition conditions along the convex surface. The deposition efficiency ratio increases very slowly until a pressure of ∼1 Pa is reached. It then increases slowly before declining as the highest chamber pressures were approached. The slow increase is due to an increase in efficiency along both the inner and external surfaces with pressure.

The total deposition efficiencies on the four surfaces is shown for several chamber pressures in Table 6.1 for a pressure ratio of 5 and channel width of 12 mm. The table shows a similar trend to the midpoint deposition efficiencies in Figure 6.15. For this set of conditions, the highest deposition efficiency was achieved at a pressure of 10 Pa. The results in the table demonstrates that the continued increase of the ratio of midpoint deposition efficiency found in Figure 6.15(c and d) at the highest pressure ratios results from a decrease in deposition efficiency on the external surfaces, rather than an increase in efficiency on the inner surfaces. Deposition efficiency on the inner surfaces also declined between 10 and 100 Pa, but at a lower rate.

	Total deposition efficiencies percentage (%)			
Chamber pressure	Outer concave	Inner convex	Inner concave	Outer convex
0.01	3.6	1.0	1.2	4.0
1	4.5	1.9	1.3	5.6
10	7.0	4.5	2.7	10.5
100	2.3	2.6	2.2	5.9

Table 6.1: Total deposition efficiencies along each surface at several chamber pressures. The deposition efficiency on the outer surfaces decreased with increasing chamber pressure. Depositions were performed for a pressure ratio of 5 and a channel width of 12 mm.

6.5 Discussion

6.5.1 Role of diffusive transport

The deposition conditions resulting in best coating uniformity along the inner substrate surfaces occurred when the vapor in the inter-airfoil channel had been fully depleted just as the flow reached the exit of the channel (either the trailing or leading edge, depending on substrate orientation). This situation is schematically illustrated in Figure 6.16, where the vapor concentration profile between adjacent channel surfaces are shown. The vapor is first depleted from regions nearest to the substrate surfaces creating a concentration gradient across the channel width. As the flow progresses through the channel, gas phase scattering enables transverse diffusion of the vapor into the vapor depleted region, and this then condenses upon the interior surfaces.

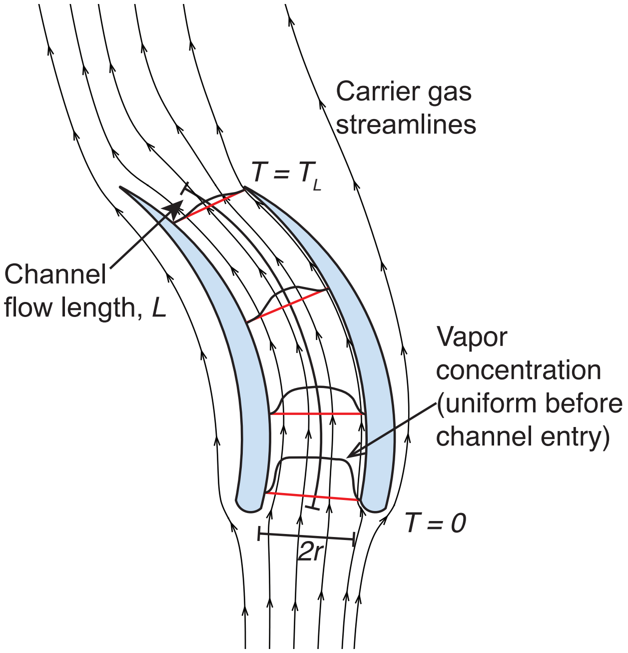

Figure 6.16: Schematic of vapor concentration depletion during flow through the substrate. Under ideal conditions, the vapor concentration is depleted just before reaching the end of the channel.

This balance between diffusion and convection can be expressed through balancing the flow time through the channel, T_L, and the time required to for vapor to diffuse from the channel midpoint to a substrate surface, T_r. T_L can be estimated by dividing the channel length, L, by the average flow velocity, $\overline{u}$;

$$T_L = \frac{L}{\overline{u}}. \tag{6.1}$$

T_r can be estimated from the one-dimensional diffusion length given by Fickian diffusion [94];

$$T_r = \frac{(r/2)^2}{D}. \tag{6.2}$$

where r is half of the channel width and D is the coefficient of diffusion of a trace species through a background gas given by the Chapman-Enskog approximation

[45];

$$D = \frac{4\beta}{3\pi n_g {\sigma_{12}}^2}\left(\frac{2kT}{m_v}\right)^2\left[\frac{9}{64}\frac{\pi^{1/2}}{\beta}\left(1+\frac{1}{\beta^2}\right)^{1/2}\right]. \tag{6.3}$$

where n_g is the number density of the background gas, σ_{12} is the average collisional cross-section of the two species (tabulated in [105]), and m_v is the mass of the vapor species. β is the square root of the ratio of carrier gas and vapor species molecular mass defined by;

$$\beta = \sqrt{\frac{m_g}{m_v}} \tag{6.4}$$

where m_g is the mass of the background gas. D is inversely proportional to the background (deposition chamber) pressure. Depletion of the vapor concentration near the channel exit will occur when $T_r \propto T_L$.

To demonstrate the importance of diffusion to the vapor deposition, the carrier gas (top row) and vapor atom (lower row) velocities in the cross-channel direction are shown in Figure 6.17 for several chamber pressures (left column) and three locations along the inner channel (right) column. The positive transverse direction was defined as being to the right of the channel midline, while the negative transverse direction was towards the left. For all pressures, vapor atom velocity is significantly higher than carrier gas velocity. Vapor atom velocities increase with decreasing pressure. This occurs due to the increase in diffusion coefficient with decreasing pressure, Equation 6.3.

Both the carrier gas and vapor species transverse velocities are quite similar along the inner channel's length. The carrier gas and vapor atom transverse velocities are respectively shown in Figure 6.17 (b) and (d). The orientation of the transverse velocities was determined at each location by calculating the direction of highest carrier gas velocity at the channel midpoint (which closely followed the local tangent

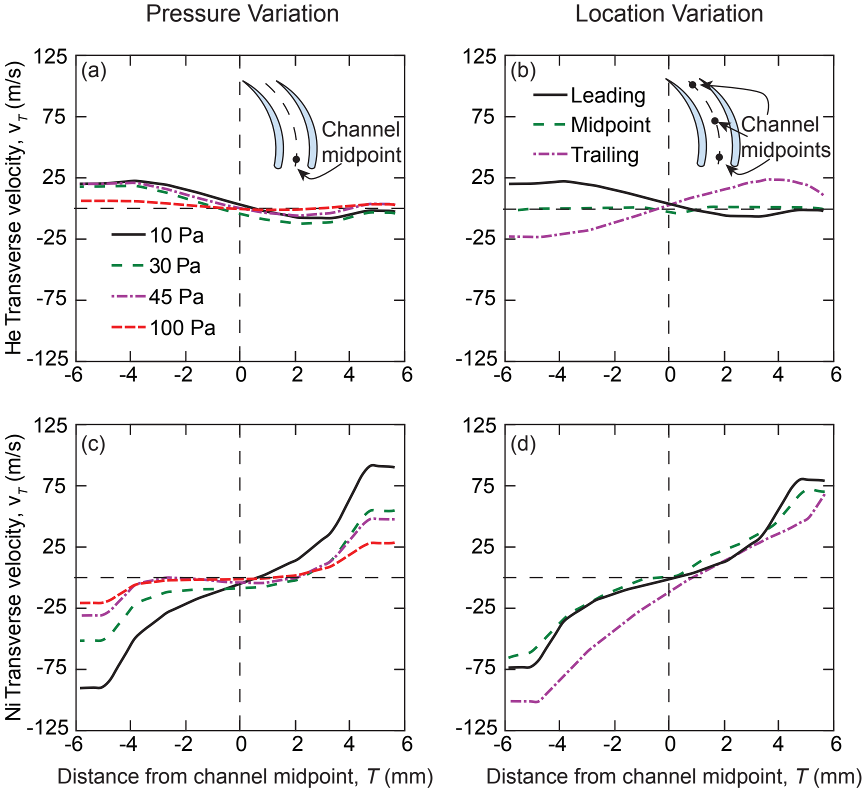

Figure 6.17: Comparison of the transverse velocity v_T of (a and b) carrier gas and (c and d) vapor atoms for variations in chamber pressure, location, and carrier gas species. Simulations were performed for stationary $\alpha = 0°$ airfoil orientation with a pressure ratio of 5.0 and channel width of 12 mm.

of the channel's midline) and then determining the perpendicular angle. The results show that carrier gas flow varies by ±25 m/s along the channel width. At the leading edge, there is a carrier gas flow towards the channel midpoint from each direction. However, at the channel midpoint, the carrier gas velocity is extremely low. There is almost no net movement in the transverse direction. Near the trailing edge, the carrier gas flows away from the channel midpoint, as the gas expands from the channel. The transverse vapor atom velocities do vary as much with location along the channel length. The profiles at the channel entrance and midpoint are quite similar, varying by less than 5 m/s across the channel width. The vapor atom velocity is skewed towards the positive transverse-direction at the trailing edge opening.

6.6 Coating thickness optimization

In a gas turbine, doublets are often used in a stationary vane stage after flow exits the combustion chamber. During engine use, the doublet surfaces experience virtually identical conditions regardless of their location along the interior or exterior of each individual doublet component. If the coating at all points on the surface of a doublet guide vane are subjected to the same thermal boundary condition during operation, the coating thickness over the entire surface should be as uniform as possible. In Chapter 5 it was shown that the thickness on the two sides of a single airfoil could be controlled through dynamical manipulation of the source evaporation and substrate rotation rates during each rotational period. It is therefore reasonable to ask if an optimized non-uniform rotation rate can be found that minimizes the difference in coating thickness (i.e deposition efficiency) between the inner and outer convex, and inner and outer concave surfaces of the doublet guide vane substrate.

To allow the substrate dwell time to be varied during a rotation, the simulated vapor deposition efficiencies at the eight stationary orientations were assigned a variable weight coefficient. As with the single airfoil optimization, the total deposition efficiency, j, on each simulated surface region was then calculated as;

$$j = \sum_{m=1}^{8} a_m f_m \tag{6.5}$$

where f_m is the deposition efficiency at each of the 8 orientation angles of the substrate, and a_m is the orientation coefficient to be determined. The total deposition efficiency difference between each convex or concave pair of inner and outer airfoil surfaces is then expressed by;

$$\Delta J = \sum_{n=1}^{40} |j_{outer,n} - j_{inner,n}| \tag{6.6}$$

where $j_{inner,n}$ and $j_{outer,n}$ are the total deposition efficiency at each of the n substrate regions along the concave and convex surfaces($n = 1 - 40$ surface regions). The summation began at the convex and concave surface origins (near the leading edge) and proceeded along each surface towards the trailing edge (increasing n). The coefficients were constrained so that each deposition had a maximum/minimum rotation rate ratio of 8 (the maximum allowable dwell coefficient was eight times larger than the minimum). Finally, the total deposition efficiency differences between each pair of inner/outer surfaces were added together to create the final optimization objective function;

$$\Delta J_{tot} = w_x \Delta J_{convex} + w_v \Delta J_{concave} \tag{6.7}$$

where ΔJ_{convex} is the total deposition efficiency difference between the inner and outer convex surfaces, $\Delta J_{concave}$ is the total deposition efficiency difference between the inner and outer concave surfaces, and w_x and w_v are weighting coefficients for the deposition efficiency difference of each surface pair.

The resulting deposition efficiency profiles at constant and optimized rotation are shown in Figure 6.18 for optimization of a coating deposited at a chamber pressure of 45 Pa, a pressure ratio of 5.0, and channel width of 12 mm. The values of w_x and w_v were both set to 1.0, giving equal weight to the convex and concave surfaces. The profiles along the inner and outer concave surfaces are shown in

Figure 6.19(a). The concave surface coating thicknesses versus distance from the leading edge obtained using the optimal rotation rate sequence were thicker, and near the middle of the airfoils more similar in thickness than those for deposition using a constant rate of rotation. However, the deposition efficiency near the leading edge on the concave surface was much higher compared to the constant rotation case because of the additional time that it remained in line-of-sight of the vapor source.

The deposition efficiency along the inner and outer convex surfaces are shown in Figure 6.18(b). Along the convex surfaces, the optimized rotation increased the deposition efficiency on the inner surface while decreasing that on the outer surface. These variations combined to decrease the deposition efficiency differences everywhere on the two surfaces. By comparing the optimized thickness profiles in Figures 6.18(a) and (b) it is clear that the optimized process resulted in similar thickness coatings on all four surfaces with the exception of the leading edge of the inner concave surface, Figure 6.18(a).

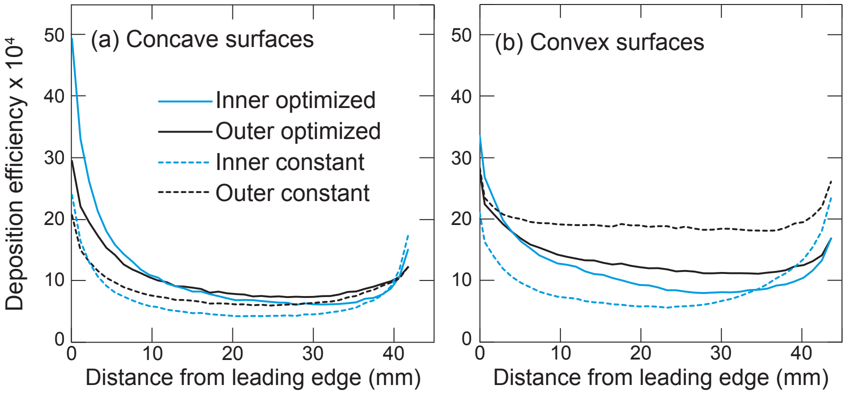

Figure 6.18: Simulated deposition efficiency profiles for constant (solid lines) and optimized (dashed lines) substrate rotation along the inner and outer surfaces. Simulations were performed at a chamber pressure of 45 Pa, a pressure ratio of 5.0, and a channel width of 12 mm.

The effect of chamber pressure upon the coating thickness difference between the inner and outer surface pairs for a wide range of pressures using a channel width of 12 mm and pressure ratio of 5 are shown in Figure 6.19. Figure 6.19(a) shows the difference in deposition efficiency ΔJ obtained by subtracting the integrated flux (along the entire surface) of the inner surface from that of the outer surface for the concave and convex surface pairs. Below a chamber pressure of 10 Pa, the optimization method converges to the constant rotation rate pattern. It is unable to overcome the consequences of a long vapor atom mean free path (compared to the channel width) encountered with deposition at the low chamber pressures. Above 10 Pa, the optimization routine reduces the deposition efficiency differences along both the convex and concave surface pairs. The greatest reduction is observed along the convex surfaces.

The optimization method typically reduces the flux difference between the inner and outer surfaces by reducing the deposition efficiency on the outer surfaces while increasing the deficiency on the inner surfaces. Figure 6.19(b) shows the ratio of total deposition efficiencies calculated using optimized and constant rotation along the inner and outer convex surfaces. A ratio less than one indicates that the optimization routine reduced the amount of vapor deposited on the surface during deposition, while a ratio greater one indicates an increase in total deposition efficiency on the surface. At pressures below 10 Pa, the ratio is unity (due to the optimization converging to the constant rotation solution). The inner surface ratio then increases before reaching a roughly constant value between 1.3 and 1.4 for pressures of 22 Pa and higher. The outer surface ratio decreases to lower values, reaching a value between 0.6 and 0.7 for pressures of 65 and 100 Pa.

The optimized dwell fractions calculated for several representative chamber pressures are shown in Table 6.2. At all pressures 16 Pa and higher, the optimiza-

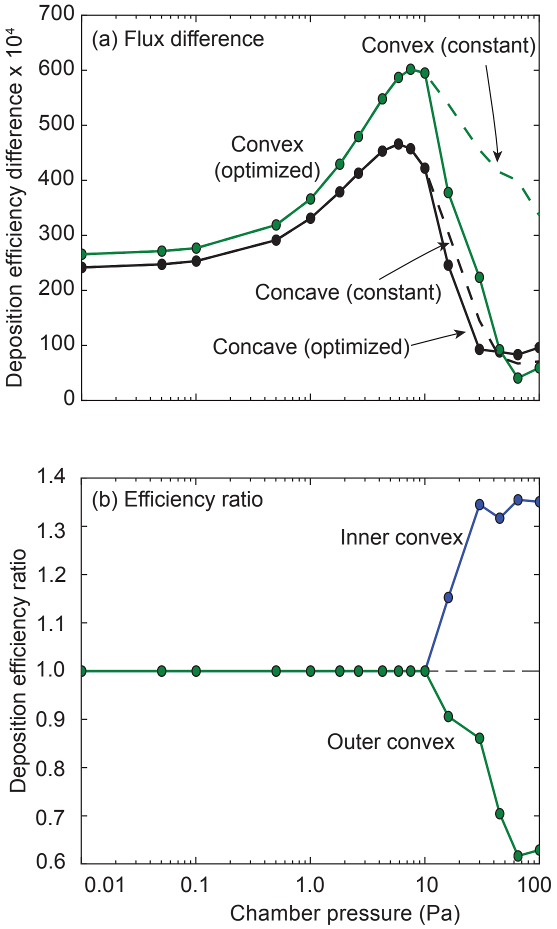

Figure 6.19: Optimized results showing (a) the difference between the total deposition efficiency along the inner and outer convex and concave surfaces for optimized and unoptimized dwell fraction simulations. (b) Shows the ratio of optimized to unoptimized deposition efficiency along the inner and outer convex surfaces. All simulations were performed with a channel width of 12 mm and a pressure ratio of 5.

tion process led to increases of the dwell time fraction at orientations where the substrate's channel was at least partially aligned with the incident vapor jet (0, 45, 225, and 315°). The dwell time fraction was correspondingly reduced for the orientations where the axis of the inner channel was predominantly transverse to the gas jet axis. It is also evident that those orientations with the largest dwell time fractions had dwell times that varied the most with changing chamber pressure.

	Dwell fraction during a rotation, a_m				
Dwell orientation, α (deg)	0.01 Pa	2.625 Pa	16 Pa	45 Pa	100 Pa
0	0.125	0.125	0.305	0.281	0.057
45	0.125	0.125	0.099	0.061	0.057
90	0.125	0.125	0.099	0.061	0.057
135	0.125	0.125	0.099	0.061	0.057
180	0.125	0.125	0.099	0.061	0.057
225	0.125	0.125	0.099	0.091	0.057
270	0.125	0.125	0.099	0.061	0.057
315	0.125	0.125	0.099	0.324	0.603

Table 6.2: Optimized dwell times during rotation segments for several chamber pressures. Simulations were performed for a channel width of 12 mm and a pressure ratio of 5.0.

The above optimization method demonstrates an important issue with deposition onto complex substrates: it is difficult (or sometimes impossible) to isolate deposition onto a subset of substrate surfaces. For example, to improve deposition onto the inner convex surface, the substrate must be oriented for vapor to pass between the leading or trailing edges. However, at these orientations there is significant deposition onto other surface regions near the leading or trailing edges. Optimizing coating thickness along comparable surfaces is possible, but may not result in optimum total uniformity. The small Reynolds numbers found at these deposition conditions (Re < 10) prevents the manifestation of non-laminar flow patterns that might enable more selective deposition patterns. Finally, while the use of higher chamber pressures enables more confined vapor plumes with better tuned flow patterns, it also promotes the formation of vapor clusters that may be detrimental to the coating process [2].

6.7 Conclusions

The mechanisms controlling deposition in doublet guide vane channels have been studied. The results show that deposition uniformity can be improved by varying the gas velocity, substrate geometry, and chamber pressure. The directed vapor deposition was shown to be capable of depositing a compliant thermal barrier coating around the entire surface of a model doublet guide vane. Substrate rotation was necessary to obtain a conformal coating with a consistent microstructure around the surfaces. Coating uniformity can be adjusted by modifying the deposition conditions and was found to trend with the ratio of bulk flow along the channel and transverse diffusion to the channel walls.

Chapter 7

Physical Vapor Deposition on Doublet Airfoil Substrates: Simulation of Coating Microstructure[1]

7.1 Synopsis

Gas jet assisted physical vapor deposition (PVD) techniques operate at higher pressures than conventional PVD processes, and have shown promise for coating complex shaped substrates including those with non-line-of-sight (NLS) surface regions. Compared to regions of the same substrate that are in line-of-sight (LS) of the vapor source, NLS regions receive a broader vapor atom incident angular

---

[1] Adapted from a technical article in preparation [133].

distribution at a lower flux. The coatings thickness and microstructure deposited upon these two types of surface region are therefore likely to different, and this could significantly affect coating behavior. To investigate such effects, the thickness and microstructure variation along the inner (curved channel) surfaces of a model doublet airfoil substrate containing NLS regions has been investigated. Results from atomistic simulations are first compared to those of experiments, and confirm that the coating's thickness in flux-shadowed regions is thinner than other regions. They also indicated that the coatings columnar microstructure and pore volume fraction vary slowly with surface location through the LS to NLS transition zone of airfoil surface. A substrate rotation strategy for optimizing the thickness over the entire doublet airfoil surface is also investigated, and resulted in identification of process conditions that incurred a small variation of coating thickness along all doublet airfoil surfaces with only a small change to the columnar growth angle and pore volume fraction.

7.2 Introduction

In this chapter we combine the DSMC method with a kinetic Monte Carlo (kMC) multiscale simulation methodology and explore control of coating microstructure on a doublet guide vane surface. Since the microstructure on the outer surfaces were very similar (for all but the widest channel width substrates) to those of a recent study of deposition on single airfoils, Chapter 5. We focus the study on the interior channel surfaces, Figure 7.1(b). We first investigate the vapor flux deposited upon the interior surfaces at various orientations during rotated deposition. The IAD along these surfaces will then be determined and used to simulate the deposition of coatings on the surfaces. The variation in columnar growth angle and coating porosity as the deposition conditions were varied is then systematically investigated. Finally, the rotation optimization method previously proposed for controlling airfoil coating thickness uniformity in Chapters 5 and 6 is investigated here to reduce variations of deposition efficiency and microstructure differences between the inner and outer airfoil surfaces.

7.3 Methods

A combination of experimental and simulated studies were performed to evaluate coating properties. A combined multi-phase direct simulation Monte Carlo (DSMC) and kMC simulation scheme was used to create the simulated microstructure, as discussed in Chapter 5. In addition to the chamber pressure and pressure ratio that were varied in the previous paper, here the inter-vane channel width was also varied between 8, 12, and 16 mm measured between the leading edges. A schematic is shown in Figure 7.1 showing the definition of the substrate geometry and the definition of the angles used to describe the simulations.

As in Chapter 5, three angles play important roles in microstructure development within the coating. Two of these, the substrate orientation angle, α, and vapor incident angle, θ, are defined in Figure 7.1(a). The substrate orientation angle is defined as the angle between the gas jet axis and the orientation axis of the substrate as indicated in the figure. These axes are collinear at $\alpha = 0$ and both pass through the center of rotation of the substrate. The Incidence angle of the vapor was defined using the normal to the local surface as shown in Figure 7.1(a). The columnar growth angle ϕ, was defined identically to the vapor incident angle, θ, with a value

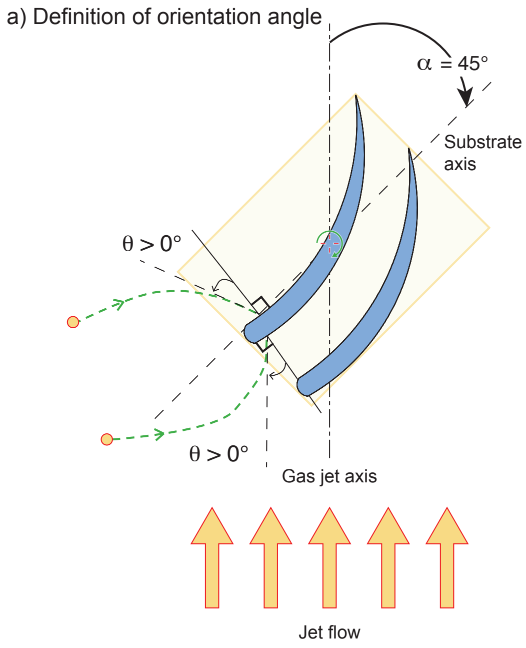
a) Definition of orientation angle

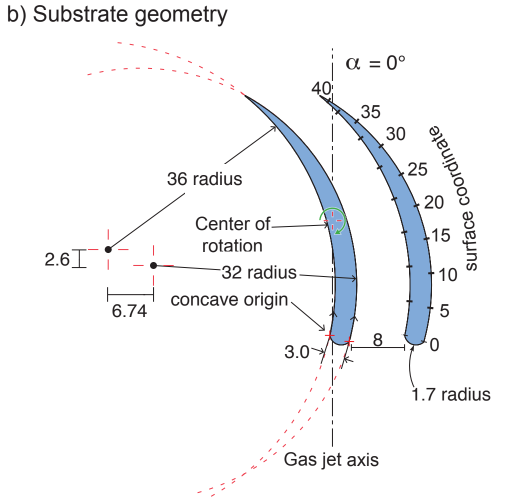
b) Substrate geometry

Figure 7.1: (a) Definition of the incidence angle, θ of a vapor atom relative to the airfoil substrate's local surface normal, and the orientation of the substrate, α relative to the jet flow axis. (b) A schematic illustration of the coordinate system for the model 2D doublet airfoil substrate. During stationary deposition, the airfoil was aligned with the gas jet flow direction and for the other simulations and experiments it was rotated clockwise about the center of rotation. (All dimensions are in mm).

of zero corresponding to columnar growth perpendicular to the local surface. The α and θ angles were defined as positive when oriented towards the leading edge of the substrate and negative when directed towards its trailing edge. Vapor atoms depositing from similar trajectories onto different substrate surface (as shown in Figure 7.1(a)) will have the same value of θ.

Both the simulation and the experiment utilized the same doublet airfoil substrate. The design of the two individual airfoils was identical to that previously used in an investigation of single airfoil deposition (Chapter 5) and a study of coating thickness on a doublet guide vane (Chapter 6). During the simulations, the doublet airfoils were assumed perfectly two-dimensional. For experiments, the airfoils were 31.75 mm high (in the out of plane direction) and were capped on each side by a thin backing plate, Figure 6.1(a). This height was sufficient that the mounting plates did not influence deposition profiles at the midline cross-section of the doublet. A surface coordinate was defined for each of the 4 airfoil surfaces as shown in Figure 7.1(b). Its origin was defined as the intersection of the circular leading edge circumference with that of the airfoil.

7.3.1 Simulation methods

The numerical simulation method combined the gas-phase direct simulation Monte Carlo method with a coating assembly kinetic Monte Carlo modeling approach to simulate the deposition of a nickel coating. The procedure was identical to that described in Chapter 5. As in earlier studies of deposition nickel upon a single airfoil, the vapor flux incident upon the substrates was determined using the Icarus DSMC code [105]. It propagated atoms from a nickel vapor-emitting source to the substrate by tracking binary collisions between the vapor atoms and those of an inert gas jet in which they were entrained.

The kMC simulations were performed on a substrate rotated at 6 rpm; the same as that used for experiments. This was implemented by assigning a fixed dwell time of 1.25 seconds at each of the eight simulated substrate orientations. Atoms were deposited using the input variables for each substrate orientation until the dwell time elapsed whereupon the input variables were changed to the next orientation's properties, and the simulation resumed. This cycle continued until the desired number of atoms were deposited. An evaporation rate of 8.8 x 10^{20} atoms $m^{-2}s^{-1}$ was used for all simulations. The number of atoms deposited in each surface region and the orientation dependent deposition rate were calculated using the method described in Section 5.3.1.

7.3.2 Experimental methods

Experimental depositions using a nickel source were performed using an EB-DVD method, and were conducted in an identical manner to that described in the previous study of coating thickness uniformity on the same substrate discussed in Chapter 6. Doublet airfoil substrates with a height of 31.75 mm and a channel width (measured between the origins of the inner convex and concave surfaces) of 16 mm were mounted between 3 mm wide flat mounting plates, Figure 6.1. The substrates were made from 303 stainless steel and shaped by wire-cut electric discharge machining. Depositions were performed for approximately 70 minutes. The substrates were not intentionally heated during deposition, however radiative heat from the electron beam-vapor source interaction resulted in a substrate temperature of 150 °C ($T/T_m = 0.243$) during the depositions. Experimental depositions were performed at a chamber pressure of 22 Pa and a pressure ratio of 5.45. After deposition, samples were cross-sectioned at the midpoint between the pair of 40 mm x 32 mm rectangular mounting plates, polished, and imaged in an SEM.

7.4 Results

For ideal deposition, a coating of identical thickness and structure would be be deposited upon all surfaces of the doublet guide vane, including the leading edge and the (four) convex and concave surfaces of the two airfoils. The results in this section focus on the inner convex and concave airfoil surfaces. The coating properties along the outer surfaces of the doublet substrate investigated here were found to be very similar to those observed on a single airfoil substrate as long as the doublet airfoil channel width (8-16 mm here) remained smaller than the incident vapor plume, whose width ranged from 110 mm at 1 Pa to 75 mm at 100 Pa. Thus the reader is referred to Chapter 5 for a discussion of microstructural variation around the exterior surfaces of the single airfoil, and Chapter 6 for an investigation of coating thickness variations over both the inner and outer surfaces of the same doublet substrate coating microstructure investigated here.

7.4.1 Incidence Angle Distribution

The nickel vapor IAD determined from DSMC simulations was used to determine the average skew and breadth of the impact angles of depositing vapor atoms. For stationary vapor deposition onto a flat sample oriented at right angles to source

- sample direction and placed directly over the epicenter of the source, the IAD changes slowly with position across the substrate surface. However, the introduction of substrate rotation causes the distribution to vary with the angle of the rotation. Furthermore, when deposition is performed on a complex shaped substrate, significant IAD variation across the substrate also occurs during both stationary and rotated deposition. This IAD variation in turn, results in microstructure variations over the substrate surface.

The IADs at two locations (3.39 and 42.9 mm from the origin) along the inner convex surface for a stationary simulation at $\alpha = 0°$ are shown in Figure 7.2. IADs are typically well described by the full width at half maximum θ_w and the maximum incidence angle θ_m, both of which are indicated in Figure 7.2. Between the two surface locations, the IADs go through a gradual transition between those shown. From the leading to trailing edge, θ_w slowly increases and θ_m approaches the local surface normal. Even though the surface region along this surface trajectory changes from being directly within line-of-sight of the vapor source through a NLS configuration, gas phase scattering from the confined jet flow through the channel prevents any sudden variations in the IAD.

The variation of θ_m and θ_w are shown along the inner surfaces at the eight stationary substrate orientations used for simulations of rotated deposition at a chamber pressure of 22 Pa, pressure ratio of 5.45, and channel separation of 16 mm are shown in Figure 7.3. To simplify presentation of the results, the inner substrate surfaces were divided into thirds. For orientations where one of the channel openings was reasonably well aligned with the gas jet axis ($\alpha = 0$, 45, 180, and 315°), significant channel penetration by the gas jet occurs and θ_m was quite large (up to $\sim 30°$) but varied little along the entire surface, Figure 7.3(a) and (b). At

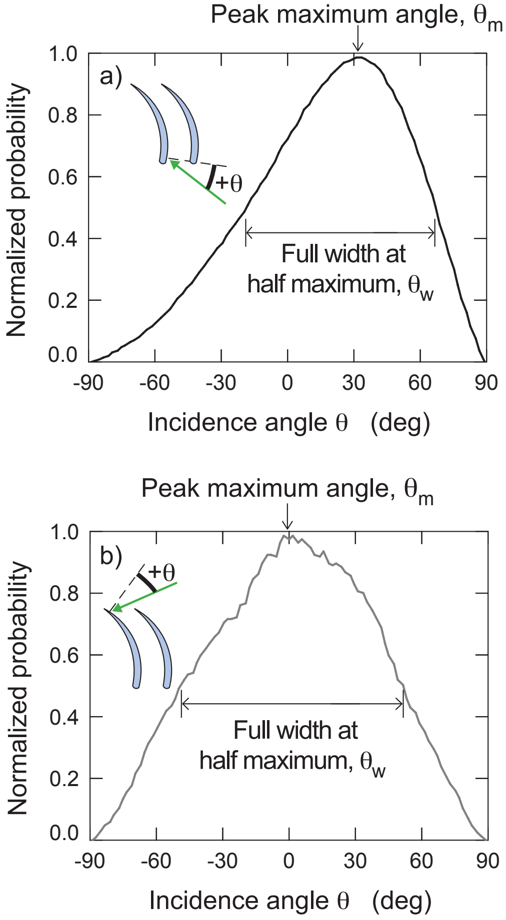

Figure 7.2: Incident angle distribution (IAD) experienced on two inner convex surface regions at a substrate orientation, $\alpha = 0$. The chamber pressure was 16 Pa, the pressure ratio was 5, and channel width was 8 mm. (a) shows the IAD at a region 3.39 mm from the leading edge. (b) shows the IAD at a region 42.9 mm from the leading edge.

orientations where the channel was perpendicular to the gas jet ($\alpha = 90$ and 270°), θ_m was more strongly dependent upon position and typically oriented towards the nearest channel opening. The average magnitude of θ_m was also reduced.

Figure 7.3(c) and (d) show distribution width, θ_w for each orientation. At orientations where significant vapor flow penetrated into the channel ($\alpha = 0$ and 225°) the distribution was narrowest near the channel opening closest to the vapor source. The most notable case was found at $\alpha = 225°$ where θ_w near the trailing edge (the black line) was 20° less than further along the channel. This decrease in θ_w also corresponds with an increase in magnitude of θ_w. Many vapor atoms were deposited on this surface from trajectories roughly parallel to the jet flow direction within the channel. At orientations with minimal channel penetration ($\alpha = 90$ and 270°), θ_w was typically large and remained mostly uniform along the channel length.

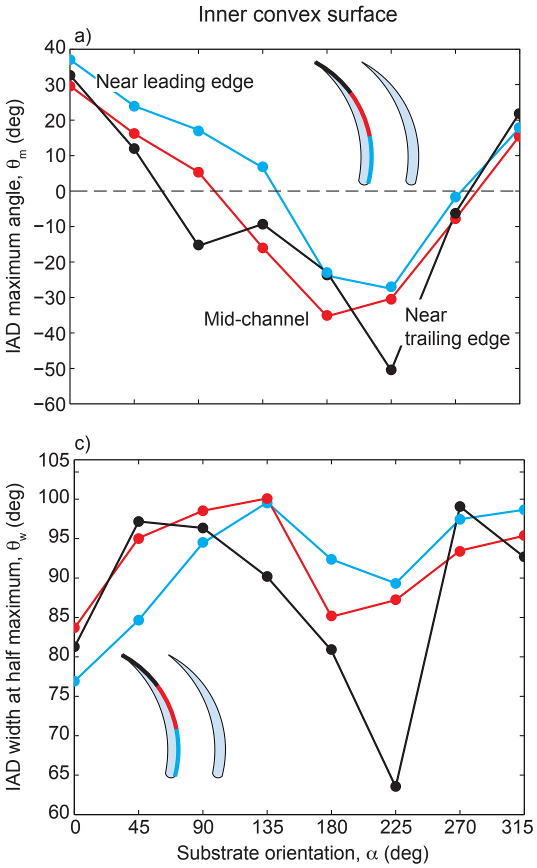

Figure 7.3: Variation of peak maximum incident angle θ_m (a and b) and IAD full width at half maximum, θ_w (c and d) with substrate orientation along the inner surfaces. Each line represents the average over a third of the surface's length. Simulations were performed at a pressure of 22 Pa and pressure ratio of 5.45. The substrate's channel width was 16 mm.

The IAD maximum and width values along the surface show that the vapor plume's properties quickly equilibrate as a flow entered the channel. Near the channel endpoints, the distribution was narrower and more skewed from the local substrate normal. Deposition in these regions was highly influenced by the specific gas jet environment, as vapor atoms near the substrate surfaces required few scattering collisions to deposit on the substrate and their trajectories retained much of their pre-channel entry character. Along channel regions far from either endpoint, vapor atoms had typically experienced multiple scattering collisions before deposition, and arrived from a broad range of incident angles.

7.4.2 Simulated and experimental comparisons

Examples of kMC simulated coating microstructures at three locations along the inner convex and concave surfaces are shown in Figure 7.4. The simulations were performed at a chamber pressure of 22 Pa, with a pressure ratio of 5.45, and a channel width of 16 mm using a simulated rotation rate of 6 rpm. A continuous coating was deposited along the inner surfaces. However, there were variations in the coating thickness and microstructure along each surface. Under these deposition conditions, the coatings were thickest near the channel endpoints, while the thinnest regions occurred at the midpoints of both interior surfaces. The coatings were columnar everywhere, but the columnar growth angle varied with location. The growth columns were oriented towards the nearest endpoint, and the magnitude of ϕ decreased away from these endpoints resulting in columns oriented perpendicular to the airfoil surface near the channel midpoint.

Experimental depositions were performed using the same deposition conditions to verify the simulation results. The resulting experimental microstructures are shown in Figure 7.5. Like the simulation results, the coatings had a columnar

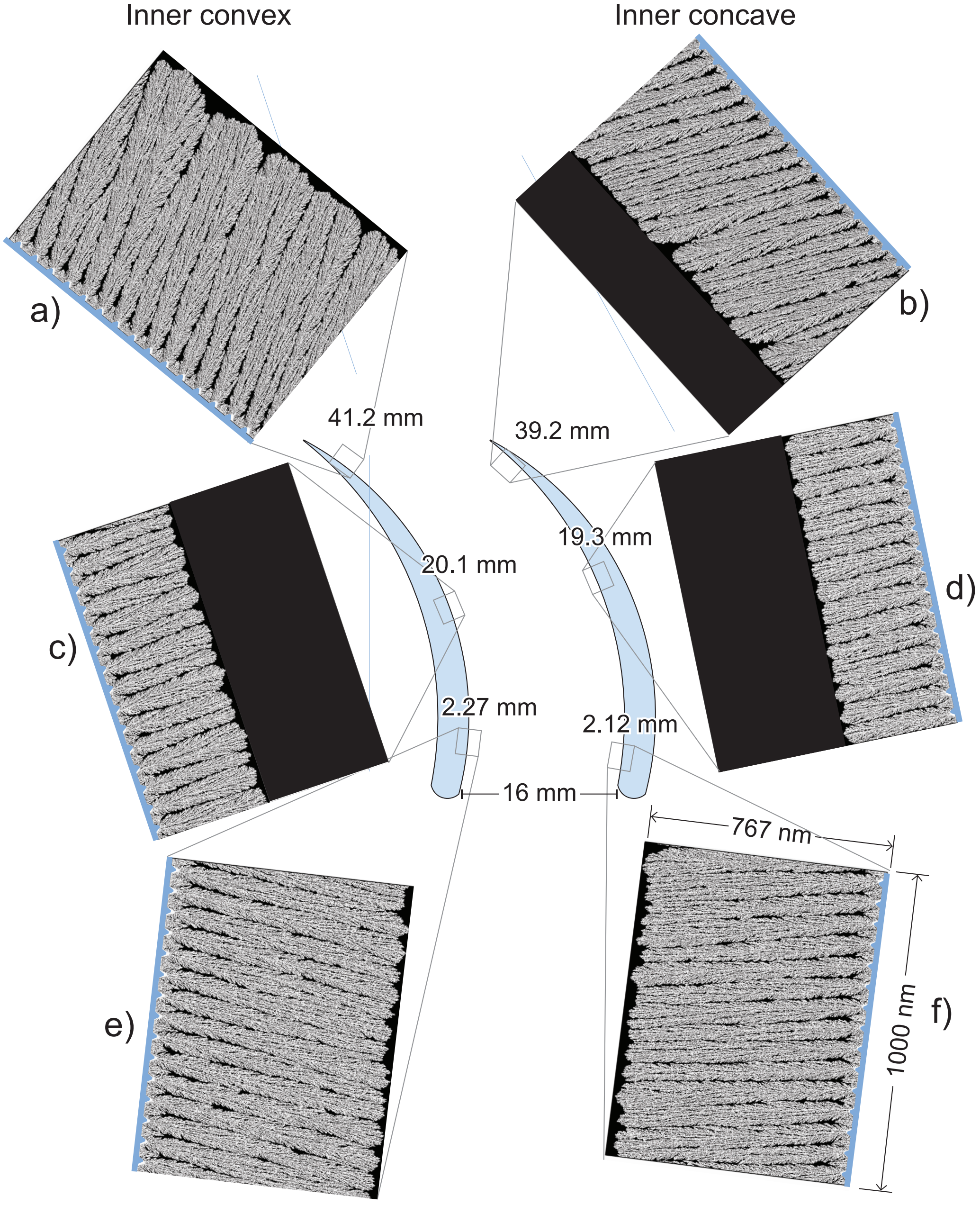

Figure 7.4: Simulated microstructures along the inner surfaces of a doublet airfoil substrate. The coatings were deposited using a rotation rate of 6 rpm at a chamber pressure of 22 Pa, a pressure ratio of 5.45, a substrate homologous temperature $T/T_m = 0.243$, a channel width of 16 mm, and an evaporative flux of 8.8 x 10^{20} atoms $m^{-2}s^{-1}$.

structure. The coating thickness was greatest at the leading edge and trailing end of the airfoils, and thinner near the midpoint of the airfoils. Again, like the simulations, the growth columns were inclined towards the nearest end of the airfoil and were approximately perpendicular to the airfoil surface near the airfoil midpoints.

The average growth column angle has been measured for the experimental coatings as a function of the location coordinate along the two interior surfaces of the doublet and is shown in Figure 7.6. The orientation angle of the experimental coatings had a standard deviation of 5° at each location of measurement. This variability appeared to be a consequence of the substrates surface roughness. A comparison with the simulated coatings columnar growth angle distribution is also shown in Figure 7.6 for comparison. The growth angle profiles for the simulation and experiment were in good agreement. The largest growth angles (of approximately 30° on the inner concave surface) occurred near the channel endpoints and progressively decreased to zero degrees at the midpoints of the airfoil surfaces. The growth columns of both the experimental and simulated coatings were less inclined at the leading and trailing end of the convex airfoil surface (∼10-15°) but again, this decreased to zero at the convex surface midpoint.

7.5 Coating variation with deposition conditions

Previous studies have shown that the thickness uniformity on the interior surface of the doublet airfoil substrate was strongly dependent upon the channel width and so its influence upon the coating microstructure is investigated in the following section. Many studies have also shown that columnar coating structure can by modified by manipulation of the process parameters used during deposition [28, 119]. The DVD

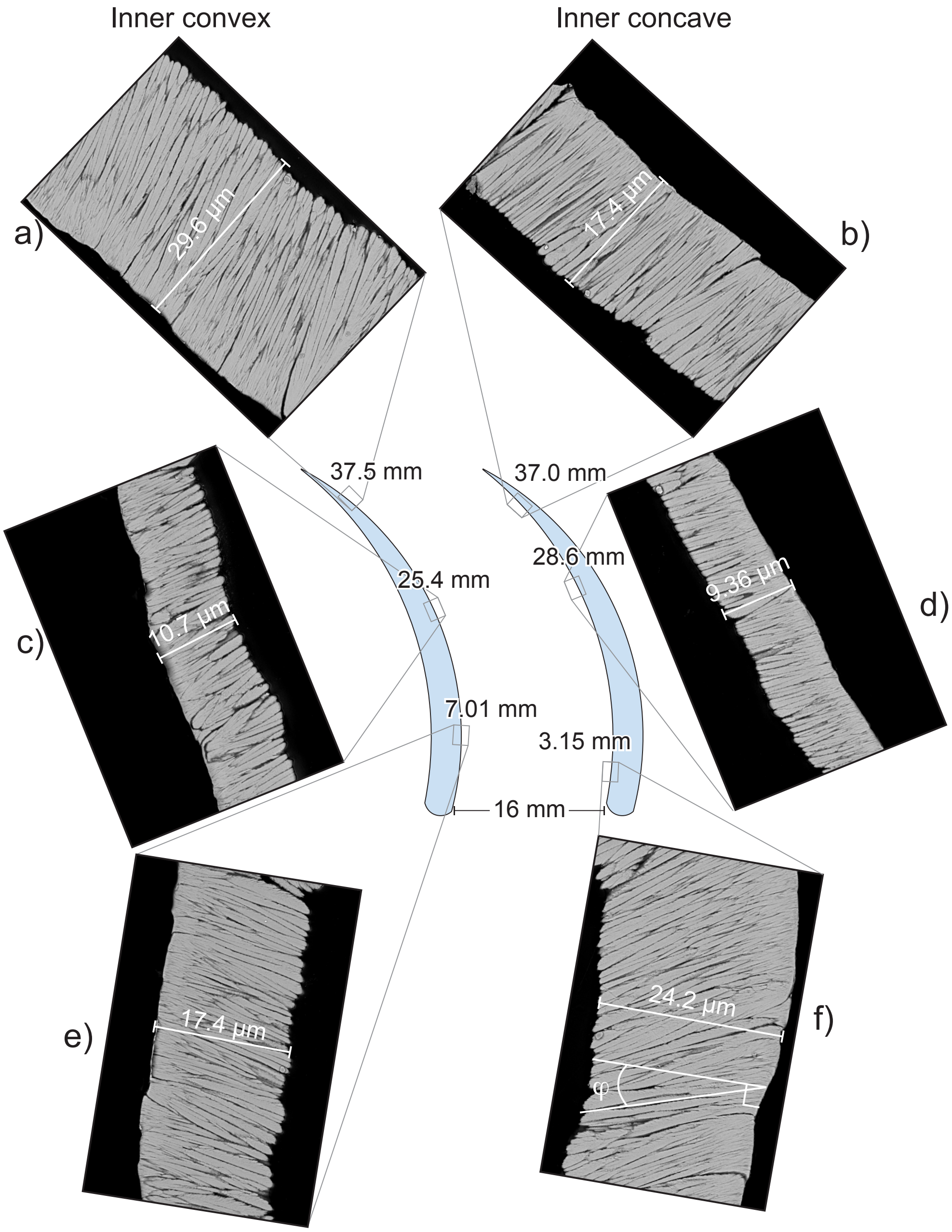

Figure 7.5: Experimental nickel coatings deposited at a chamber pressure of 22 Pa, pressure ratio of 5.45, rotation rate of 6 rpm, and channel width of 16 mm. The substrate temperature was $T/T_m = 0.243$ during deposition. An example of the columnar growth angle is indicated in f).

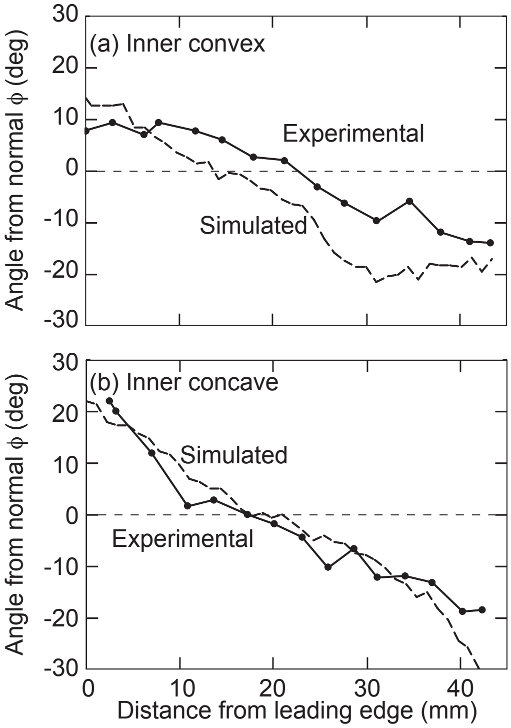

Figure 7.6: Experimental and simulated columnar growth angles along the inner doublet surfaces. Both studies were performed at a chamber pressure of 22 Pa, pressure ratio of 5.45 and channel width of 16 mm.

method simulated here allows the deposition chamber pressure and the pressure ratio upstream/downstream of the choked inlet nozzle to be independently varied, and their effects upon the microstructure are also investigated [35].

7.5.1 Variation with channel width

As shown in Chapter 6, the fraction of evaporated material that is deposited on inner doublet surfaces is highly dependent on the channel width between the pair of airfoils. The simulation procedure described above have therefore been repeated using doublet substrates with channel widths of 8, 12 and 16 mm. Figure 7.7 shows the variation in local deposition efficiency, the columnar growth angle, and coatings porosity as a function of position along the two interior airfoil surfaces. During the simulations, the chamber pressure was fixed at 16 Pa, the upstream/downstream pressure ratio was 5, and a simulated rotation rate of 6 rpm was used. The deposition efficiency is shown in Figure 7.7(a) and (b) for the inner concave and convex surfaces. Since the local deposition efficiency scales the local thickness (provided the porosity remains constant), the profiles are surrogates for the coating thickness. The results show that the coating thickness at the leading edge and trailing ends of the airfoils is unaffected by the channel width, that thickness at the channel midpoint is strongly dependent upon this parameter. The non-uniformity of the thickness decreases progressively with increase in channel width on both surfaces.

The variation of the columnar growth angle along each interior surface is shown in Figure 7.7(c) and (d). Changing the airfoil separation distance had little effect upon the variation of growth column angle with position on the interior surface. Figures 7.7(e) and (f) show the total pore fraction as well as the intercolumnar and smaller-diameter intracolumnar porosity as functions of location along each interior surface for the three airfoil separation distances. The total pore fraction showed little variation with channel width. However, the intra-and-intercolumnar pore fraction components showed a more significant variation near the midpoint of the airfoils. The smallest 8 mm channel width substrate (with the most severe NLS region) showed a modest decrease in small-scale intracolumnar porosity and complimentary increase in large intercolumnar pore fraction near the channel midpoint where the NLS effect was most significant. This variation is consistent with the coatings in these regions having slightly denser columns and slightly wider gaps intercolumnar gaps. The coatings on all channel width substrates exhibited an increase in total porosity near the concave surface's trailing edge. This increase

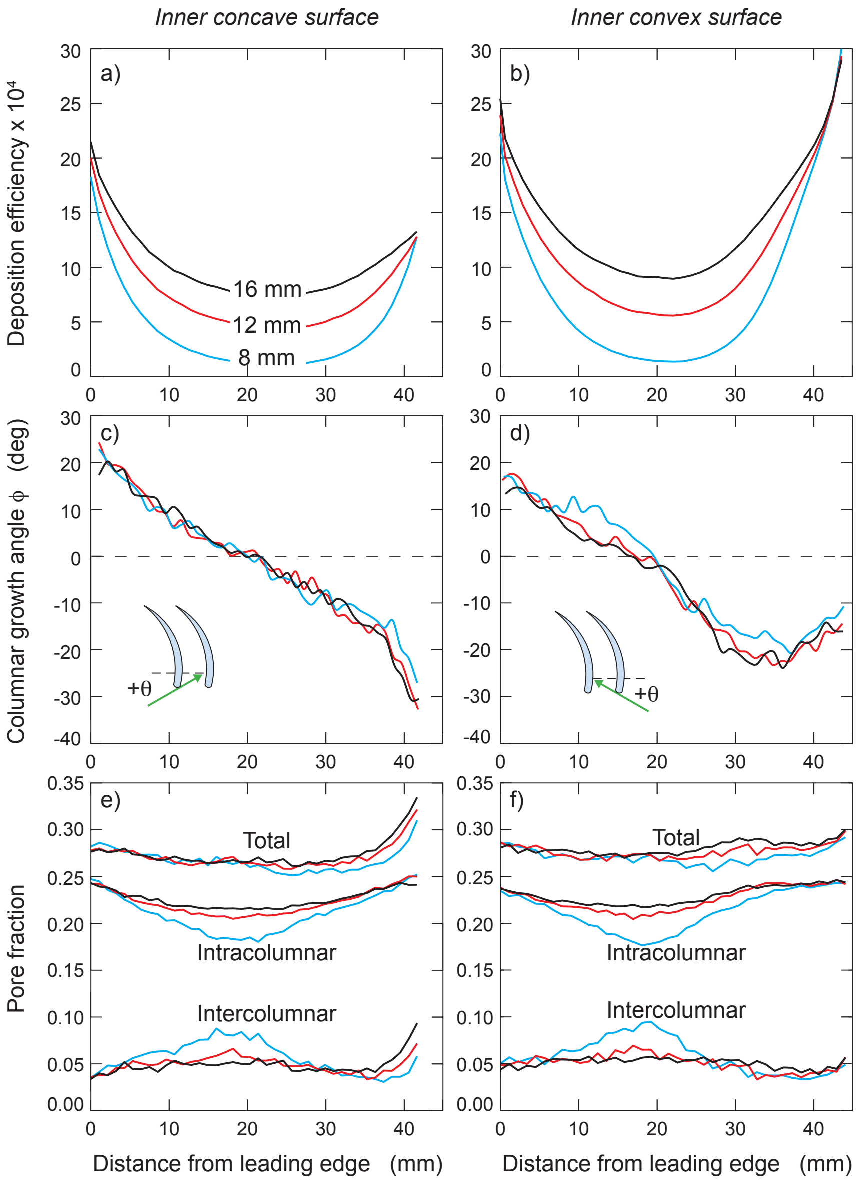

Figure 7.7: Variation of inner surface deposition efficiency, columnar growth angle, and pore fraction with channel width for the two interior surfaces of the doublet airfoil using a chamber pressure of 16 Pa and a pressure ratio of 5.0.

corresponded with the region of increased columnar growth angle.

7.5.2 Effect of chamber pressure

Simulations were conducted using chamber pressures of 1, 7.5, 16, 45, and 100 Pa. A channel width of 12 mm, a rotation rate of 6 rpm, and a pressure ratio of 5 was used for all simulations. The effects of deposition chamber pressure upon deposition efficiency, columnar growth angle and pore fraction versus location on the airfoil surface are summarized in Figure 7.8. Deposition efficiency profiles along the inner concave and convex surfaces are shown in Figure 7.8(a) and (b). They indicate that the coating thickness at the leading edge and trailing ends of the airfoils increases with the deposition pressure while that near the midpoint of the surfaces is maximized at chamber pressures of 16 to 45 Pa. Within this pressure range, the midpoint thickness was typically 25-30% that deposited at the airfoil ends.

The coating's growth column angle was also significantly affected by chamber pressure. Figure 7.8(c) and (d) show the variation in growth angle with position on the two airfoil surfaces At all the pressures the highest growth column angles were found at the leading edge and trailing end of the airfoils, and the columns at the midpoint locations remained perpendicular to the airfoil surface all pressures. However, the angle of the growth columns at the leading edge and trailing end of the concave was inversely dependent upon the deposition pressure. There was almost no change in this growth angle along this airfoil surface for the highest (100 Pa) pressure deposition. The growth column angles on the convex surface also tended to decrease with pressure, but at the lowest pressures investigated, the location of

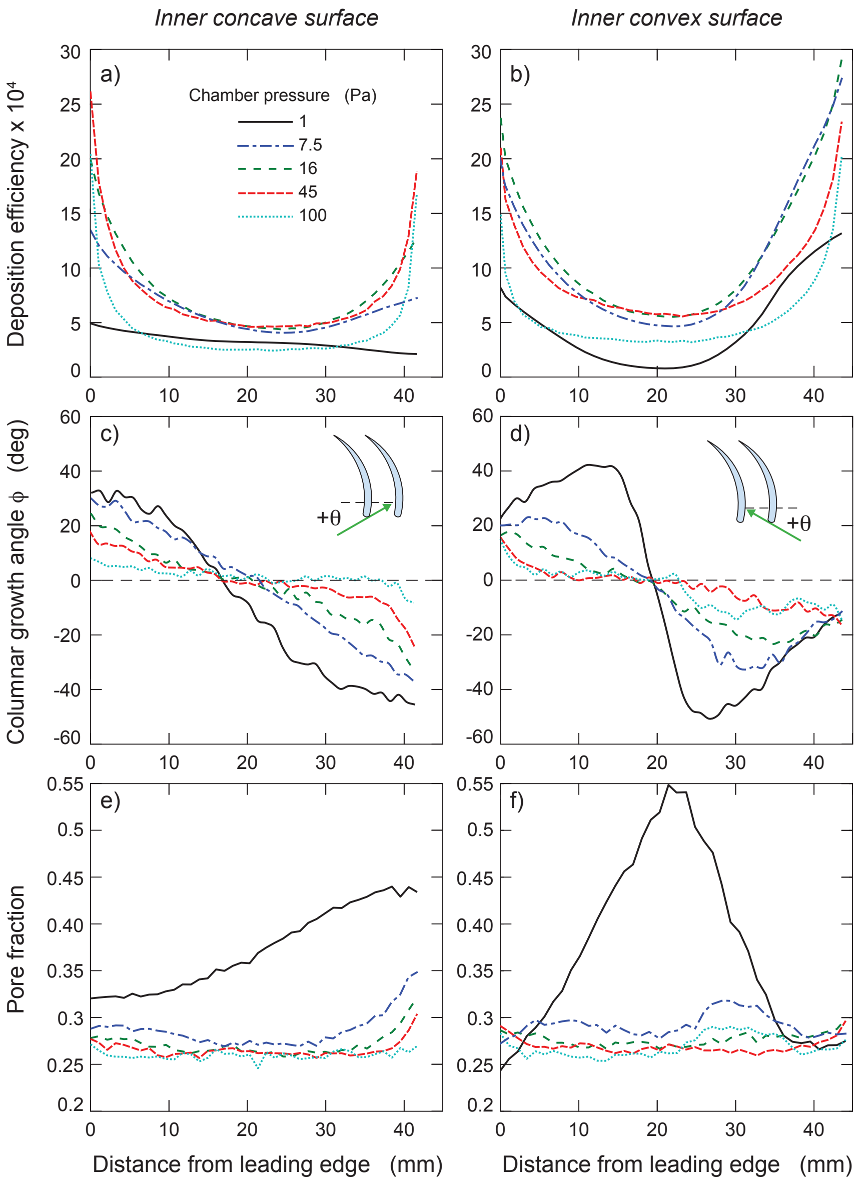

Figure 7.8: Deposition efficiency, columnar growth angle, and total pore fraction along the interior surfaces of the rotated doublet airfoil as the chamber pressure was varied. The channel width was 12 mm and a pressure ratio of 5.0 was used for all the calculations. At 1 Pa, the mean free path became comparable to the channel width, resulting in a sudden transition of coating properties.

the maximum angle shifted from the leading and trailing edges towards the interior of the airfoil. As a result, the convex surface coating applied at 1 Pa had a very short region near the midpoint where the growth columns were perpendicular to the coating surface.

The total pore fraction is plotted along the two surfaces in Figure 7.8(e) and (f). In general, the porosity on both sides of the channel decreased as the pressure increased with the majority of the decrease occurring as the pressure was increased from 1 to 7.5Pa. On the concave surface, porosity increases with decreasing chamber pressure. The coating deposited near the midpoint of the convex surface at 1 Pa (the region most hidden from the vapor source) had a very high pore fraction (55%), almost double the value at any other condition. This porosity resulted from the growth of wide columns, with large columnar pore between them.

The significant variation in coating thickness, column orientation and pore fraction occurred as the chamber pressure was decreased from 7.5 and 1 Pa. At 7.5 Pa, the gas-phase mean free path length between collisions (MFP) was approximately 1 mm, while at 1 Pa, the MFP increased to ~8 mm, leading to a significant reduction in the frequency of gas-phase scattering collisions within the channel. Figure 7.9 shows the IADs for the eight simulation orientations at the midpoint of the inner convex surface for chamber pressures of 7.5 and 1 Pa (in subplots (a) and (b) respectively). An increase in θ_m and a corresponding decrease in θ_w is observed at all orientations as the pressure was decreased from 7.5 to 1 Pa. At 1 Pa, incident atoms primarily deposit from glancing angle-trajectories from both the leading and trailing edges of the channel (depending on orientation). This leads to significant increase in flux shadowing and a corresponding increase in the coating porosity.

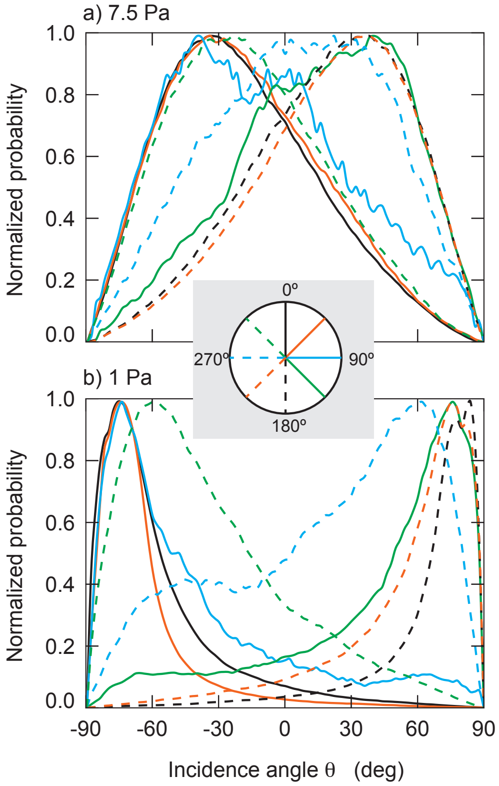

Figure 7.9: Incidence angle distributions at the eight simulation orientations at the inner convex surface midpoint. Simulations were performed at a pressure ratio of 5 and channel width of 12 mm.

The simulated coating microstructure for coatings deposited at 7.5 Pa are shown in Figure 7.10, while those deposited at 1 Pa are shown in Figure 7.11. While the coatings show similarities in coating structure at many of the regions near the channel openings, significant differences can also be seen. At the midpoint of the convex surface (location (c) in Figures 7.10 and 7.11), both coatings are thin compared to the ends of the airfoils. However, the coating deposited at 7.5 Pa had a thin but continuous coating along the central region of its surface. However, the coating deposited at 1 Pa received very few atoms in this central region, resulting in widely separated column nucleation events and very large intra columnar gaps with poor substrate coverage. Large columnar gaps are also present at other locations on the coating deposited at 1 Pa; notably locations (b) and (d) where the incident flux was again very low. It is also evident that depositions at the end locations was dominated by flux that penetrated the leading or trailing edge gaps (whichever was closest to the source during rotation), resulting in significant inclination of the column growth angle towards the nearest opening.

7.5.3 Influence of pressure ratio

The pressure ratio upstream and downstream of the carrier gas inlet controls the gas jet velocity with higher pressure ratios resulting in faster jet velocities (Table 4.1). The effects of varying the pressure ratio from 3, to 5 and finally 10 up on deposition efficiency, columnar growth angle, and pore fraction are shown in Figure 7.12. All simulations were performed with a chamber pressure of 45 Pa, channel width of 12 mm, and rotation rate of 6 rpm. The deposition efficiency profiles are shown along the inner surfaces for the three pressure ratios in Figure 7.12(a) and (b). Increasing the pressure ratio slightly reduced the coating thickness at the ends of the airfoils but increased that at the midpoint locations, especially on the concave inner surface. This resulted from a reduction in the time available for vapor atom scattering onto the interior surfaces as the gas flow started to propagated through the channel between the airfoils, Chapter 6. This led to a higher retained vapor atom concentration at the midpoint locations and a thicker coating.

The effect of increasing the pressure ratio upon the columnar growth angle is shown in Figure 7.12(c) and (d). The growth angle, especially at the airfoil ends, increased with increasing pressure ratio, and resulted from increasingly skewed IADs at higher pressure ratios. Increasing the pressure ratio resulted in a higher

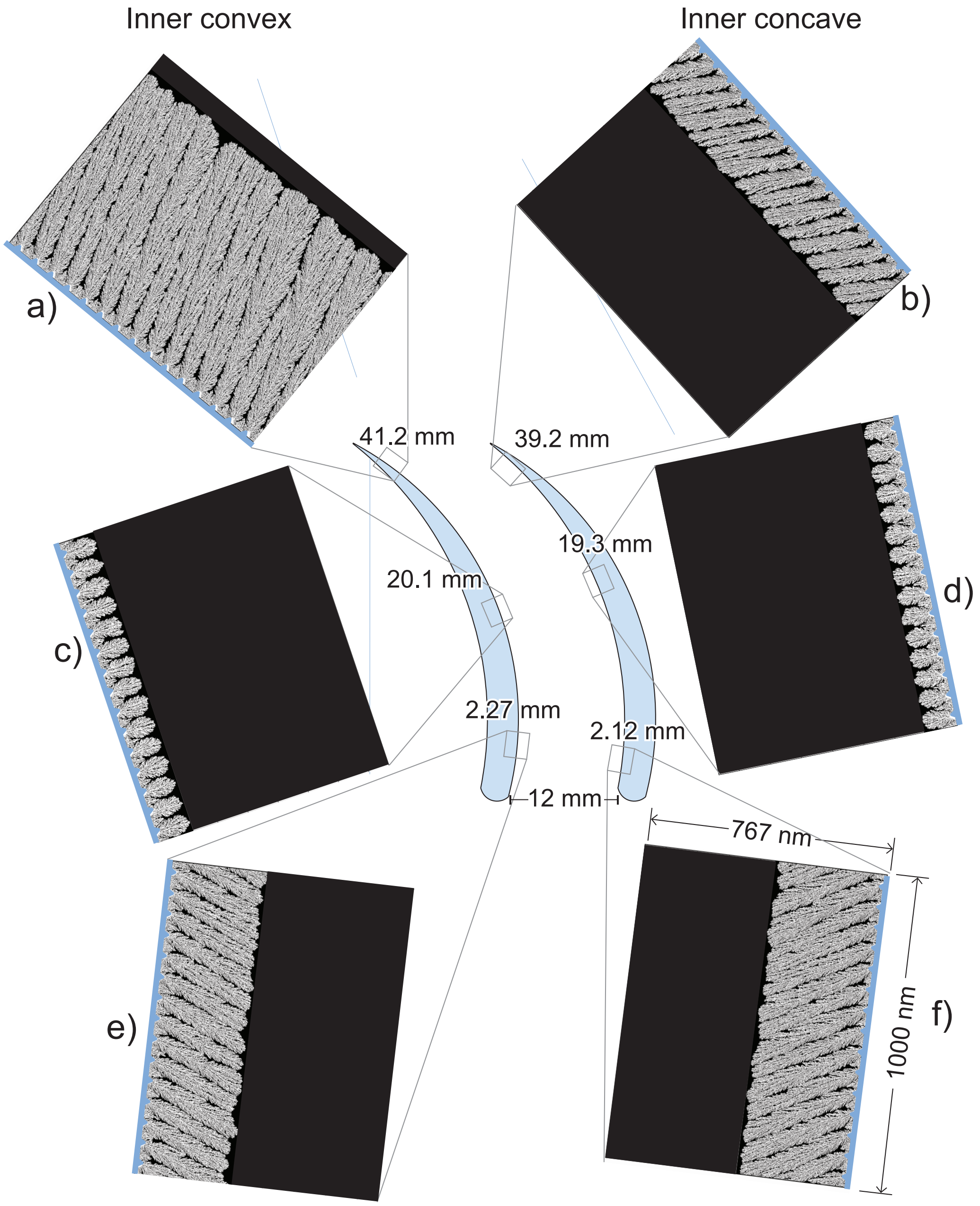

Figure 7.10: Simulated microstructures for coatings deposited at a chamber pressure 7.5 Pa, a pressure ratio of 5, and a channel width of 12 mm.

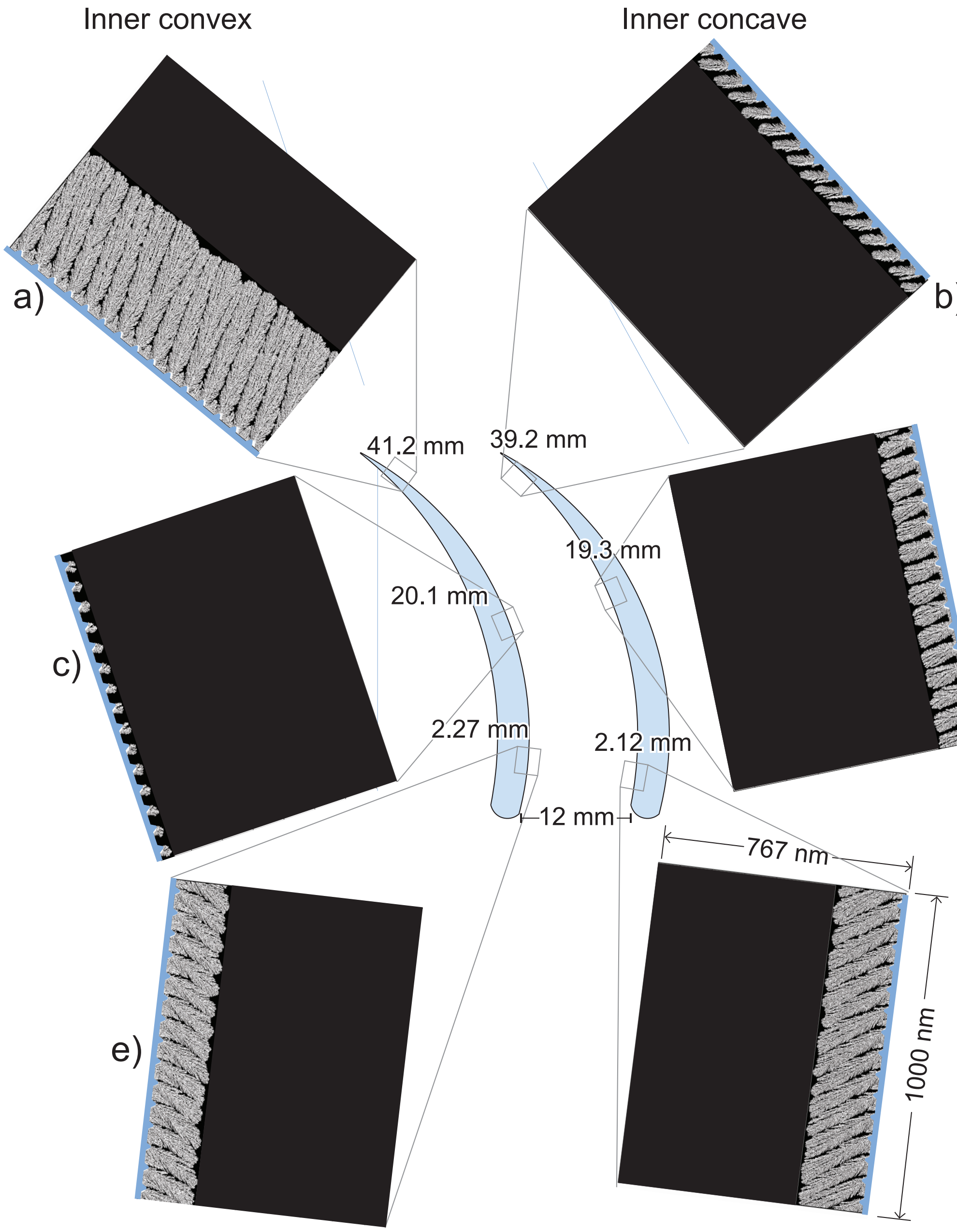

Figure 7.11: Simulated coatings for depositions performed at a chamber pressure of 1 Pa, a pressure ratio of 5, and a channel width of 12 mm.

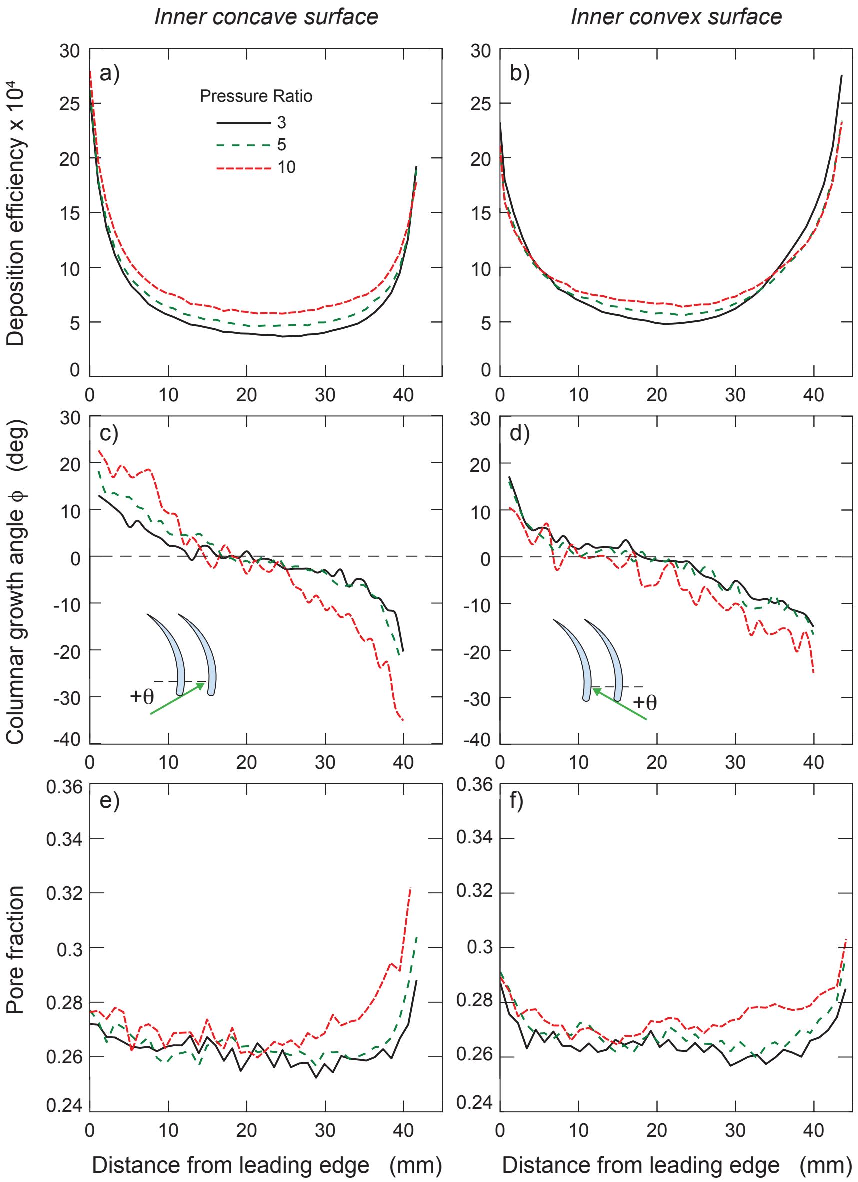

Figure 7.12: Deposition efficiency, columnar growth angle, and total pore fraction profiles on the interior surfaces of the substrate as the pressure ratio was varied. Simulations were performed at a chamber pressure of 45 Pa and a channel width of 12 mm.

fraction of the vapor impacts with a highly inclined trajectory at these faster flow velocities. The porosity variation with pressure ratio is shown in Figure 7.12(e) and (f), and shows that the pore fraction was highest at the ends of the airfoils where the incident flux was more likely to make a glancing impact with the surface. Increasing the pressure ratio in these regions then further increased the fraction of glancing impacts and thus the likely hood of local flux shadowing by locally high features (growth column tips) on the growth surface.

7.5.4 Coating variation with optimization

In Chapter 5 it was demonstrated that an optimized substrate rotation pattern can decrease the variation in deposition efficiency between the inner and outer substrate surfaces. Although the optimization routine can improve deposition efficiency uniformity, it could introduce undesirable variations in the coating microstructure. The optimization routine increases the amount of flux received on the substrate from a few orientations while decreasing it for others. This could lead to an increase of the columnar growth angle or pore fraction. To evaluate this effect, microstructures were simulated using both constant and optimized dwell fractions at a chamber pressure of 45 Pa, pressure ratio of 5.0, and airfoil spread of 12 mm. The uniform rotation rate was simulated as 6 rpm, while the optimized rate was allowed to vary between 2 and 32 rpm.

The resulting deposition efficiency, growth angle, and pore fraction profiles for both the inner and outer surfaces are shown in Figure 7.13 and compared to an otherwise identical simulation that used a constant rotation rate of 6 rpm. The values of w_x and w_v (from Equation 6.7) were set to 10 and 1.0, respectively. The coating deposited on the inner and outer concave surfaces using the optimized rotation pattern were both thicker than of those of the constant rotation coating. This arose because the optimized rotation increased the dwell fraction while the ends of the airfoils were close to, and in the line-of-sight of the vapor source, the leading edge coating thickness was substantially increased over the constant rotation case. Deposition of a coating the convex surfaces using the optimized rotation procedure increased the deposition efficiency on the inner surface and decreased it on the outer surface. These changes then combined to significantly decrease the coating thickness differences between the four surfaces.

The columnar growth angles as a function of position along the airfoil surfaces is in Figure 7.13(c) and (d). The optimization resulted a modest increase in the columnar growth angle at the end of the inner concave surface (from 35 to 45°), but otherwise had little effect along all other surfaces. Figure 7.13(e) and (f) shows that the pore volume fraction in the optimized coating also increased in regions of the coating where the column inclination also increased. The most apparent new variation is near the ends of the inner concave surface. At the trailing edge, porosity increases by 7% over the uniform rotation result. Examples of the simulated microstructures at the four surface midpoints are shown in Figure 7.14. They show that very similar thicknesses on all four surfaces are achieved by this optimized rotation scheme when practiced at this high pressure and pressure ratio. The coatings growth columns are also confirmed to be oriented normal to the substrate surface and contain similar levels of porosity.

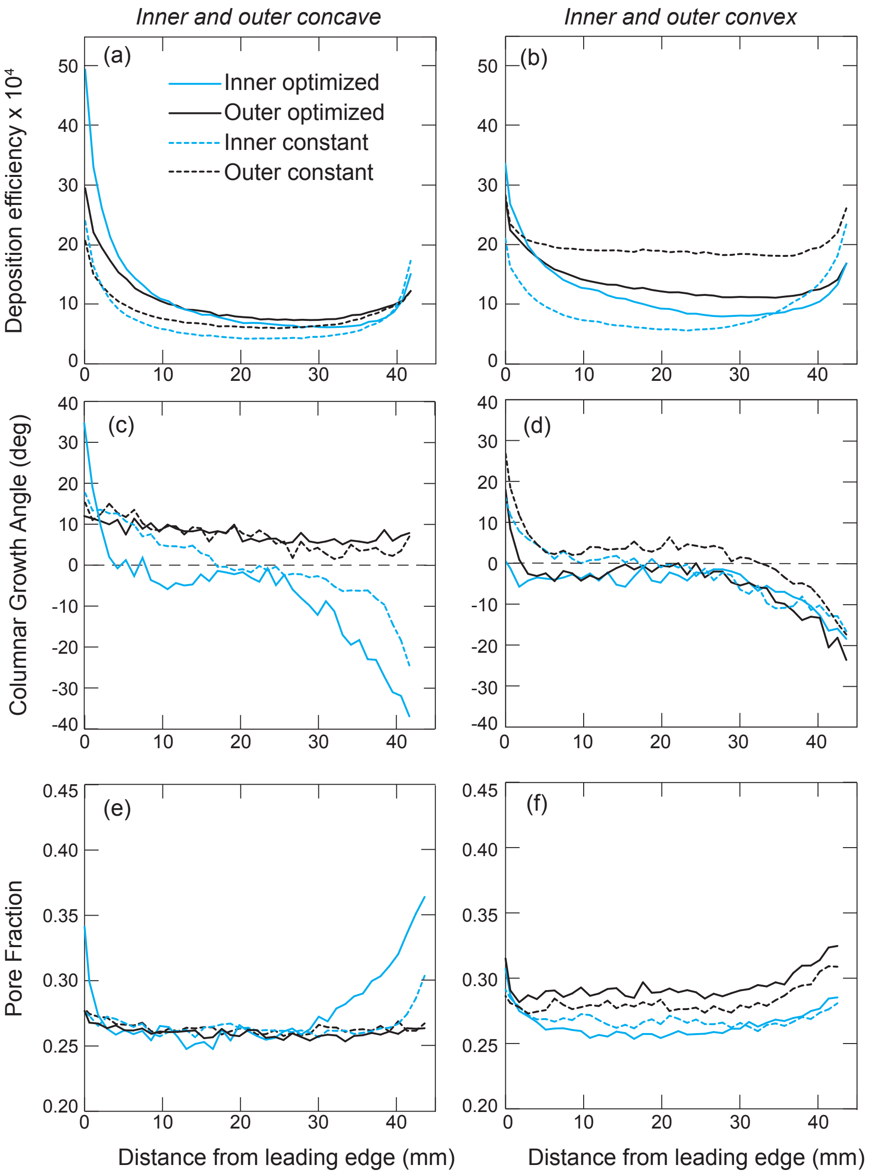

Figure 7.13: Comparison of deposition efficiency, columnar growth angle, and total pore fraction for optimized (solid lines) and constant rotation (dashed lines) simulated deposition around a doublet substrate. The simulations were performed at a chamber pressure of 45 Pa, a pressure ratio of 5 and a separation width of 12 mm.

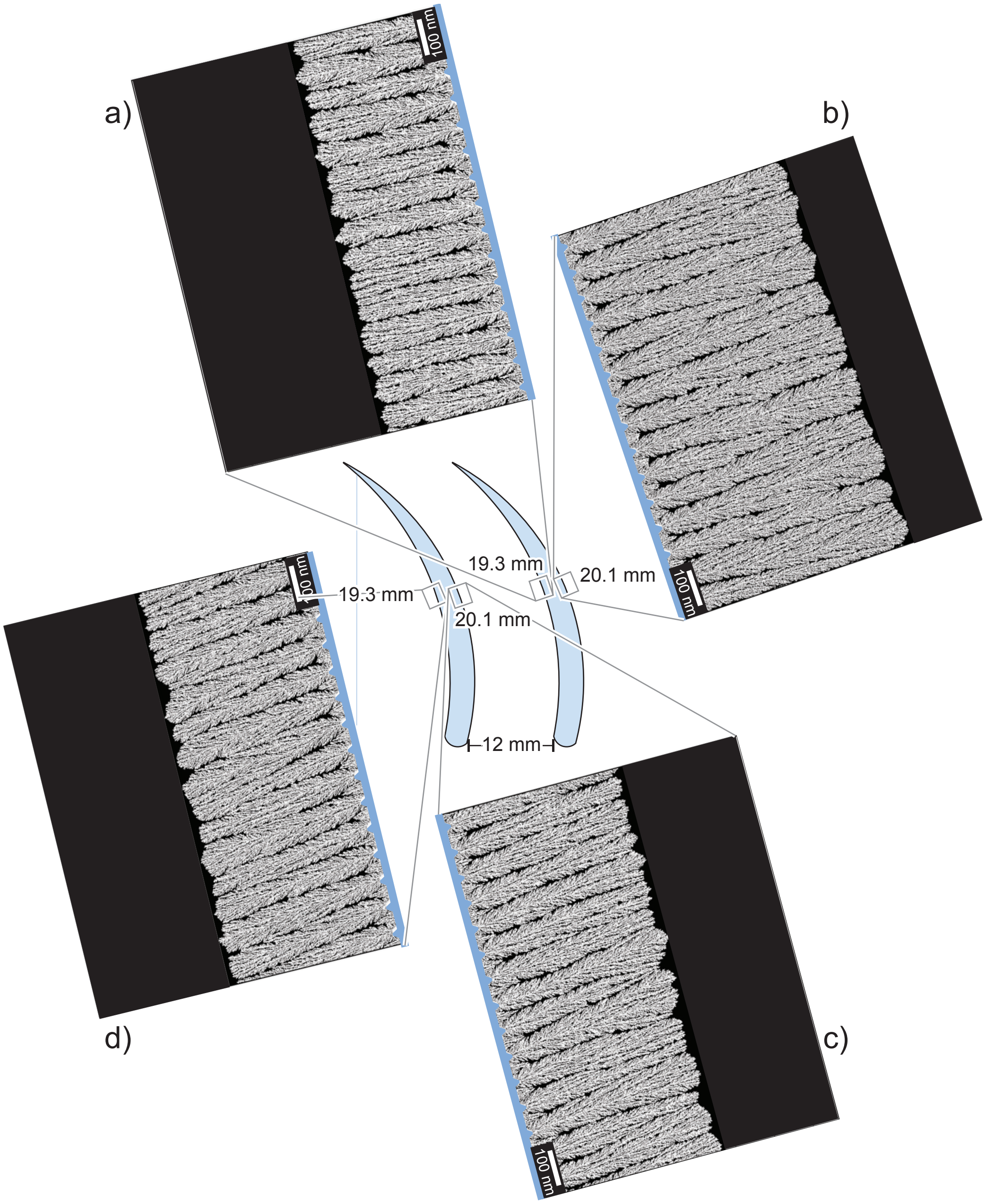

Figure 7.14: Simulated microstructures at the four surface midpoints using the optimized rotation inputs. Simulations were performed at a chamber pressure of 45 Pa, a pressure ratio of 5, and a channel width of 12 mm.

7.6 Conclusion

Gas jet assisted physical vapor deposition (PVD) techniques operate at higher pressures than conventional PVD processes, and have been shown enable the coating of complex shaped substrates including those with non-line-of-sight (NLS) surface regions. The NLS regions were shown to receive a broader vapor atom incident angular distribution but with a lower flux. To investigate the consequence of such effects, the thickness and microstructure variation along the inner (curved channel) surfaces of a model doublet airfoil substrate containing NLS regions was investigated.

- Both atomistic simulations and an experimental deposition using a nickel vapor source have confirmed that the coating's thickness in flux-shadowed regions is thinner than other regions.
- The simulations and experimental deposition indicated that the coatings columnar microstructure and pore volume fraction varied slowly along the inner airfoil surfaces during the transition from LS to NLS deposition.
- Largely NLS regions on the substrate are shown to contained extremely uniform porosity, while surface areas that spent a substantial amount of time in (or near) the line-of-sight of the source showed a greater variation in growth column angle and porosity content.
- A substrate rotation strategy for maximizing the coating thickness uniformity successfully reduced the variation of coating thickness along all doublet airfoil surfaces and incurred only small changes to the columnar growth angle and pore volume fraction.

Chapter 8

Discussion

This dissertation has investigated the use of gas-jet assisted physical vapor deposition processes for the coating of airfoil substrates with regions either partially or fully hidden from line of sight of the vapor source. It has accomplished this dissertation object by implementing a multiscale DSMC/kMC simulation method capable of modeling the deposition process from vapor creation to coating microstructural evolution. The validity of the simulation approach was evaluated by comparing Ni coating simulations with experimentally deposited coatings. In this chapter, the knowledge gained through these paired fields of investigation is discussed. These insights are used to illuminate the essential physics of the deposition processes, and assess the value of simulations form optimizing multiscale vapor deposition processes. The key scientific findings are presented in conjunction with the computation innovations implemented here that enabled them.

8.1 Gas-jet assisted deposition mechanisms and thickness uniformity

At the outset of the dissertation, the mechanisms influencing non-line-of-sight deposition that is achievable when conducted in the 1 to 100 Pa pressure range were largely unstudied. Previous work using the DVD approach by Hass and Queheillalt [35, 49] focused on substrates with small-scale features responsible for flux shadowing. All substrate regions were within a short (reachable) distance of the primary vapor plume streamlines, and deposition was the most uniform when the flow rate of the carrier gas near the substrate was low (i.e. under low upstream/downstream nozzle pressure ratios), providing sufficient time for gas phase vapor diffusion to the substrate surface.

Both the single and doublet airfoil substrates studied in this dissertation presented a much different deposition environment. These 40 mm long surfaces required substantial redirection of the gas jet flow and it's entrained vapor to achieve deposition on all surfaces. The best conditions to achieve coating uniformity were found to be different for deposition on curved stationary, rotated, and inner-channel substrate surfaces. In the remainder of Section 8.1, the dynamics controlling coating thickness on single and doublet airfoil substrates are discussed.

8.1.1 Single airfoil substrate

Coatings deposited on rotated airfoil substrate at typical DVD conditions (1-40 Pa) exhibit two unexpected thickness trends. First, along both the concave and convex surfaces, coatings were thinnest near the surface midpoint and thickest at their endpoints. Second, the coating deposited on the concave surface had a smaller average thickness than that on the convex. These thickness trends are the result of substrate and carrier gas flow interactions and are shown by the convex and concave deposition efficiency profiles in Figure 8.1.

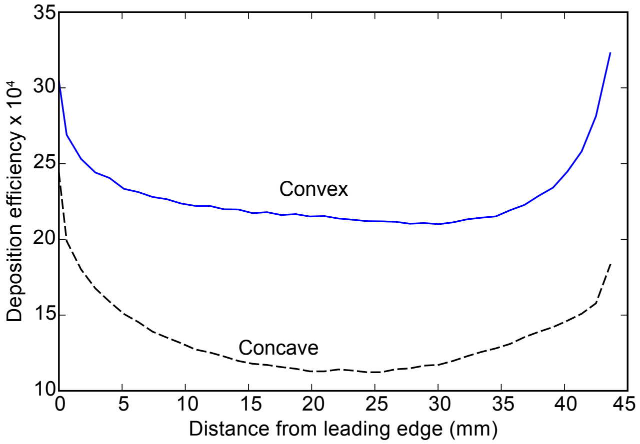

Figure 8.1: Deposition efficiency profiles along the convex and concave surfaces of a single airfoil substrate simulated at a chamber pressure of 16 Pa and pressure ratio of 10.

As shown in Chapters 4 and 5, deposition non-uniformity extremes were encountered for airfoil orientations such that the airfoil's chord was either parallel or perpendicular to the incident gas flow direction. Illustrative vapor atom streamlines and pressure contours are shown in Figure 8.2 to demonstrate the differences in deposition behavior between these two orientations. When the substrate was oriented parallel with the flow as in Figures 8.2(a) and (b), the highest deposition rates were observed near whichever airfoil endpoint was closest to the vapor source. This deposition near the airfoil end depleted vapor from streamlines near the substrate and resulted in a reduced deposition rate on the downstream substrate surface, which contributed to the thickness profile's non-uniform distribution.

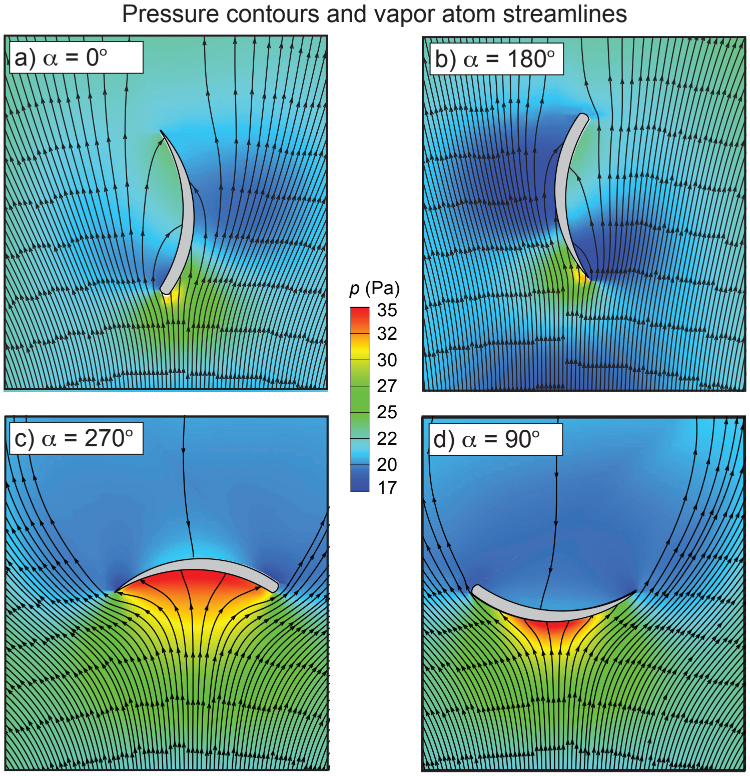

Figure 8.2: Pressure contours and vapor atom streamlines at four orientations of an airfoil substrate. Simulations were performed with a chamber pressure of 22 Pa and a pressure ratio of 5.45

The substrate orientations corresponding to Figures 8.2(a) and (b) also resulted in a significant portion of the substrate being out of the source's line-of-sight. At both $\alpha = 0°$ and 180°, the concave surface was completely shadowed from the vapor source while half of the convex surface was visible at either orientation. The convex surface regions within the line-of-sight received significantly higher deposition rates (3-6 times greater) than the shadowed concave surface, which depended on vapor diffusion across the carrier gas streamlines. This contributed to the lower average coating thickness along the concave surface of rotated airfoils.

Considerably different deposition behaviors were found when the substrate was oriented perpendicular to the carrier gas flow Figures 8.2(c) and (d). At these orientations, one entire side of the airfoil was located in the line-of-sight of the vapor source, increasing the deposition rate upon it. However, due to the large obstruction to flow caused by the substrate surface, a higher-than-background stagnation pressure was observed near the substrate surface. This resulted in a higher mean free path near the substrate surface and required the incident carrier gas jet to turn significantly to flow around the substrate, and increase the flows velocity component parallel to the substrate surface. These two factors combined to decrease the rate of vapor deposited near the midpoint of this substrate surface, because the incident vapor was rapidly pushed away from the midpoint and towards the surface ends.

At these perpendicular substrate orientations, the deposition rate depended on whether the convex or concave surface faced the vapor source. In the concave surface case, the region of high stagnation pressure was much greater than that above the concave facing surface situation. This resulted from the concave curvature more effectively confining the incident carrier gas flow and requiring incident streamlines to bend more than 90° to flow around the surface. The shortened mean free path in the high-pressure region also reduced the rate at which incident vapor was deposited on the concave surface. On the convex surface, the airfoil tips curve away from the vapor source and incident streamlines were deflected by less than 90° to curve around the substrate. The region of stagnation pressure was reduced along this surface, allowing vapor more rapid access to the substrate surface than along the concave side. As a result, deposition rates were significantly lower along the concave surface. Deposition profiles also had differing shapes between the surfaces. At 90° along the convex surface, the deposition rate maximum was found at the surface midpoint. At 270° along the concave surface, the maximum was located at the surface endpoints. This contributed to the more uniform thickness profiles typically observed on the convex surface.

The thickness non-uniformity along each surface and between the convex and concave surfaces both decreased with decreasing pressure ratio and chamber pressure. Lower velocities and pressures resulted in fewer scattering collisions (reducing the fraction of vapor depositing near the endpoints for parallel deposition orientations) and reduced substrate-gas jet interaction (leading to a smaller region of a lower stagnation pressure for perpendicular deposition orientations). The trends of deposition efficiency profiles with chamber pressure along the convex and concave surfaces is shown in Figure 5.15 (a) and (b). At a chamber pressure of 1 Pa, deposition thickness profiles for rotated substrate depositions were extremely uniform around the substrate. However, there remained a slight mismatch in thickness between the two surfaces since the concave surface remained in the vapor source's line-of-sight for a slightly longer duration. When the chamber pressure was reduced even further to PVD-like chamber pressures (e.g. 0.015 Pa), uniform coatings were deposited along the entire substrate surface and the mismatch between the surfaces was negligible. At these pressures, the mean free path was orders of magnitude larger than the substrate's length and vapor streamlines that miss the substrate surface (even by only a fraction of a mm) were lost to the deposition chamber walls.

Increasing the chamber pressure above typical DVD conditions increased both the non-uniformity along each rotated airfoil surface and between the convex and concave sides. At parallel substrate orientations, vapor streamlines near the substrate deposited rapidly near the leading edge and low diffusion coefficients prevented significant deposition further along the substrate surfaces. At perpendicular substrate orientations, the carrier gas-substrate interaction is increased, which resulted in a larger region of high stagnation pressure and a lower overall deposition rate.

8.1.2 Doublet airfoil substrate

The use of a substrate with inner channels (such as a doublet guide vane) creates additional effects upon the deposition behavior. Deposition on the outer doublet surfaces closely matched that on a single airfoil. However, the deposition environments experienced by the inner surfaces were substantially different. Confinement of the flow between these surfaces decreased the number of orientations at which they received significant flux and altered the mechanism from which vapor deposition primarily occurred by reducing the influence of line-of-sight deposition and increasing the importance of deposition from scattering collisions. However, since the internal and external surface regions experience nearly identical thermal environments during operation in an engine, their coatings should ideally be as identical as possible.

As with single rotated airfoil depositions, incident flux extremes were found when the substrates were either parallel or perpendicular to the incident carrier gas flow. The carrier gas streamlines at these two orientations are shown in Figure 8.3. At $\alpha = 0°$, Figure 8.3(a), several carrier gas streamlines enter the inter-airfoil region and flow through the channel's length. At $\alpha = 270°$, Figure 8.3(b), no streamlines enter the inter-airfoil region and no net flow occurs through the channel. As with the carrier gas streamlines, few vapor atoms enter the channel and deposition rates are negligible. As a result, fewer orientations led to significant incident flux upon the interior surfaces compared to the exterior surfaces.

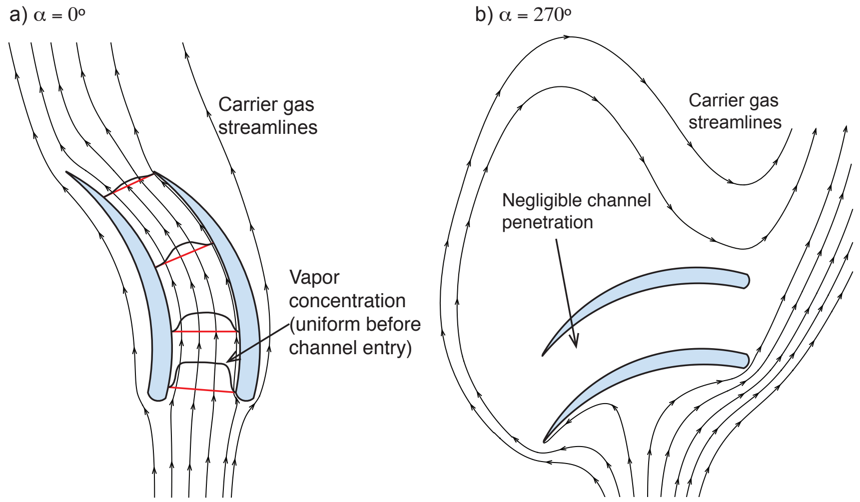

Figure 8.3: Carrier gas streamlines around a doublet guide vane at (a) $\alpha = 0$ and (b) $\alpha = 270$.

At orientations where significant deposition along the inner surfaces does occur, behavior is significantly different than along external regions. On a single-component substrate with only external surfaces (such as an individual airfoil), deposition occurs from an unconfined incident jet. The substrate surface can receive flux from a large fraction of the total vapor plume. With the use of doublet substrates, the finite width of the interior channel constrains the fraction of vapor that can enter the channel and conceivably deposit on the inner substrate surfaces. Decreasing the channel width reduced the fraction of vapor that was able to enter the channel and resulted in lower average coating thicknesses. For depositions at 16 Pa, reducing the channel width from 16 to 12 mm lowered the minimum coating thickness by 50 %. Further decreasing the channel width from 12 to 8 mm resulted in an additional decrease of 70 % from the already reduced 12 mm thickness minimum.

Once within the channel, vapor was deposited primarily by binary scattering from the carrier gas streamlines. As with deposition on external surfaces, coating thickness maxima were located near the surface ends. At typical DVD conditions, much of the incident vapor quickly deposited upon entering the channel. However, some concentration of flux remained and gradually diffused across the channel width as carrier gas flow continued through the channel as is shown in Figure 8.3(a). This gradual diffusion enabled deposition in inner regions of the channel and allowed for the deposition of conformal coatings.

At low chamber pressures and pressure ratios, coating uniformity was reduced due to large diffusion coefficients and slow gas flow velocities, leading to rapid depletion of the vapor from the plume. The vapor concentration was exhausted before traveling a significant length down the channel. Additional reductions in uniformity were observed when the mean free path length became comparable to the channel width, e.g. near 1 Pa for the geometries studied here, Figure 6.14. Below this pressure, coating uniformity was poor and conformal coatings were not deposited along the entire inner channel surfaces.

When chamber pressures above 45 Pa were used, a larger fraction of the vapor concentration propagated along the entire channel length. However, the low diffusion rates at these pressures prevented much of the vapor from depositing on the inner surfaces and much of the vapor was lost through the rear channel opening. Along the inner concave surface, the minimum thickness for a deposition conducted at a pressure of 100 Pa was less than that at 1 Pa. Additionally, the use of high chamber pressures is likely to encourage gas-phase cluster formation, and coating quality is likely to be reduced by the deposition of these larger particulates [2].

8.2 Factors controlling coating microstructure

In addition to variations of coating thickness, the coating microstructure is also heavily influenced by the deposition conditions. Columnar microstructures were observed at all locations for every deposition condition studied. However, the growth angles and pore fractions within the columnar structures showed significant process condition dependencies. These variations could be linked to the gas-phase deposition conditions via the local incidence angle distribution (IAD), which specified the most likely angle of vapor impingement (θ_m) as well as the width of the distribution (θ_w).

8.2.1 Single airfoil substrates

Stationary deposition on an airfoil substrate resulted in significant variation in coating microstructure around the substrate surface. In regions near the leading edge, vapor was deposited from trajectories highly inclined to the local surface normal (the IAD maximum angle reached values of ~70°), Figure 5.4. This resulted in highly inclined growth angles with a maximum angle of ~45° in this region, Figure 5.6(c and d), and was accompanied by a significant increase in large-scale intracolumnar pore fraction. The oblique incident flux experienced significant shadowing, leading to this increase in pore fraction. Near the trailing edge, the coating pore fraction and growth angle were reduced since vapor was deposited from a broad IAD due undergoing scattering collisions before deposition, Figures 5.4 and 5.6. Pore fraction and growth angle were nearly constant for coatings grown in these non-line-of-sight regions at the studied conditions. However, the coating thickness was quite low and motivated the use of substrate rotation.

As with coating thickness, microstructural variation was reduced when substrate rotation was introduced for depositions at typical DVD conditions, Fig 5.12. Columnar growth inclination angles were generally less than 20° from the surface normal. The coatings pore fraction was also improved with substrate rotation, Figure 5.12(e and f). Total pore fraction varied between 0.25 and 0.35 over nearly the entire substrate surface. Substrate rotation served to effectively broaden the width and reduce the skew of the incident IAD, Figure 5.9. The IAD variation between surface regions was also reduced, as all regions were at some point in the line-of-sight of the vapor source during the rotation cycle.

Deposition conditions also played an important role in microstructural evolution on a single airfoil substrate. Columnar growth angles showed significant variation with chamber pressure, Figure 5.15(c and d) . In general, growth angle magnitude reduced with increasing pressure, as the number of scattering collisions increased and IADs became more and more equally distributed about the surface normal. At chamber pressures below 16 Pa, coating microstructure variation became more stable as the mean free path increased from 0.5 mm to 7 mm at 1 Pa. At the lowest, PVD-like chamber pressure, growth angles switched orientations near the airfoil's leading edge. This resulted from the transition from a line-of-sight only to non-line-of-sight enabled deposition process (due to the large mean free path of 50 cm). At these low chamber pressures below 16 Pa, an increase in pore fraction variation was also observed.

8.2.2 Doublet airfoil substrates

On inner channel surfaces, the coating's columnar growth angles varied significantly along the surface length, Figure 7.6. Within the channel, most vapor deposited from flow through the nearest channel opening. This resulted in IADs and growth columns skewed towards the nearest opening. At typical DVD conditions, growth angles reached maximums of ± 30° near the channel openings. Growth angles gradually varied between these maxima, and were oriented at near the surface normal at the channel midpoint where a nearly equal amount of vapor was deposited from each channel opening. Growth angle variation was found to increase with decreasing pressure as fewer and fewer scattering collisions occurred, Figure 7.8(c and d). Angle variation also increased with increasing flow velocities as vapor arrived from more skewed trajectories.

Although significant growth angle variation was observed along the surface at typical DVD conditions coating pore fraction remained extremely constant along the surfaces, Figure 7.8(e and f). As for deposition on rotated single airfoil substrates, total pore fraction generally remained between 0.25 and 0.3. Along the inner surfaces, there was a moderate increase in pore fraction (up to 0.35) near the surface endpoints. This increase in pore fraction corresponded to the increased columnar growth angle and the greater flux shadowing experienced by a highly skewed incident vapor. Both coating pore fraction and columnar growth angle remained unchanged with variation of channel width.

Pore fraction and columnar growth angles did vary with deposition conditions, Figure 7.8. At a low chamber pressure of 1 Pa, both growth angle and pore fraction varied significantly along the inner surfaces. Maximum growth angles reached values of ± 50° while pore fractions reached a maximum of 0.55. Both of these maximums were found near the midpoint of the inner convex surface, which was also the location of the coating's minimum thickness. These variations indicated that a conformal coating was not deposited along this surface. At this condition, the mean free path was similar in magnitude to the channel width, and deposition was by a nearly line-of-sight mechanism. Thickness uniformity was also poor at a high chamber pressure of 100 Pa, due to the slow diffusion rate of the vapor species. Simulations predicted that coating pore fraction and columnar growth angle were quite uniform along the inner surfaces, due to the many scattering collisions experienced by the incident vapor before deposition.

8.3 General remarks

8.3.1 Variation with substrate size

An important issue for further investigation is the applicability of these findings to substrates of different length-scales or shapes. Although an identical airfoil substrate was used for all studies presented here, variation of the channel widths and substrate orientations present a diverse range of deposition configurations for analysis. During the dissertation, several key factors were determined to control the behavior of deposition regardless of substrate design or length-scale. First, the relationship between gas-phase MFP and the characteristic length scales of the substrates was always important. When the MFP is of comparable size or larger than a substrate feature (channel opening, radius of curvature, etc.), deposition will be extremely reduced in the shadowed regions. Decreasing feature sizes requires a corresponding increase in chamber pressure (to maintain the MFP/feature size ratio). The use of substrates with very small features require high pressures that greatly increases the rate of undesirable gas-phase clustering.

Second, when higher chamber pressures and jet velocities are used, the incident vapor plume becomes increasingly narrower and more concentrated, and the deposition rate is increasingly dominated by orientations with a direct line-of-sight to the vapor source. When an airfoil substrate is oriented transverse to the flow at these conditions, a significant stagnation pressure will develop along with a flow velocity parallel to the substrates surface. When the substrate is oriented parallel to the flow direction, a significant portion of the vapor plume flows past the substrate without depositing.

Lastly, when depositing in an inner substrate channel, the vapor diffusion length transverse to the flow direction should be of comparable or smaller in size to the channel width. If the diffusion length is larger than the channel width, the vapor plume will be completely depleted before traveling through the channel length. Longer channels of identical width require higher flow velocities (resulting from larger pressure ratios), slower diffusion rates (found at higher chamber pressures), or a combination of the two.

Chapter 9

Conclusions

1. The surfaces of a complex shaped substrate undergoing gas-jet assisted vapor deposition can typically be divided into three classes of surface region: in the "line-of-sight" of the vapor source, completely "non-line-of-sight", and scattering collision dependent. During the rotation of such a substrate, the classification of a surface region can change with the angle of substrate orientation.

   Type I (line-of-sight): Type I surfaces are directly in the line-of-sight of the vapor source. The gas jet reaches these regions without first flowing along depleting substrate surfaces. These surfaces receive the highest vapor fluxes of all surface types and, when surface diffusion is low, the resulting coating is columnar with growth columns oriented towards to the incident gas jet. Deposition can occur in these regions at very low pressures (typical PVD conditions) without need of gas-phase scattering collisions. The front surface of a stationary substrate typically used in lab-scale deposition experiments is an example of a Type I surface.

Type II (non-line-of-sight): Type II surfaces are completely shadowed from sight of the vapor source. These surfaces have the lowest overall deposition rates. Vapor deposition onto these surfaces is entirely dependent on gas-phase scattering collisions and the condensing flux has a wide incidence angle distribution typically centered around the surface normal. Deposition in these regions is maximized when the local flow velocity is small; allowing vapor atoms to diffuse across stream lines to the substrate surface. The rear surface (inclined away from the source) of a stationary substrate coupon is a Type II surface.

Type III (scattering collision dependent): Type III surfaces can include regions both in and out of the line-of-sight of the vapor source. These regions are the recipients of deposition from the carrier gas/vapor atom flow along the surface. The deposition behavior in these regions is highly dependent on the gas flow conditions used. Gas-phase scattering collisions are required to induce vapor diffusion (and subsequent deposition) from the nearby flow streamlines. However, a high rate of deposition on surface regions near the vapor source can deplete the available gas-phase vapor and greatly reduce the deposition further along the surface. Optimum deposition in these regions require a balance of scattering collisions and convective flow. Type III surfaces are found when the airfoil substrates studied her are oriented somewhat parallel to the carrier gas flow ($\alpha = 0°$) or on a substrate coupon whose primary surfaces are parallel to the gas flow.

2. Interior surfaces of substrate with channel-like openings (such as the doublet airfoils studied here) can be classified as Type III surfaces, but have additional constraints on the fraction of evaporant available for deposition due to the finite flow volume. Variation of the substrate channel width (at widths much larger than the gas-phase mean free path) showed little influence on coating microstructure, but significantly modified the thickness profiles due to variation in the cross-section of incident vapor within the channel. When the channel width and mean free path lengths became similar, inner surface coating microstructure also varied.

3. Coating thickness and microstructural uniformity around complex substrates was found to be greatly improved with substrate rotation. Substrate rotation at typically rates (∼4 rpm) result in a rotational motion that is much slower than the incident flow velocity (∼100 m/s), which allows the use of multiple stationary DSMC simulations to approximate the rotated deposition case.

4. When depositing on complex substrates, it is important to consider both the coating uniformity and total deposition efficiency. Depending on the substrate design, the most uniform depositions may occur for conditions with low overall deposition efficiencies.

5. It is also important to consider deposition behavior on all surface types for complex shaped substrates. Often, it is impossible to increase the deposition flux to non-line-of-sight Type III surface regions without also increasing the flux to Type I regions.

6. The multiscale kMC/DSMC simulation method developed provides a powerful platform to optimize deposition conditions to achieve thickness uniformity.

The optimization method allows adjustment of a variable substrate rotation rate and/or source evaporation rate. The method is somewhat limited by only using 8-substrate orientations for the adjustment (optimizing the rotation pattern in smaller increments may improve optimizations). At higher chamber pressures, it is difficult to achieve perfectly uniform deposition efficiency profiles. However, deposition can be adjusted to match deposition profiles on multiple surfaces or fit other non-uniform profile. Coating microstructures resulting from the optimized deposition patterns can then be simulated with the kMC method.

7. For coatings deposited on the inner channels of a rotated doublet guide vane substrate, columnar growth angles are skewed in the direction of the nearest channel opening. These growth column angles are increased if the influence of scattering collisions is reduced (lower chamber pressures and/or higher jet velocities).

8. Deposition onto inner substrate surface regions far from doublet guide vane substrate openings is only possible from gas-phase scattering collisions. If the flow momentum is sufficiently large that it ensures the propagation of vapor through the entire substrate channel, the deposition rate on inner surfaces is controlled by the rate of vapor diffusion through the background gas. This rate is proportional to the coefficient of diffusion, D, which increases with decreasing chamber pressure. This results in a more rapid depletion of the vapor volume at lower pressures, and the requirement of a higher-momentum carrier jet to ensure propagation through the substrate.

9. When the gas-phase mean free path approaches the channel width (e.g. due to

a decrease of the chamber pressure), the coating deposition efficiency rapidly decreases. Additionally, inner surfaces receive almost all of their flux from highly skewed incidence angles resulting in coatings with very high porosities and inclined columnar growth angles.

Appendix A

Simulation scripts

This appendix contains example input files for the DSMC and KMC simulations. Additional computational files can be found on the University of Virginia's Online Archive at libra.virginia.edu.

A.1 DSMC input files

A.1.1 Grid specification file (dvd2-doublefoil)

```
*--------------------------------------------------------------------------

* astrick is comment
*--------------------------------------------------------------------------


*
* DVD2 Simulator
```

```
*
*-----------------------------------------------------------------------

*
control 1 -1 - grid only/ 1 - full  initialization
*
type 0      0/1 for  X&Y or R/Z flow
overwrite  files  1
debug flag 0
 inlet  file  inlet-3ratio
species  file  spec-Ni
surface  file  surfbc_wafer
wafer surface  2
*
*
*
read general grid
*-----------------------------------------------------------------------

*                    Region Definition
*-----------------------------------------------------------------------

   31     number of regions (<= 30)
  109    number of global points (<= 120)
*-----------------------------------------------------------------------

* Global Corner Points
```

```
* Pt  z(m)  r(m)
*----------------------------------------------------------------------------

1 0.0      0.00904
2 0.0      0.032
3 0.0      0.092
4 0.0001     0.11496
5 0.0159     0.03611
6 0.0159     0.08789
7 0.0313     0.0405
8 0.0313     0.0835
9 0.04071   0.0465
10  0.04071   0.0775
11  0.04227   0.0475
12  0.04227   0.0765
13  0.0462     0.037
14  0.0462     0.05
15  0.0462     0.062
16  0.0462     0.074
17  0.0462     0.087
18  0.0492     0.0405
19  0.0492     0.0835
20  0.0532     0.0
21  0.0532     0.0455
22  0.0532     0.0475
23  0.0532     0.0765
24  0.0532     0.0785
```

```
25 0.115 0.0
26 0.115 0.0475
27 0.115 0.05
28 0.115 0.062
29 0.115 0.074
30 0.115 0.0765
31 0.115 0.124
32 0.141 0.0
33 0.141 0.062
34 0.141 0.124
35 0.167 0.0
36 0.167 0.062
37 0.167 0.124
38 0.193 0.0
39 0.193 0.062
40 0.193 0.124
41 0.219 0.0
42 0.219 0.062
43 0.219 0.124
44 0.242 0.0
45 0.242 0.062
46 0.242 0.124
47 0.224 0.0
48 0.224 0.062
49 0.224 0.124
50 0.25  0.0
51 0.25  0.062
```

```
52  0.25    0.124
53  0.0532    0.124
54  0.0159    0.01866
55  0.0313    0.02798
56  0.04071   0.0336775
57  0.242   0.0495
58  0.242   0.0745
59  0.2511195304   0.0608804696
60  0.2511205304   0.0631195304
61  0.39    0.0
62  0.39    0.062
63  0.39    0.124
64  0.2891231207   0.03836398107
65  0.2891231207   0.03836418107
66  0.2891231207   0.0
67  0.2891231207   0.124
68  0.39    0.0745
69  0.39    0.0495
70  0.0532    0.0
71  0.0532    0.014
72  0.0532    0.11
73  0.0532    0.124
74  0.115   0.014
75  0.115   0.11
76  0.236   0.0
77  0.236   0.014
78  0.236   0.11
```

```
79  0.236    0.124
80  0.2891231207    0.028
81  0.2891231207    0.096
82  0.316    0.0
83  0.316    0.028
84  0.316    0.096
85  0.316    0.124
86  0.236    0.062
87  0.236    0.0631195304
88  0.115    0.062
89  0.115    0.0631195304
90  0.316    0.062
91  0.316    0.0631195304
92  0.2511195304 0.062
93  0.236    0.065
94  0.236    0.068
95  0.236    0.049
96  0.236    0.055
97  0.236    0.066
98  0.236    0.0717
99  0.2515354159 0.053
100 0.2510189714 0.056
101 0.2515354159 0.068
102 0.2510189714 0.071
103 0.2891231207 0.05431919427
104 0.2891231207 0.05431939427
105 0.02951200304 0.062
```

```
106 0.2891231207 0.05
107 0.2703292683 0.05552700537
108 0.2703292683 0.062
109 0.2703292683 0.06754512467
read test points 1
26  0.3 0.001
*
*
*
*
*------------------------------------------------------------------

*                Individual Region Definitions Follow
*                --REGION NUMBERS MUST BE SEQUENTIAL--
*------------------------------------------------------------------

*======================================================================

region    1  <------ Inputs specific to this region follow
*======================================================================

*fnum multiplier 5.0
grid
1   global points
2
5
54
```

```
15    number of cells along 1 and 3
15    number of cells along 2 and 4
0   sides 1 and 3 curvature: 0/1 for line/arc
0   sides 1 and 3 cell spacing
0   sides 2 and 4 cell spacing
5
−31
5
7
2
*
*   Side  Cell1  Cell2   elem/cell  Spec. refl .   Temp. K   Material#    Value
*
  1      1      35      1          0.0         300.0      1         0
  3      1    35      1          0.0       300.0      1         0
*
* Region interface matching
*
1 0
2 0
3 0
4 1 2 3
*===================================================================

region       2  <−−−−−− Inputs specific to this region follow
*===================================================================
```

```
*fnum multiplier 5.0
grid
6   global points
3
4
17
15    number of cells along 1 and 3
15    number of cells along 2 and 4
0   sides 1 and 3 curvature: 0/1 for line/arc
0   sides 1 and 3 cell spacing
3 1.05 100    sides 2 and 4 cell spacing
7
5
-32
5
2
*
*   Side  Cell1  Cell2   elem/cell  Spec. refl .   Temp. K   Material#    Value
*
  2     1     35     1         0.0        300.0     1        0
  4     1   35     1         0.0      300.0     1        0
*
* Region interface matching
*
1 1 3 4
2 0
3 0
```

```
4 0
*----------------------------------------------------------------------

region   3    <------ inputs specific to this  region follow
*----------------------------------------------------------------------

*fnum multiplier 5.0
grid
  54
  5
  7
  55
  15
  15
  0
  0
  0
  5
  7
  5
  7
  2
*
*    Side   Cell1   Cell2    elem/cell   Spec.  refl .     Temp. K     Material#      Value
*
  1       1       30       1           0.0          300.0       1          0
  3       1    30       1           0.0        300.0       1          0
```

```
*
* Region interface matching
*
1 0
2 1 4 1
3 0
4 1 2 5
*---------------------------------------------------------------
region   4    <------- inputs specific to this region follow
*---------------------------------------------------------------
*fnum multiplier 5.0
grid
  8
  6
  17
  19
  15
  12
  0
  0
  0
  7
  5
  7
  5
```

```
  2
*
*   Side   Cell1   Cell2   elem/cell   Spec.  refl .   Temp. K   Material#   Value
*
  2     1     12     1        0.0        300.0     1        0
  4     1    12     1        0.0      300.0     1        0
*
* Region interface matching
*
1 1 3 6
2 0
3 1 1 2
4 0
*----------------------------------------------------------------------

region   5   <------- Inputs specific to this region follow
*---------------------------------------------------------------------

*fnum multiplier 5.0
grid
  55
  7
  9
  56
  10
  10
  0
```

```
  0
  0
  5
  7
  5
  7
  2
*
*   Side  Cell1  Cell2   elem/cell  Spec. refl.   Temp. K   Material#    Value
*
  1     1     20     1          0.0         300.0     1         0
  3     1   20     1          0.0       300.0     1         0
*
* Region interface matching
*
1 0
2 1 4 3
3 0
4 1 2 27
*--------------------
region  6  <--------- Inputs specific to this region follow
*-----------------------------
*fnum multiplier 5.0
grid
  10
  8
  19
```

```
  24
  12
  10
  0
  0
  0
  7
  5
  7
  5
  2
*
*   Side   Cell1   Cell2    elem/cell   Spec.  refl .    Temp. K    Material#     Value
*
  2       1       10       1           0.0          300.0       1          0
  4       1     10       1           0.0        300.0       1          0
*
* Region interface  matching
*
1 1  3  8
2 0
3 1  1  4
4 0
*--------------------------------------------------------------
region   7   <----- Inputs specific  to  this  region follow
*--------------------------------------------------------------
*fnum multiplier 5.0
```

```
grid
  9
  11
  22
  21
  16
  4
  0
  0
  0
  7
  5
  7
  5
  2
*
*   Side  Cell1  Cell2   elem/cell  Spec. refl .   Temp. K   Material#    Value
*
  2      1      4     1          0.0          2300.0       1          0
  4      1    4       1          0.0       300.0       1          0
*
* Region interface matching
*
1 1 3 27
2 0
3 1 1 9
4 0
```

```
*--------------------
region   8    <------ region number
*-----------
*fnum multiplier 5.0
grid
  12
  10
  24
  23
  16
  4
  0
  0
  0
  7
  5
  7
  5
  2
*
*   Side  Cell1  Cell2   elem/cell  Spec.  refl .   Temp. K   Material#    Value
*
  2     1     4    1         0.0        2300.0      1        0
  4     1   4      1         0.0      300.0      1        0
*
* Region interface  matching
*
```

```
1 1 3 12
2 0
3 1 1 6
4 0
*----------
region   9 <------- Inputs specific to this region follow
*------------------
*fnum multiplier 0.2
grid
  11
  14
  27
  26
  25
  2
  0
  0
  0
  7
  5
  7
  7
  1
*
*   Side   Cell1   Cell2    elem/cell   Spec.  refl .    Temp. K    Material#     Value
*
  2      1      2    1         0.0        2300.0      1        0
```

```
* 4     1   4     1        0.0     300.0    0      0
*
* Region interface  matching
*
1  2  3  14 3  7
2  0
3  1  1  10
4  1  2  17
*-----------
region   10 <-------- Inputs specific to this region follow
*----------------------
*fnum multiplier 0.2
dt  multiplier  0.1
grid
  14
  15
  28
  27
  25
  5
  0
  0
  0
  7
  -53
  7
  7
```

```
  1
*
*   Side  Cell1  Cell2   elem/cell  Spec. refl .   Temp. K   Material#    Value
*
  2      1      5     1         0.0         3300.0       3          0
* 4      1    4       1         0.0       300.0      0          0
*
*
* Region interface matching
*
1 1 3 9
2 0
3 1 1 11
4 2 2 29 2 17
*----------
region  11 <------- Inputs specific to this region follow
*------------------
*fnum multiplier 0.2
dt multiplier 0.1
grid
  15
  16
  29
  28
  25
  5
  0
```

```
  0
  0
  7
  −54
  7
  7
  1
*
*   Side   Cell1   Cell2    elem/cell   Spec.  refl .     Temp. K    Material#     Value
*
  2      1       5      1           0.0          3300.0     3          0
* 4      1     4        1           0.0       300.0       0          0
*
*
* Region interface  matching
*
1  1  3  10
2  0
3  1  1  12
4  1  2  29
*−−−−−−−−−−
region   12 <−−−−−−− Inputs specific to this region follow
*−−−−−−−−−−−−−−−−−
*fnum multiplier 0.2
grid
  16
  12
```

```
  30
  29
  25
  2
  0
  0
  0
  7
  5
  7
  7
  1
*
*   Side  Cell1  Cell2   elem/cell  Spec.  refl .   Temp. K   Material#    Value
*
  2     1     2    1        0.0        300.0     1       0
*
*
* Region interface  matching
*
1 1 3 11
2 0
3 2 1 8 1 15
4 1 2 29
*----------
region   13 <------- Inputs specific to this region follow
*------------------
```

```
*fnum multiplier 10
grid
  20
  71
  77
  76
  200
  8
  0
  0
  0
  3
  5
  7
  7
  1
*
*   Side   Cell1   Cell2    elem/cell   Spec.  refl .     Temp. K     Material#      Value
*
  2       1       8       1            0.0           300.0       1           0
*
*
* Region interface  matching
*
1 0
2 0
3 2 1 14 1 17
```

```
4 1 2 18
*----------
region  14 <------- Inputs specific to this region follow
*------------------
*fnum multiplier 0.2
grid
  71
  22
  26
  74
  20
  10
  0
  0
  0
  7
  5
  7
  7
  1
*
*   Side  Cell1  Cell2   elem/cell  Spec. refl .   Temp. K   Material#    Value
*
  2     1     10     1        0.0        300.0     1        0
*
*
* Region interface matching
```

```
*
1 1 3 13
2 0
3 1 1 9
4 1 2 17
*----------
region   15 <------- Inputs specific to this region follow
*-----------------
*fnum multiplier 0.2
grid
  23
  72
  75
  30
  20
  10
  0
  0
  0
  7
  5
  7
  7
  1
*
*   Side   Cell1   Cell2    elem/cell   Spec.  refl .    Temp. K    Material#     Value
*
```

```
  2    1    10    1        0.0        300.0    1        0
*
*
*
* Region interface matching
*
1 1 3 12
2 0
3 1 1 20
4 1 2 29
*----------
region   16 <------- Inputs specific to this region follow
*------------------
*fnum multiplier 0.2
grid
  98
  79
  52
  102
  15
  30
  0
  0
  0
  7
  7
  3
```

```
  7
  0
*
*   Side   Cell1   Cell2    elem/cell   Spec.  refl .    Temp. K    Material#     Value
*
* 1       1       10       1           0.0          300.0      0          0
* 4    1    10       1           0.0       300.0      0       0
*
*
*
* Region interface  matching
1 1 4 28
2 2 4 29 4 20
3 0
4 1 2 22
*----------
region   17 <------- Inputs specific to this region follow
*-----------------
*fnum multiplier 0.2
grid
  74
  88
  86
  77
  100
  20
  0
```

```
  0
  0
  7
  7
  7
  7
  0
*
*
* Region interface  matching
*
1 1 3 13
2 3 4 14 4 9 4 10
3 1 1 29
4 3 2 19 3 24 2 18
*----------
region   18 <------- Inputs specific to this region follow
*-----------------
*fnum multiplier 0.1
grid
  76
  95
  99
  50
  15
  30
  0
```

```
  0
  0
  3
  7
  7
  7
  0
*
*
* Region interface matching
*
1 0
2 3 4 13 4 17 4 29
3 1 2 24
4 1 2 21
*----------
region   19 <------- Inputs specific to this region follow
*-----------------
*fnum multiplier 0.1
grid
  96
  97
  101
  100
  15
  5
  0
```

```
  0
  0
  7
  7
  7
  7
  0
*
*   Side  Cell1  Cell2   elem/cell  Spec. refl .   Temp. K   Material#    Value
*
* 1     1     5    1          0.0         300.0      2        0
*
*
*
*
* Region interface matching
*
1 1 4 24
2 2  4 17 4 29
3 1 2 28
4 2 2 31 2 30
*----------
region  20 <------- Inputs specific to this region follow
*-----------------
*fnum multiplier 1.0
grid
  72
```

```
  73
  79
  -78 16 2 2
  200
  8
  0
  0
  0
  7
  5
  3
  7
  1
*
*   Side   Cell1   Cell2    elem/cell   Spec.  refl .    Temp. K    Material#     Value
*
  2        1        8       1            0.0          300.0       0           0
*
*
*
* Region interface  matching
*
1  2  3  29 3  15
2  0
3  0
4  1  2  16
*----------
```

```
region   21 <------- Inputs specific to this region follow
*------------------
*fnum multiplier 0.1
grid
  50
  99
  64
  66
  40
  25
  -6 0.036 1 1
  0
  0
  3
  7
  5
  7
  1
*
*   Side  Cell1  Cell2   elem/cell  Spec. refl .   Temp. K   Material#    Value
*
* 1       1       10                 0.0          300.0      0          0
  3    1    40     1         0.0        300.0       2       0
*
*
*
* Region interface  matching
```

```
1 0
2 1 4 18
3 0
4 1 2 26
*----------
region   22 <------- Inputs specific to this region follow
*------------------
*fnum multiplier 0.1
grid
  102
  52
  67
  104
  40
  25
  -5 0.032 1 1
  0
  0
  5
  7
  3
  7
  1
*
*   Side  Cell1  Cell2   elem/cell  Spec. refl .   Temp. K   Material#    Value
*
  1     1     40     1        0.0        300.0     2        0
```

```
* 4    1    10     1          0.0       300.0     0      0
*
*
*
* Region interface matching
1 0
2 1 4 16
3 0
4 1 2 26
*----------
region   23 <------- Inputs specific to this region follow
*------------------
*fnum multiplier 1.0
grid
  107
  108
  106
  65
  20
  5
  -5 0.032 1 1
  0
  0
  5
  7
  7
  7
```

```
  1
*
*   Side  Cell1  Cell2   elem/cell  Spec. refl .   Temp. K   Material#    Value
*
  1     1     20     1          0.0         300.0     2         0.0
*
*
* Region interface matching
*
1 0
2 1 4 30
3 1 1 25
4 1 2 26
*------------
region   24 <-------- Inputs specific to this region follow
*----------------------
*fnum multiplier 0.25
grid
  99
  95
  96
  100
  10
  20
  -5 0.0017 1 2
  0
  0
```

```
  5
  7
  7
  7
  1
*
*   Side   Cell1   Cell2    elem/cell   Spec.  refl .    Temp. K    Material#     Value
*
  1       1       10       1           0.0          300.0       2          0
*
*
*
*
* Region interface matching
*
1 0
2 1 3 18
3 1 4 17
4 1 1 19
*----------
region   25 <------- Inputs specific to this region follow
*-----------------
*fnum multiplier 1.0
grid
  108
  109
  103
```

```
  106
  20
  5
  −6 0.036 1 1
  0
  0
  7
  7
  5
  7
  1
*
*   Side   Cell1   Cell2    elem/cell   Spec.  refl .    Temp. K    Material#     Value
*
  3       1       20       1            0.0           300.0       2           0.0
*
*
* Region interface  matching
*
1 1 3 23
2 1 4 31
3 0
4 1 2 26
*----------
region   26 <------- Inputs specific to this region follow
*------------------
*fnum multiplier 1.0
```

```
grid
  66
  67
  63
  61
  25
  50
  0
  0
  0
  3
  9
  3
  3
  1
*
*   Side   Cell1   Cell2    elem/cell   Spec.  refl .    Temp. K    Material#     Value
*
  2       1       50      1          0.0          300.0       2          1.0
*
*
*
*
* Region interface  matching
*
1 0
2 6 4 21 4 −1 4 23 4 25 4 −1 4 22
```

```
3 0
4 0
*----------
region   27 <------- Inputs specific to this region follow
*-----------------
*fnum multiplier 1.0
grid
  56
  9
  21
  13
  10
  10
  0
  0
  0
  5
  7
  7
  5
  2
*
*   Side   Cell1   Cell2    elem/cell   Spec.  refl .    Temp. K    Material#     Value
*
  1      1      10      1          0.0          300.0      1          0
  4   1    10      1          0.0       300.0      1      0
*
```

```
*
*
* Region interface  matching
1 0
2 1 4 5
3 1 1 7
4 0
*----------
region   28 <------- Inputs specific to this region follow
*-----------------
*fnum multiplier 0.1
grid
  101
  97
  98
  102
  10
  25
  -5 0.0017 1 2
  0
  0
  5
  7
  7
  7
  1
*
```

```
*   Side  Cell1  Cell2   elem/cell  Spec. refl .   Temp. K   Material#    Value
*
  1     1     10     1        0.0        300.0     2       0
*
*
*
*
* Region interface matching
*
1 0
2 1 3 19
3 1 4 29
4 1 1 16
*----------
region  29 <------- Inputs specific to this region follow
*-----------------
*fnum multiplier 1.0
grid
  88
  75
  -78 16 2 2
  86
  100
  20
  0
  0
  0
```

```
  7
  7
  7
  7
  0
*
*   Side   Cell1   Cell2    elem/cell   Spec.  refl .    Temp. K    Material#     Value
*
* 1       1       10       1           0.0          300.0      0          0
* 4    1     10       1           0.0        300.0      0       0
*
*
*
* Region interface  matching
1  1  3  17
2  4  4  10 4  11  4  12 4  15
3  1  1  20
4  3  2  16 3  28 2  19
*----------
region   30 <------- Inputs specific to this region follow
*-----------------
*fnum multiplier 1.0
grid
  100
  -105 19 4 2
  108
  107
```

```
  20
  5
  −5 0.032 1 1
  0
  0
  5
  7
  7
  7
  1
*
*   Side   Cell1   Cell2    elem/cell   Spec.  refl .    Temp. K    Material#     Value
*
  1      1      20      1          0.0         300.0      2         0
* 3    1     25       1          0.0       300.0      2       0
*
*
*
* Region interface  matching
1 0
2 1 4 19
3 1 1 31
4 1 2 23
*−−−−−−−−−−
region   31 <−−−−−−− Inputs specific to this region follow
*−−−−−−−−−−−−−−−−−
*fnum multiplier 1.0
```

```
grid
  −105 19 4 2
  101
  109
  108
  20
  5
  −6 0.036 1 1
  0
  0
  7
  7
  5
  7
  1
*
*   Side   Cell1   Cell2    elem/cell   Spec.  refl .     Temp. K     Material#      Value
*
* 1       1       25       1            0.0          300.0       2          0
  3    1     20       1            0.0        300.0       2       0
*
*
*
* Region interface  matching
1  1  3  30
2  1  4  19
3  0
```

4 1 2 25

END

A.1.2 Species specification file (spec-Ni)

```
*************************************
*          new species data file            *
*************************************
*
3                   number of species
*
3                   internal structure of most complex molecule:
*                          3-monatomic, 4-rotation, 5-rotat. + vibrat.
*
0                   # of chem. rx. (from file chem)
*
*
*-----------------------------------------------------------------------------

*  ID
*  Mwt     Mol. mass   Diam.   #Rot.Deg.      Rot.Rel.  #Vit.  Deg. Vib.  Rel.  Vib.Temp.
     specie  wt. charge   omega  tref     alpha
*              (kg)         (m)      Freedom      Coll. #     Freedom     Coll. #      (K)
*-----------------------------------------------------------------------------

  He
  4.02   0.665e-26 0.24e-9    0.              5.            0.              0.             0.         1.0
              0.0   0.633   300.0   1.0
```

```
  O2
32.00 0.5313e−25 0.3558e−9 2.0         5.0        0.0          0.0        0.     0.5       0.0
     0.77 300.0  1.0
  Ni
58.7 9.7e−26  0.6619e−9 0.0          5.0        0.0        0.0        0.     0.001       0.0   1
     300.0  1.0
END
```

A.1.3 Boundary conditions file (inlet-3ratio)

```
* Test  inlet  table  for  copied geometry, only include He
*
*
5    number of tables
*
0
4.229467545e21 0.0 0.0 298.0 298.0 298.0 1.0 0.0 0.0  0.0
*
*
*
*
1   1   2   2   table  number,# of multiple  tables ,  number of  entries ,  BC type
*    #/s
*   location    #/m^2s  Vx  Vy   Tt    Tr    Tv    He O2  Zr
0.00904  5.0e24 300  0.0  298.  298.  298.  0.909 0.0909 0.0
0.032       5.0e24 300  0.0  298.  298.  298.    0.909 0.0909 0.0
*
*
```

```
2  1  2  2  table number,# of multiple tables , number of entries , BC type
*   #/s
*  location   #/m^2s  Vx  Vy  Tt  Tr  Tv  He O2 Zr
0.092    5.0e24 300  0.0  298. 298. 298. 0.909 0.0909 0.0
0.11496  5.0e24 300  0.0  298. 298. 298. 0.909 0.0909 0.0
*
*
3 1 3 2
0.05575 8.80177731e20 50 0.0 3000 298. 298. 0.0 0.0 1.0
0.058875 8.80177731e20 50 0.0 3000 298. 298. 0.0 0.0 1.0
0.062 8.80177731e20 50 0.0 3000 298. 298. 0.0 0.0 1.0
4 1 3 2
0.062   8.80177731e20 50 0.0 3000 298. 298. 0.0 0.0 1.0
0.065125  8.80177731e20 50 0.0 3000 298. 298. 0.0 0.0 1.0
0.06825 8.80177731e20 50 0.0 3000 298. 298. 0.0 0.0 1.0
END
```

A.1.4 Surface conditions file (surfbc$_{w}afer$)

```
*
* Surface Reaction File for DVD2
*
* He, O2, Zr
* 1   2   3
*
3 number of material table types
*
* material type (1)
```

```
1 3 1.75e19
1  1  0  0  0.0 0.0 0.0 0.0
1  2  0  0  0.0 0.0 0.0 0.0
1  3  0  0  0.0 0.0 0.0 1.0
*
* material type (2)
2 3 1.75e19
1  1  0  0  0.0 0.0 0.0 0.0
1  2  0  0  0.0 0.0 0.0 0.0
1  3  0  0  0.0 0.0 0.0 1.0
* material type (3)
3 3 1.75e19
1  1  0  0  0.0 0.0 0.0 0.0
1  2  0  0  0.0 0.0 0.0 0.0
1  3  0  0  0.0 0.0 0.0 0.0
END
```

A.2 KMC input file (kmc.in)

```
1.125000e+04 #Base number of atoms deposited per orientation
5.000000e+00 #Number of initial layers
8.783658e-08 #Base deposition rate (m/s)
2.800000e+02 #Temperature (in K)
4.001000e+03 #Domain width (# of lattice sites )
2.000000e-01 #Assumed density
-1.000000e+00 #Number of timesteps to record a movie (< 0, none)
1.000000e+00 #Surface roughness on/off ( 1 = on, else = off)
```

```
1.500000e+01 #Number of surface asperities
1.000000e+02 #Asperity width
7.500000e+01 #Asperity height
0.000000e+00 #Resume previous simulation (1 = yes, else = no)
5.000000e+00 #Number of existing rows
1.000000e+00 #Rotation or stationary switch (1 = rotate , 0 = stationary )
8.000000e+00 #Number of input files per rotation cycle
1.000000e+02 #Number of rotation cycles
8.783658e−08 #Deposition rate at orientation 1
2.959128e−08 #Deposition rate at orientation 2
4.878960e−10 #Deposition rate at orientation 3
1.239009e−09 #Deposition rate at orientation 4
3.566239e−08 #Deposition rate at orientation 5
5.452767e−08 #Deposition rate at orientation 6
1.210261e−09 #Deposition rate at orientation 7
3.097820e−08 #Deposition rate at orientation 8
3.273000e+04 #Number of atoms to deposit at orientation 1
1.102400e+04 #Number of atoms to deposit at orientation 2
1.850000e+02 #Number of atoms to deposit at orientation 3
4.560000e+02 #Number of atoms to deposit at orientation 4
1.328800e+04 #Number of atoms to deposit at orientation 5
2.032400e+04 #Number of atoms to deposit at orientation 6
4.560000e+02 #Number of atoms to deposit at orientation 7
1.153700e+04 #Number of atoms to deposit at orientation 8
```

Appendix B

Kinetic Monte Carlo Code

```
! Header to specify common variables shared throughout subroutines
module globalVariables

! parameter (nbyte=4,ibyte=4) This is from Bartel, dunno if its necessary, it sets the data size
! for different types, which would be useful, but I dunno how to do it right

! Deposition constants, need common after to make the accessible

  integer :: atomsToDeposit, numberOfInitialLayers, substrateWidth, coordination, singleNeighborLocation, existingRows
  integer :: atomCount, xIndex, yIndex, deposited, filmHeightMax, yVaporInitial, gridMaxHeight, boundaryConditionModifier
  real :: substrateTemperature, depositionTime, deltaYGrid, deltaXGrid, assumedDensity, start, finish, depositionRate
```

```
  integer :: evenIndex, oddIndex, numberOfDiffusions, moundNumber, moundSwitch, moundWidth,moundHeight,resumeSwitch
  integer :: loopSwitch, loopNumber, loopIndex, cycleMultiplier, gridMaxXValue
  real, dimension(:), allocatable :: loopDepositionRate
  integer, dimension(:), allocatable :: loopAtomsToDeposit
  integer, dimension(:,:), allocatable :: atomPath
  integer, parameter :: shortInt = selected_int_kind (2)
  integer, parameter :: gridInt = selected_int_kind (1)
  real, parameter :: pi = 3.141592653589793


! Creates a struct for gridLocations
! If we use array indices, we don't need the separate xIndex and yIndex
! (I think we can just use movieGrid for this)
! The variable color will be used to make movies of the simulation process.
! The color code is as follows: 1 = black, 2 = red, 3 = orange, 4 = grey, 5 = blue, 6 = brown, 0 = white (vacant)
  type, public :: gridIndex
!   integer :: xIndex
!   integer :: yIndex
    integer(kind = gridInt) :: occupationNumber
    !integer :: color
  end type gridIndex

  !Create movieGrid as a three dimensional array (x,y,timestep), I'm not sure if this will work...
  integer, dimension(:,:, :), allocatable :: movieGrid
```

```
 integer, dimension(:,:), allocatable :: initialGrid
integer :: movieIndex, movieIndexMax

! type(gridIndex) :: currentIndex


! Define an array of variable dimensions, is this the right syntax for two dimensions?
! Grid as two values for each spot
! occupationNumber = 1 if occupied, 0 otherwise
! diffusionIndex = 1 if moveable, 0 if in bulk for good
type(gridIndex), dimension(:,:), allocatable :: grid

! common /bk02/ depositedAtom


! Create struct for vapor−phase atoms (one at a time)
type, public :: vaporAtom
  real :: xVapor
  real :: thetaVapor
  integer :: yVapor
  real :: deltaYVapor
end type vaporAtom

!Create a variable of the struct type
type(vaporAtom) :: newAtom

 real, dimension(:,:), allocatable :: depositionFlux
 real, dimension(−45:45) :: iAD, iADNormalized, modifiedIAD
real :: depositTimeInterval, depositTime
```

```

  !Jump energy Indexing:
  !energyIndex = Schoewbel down left, +1 = Schoewbel down right, +2 = jump left, +3 =
      jumpRight
  !+4 = Schoewbel up left, +5 = Schoewbel up right
  real, dimension(:), allocatable :: jumpTree
  real, dimension(20) :: probabilities
  integer (kind = shortInt), dimension(:), allocatable :: jumpEnergies
  integer :: leafN, treeSize, firstLeafIndex
  real :: maxLatticePoints

  !Create variables to allow for active adjustment of the input IAD based on columnar
      top surface normals.
  integer :: typicalColumnWidth, surfaceNormalCheckInterval, columnDensity,
      columnAngleSign



end module globalVariables




!
    ----------------------------------------------------------------------------------------------------------------


!kMSeed -- A 2D kinetic Monte Carlo program for deposition simulation
!Theron Rodgers 4/13/11
!This is the main subroutine for the kinetic Monte Carlo code!
```

```
!This version supports either stationary substrate deposition or rotated deposition with eight input orientations

program main

  use globalVariables

  integer :: i,j,k
  character(len=1024) :: filename
  integer :: totalAtomsDeposited = 0


  call CPU_TIME(start)
  call input
  print *, 'Input executed'

  !Set the maximum size of coating allowed in memory. This would be a prime area to cut usage.
  if (loopSwitch == 1) then
    filmHeightMax = CEILING(numberOfInitialLayers + existingRows + ((atomsToDeposit/substrateWidth)/assumedDensity)*(loopNumber*cycleMultiplier))
  else
    filmHeightMax = CEILING(numberOfInitialLayers + existingRows + (atomsToDeposit/substrateWidth)/assumedDensity)
    loopNumber = 1
  endif
```

```
print *, 'Film height max', filmHeightMax

!Set up the grid() and movieGrid() arrays. Account for mounds or restart conditions
call gridInitialize
print *, ' gridInitialize executed'

!Create a list of atoms to deposit
call vaporInitialize
print *, ' vaporInitialize executed'
! Initialize the parameters used during diffusion
call diffusionInitialize
print *, ' diffusionInitialize executed'
!Determine the size of the jumpTree
call jumpTreeInitialize
print *, 'jumpTreeInitialize executed'

movieIndex = 1
numberOfDiffusions = 0



!Start the main loop of the program
do k = 1, cycleMultiplier
  do j = 1, loopNumber

    loopIndex = j
    !Update the IAD, atomsToDeposit, and depositionRate
    if (j > 1) then
```

```
    !Write the desired fileName to character variable
    write(filename, "(A,I0,A)") 'iad', FLOOR(22.5*(j-1)), 'Deg.in'

    !Read in the new IAD
    open (unit = 13, file = trim(filename))
    do i = -45,44
      read (unit = 13, fmt = *), iAD(i)
    enddo

    modifiedIAD = iAD

    !Update varaibles
    atomsToDeposit = loopAtomsToDeposit(j)
    depositionRate = loopDepositionRate(j)

    !Update the time intervals between depositions
    depositTimeInterval = SQRT(3.0) * deltaXGrid /(2 * substrateWidth *
        depositionRate)
    close(13)
    deallocate(depositionFlux)
    call vaporInitialize

  endif

  !This is the main deposition loop.
  do i = 1, atomsToDeposit
```

```
        atomCount = i
        totalAtomsDeposited = totalAtomsDeposited + 1
        call hexDeposit
    !   print *, 'hexDeposit executed ', i
        call diffuse
    !   print *, 'diffuse executed ', i
        !See if an appropriate number of atoms have been deposited and calculate the
            tip's surface normal
        if (MOD(totalAtomsDeposited, surfaceNormalCheckInterval) == 0) then
          call IADAdjust
        endif
      enddo
      !Call the output for each major step, need to label files in the subroutine


    enddo
    if (MOD(k,10) == 0) then
      call output
    endif
  enddo
  call output

end

!
    ----------------------------------------------------------------------------------------
```

```
!Reads in input files which include kmc.in, the main control file ; iad.in, the IAD file ; kmc.txt, the restart file
!The variables included in kmc.in are (in order)
!atoms to deposit
!number of initial layers
! deposition rate
! substrate temperature
! substrate width
!assumed density
!movie index maximum
!mound on/off switch
!number of mounds
!mound width
!mound height
! restart on/off switch
!number of existing rows
!loop on/off switch (for rotation)
!loop number (for rotation, will usually be 0 or 8)
!Modules & subroutines called
! globalVariables
subroutine input()

  use globalVariables

  ! character*80 :: filename
  ! character*80 :: str
  integer :: i,j
```

```
!Open the input files
open (unit=11,file = ”kmc.in”)
!Read in the distribution of inlet files
open (unit=13, file = ”iad.in”)
!For easy resuming of simulations, read in the kmc.txt file . This file is just a series of 1’s and 0’s
!to signify filled and unfilled sites respectively .
open (unit=15, file = ”kmc.txt”)

!Read in control data from kmc.in
read (unit = 11, fmt = *), atomsToDeposit
read (unit = 11, fmt = *), numberOfInitialLayers
read (unit = 11, fmt = *), depositionRate
read (unit = 11, fmt = *), substrateTemperature
read (unit = 11, fmt = *), substrateWidth
!Assumed density allows for a larger grid to account for porosity
read (unit = 11, fmt = *), assumedDensity
read (unit = 11, fmt = *), movieIndexMax
!Are there mounds?
!Mound input. moundWidth should be odd, while substrateWidth should be
! divisible by moundNumber for most ease.
!Mound height should be equal or smaller than moundWidth
read (unit = 11, fmt = *), moundSwitch
read (unit = 11, fmt = *), moundNumber
read (unit = 11, fmt = *), moundWidth
```

```
read (unit = 11, fmt = *), moundHeight
read (unit = 11, fmt = *), resumeSwitch
read (unit = 11, fmt = *), existingRows
!Read in what interval the columns should be adjusted at
read (unit = 11, fmt = *), surfaceNormalCheckInterval
read (unit = 11, fmt = *), typicalColumnWidth
read (unit = 11, fmt = *), columnDensity
!Read in values that help with looping
read (unit = 11, fmt = *), loopSwitch
read (unit = 11, fmt = *), loopNumber
read (unit = 11, fmt = *), cycleMultiplier

!Allocate memory for deposition parameters
allocate(loopDepositionRate(loopNumber))
allocate(loopAtomsToDeposit(loopNumber))

!Read in the listed parameters for looping from the input file.
do i = 1,loopNumber
  read(unit = 11, fmt = *), loopDepositionRate(i)
enddo
do i = 1,loopNumber
  read(unit = 11, fmt = *), loopAtomsToDeposit(i)
enddo

!Echo what was read for verification
print *, 'Atoms to Deposit', atomsToDeposit
print *, '# of Initial Layers', numberOfInitialLayers
```

```
print *, 'Deposition Rate', depositionRate
print *, 'Substrate Temperature', substrateTemperature
print *, 'Substrate Width', substrateWidth
print *, 'Assumed Density', assumedDensity
print *, 'maximum movie Index', movieIndexMax
print *, 'Mound on/off switch', moundSwitch
print *, 'number of mounds', moundNumber
print *, 'Resume on/off switch',resumeSwitch
print *, 'number of existing rows',existingRows
print *, 'loop on/off switch', loopSwitch
print *, 'number of unique loops', loopNumber
print *, 'How many times to loop', cycleMultiplier
if (loopNumber /= 0) then
  do i = 1, loopNumber
    !print *, loopDepositionRate(i)
    !print *, loopAtomsToDeposit(i)
  enddo
endif


close(11)


!Read in IAD data from iad.in and store in array
do i = -45,45
  read (unit = 13, fmt = *), iAD(i)
  !Print the first and last values to make sure they're zero
enddo
```

```
  print *, iAD(-45)
  print *, iAD(45)

  close(13)

  !Read in kmc.txt if resumeSwitch = 1, Read the input grid into a 1D array, and then
      translate that into
  !the usual grid format
  !I have been following the convention of (column, row) for arrays in the program,
      which now seems backwards...
  if (resumeSwitch == 1) then

    allocate( initialGrid (substrateWidth, existingRows))
    do i = 1, existingRows
      read(unit =15, fmt = *)( initialGrid (j,existingRows -i +1), j=1,substrateWidth)
      !print *, initialGrid (: , existingRows -i + 1)
    enddo
  endif

  close(15)

end subroutine input


!
    ---------------------------------------------------------------------------
```

```
!Subroutine to create an initial grid for simulation. Using a hexagonal-packed lattice.
!All positions initially vacant or generates grid from restart information.
!Variables:
!grid(:,:), substrateWidth, filmHeightMax, numberOfInitialLayers, deltaYGrid, deltaXGrid, gridMaxHeight
!Allocates:
!grid, movieGrid
!Modules & subroutines
!globalVariables

subroutine gridInitialize()

  use globalVariables
  integer :: i,j, moundInterval, moundCenter, oddModifier, oppositeMod

! Create array of gridIndex objects using the width and height needed
  allocate(grid(substrateWidth, filmHeightMax+10))

  !Create array for depositionAtom path. Maximum filmHeight * 29, faster than allocating each time
  allocate(atomPath(filmHeightMax*29,3))

  !Allocate movieGrid if needed. This was wasting space the size of one iteration earlier.
  !Need to make sure all movie features are optional.
  if (movieIndexMax > 0) then
    allocate(movieGrid(substrateWidth, filmHeightMax, movieIndexMax))
```

```
 endif


! Set occupationNumber to vacant = 0, except for the first rows as specified by
   numberOfInitialLayers
 grid(1:substrateWidth, numberOfInitialLayers + 1:filmHeightMax)%
     occupationNumber = 0
 grid(1:substrateWidth, 1:numberOfInitialLayers)%occupationNumber = 1


! Set the initial movie color codes of the lattice sites . (We'll set all the steps as
    this, as they should be similar
 if (movieIndexMax > 0) then
   movieGrid(1:substrateWidth, 1:numberOfInitialLayers, :) = 1
   movieGrid(1:substrateWidth, numberOfInitialLayers + 1:filmHeightMax, :) = 0
 endif


 if(MOD(numberOfInitialLayers,2) /= 0) then
   oddModifier = 1
   oppositeMod = 0
 else
   oddModifier = 0
   oppositeMod = 1
 endif


 !Create mounds on the initial computational grid
 !For simplicity, lets have an odd number of base atoms for each mound
 !Need to verify the shape of the mounds. It might be kinda wonky
 if (moundSwitch == 1) then
```

```
moundInterval = substrateWidth/moundNumber

do i = 1, moundNumber
  !Put mound center at midpoint of moundInterval
  moundCenter = (i−1)∗moundInterval + moundInterval/2 − oddModifier

  grid(moundCenter − FLOOR(moundWidth/2.0):moundCenter + FLOOR(
      moundWidth/2.0), numberOfInitialLayers+1)%occupationNumber=1
  do j = 2, moundHeight
    if (MOD(j,2) == 0) then

      if (oddModifier == 1) then
        grid(moundCenter−FLOOR(moundWidth/2.0) +(j/2):moundCenter+
            FLOOR(moundWidth/2.0) −(j/2−1),&
        numberOfInitialLayers+j)%occupationNumber = 1
      else
        grid(moundCenter−FLOOR(moundWidth/2.0) +(j/2−1):moundCenter+
            FLOOR(moundWidth/2.0) −(j/2),&
        numberOfInitialLayers+j)%occupationNumber = 1
      endif
    else
      grid(moundCenter−FLOOR(moundWidth/2.0) +FLOOR(j/2.0):moundCenter+
          FLOOR(moundWidth/2.0) −FLOOR(j/2.0),&
      numberOfInitialLayers+j)%occupationNumber = 1
    endif
  enddo
```

```
  enddo
  !Set max heigh with mounds
  gridMaxHeight = numberOfInitialLayers + moundHeight
endif

!Import the initial grid. Need to modify this to account for even/oddness. I don't think I'll need to do this
if (resumeSwitch == 1) then

  do i = 1, substrateWidth
    do j = 1, existingRows
      if(initialGrid(i,j) == 1) then
        grid(i,j)%occupationNumber = 1
        if (movieIndexMax > 0) then
          movieGrid(i,j,:) = 1
        endif
      elseif(initialGrid(i,j) == 0) then
        grid(i,j)%occupationNumber = 0
      else
        print *, 'The grid was not right', i, j
      endif
    enddo
  enddo

  !Set max height with read in data
  gridMaxHeight = existingRows
endif
```

```
! Set the coordinate spacing for the grid
! In meters
  deltaYGrid = 2.158000463e−10
  deltaXGrid = 2.491844297e−10

end subroutine gridInitialize




!
    −−−−−−−−−−−−−−−−−−−−−−−−−−−−−−−−−−−−−−−−−−−−−−−−−−−−−−−−−−−−−−−−−−−−−−−−−−−−−−−−−−−
!Creates a random sequence of vapor atoms from an inputted IAD.
!Random number creation can vary from compiler to compiler (check for cluster )
!
! Variables
!randomNum, i,j, iADSum, iADNormSum, depositionFlux(:,:), atomsToDeposit, iAD(:),
    iADNormalize(:)
!Modules & subroutines
! globalVariables, random_seed, random_number
subroutine vaporInitialize()

  use globalVariables
  use indexConversion
  use ifport
```

```
!IAD = Incident Angle Distribution, real angle value is iAD*2
!Measured from substrate normal
real :: randomNum
integer :: i, j
integer, dimension(8) :: timeValues
real :: iADSum, angleProb


call date_and_time(VALUES=timeValues)
call seed(timeValues(8))

!Create nx2 array, one column with the initial x position and another with angle ( theta )
allocate(depositionFlux(atomsToDeposit,2))
! call random_seed() !Seeds random generator, some compilers need different method


!Read in IAD from file
iADSum = 0.0
angleProb = 0.0

!Sum IAD and perform normalization
do i = -45, 44
  iADSum = iADSum + modifiedIAD(i)
end do

!iADNormalized is the sum of probabilities between 0 and 1
```

```
do i = -45, 44
  if (i == -45) then
    iADNormalized(i) = modifiedIAD(i)/iADSum
  else
    iADNormalized(i) = modifiedIAD(i)/iADSum + iADNormalized(i-1)
  endif
end do


!Create the deposition array
do i = 1 , atomsToDeposit

  !Assign the inlet location in real coordinates
  !This random generation doesn't quite line up to the grid used in deposition, as it creates atoms with an
  !x-minimum of 0, instead of 1 on the grid, but this can be accounted for by checking the boundary conditions
  !upon generation
  randomNum = rand()
  depositionFlux(i,1) = boundaryFloat(randomNum * (substrateWidth))
  !print *, depositionFlux(i,1)
  !Choose a random angle
  randomNum = rand()
  angleProb = randomNum

  !Assign the angle value, use the random number between 0 and 1 to deteremine angle
  do j = -90, 90, 2
```

```
      if (angleProb <= iADNormalized(j/2)) then
        depositionFlux(i,2) = j
        exit
      endif
    enddo
    !print *, 'depositionArray', depositionFlux(i, :)
  enddo

end subroutine vaporInitialize


!
    ----------------------------------------------------------------------------

!Jump probability calculator
!Returns an array of the jump probabilities for given conditions
!Will be constant during each simulation, but vary with temperature
!This is also a good location to set the deposition time interval
!
! Variables
! vibrationRate, kB, i, j, probabilities (:,:), barrier (:,:), substrateTemperature,
     depositTimeInterval, deltaXGrid
!substrateWidth, depositionRate
!
!Modules & subroutines
! globalVariables
subroutine diffusionInitialize ()
```

```

use globalVariables

!Set vibrationRate and Boltzmann's constant (kB) both are invarient
real, parameter :: vibrationRate = 5.0e12
real, parameter :: kB = 8.6173324e−5

!Calculate the probabilities for each jumpEnergy
!Energies are sorted in ascending order, which makes the probabilities sorted in descending
probabilities(1) = vibrationRate∗EXP(−0.017/(kB ∗ substrateTemperature))
probabilities(2) = vibrationRate∗EXP(−0.335/(kB ∗ substrateTemperature))
probabilities(3) = vibrationRate∗EXP(−0.408/(kB ∗ substrateTemperature))
probabilities(4) = vibrationRate∗EXP(−0.447/(kB ∗ substrateTemperature))
probabilities(5) = vibrationRate∗EXP(−0.472/(kB ∗ substrateTemperature))
probabilities(6) = vibrationRate∗EXP(−0.543/(kB ∗ substrateTemperature))
probabilities(7) = vibrationRate∗EXP(−0.706/(kB ∗ substrateTemperature))
probabilities(8) = vibrationRate∗EXP(−0.739/(kB ∗ substrateTemperature))
probabilities(9) = vibrationRate∗EXP(−0.819/(kB ∗ substrateTemperature))
probabilities(10) = vibrationRate∗EXP(−0.821/(kB ∗ substrateTemperature))
probabilities(11) = vibrationRate∗EXP(−0.822/(kB ∗ substrateTemperature))
probabilities(12) = vibrationRate∗EXP(−0.848/(kB ∗ substrateTemperature))
probabilities(13) = vibrationRate∗EXP(−0.92/(kB ∗ substrateTemperature))
probabilities(14) = vibrationRate∗EXP(−1.089/(kB ∗ substrateTemperature))
probabilities(15) = vibrationRate∗EXP(−1.09/(kB ∗ substrateTemperature))
probabilities(16) = vibrationRate∗EXP(−1.101/(kB ∗ substrateTemperature))
probabilities(17) = vibrationRate∗EXP(−1.121/(kB ∗ substrateTemperature))
```

```
  probabilities(18) = vibrationRate*EXP(-1.142/ (kB * substrateTemperature))
  probabilities(19) = vibrationRate*EXP(-1.204/ (kB * substrateTemperature))
  probabilities(20) = 0.0

  !Calculate interval between atom arrivals
  !from the formula dt = Sqrt(3) *a/(2*n*R)
  !Units: deltaXGrid - m, depositionRate - m/s, substrateWidth - none (its # of atoms)
  depositTimeInterval = SQRT(3.0) * deltaXGrid /(2 * substrateWidth * depositionRate)
! print *, deltaXGrid, substrateWidth, depositionRate
! print *, 'depositTimeInterval', depositTimeInterval
! print *, 'probabilities', probabilities

end subroutine diffusionInitialize


! ------------------------------------------------------------------------------------------------

! Initialize the jump tree for the first time
!Create the properly sized binary tree, and then fill it
!Nodes should be organized in order from left to right and then bottom up (as tie-breaker)
!Need to fill the tree as evenly as possible on right and left sides,
!so the tree should fill up left to right, but alternate which side of the halfway point they fall on
!We use an array to store the binary tree information, as described in the wikipedia "Binary Tree" article
```

```
!The root node has index i = 0, left child at 2i+1 and right child at 2i+2, and parent
    at (i−1)/2
!Minimizing the size of the tree could be quite useful
!
! Variables :
! maxLatticePoints, leafN, n, treeSize, jumpTree(:), firstLeafIndex
!
!Modules & subroutines
! globalVariables
subroutine jumpTreeInitialize()

  use globalVariables
  integer :: n
  !Find the number of points the jumpTree must cover
  maxLatticePoints= substrateWidth*filmHeightMax

  n = 1
  !Loop to find leafN, the total number of levels in the tree
  do
    if (2**(n −1) > maxLatticePoints) then

      leafN = n
      exit
    else
      n = n +1
    endif
```

```
enddo

treeSize = 2**leafN -1
print *, 'The jumpTree has this many nodes:', treeSize

!Create a 1d list containing the b-tree with root node @ zero
allocate(jumpTree(0:treeSize -1))

jumpTree(:) = 0.0

!Determine where the leaf nodes being in the array. Total - # of leafNodes
!The first leaf index should be odd, since we're beginning at zero
firstLeafIndex = 2**(leafN -1) -1
if (MOD(firstLeafIndex,2) == 0) then
  print *, 'The First leaf index is even, not good)', firstLeafIndex
endif

print*, 'The first leaf index is', firstLeafIndex

! Initialize the pointer array for jumpEnergies. Allocate the size of jumpTree*6
allocate(jumpEnergies(1:2**(leafN -1)*6))
!Make all of jumpEnergies point to the zero value of probabilities
jumpEnergies(:) = 20



!print *, jumpEnergies

```

```
end subroutine jumpTreeInitialize




! ------------------------------------------------------------------------------------------

!New deposition file to replace deposit.f03, momentumDeposit.f03, and trajectoryHelpers.f03.
!Additions will be needed to cover all the functionality of the old files. AKA Movie features
!The steps in the new process are listed below
!We've simplified the deposition process and hopefully it works correctly now.
!Now we find the initial position, and slowly increase the distance the atom travels.
!With each step we determine the four nearest lattice sites, and measure the distance between them and the vapor atom
!Need to account for even/odd rows when determining closest neighbors and distances.
subroutine hexDeposit()

use globalVariables
use indexConversion

 real, dimension(2) :: initialLocation, vaporCoords
 real, dimension(2) :: siteCoords
 real, dimension(2,2) :: currentLocations
 integer, dimension(2,11) :: movieCoordinates
 integer, dimension(4) :: latticeNodeTest
```

```
 real, dimension(4,2) :: nearestNodes
 real, dimension(4) :: distances
 real, parameter :: deltaDistance = 0.1
real :: deltaY, distance, thetaVapor, doubleX, evenModifier
integer :: i ,j, distanceCount

!open (unit = 18, file = ” trajectory . txt”, status = ’replace’ )



distance = 0
distanceCount = 0
deltaY = 0.8660254038
j = 1
evenMOdifier = 0
depositTime = 0.0

!Assign initial values
 initialLocation (1) = depositionFlux(atomCount,1)
 initialLocation (2) = (gridMaxHeight + 2)*deltaY
thetaVapor = REAL(depositionFlux(atomCount,2))

!Update the movieGrid
if (movieIndex <= movieIndexMax) then
  movieCoordinates = movieCoordinateFinder(boundaryConditionChecker(NINT(
      initialLocation(1))) &
  , NINT(initialLocation(2)))
  movieGrid(movieCoordinates(1,1), movieCoordinates(2,1), movieIndex) = 2
```

```
endif

!Start at the initial location and go until deposited
outer: do

  !Save the previous location
  if (j /= 1) then
    currentLocations(2,:) = currentLocations(1,:)
    !write(unit = 18, fmt = *), currentLocations(1,1),currentLocations(1,2)/deltaY, nearestNodes(1,:),&
    ! nearestNodes(2,:), nearestNodes(3,:),nearestNodes(4,:)
  endif

  !Find the current location
  currentLocations(1,1) = initialLocation(1) -SIN(thetaVapor * pi/180.0)*distance
  currentLocations(1,2) = initialLocation(2) -COS(thetaVapor * pi/180.0)*distance
  doubleX = currentLocations(1,1)*2.0

  !Keep the unwrapped coordinates to calculate distance
  nearestNodes(1,1) = FLOOR(doubleX)/2.0
  nearestNodes(2,1) = nearestNodes(1,1)
  nearestNodes(3,1) = CEILING(doubleX)/2.0
  nearestNodes(4,1) = nearestNodes(3,1)
  nearestNodes(1,2) = FLOOR(currentLocations(1,2)/deltaY)
  nearestNodes(2,2) = CEILING(currentLocations(1,2)/deltaY)
  nearestNodes(3,2) = CEILING(currentLocations(1,2)/deltaY)
  nearestNodes(4,2) = FLOOR(currentLocations(1,2)/deltaY)
```

```

!Check the location of the atom vs even/odd rows
!If we are above an even row, the lower atoms will be at half integers while the higher will be at full integers
if (MOD(NINT(nearestNodes(1,2)), 2) == 0) then

  if (MOD(nearestNodes(1,1),1.0) == 0) then
    latticeNodeTest(1) = 0
    latticeNodeTest(2) = 1
    latticeNodeTest(3) = 0
    latticeNodeTest(4) = 1
  elseif (MOD(nearestNodes(4,1),1.0) == 0) then
    latticeNodeTest(1) = 1
    latticeNodeTest(2) = 0
    latticeNodeTest(3) = 1
    latticeNodeTest(4) = 0
  else
    !print*, 'MOD error, checks arent working right 1', MOD(nearestNodes(1,1),1.0), MOD(nearestNodes(4,1),1.0),&
    !nearestNodes(1,1), nearestNodes(4,1),FLOOR(doubleX), CEILING(doubleX), currentLocations(1,1), distance
  endif
else
  if (MOD(nearestNodes(1,1),1.0) == 0) then
    latticeNodeTest(1) = 1
    latticeNodeTest(2) = 0
    latticeNodeTest(3) = 1
```

```
      latticeNodeTest(4) = 0
    elseif (MOD(nearestNodes(4,1),1.0) == 0) then
      latticeNodeTest(1) = 0
      latticeNodeTest(2) = 1
      latticeNodeTest(3) = 0
      latticeNodeTest(4) = 1
    else
      !print*, 'MOD error, checks arent working right 2', MOD(nearestNodes(1,1),1.0),
          MOD(nearestNodes(4,1),1.0),&
      !nearestNodes(1,1), nearestNodes(4,1), FLOOR(doubleX), CEILING(doubleX),
          currentLocations(1,1), distance
    endif
  endif

  distanceCount = 0


  !Find the distances from the real lattice sites
  !Need to account for the atom wrapping around the boundary multiple times! (it seems
      to be happening on the little grids).
  do i = 1,4


    if (MOD(NINT(nearestNodes(i,2)),2) == 0) then
      !Need to account for 0 indices
      !print *, NINT(nearestNodes(i,1)-.5), multiBCC(NINT(nearestNodes(i,1)-.5))
      if (grid(multiBCC(NINT(nearestNodes(i,1)-.5)),NINT(nearestNodes(i,2)))%
          occupationNumber == 1 &
      .and. latticeNodeTest(i) ==1) then
```

```
        distances(i) = SQRT((currentLocations(1,1) - nearestNodes(i,1))**2 + (
            currentLocations(1,2) - nearestNodes(i,2)*deltaY)**2)
        distanceCount = distanceCount + 1
        !print *, 'distance 1', distances(i), i
        evenModifier = 0.5
      else
        distances(i) = 10
      endif
    else
      if(grid(multiBCC(NINT(nearestNodes(i,1))),NINT(nearestNodes(i,2)))%
          occupationNumber == 1 .and. latticeNodeTest(i) ==1) then
        distances(i) = SQRT((currentLocations(1,1) - nearestNodes(i,1))**2 + (
            currentLocations(1,2) - nearestNodes(i,2)*deltaY)**2)
        distanceCount = distanceCount + 1
        !print *, 'distance 2', distances(i), i
      else
        distances(i) = 10
      endif
    endif

    if(distanceCount > 1) then
      !print *, 'We have multiple qualifying deposition sites, should check out further'
    endif

    if(distances(i) < 1.0) then

      vaporCoords(1) = currentLocations(1,1)
```

```
      vaporCoords(2) = currentLocations(1,2)/deltaY
      siteCoords(1) =  nearestNodes(i,1)
      siteCoords(2) = nearestNodes(i,2)


      !print *, distances
      !print *, vaporCoords, siteCoords
      !print *, multiBCC(CEILING(nearestNodes(i,1))), &
      !NINT(nearestNodes(i,2))
      call stickSiteFinder(vaporCoords, siteCoords)
      exit outer
    endif
  enddo


  distance = distance + deltaDistance
  !print *, 'Not close enough, distance = ', distance
  j = j+1
enddo outer


end subroutine hexDeposit



!
    ----------------------------------------------------------------------------------------------------------------


!Moves atoms around surface until next atom is deposited
!Builds a binary tree of all possible moves and then selects them
!Need subroutines to build tree, choose the jump, and perform it
```

```
!The binary tree will be empty at first and only fill up once the atoms begin depositing
!We don't need to put in everynew deposited atom or spot, just remember the rules
!
!11/14 Update: Changed the if statements for jumpTree values (> 0.0 instead of >0.001)
!Make sure jumpEnergies are initialized properly, we need to do this somewhere...
!12/3: I don't think making jumpEnergies pointers will change this file at all. We only
! reference the values, not change or reassign them.
! Variables used:
!randomNum, jumpEnergySum, i, j, firstLeafIndex, jumpTree, depositTime, depositTimeInterval
!Modules & subroutines
! globalVariables, random_number, jumpTreeInitialize, jumpUpdate
subroutine diffuse()

  use globalVariables
  use indexConversion
  use coordinationHelpers
  use ifport
  real :: randomNum, jumpEnergySum
  integer :: j, i
   integer, dimension(1,2) ::coord

! print *, 'Starting diffuse'

  !Before every diffuse step, reset the depositTime to the value between jumps
  depositTime = depositTimeInterval
```

```
  !print *, 'depositTime', depositTime
  j = 0
  i = 0

  !Go down the jumpTree randomly until you reach a leaf node
  do
    i =0
!   print *, 'Starting loop'
    do
      if (i >= firstLeafIndex) then
        !print *, 'I found a leaf', i
        !print * ,'Leaf error', i
        exit
      else
        !May need to reseed the random_number routine as in vaporInitialize
        !Scale the random number to the sum of the two leaf nodes
        !print *, 'in the thick of it', i
        randomNum = rand()

        !Check if both children have values, if not select the valued one
        if(jumpTree(2*i+1) > 0.0 .and. jumpTree(2*i+2) > 0.0) then
          !Lower energy values should be select perferentially
          randomNum = (jumpTree(2*i+1) + jumpTree(2*i+2)) * randomNum
          !!print *, 'Two children'
          !!print *, 'left' ,jumpTree(2*i+1), 'right', jumpTree(2*i+2)
          !Check if smaller than left child, select if so
          if (randomNum < jumpTree(2*i + 1)) then
```

```
    i = 2*i + 1
  !!print *, 'leftist'
  !Pick the right side
  else
    i = 2*i + 2
    !!print *, 'rightest'
  endif
elseif (jumpTree(2*i+1) == 0.0 .and. jumpTree(2*i + 2) /= 0.0) then
  !!print *, 'One child'
  i = 2*i + 2
elseif (jumpTree(2*i+2) == 0.0 .and. jumpTree(2*i + 1) /= 0.0) then
  !!print *, 'One child'
  i = 2*i + 1
else
!This is happening on the initial deposition. Do we want to wait a certain number
!of depositions before beginning diffusion?, or make template ones elgible?
  !print *, 'Tree selector error, ended up with two zeros (crikey!)', jumpTree(i)
  ! firstLeafIndex, i, jumpTree(i), jumpToGrid(2*i+1), movieIndex
  coord = jumpToGrid(2*i+1)
  !!print*, coordinationCalculation(coord(1,1),coord(1,2))
  ! If we get caught in this loop, it'll be good just to give up and reset the index
  i = 0
endif
```

```
      endif
    enddo
 ! print *, 'Naviagted jumpTree'

    !Pick the specific jump from the leaf node
    if (i < firstLeafIndex) then
      print *, 'Error, incorrect leaf index'
    else
      !Start j at 1, and have 6 elements per site
      !Uses the formula 6*x-5 to relate leaf to energy index
      j = jumpToEnergy(i)
    ! print *, 'jumpEnergies', jumpEnergies(j:j+5), probabilities (jumpEnergies(j:j+5))
      !Can jump to left
      if ( probabilities (jumpEnergies(j+2)) > 0.0) then
        ! Jump left and right
        if ( probabilities (jumpEnergies(j+3)) > 0.0) then

          jumpEnergySum = probabilities(jumpEnergies(j+2)) + probabilities(
              jumpEnergies(j+3))
          randomNum = rand()
          randomNum = jumpEnergySum * randomNum
          if (randomNum < probabilities(jumpEnergies(j + 2))) then
        !   !print *, 'jump', 2
            call jumpUpdate(i, j + 2)
          else
        !   !print *, 'jump', 3
            call jumpUpdate(i, j + 3)
```

```
  endif
!Jump left, Schwoebel up right
elseif ( probabilities (jumpEnergies(j+5)) > 0.0) then

  jumpEnergySum = probabilities(jumpEnergies(j+2)) + probabilities(
      jumpEnergies(j+5))
  randomNum = rand()
  randomNum = jumpEnergySum * randomNum
  if (randomNum < probabilities(jumpEnergies(j+2))) then
!    !print *, 'jump', 4
    call jumpUpdate(i, j + 2)
  else
!    !print *, 'jump', 5
    call jumpUpdate(i, j + 5)
  endif
!Jump left, Schwoebel down right
elseif ( probabilities (jumpEnergies(j+1)) > 0.0) then

  jumpEnergySum = probabilities(jumpEnergies(j+2)) + probabilities(
      jumpEnergies(j+1))
  randomNum = rand()
  randomNum = jumpEnergySum * randomNum
  if (randomNum < probabilities(jumpEnergies(j + 2))) then
    !!print *, 'jump', 2
    call jumpUpdate(i, j + 2)
  else
    !!print *, 'jump', 1
```

```
      call jumpUpdate(i, j + 1)
    endif
  !Jump left only
  else
    !!print *, ’jump’, 2
    call jumpUpdate(i, j + 2)
  endif
!Can jump right or Schwoebel left only
elseif ( probabilities (jumpEnergies(j+3)) > 0.0) then
  !Jump right, Schwoebel up left
  if ( probabilities (jumpEnergies(j+4)) > 0.0) then

    jumpEnergySum = probabilities(jumpEnergies(j+3)) + probabilities(
        jumpEnergies(j+4))
    randomNum = rand()
    randomNum = jumpEnergySum * randomNum
    if (randomNum < probabilities(jumpEnergies(j + 3))) then
      !!print *, ’jump’, 3
      call jumpUpdate(i, j + 3)
    else
      !!print *, ’jump’, 4
      call jumpUpdate(i, j + 4)
    endif
  !Jump right, Schwoebel down left
  elseif ( probabilities (jumpEnergies(j)) > 0.0) then
```

```
          jumpEnergySum = probabilities(jumpEnergies(j+3)) + probabilities(
              jumpEnergies(j))
          randomNum = rand()
          randomNum = jumpEnergySum * randomNum
          if (randomNum < probabilities(jumpEnergies(j+3))) then
            !!print *, 'jump', 3
            call jumpUpdate(i, j + 3)
          else
            !!print *, 'jump', 0
            call jumpUpdate(i, j)
          endif
        !Jump right only
        else
          !!print *, 'jump', 3
          call jumpUpdate(i, j+3)
        endif
      else
        !print *, 'Error: atom is immobile'
      endif
    endif

    !Advance deposit time, need to find the formula for deposit time
  ! print *, 'depositTime before', depositTime, jumpTree(0)
    depositTime = depositTime - 1/jumpTree(0)
  ! print *, 'depositTime after', depositTime

    !Check deposit time interval and exit if moved for long enough
```

```
    randomNum = rand()
    numberOfDiffusions = numberOfDiffusions +1


    !If the depositTime is greater that the residency time (1/jumpTree(0)), then continue
    !If it is less than, see if their ratio is greater than a random number
    !If neither are true, end the diffusion routine.
    !print *, 'depositTime', depositTime, depositTimeInterval, '1/jumpTree', 1/jumpTree(0)
    if (depositTime > 1/jumpTree(0)) then
    elseif (depositTime*jumpTree(0) >randomNum) then
      depositTime = 0
    else
      exit
    endif
  ! !print *, 'Made it through loop some'
  enddo
end subroutine diffuse



! ----------------------------------------------------------------------------------

!This routine will measure the approximate orientation of the surface normal along the tallest column's tip.
!The IAD will then be adjusted to make the newly measured surface normal, the distribution's 0 value.
```

```
!Need a subroutine to perform the column surface normal calculation .
!We need to account for both angle shifts left and right, as we can't predict which way the angles will bend after
!the first round of adjustments!
subroutine IADAdjust()
  use globalVariables
  use indexConversion

  real :: xMeasurementDistance, yLocation, occupancyRatioLeft, occupancyRatioRight
  integer :: i,k, siteCountLeft, siteOccupancyLeft, ySite, angleShift, siteCountRight, siteOccupancyRight, negativeOrNot
  integer,dimension(2) :: initialLocation

  siteCountLeft = 0
  siteOccupancyLeft = 0
  siteCountRight = 0
  siteOccupancyRight = 0
  angleShift = 0
  !Determine whether to add or subtract from the IAD
  negativeOrNot = 0

  initialLocation (1) = gridMaxXValue
  initialLocation (2) = gridMaxHeight

  !Go through all the angles until the column density condition is satisfied . Our angle should not be particularly
  !small, so we should be able to start just below 90.
```

```
!We can check to the left and right during the same loop, just add/subtract our values
    .
do i = 50, 180

  siteCountLeft = 0
  siteOccupancyLeft = 0
  siteCountRight = 0
  siteOccupancyRight = 0
  negativeOrNot = 0
  angleShift = 0

  xMeasurementDistance = SIN(i*pi/180.0) * typicalColumnWidth

  !Go through across the distance in x and determine if the closest site is occupied
      or not. I'm not sure if we
  ! really need to account fr the hexagonal nature of the grid in this calc.
  do k = 0, NINT(xMeasurementDistance)
    yLocation = initialLocation(2) - COS(i*pi/180.0) * k * 0.8660254038
    ySite = NINT(yLocation)

    !Check if the site is occupied
    if (grid(multiBCC(initialLocation(1) - k),ySite)%occupationNumber == 1) then
      siteOccupancyLeft = siteOccupancyLeft + 1
      print *, 'Full site found left'
    endif
    siteCountLeft = siteCountLeft + 1
```

```
        if (grid(multiBCC(k + initialLocation(1)), ySite)%occupationNumber == 1) then
          siteOccupancyRight = siteOccupancyRight + 1
          print *, 'Full site found right'
        endif
        siteCountRight = siteCountRight + 1

      enddo
      occupancyRatioLeft = REAL(siteOccupancyLeft)/siteCountLeft
      occupancyRatioRight = REAL(siteOccupancyRight)/siteCountRight

      ! If we went through the heart of a column, go ahead and shift the IAD by 90 - i!
      if (occupancyRatioLeft > columnDensity) then
        angleShift = 90 - i
        print *, 'IAD to be adjusted left by ', angleShift, occupancyRatioLeft
        negativeOrNot = -1
        exit
      elseif (occupancyRatioRight > columnDensity) then
        angleShift =  90 - i
        print *, 'IAD to be adjusted right by ', angleShift, occupancyRatioRight
        negativeOrNot = 1
        exit
      else
        print *, occupancyRatioLeft, occupancyRatioRight, columnDensity
      endif
    enddo

    if (angleShift == 0 ) then
```

```
    print *, 'Conditions not satisfied . IAD held constant'
  endif


  !Now lets shift our IAD and rerun vaporInitialize
  !This only works to shift the angle to the negative side currently (convex substrate
      surface )
  do i = -45, 44
    if (negativeOrNot < 0) then
      if (i -NINT(angleShift/2.0) >= -45) then
        modifiedIAD(i) = iAD(i - NINT(angleShift/2.0))
      else
        modifiedIAD(i) = 0
      endif
    elseif (negativeOrNot > 0) then
      if (i + NINT(angleShift/2.0) < 45) then
        modifiedIAD(i) = iAD(i + NINT(angleShift/2.0))
      else
        modifiedIAD(i) = 0
      endif
    else
      print *, 'Negative not assigned correctly . Fix it !'
    endif
  enddo


  deallocate(depositionFlux)
  call vaporInitialize
end subroutine IADAdjust
```

```
!
    ----------------------------------------------------------------------------------------------------
!Theron Rodgers 5/25/11
!Subroutine to output the deposited lattice . Outputs 1 for filled site and 0 for empty.

!Will print from bottom to top
!Will be useful to add code to calculate the porosity
!
! Variables
! i, grid (: , :) , substrateWidth, gridMaxHeight
!
!Modules & subroutines
! globalVariables
subroutine output()

  use globalVariables
  integer :: i, j,k, outputMax
  real :: density, occupiedCount, diffusionAverage
   real, dimension(1,2) :: positions
  character(1024) :: outputName, gridName
! print *, grid (: , :) %occupationNumber
  !We should change output to create files according to the current step number
  !Write the desired fileName to character variable
  write(outputName, "(A,I0,A)") "kmcOut", 45*(loopIndex−1), ".txt"
```

```
 print *, trim(outputName), outputName
 write(gridName,”(A,I0,A)”) ”grid”,45*(loopIndex−1), ”.csv”
 open (unit=12, file = trim(gridName), status = ’replace’)
 open (unit=14, file = trim(outputName), status = ’replace’)
 open (unit = 16, file = ”movie.csv”, status = ’replace’ )

 outputMax = substrateWidth * gridMaxHeight
 occupiedCount = 0
 diffusionAverage = numberOfDiffusions/atomsToDeposit
 print *, ’Average number of jumps’, diffusionAverage
! print *, grid(:,:)%occupationNumber

 !Go to each lattice site and write the coordinates and occupationNumber
 !It would probably be useful to output the real−valued coordinates, rather than
     integer site numbers
 do i = 1, substrateWidth
   do j = 1, gridMaxHeight
!    print *, grid( j,i )%occupationNumber
     if (mod(j,2) == 0) then
       k = i +1/2
     else
       k = i
     endif



     positions(1,1) = k*deltaXGrid
     positions(1,2) = j*deltaYGrid
```

```
      !Find the density
      if (j > numberOfInitialLayers) then

        if (grid(i,j)%occupationNumber == 1) then

          occupiedCount = occupiedCount + 1
        endif
      endif

      write(unit = 12, fmt = *), positions(1,1), ',', positions(1,2),',', grid(i,j)%
          occupationNumber

    enddo
  enddo

  density = occupiedCount / outputMax

  print *, 'The resulting density is', density, occupiedCount, outputMax
  close(12)
  call CPU_TIME(finish)

  print *, 'CPU time', finish-start, 'gridMaxHeight', gridMaxHeight

!This will be the easiest way to resume the script.
  do i = 1, gridMaxHeight
```

```
    write (unit = 14, fmt = *), grid(1:substrateWidth, gridMaxHeight − i + 1)%
        occupationNumber

  enddo
  close(14)
  !Output the movie file for the desired number of steps
  !This will output three columns of information, color, x, y
  if (movieIndexMax > 1) then
    do k = 1, movieIndex
      do i = 1, substrateWidth
        do j = 1, gridMaxHeight
            write(unit = 16, fmt = *), movieGrid(i,j,k), i,j
        enddo
      enddo
  !   write (unit = 16, fmt = *), −10, 1, 1
    enddo
  endif



  close(16)
end subroutine output



!
    ------------------------------------------------------------------
```

```
!Subroutine to determine the number of atoms around a lattice site
!Useful during deposition routines and diffusion
!Checks all boundary conditions, which were getting tedious to do in-line
!Returns the coordination, and if its value is 1, also the position of the atom
! Starting with 1 at the lower left corner and increasing clockwise around the atom with 6 total spots
!
!We need to change the function of this routine.
!Needs to associate coordination number with the lattice site.
!Needs to cite location of the neighbors
!
! Variables
! cooridnation, boundaryConditionModifier, evenIndex, oddIndex, xIndex, yIndex, evenness, substrateWidth
!grid(;,:)
!
!Modules & subroutines
! globalVariables
module coordinationHelpers
  use globalVariables
  use indexConversion
  public :: coordinationCalculation, singleNeighborFinder

  contains
  !coordinationCalculation is not side effect free currently. It should be soon however
```

```
function coordinationCalculation(xIndex, yIndex) result (coordination)


   integer, intent(in) :: xIndex, yIndex
  integer :: coordination, oddModifierLocal
  boundaryConditionModifier = 0
  !evenIndex & oddIndex are modifiers to eliminate if statements in the momentum deposit program
  !Don't we need to use these in the boundary condition situations as well? I think that's what boudnary condition oen is
  !Need to convert this to a more standard format
  coordination = 0

  !Determine the evenness of the lattice site
  if (mod(yIndex,2) > 0) then
    oddModifierLocal = 1
  else
    oddModifierLocal = 0
  endif

! !print *, 'xIndex', xIndex, 'yIndex', yIndex
  if (xIndex > substrateWidth .or. xIndex < 0) then
    !print *, 'Atom outside of simulation region!', xIndex
  endif

  !Calculate coordination number for bulk lattice sites
  coordination = grid(boundaryConditionChecker(xIndex −oddModifierLocal), yIndex −1)%occupationNumber + &
```

```
  grid(boundaryConditionChecker(xIndex−1),yIndex)%occupationNumber + &
  grid(boundaryConditionChecker(xIndex−oddModifierLocal),yIndex+1)%
      occupationNumber + &
  grid(boundaryConditionChecker(xIndex +1 −oddModifierLocal), yIndex+1)%
      occupationNumber + &
  grid(boundaryConditionChecker(xIndex +1), yIndex)%occupationNumber + &
  grid(boundaryConditionChecker(xIndex +1 −oddModifierLocal), yIndex −1)%
      occupationNumber

  end function coordinationCalculation


function singleNeighborFinder(xIndexLocal,yIndexLocal) result(
    singleNeighborLocation)
!Point to where the single atom is located around the lattice site, for all BC's

    integer, intent(in) :: xIndexLocal, yIndexLocal
    integer :: singleNeighborLocation, evenness
    !Determine the evenness of the lattice site
    if (mod(yIndexLocal,2) /= 0) then
      evenness = 0
    else
      evenness = 1
    endif

    if (grid(boundaryConditionChecker(xIndexLocal −1 + evenness), yIndexLocal −1)
        %occupationNumber ==1) then
      singleNeighborLocation = 1
```

```
      elseif (grid(boundaryConditionChecker(xIndexLocal - 1), yIndexLocal)%
         occupationNumber == 1) then

        singleNeighborLocation = 2
      elseif (grid(boundaryConditionChecker(xIndexLocal -1 +evenness), yIndexLocal
         + 1)%occupationNumber == 1) then

        singleNeighborLocation = 3
      elseif (grid(boundaryConditionChecker(xIndexLocal + evenness), yIndexLocal +
         1)%occupationNumber == 1) then

        singleNeighborLocation = 4
      elseif (grid(boundaryConditionChecker(xIndexLocal +1), yIndexLocal)%
         occupationNumber == 1) then

        singleNeighborLocation = 5
      elseif (grid(boundaryConditionChecker(xIndexLocal + evenness), yIndexLocal
         -1)%occupationNumber == 1) then

        singleNeighborLocation = 6
      else
        !print *, 'Neighbor locator error 1'
      endif
      !print *, 'singleNeighborLocation', singleNeighborLocation
    end function singleNeighborFinder

end module coordinationHelpers
```

```

!
  ------------------------------------------------------------------------------------------------

!Module to calcualte the leafIndex or gridIndex for a given lattice site
!Will allow for easy and independent conversion
!
! Variables
!xIndex, yIndex, leafIndex, substrateWidth
!
!Modules & subroutines
! globalVariables, gridToJump, jumpToGrid, jumpToEnergy (these are two contained in this file, which I like, but need tweaked
!
! Possible issues?
!There could be some conflicts immediately around the halfway point of the leaf nodes, although I doubt there will
!be enough data to cause a collision (that would require a nearly full tree)
! !! THIS NEEDS TO BE MODIFIED TO RETURN THE INDEX VALUE WITHIN THE ENTIRE BINARY TREE
module indexConversion
  use globalVariables
  public :: gridToJump, jumpToGrid, jumpToEnergy, boundaryConditionChecker, movieCoordinateFinder, boundaryFloat, multiBCC
```

```fortran
contains
!Need indices and substrateWidth to calculate
function gridToJump(xIndexLocal, yIndexLocal) result(leafIndexLocal)

  integer, intent(in) :: xIndexLocal, yIndexLocal
  integer :: leafIndexLocal,leafIndexLocal1

  ! Let's not worry about keeping the tree balanced, and keep conversions simple, later we could tweak
  !We should return the actual position in the tree, not the position in the leaves
  leafIndexLocal1 = (xIndexLocal + (yIndexLocal -1) * substrateWidth) + firstLeafIndex -1
  leafIndexLocal = (boundaryConditionChecker(xIndexLocal) + (yIndexLocal -1) * substrateWidth) + firstLeafIndex -1
end function gridToJump

!Need one index and substrateWidth to calculate
!Returns a row vector of x and y indices
function jumpToGrid(leafIndexLocal) result(indexesLocal)

  integer, intent(in) :: leafIndexLocal
  integer, dimension(1,2) :: indexesLocal

  !Ignore the even and oddness
  indexesLocal(1,2) = CEILING((leafIndexLocal-firstLeafIndex +1.0)/substrateWidth)
  indexesLocal(1,1) = CEILING((leafIndexLocal -firstLeafIndex +1.0) - (indexesLocal(1,2) -1)*substrateWidth)
```

```
   !!print *, 'leafIndex', leafIndexLocal, 'indexes',indexesLocal, 'jumpToGrid'
  end function jumpToGrid

  !Takes the leafNode index and returns the location in the energy array
  !Will need to select a specific jump from the array
  function jumpToEnergy(leafIndexLocal) result(energyIndexLocal)
    integer, intent(in) :: leafIndexLocal
    integer :: energyIndexLocal

    energyIndexLocal = (leafIndexLocal +1 - firstLeafIndex)*6 - 6
    !!print *, 'leafIndex', leafIndexLocal, 'energyIndex', energyIndexLocal,
        'firstLeafIndex', firstLeafIndex, 'jumpToEnergy'
  end function jumpToEnergy

  !Takes in an x-coordinate and checks for boundary conditions. If needed, loops it
      around
  function boundaryConditionChecker(xIndexLocal) result(newXIndex)
    integer, intent(in) :: xIndexLocal
    integer :: newXIndex




    if (xIndexLocal > substrateWidth) then
      newXIndex = xIndexLocal -substrateWidth
    elseif (xIndexLocal < 1) then
      newXIndex = xIndexLocal + substrateWidth
    else
```

```
      newXIndex = xIndexLocal
    endif
  end function boundaryConditionChecker


  !works like boundaryConditionChecker, but allows for multiple loops.  Good during
      deposition
  function multiBCC(xIndexLocal) result(newXIndex)
    integer, intent(in) :: xIndexLocal
    integer :: newXIndex, wrapDivisor
    real :: wrapCount

    wrapCount = xIndexLocal/(real(substrateWidth)+0.01)
    if(wrapCount > 1.0) then
      wrapDivisor = FLOOR(wrapCount)
      !print *, 'Wrapped around!', wrapDivisor
    elseif(wrapCount < 0.0) then
      wrapDivisor = FLOOR(wrapCount)
      !print *, wrapDivisor
    else
      wrapDivisor = 0
    endif




    newXIndex =xIndexLocal - wrapDivisor*substrateWidth
    !print *, 'newXIndex', newXIndex, 'xIndexLocal', xIndexLocal
```

```
  if (xIndexLocal == 0) then
    newXIndex = substrateWidth
  endif
end function multiBCC

!Takes in a floating point value and determines whether we need to wrap around. We'll draw the wrap line at
! integer substrate width plus .75 to ensure a continuous grid upon wrapping
function boundaryFloat(xLocation) result(xLocationNew)
  real, intent(in) :: xLocation
  real :: xLocationNew

  !I'm not sure if the substrate width is always the proper quantity to add or subtract .

  if (xLocation > substrateWidth + .75) then
    xLocationNew = xLocation - substrateWidth
  elseif (xLocation < .75) then
    xLocationNew = xLocation + substrateWidth
  else
    xLocationNew = xLocation
  endif

end function boundaryFloat

!Returns the called index and its neighbor atoms for easy use in the movie recording scheme
```

```
 !Could easily be adapted to be of more general use
 function movieCoordinateFinder(xIndexLocal, yIndexLocal) result(movieCoordinates)
   integer, intent(in) :: xIndexLocal, yIndexLocal
   integer, dimension(2, 11) :: movieCoordinates
   integer :: oddModifier

   if (mod(yIndexLocal,2) > 0) then
     oddModifier = 1
   else
     oddModifier = 0
   endif
!  !print*, 'xIndex', xIndexLocal, 'yIndex', yIndexLocal

   movieCoordinates(:,1) = (/boundaryConditionChecker(xIndexLocal), yIndexLocal/)
   movieCoordinates(:,2) = (/boundaryConditionChecker(xIndexLocal −oddModifier),
        yIndexLocal −1/)
   movieCoordinates(:,3) = (/boundaryConditionChecker(xIndexLocal −oddModifier),
        yIndexLocal +1/)
   movieCoordinates(:,4) = (/boundaryConditionChecker(xIndexLocal +1 −
        oddModifier), yIndexLocal −1/)
   movieCoordinates(:,5) = (/boundaryConditionChecker(xIndexLocal +1 −
        oddModifier), yIndexLocal +1/)
   movieCoordinates(:,6) = (/boundaryConditionChecker(xIndexLocal −1 −
        oddModifier), yIndexLocal −1/)
   movieCoordinates(:,7) = (/boundaryConditionChecker(xIndexLocal +2 −
        oddModifier), yIndexLocal −1/)
```

```
    movieCoordinates(:,8) = (/boundaryConditionChecker(xIndexLocal −1 − oddModifier), yIndexLocal +1/)
    movieCoordinates(:,9) = (/boundaryConditionChecker(xIndexLocal +2 − oddModifier), yIndexLocal +1/)
    movieCoordinates(:,10)= (/boundaryConditionChecker(xIndexLocal −1), yIndexLocal/)
    movieCoordinates(:,11)= (/boundaryConditionChecker(xIndexLocal +1), yIndexLocal/)
!    !print *, movieCoordinates, 'IndexConversion'
  end function movieCoordinateFinder


end module indexConversion



!
    −−−−−−−−−−−−−−−−−−−−−−−−−−−−−−−−−−−−−−−−−−−−−−−−−−−−−−−−−−−−−−−−−−−−−−−−−−−−−−−−−

!Subroutine to call when an atom is moved via diffusion, needs to perform several tasks:
!Update the occupation numbers of the lattice sites
!This program runs after a jump has been selected.  It should update both the jumpTree, and the grid
!Update the coordination of the surrounding lattice sites (of both old and new)
!Update the jump tree (leaf nodes and all above)
!We should convert our siteJumpInfo index in this routine, not in it.
!Advance the diffusion time
!
! Variables used:
```

```
! latticeIndex, indexRemainder, i, treeIntersection, leafIndex, grid(:,:), indexes(1,1),
    indexes(1,2), jumpToGrid(:), treeIndexOld
!treeIndexNew, depositTime, timeInterval

subroutine jumpUpdate(leafIndex, energyIndex)

  use globalVariables
  use coordinationHelpers
  use indexConversion

  integer :: indexRemainder, i, j
  integer, intent(in) :: energyIndex,leafIndex
! real, intent(in out) :: depositTime
  real :: jumpEnergySum
  integer, dimension(1,2) :: indexes
  integer, dimension(2,11) :: movieCoordinatesOld, movieCoordinatesNew
  integer :: oddModifier, oddModifierOld, xTemp, yTemp, energyIndexLoop,
      leafIndexLoop

  jumpEnergySum = 0.0

  !Find what type of jump we're performing, this doesn't seem right.
  indexRemainder = energyIndex - jumpToEnergy(leafIndex)
  !Update the occupation numbers, the lattice index will be the ceiling of the leafIndex
       divided by six

  !Update the vacated lattice site
```

```
!Set the previous locations occupation to zero
indexes = jumpToGrid(leafIndex)
grid(indexes(1,1),indexes(1,2))%occupationNumber = 0
movieCoordinatesOld = movieCoordinateFinder(indexes(1,1),indexes(1,2))
!Set the jumpEnergy of the vacated site to zero
!print *, 'Vacated Energy', jumpTree(leafIndex), leafIndex
jumpTree(leafIndex)= 0.0
!jumpEnergies(jumpToEnergy(leafIndex):jumpToEnergy(leafIndex)+5) = 0.0

!Determine the evenness of the lattice site
!oddModifier = 1 is odd row
if (mod(indexes(1,2),2) > 0) then
  oddModifierOld = 1
else
  oddModifierOld = 0
endif



!Calculate the lattice indices of the new point and occupy it!
!Need to call siteJumpInfo for all affected sites, don't call coordination, as that's done in siteJump
!Need to account for Schowebel jumps
!i = (indexes(1,1) -1, indexes(1,2) -1) i + 1 = (indexes(1,1), indexes(1,2) -1), etc
select case(indexRemainder)

!This is a Schowebel jump left, needs to skip more
case(0)
```

```
! print ∗, ’Jump 1’
  !Find the site jumped into and occupy it
  !xTemp and yTemp are the filled site, while indexes are the vacated site
  xTemp = boundaryConditionChecker(indexes(1,1) −1 −oddModifierOld)
  yTemp = indexes(1,2) −1
  grid(xTemp, yTemp)%occupationNumber = 1
  movieCoordinatesNew = movieCoordinateFinder(xTemp,yTemp)
  !print ∗, ’Jumped from’, leafIndex, ’to’,gridToJump(xTemp,yTemp)

  if (mod(yTemp,2) >0) then
    oddModifier = 1
  else
    oddModifier = 0
  endif

!Schowebel jump right down
case(1)
! print ∗, ’Jump 2’
  xTemp = boundaryConditionChecker(indexes(1,1) +2 −oddModifierOld)
  yTemp = indexes(1,2) −1
  movieCoordinatesNew = movieCoordinateFinder(xTemp,yTemp)
  grid(xTemp, yTemp)%occupationNumber = 1
  !print ∗, ’Jumped from’, leafIndex, ’to’,gridToJump(xTemp,yTemp)
  if (mod(yTemp,2) >0) then
    oddModifier = 1
  else
    oddModifier = 0
```

```
  endif

!Jump to the left
case(2)
  !print *, 'Jump 3'
  xTemp = boundaryConditionChecker(indexes(1,1) -1)
  yTemp = indexes(1,2)
  if (grid(xTemp,yTemp)%occupationNumber ==1) then
    !print *, 'The left site was occupied and I ruined it', jumpEnergies(energyIndex), indexRemainder, energyIndex,&
    !movieIndex
  endif
  if (coordinationCalculation(xTemp,yTemp) == 1) then
    !print*, 'Jumped over the edge! here be the problem', energyIndex, xTemp, yTemp
  endif
  grid(xTemp, yTemp)%occupationNumber = 1
  movieCoordinatesNew = movieCoordinateFinder(xTemp,yTemp)
  !print *, 'Jumped from', leafIndex, 'to',gridToJump (xTemp,yTemp)
  if (mod(yTemp,2) >0) then
    oddModifier = 1
  else
    oddModifier = 0
  endif

!jump to the right
case(3)
! print *, 'Jump 4'
```

```
  xTemp = boundaryConditionChecker(indexes(1,1) +1)
  yTemp= indexes(1,2)
  if (grid(xTemp,yTemp)%occupationNumber ==1) then
    !print *, 'The right site was occupied and I ruined it', jumpEnergies(energyIndex), indexRemainder, energyIndex,&
    !movieIndex
  endif
  if (coordinationCalculation(xTemp,yTemp) == 1) then
    !print*, 'Jumped over the edge! here be the problem', energyIndex, xTemp, yTemp
  endif
  grid(xTemp, yTemp)%occupationNumber = 1
  movieCoordinatesNew = movieCoordinateFinder(xTemp,yTemp)
  !print *, 'Jumped from', leafIndex, 'to',gridToJump (xTemp,yTemp)
  if (mod(yTemp,2) >0) then
    oddModifier = 1
  else
    oddModifier = 0
  endif


!Schowebel jump left up
case(4)
! print *, 'Jump 5'
  xTemp = boundaryConditionChecker(indexes(1,1) −1 −oddModifierOld)
  yTemp = indexes(1,2) +1
  grid(xTemp, yTemp)%occupationNumber = 1
  movieCoordinatesNew = movieCoordinateFinder(xTemp,yTemp)
```

```
      !print *, 'Jumped from', leafIndex, 'to',gridToJump(xTemp,yTemp)
      if (mod(yTemp,2) >0) then
        oddModifier = 1
      else
        oddModifier = 0
      endif

    !Schwoebel jump right up
    case(5)
    ! print *, 'Jump 0'
      xTemp = boundaryConditionChecker(indexes(1,1) +2 -oddModifierOld)
      yTemp = indexes(1,2) +1
      grid(xTemp, yTemp)%occupationNumber = 1
      movieCoordinatesNew = movieCoordinateFinder(xTemp,yTemp)
      !print *, 'Jumped from', leafIndex, 'to',gridToJump(xTemp,yTemp)
      if (mod(yTemp,2) >0) then
        oddModifier = 1
      else
        oddModifier = 0
      endif

    end select
  ! print *, 'Jumped from ', indexes
  ! print *, 'Jumped to ', xTemp, yTemp, coordinationCalculation(xTemp,yTemp)
    !Update the movie grid around the new site, most of the updating is done in the next
        timestep,
    !as that's when we'll want to display the neighbor sites
```

```
! print *, ’Working with movie’
  if (movieIndex < movieIndexMax) then
    movieIndex = movieIndex + 1
    movieGrid(movieCoordinatesNew(1,1),movieCoordinatesNew(2,1), movieIndex) = 2
    movieGrid(movieCoordinatesNew(1,1),movieCoordinatesNew(2,1), movieIndex+1:
        movieIndexMax) = 1

!   print *, ’Further’
    movieGrid(movieCoordinatesOld(1,1),movieCoordinatesOld(2,1), movieIndex) = 6
    movieGrid(movieCoordinatesOld(1,1),movieCoordinatesOld(2,1), movieIndex+1:
        movieIndexMax) = 0
  endif


  !New method to call siteJumpInfo on only nearby atom sites .  Doesn’t need to be too
      percise
  do i = −4, 4
    do j = −4,4
      if (indexes(1,2) + j > numberOfInitialLayers .and. indexes(1,2) + j <
          filmHeightMax) then
        if (mod(indexes(1,2) +j,2)>0) then
          oddModifier = 1
        else
          oddModifier = 0
        endif
        leafIndexLoop = gridToJump(boundaryConditionChecker(indexes(1,1) + i),
            indexes(1,2) +j)
```

```
          energyIndexLoop =jumpToEnergy(leafIndexLoop)
          call  siteJumpInfo(leafIndexLoop, energyIndexLoop, oddModifier)
        ! print *, 'updating  sites',  indexes,  i,  j
        endif
      enddo
    enddo



end subroutine jumpUpdate





!
    ----------------------------------------------------------------------------------

!Calculates  possible  diffusion  paths, and their  energies,  for a given  lattice  site
!Accepts one  lattice  site  and its  corresponding  index,  then  returns  the  values
    associated  with  it
!Need to  work on Schoewbel  barrier,  and also  how to handle the  energies  returned
!
! Variables  used
!jumpEnergies,  leafN,  evenness,  indexes,  grid(:,:),  n,
!modules and subroutines
! globalVariables,   coordinationCalculation
subroutine siteJumpInfo(leafIndex,energyIndex, oddModifier)
```

```
  use globalVariables
  use indexConversion
  use coordinationHelpers
  !Create a matrix with the possible jump energies the two incides will tell you what direction the jump is in
  !The value at each index will be the energy associated with the jumps, which will tell us the coordination at the new site
  ! real, dimension(n+4) :: jumpEnergies
  !The allocation should go into the diffuse routine and be run only once.
!  allocate (jumpEnergies(6))
  !Find the coordination for a given point, will need to rewrite coordination program
!  integer, intent(in) :: indexes(1,1), indexes(1,2)


  !We should accept the jumpTree leaf position as input, as this is the data type we'll work with
  integer, intent(in) :: leafIndex, energyIndex, oddModifier
  ! real, dimension(1,6), intent(in, out) :: jumpEnergies
  integer, dimension(1,2) :: indexes
  integer :: leafIndexOld, i

  !jumpToGrid returns a 1x2 index of indexes(1,1) and indexes(1,2), need to aply it to them in array form
  indexes = jumpToGrid(leafIndex)

  !!print *, leafIndex, energyIndex, oddModifier, coordinationCalculation(indexes(1,1), indexes(1,2)), 'siteJump'

```

```
  !Check whether the position is occupied and zero out the energy tree for that location
  if (grid(boundaryConditionChecker(indexes(1,1)), indexes(1,2))%occupationNumber
      /= 1) then
    !!print *, 'siteJumpInfo was called on a vacant site, exiting!'
    jumpTree(leafIndex) = 0.0
    jumpEnergies(energyIndex:energyIndex+5) = 20
    leafIndexOld = leafIndex
    !Move one rung up the tree
    leafIndexOld = FLOOR((leafIndexOld -1)/2.0)
    !Update the binary tree
    do i = 2, leafN
      jumpTree(leafIndexOld) = jumpTree(2*leafIndexOld + 1) + jumpTree(2*
          leafIndexOld +2)
!     !print *, 'old index at', i, jumpTree(leafIndexOld)
      leafIndexOld = FLOOR((leafIndexOld -1)/2.0)
    enddo
  ! !print *, 'Zeroed out a vacant site', leafIndex
    return
  endif
  !!print *, 'but still going!', leafIndex
  !Check if the atom is in the stationary inital layer area, if so, leave the subroutine
  if (indexes(1,2) <= numberOfInitialLayers) then
    !!print *, 'This is in the initial layer region, Im going home', indexes(1,2)
    return
  endif


  jumpEnergies(energyIndex:energyIndex+5) = 20
```

```
  jumpTree(leafIndex) = 0.0


  !!print *, 'What is the case? ',coordinationCalculation (boundaryConditionChecker(indexes(1,1)), indexes(1,2))
  select case (coordinationCalculation(boundaryConditionChecker(indexes(1,1)), indexes(1,2)))

  !This case can happen during deposition as well, if we look at one of the positions above the deposition
  ! site after we've processed the deposition one
  case (1)
    !print *, 'Only 1 neighbor atom, atom deleted', grid(indexes(1,1),indexes(1,2))%occupationNumber,&
    !indexes(1,1),indexes(1,2)
  ! print *, grid(indexes(1,1) -1,indexes(1,2))%occupationNumber, grid(indexes(1,1)+1,indexes(1,2))%occupationNumber
  ! print *, grid(indexes(1,1)-1:indexes(1,1)+1, indexes(1,2)-1)%occupationNumber
  ! grid(indexes(1,1),indexes(1,2)%occupationNumber = 0
    return
  !Coordination of 2 has 5 possible moves 2->2, 2->3, 2->4, 2->5, 2->3S
  !Case 2 is really the only situation where multiple moves are possible. Atom can go left or right.
  !Otherwise, direction is limited by surrounding atoms.
  case (2)
!   !print *, 'Normal coordination', indexes(1,:)
    !Two on bottom
```

```
  if (grid(boundaryConditionChecker(indexes(1,1) − oddModifier), indexes(1,2) −1)%
      occupationNumber == 1&
  .and. grid(boundaryConditionChecker(indexes(1,1) + 1 − oddModifier),indexes(1,2)
      −1)%occupationNumber ==1) then
    !!print *, 'siteJump3−1'
    !!print * ,'Coordinationcalc',  coordinationCalculation (boundaryConditionChecker(
        indexes(1,1) − 1), indexes(1,2))
    if (coordinationCalculation(boundaryConditionChecker(indexes(1,1) − 1), indexes
        (1,2)) == 3) then
      !!print *, 'siteJump3−1−1', energyIndex +2
      jumpEnergies(energyIndex+2) = 5
    elseif (  coordinationCalculation(boundaryConditionChecker(indexes(1,1) − 1),
        indexes(1,2)) == 4) then
      !!print *, 'siteJump3−1−2'
      jumpEnergies(energyIndex+2) = 4
    elseif (  coordinationCalculation(boundaryConditionChecker(indexes(1,1) −1),
        indexes(1,2)) == 5) then
      !!print *, 'siteJump3−1−3'
      jumpEnergies(energyIndex+2) = 2
    !Schwoebel jumps, and prevent  regular  jumps
    elseif (  coordinationCalculation(boundaryConditionChecker(indexes(1,1) −1),
        indexes(1,2)) == 2) then
      !!print *, 'siteJump3−1−4'
      jumpEnergies(energyIndex) = 7
      jumpEnergies(energyIndex+2) = 20
    !Edge atom with no support
    else
```

```
      !print *, '2-1 Coordination diffusion  error, no data above' ,&
      !coordinationCalculation(boundaryConditionChecker(indexes(1,1) -1), indexes(1,2)), indexes(1,1)-1, indexes(1,2),&
      !movieIndex
    endif
    if(coordinationCalculation(boundaryConditionChecker(indexes(1,1) + 1), indexes(1,2)) == 3) then
      !!print *, 'siteJump3-1-5'
      jumpEnergies(energyIndex+3) = 5
    elseif(  coordinationCalculation(boundaryConditionChecker(indexes(1,1) + 1), indexes(1,2)) == 4) then
      !!print *, 'siteJump3-1-6'
      jumpEnergies(energyIndex+3) = 4
    elseif(  coordinationCalculation(boundaryConditionChecker(indexes(1,1) +1), indexes(1,2)) == 5) then
      !!print *, 'siteJump3-1-7'
      jumpEnergies(energyIndex+3) = 2
    elseif(  coordinationCalculation(boundaryConditionChecker(indexes(1,1) +1), indexes(1,2)) == 2) then
      !!print *, 'siteJump3-1-8'
      jumpEnergies(energyIndex+1) = 7
    else
      !print *, '2-2 Coordination diffusion  error, no data above' ,&
      !coordinationCalculation(boundaryConditionChecker(indexes(1,1) +1), indexes(1,2)), indexes(1,1)+1, indexes(1,2)
    endif
  !Two on top
```

```
  elseif (grid(boundaryConditionChecker(indexes(1,1) −oddModifier), indexes(1,2)
      +1)%occupationNumber == 1 .and. &
  grid(boundaryConditionChecker(indexes(1,1) + 1 −oddModifier), indexes(1,2) + 1)%
      occupationNumber == 1) then
    !!print *, 'siteJump3−2'
    if (coordinationCalculation(boundaryConditionChecker(indexes(1,1) − 1), indexes
        (1,2)) == 3) then
      !!print *, 'siteJump3−1−9'
      jumpEnergies(energyIndex+2) = 5
    elseif ( coordinationCalculation(boundaryConditionChecker(indexes(1,1) − 1),
        indexes(1,2)) == 4) then
      !!print *, 'siteJump3−1−10'
      jumpEnergies(energyIndex+2) = 4
    elseif ( coordinationCalculation(boundaryConditionChecker(indexes(1,1) −1),
        indexes(1,2)) == 5) then
      !!print *, 'siteJump3−1−11'
      jumpEnergies(energyIndex+2) = 2
    elseif ( coordinationCalculation(boundaryConditionChecker(indexes(1,1) −1),
        indexes(1,2)) == 2) then
      !!print *, 'siteJump3−1−12'
      jumpEnergies(energyIndex+4) = 7
    else
      !print *, '2−3 Coordination diffusion error, no data below' , jumpEnergies(
          energyIndex:energyIndex+5)
    endif
    if (coordinationCalculation(boundaryConditionChecker(indexes(1,1) +1), indexes
        (1,2)) == 3) then
```

```
      !!print *, 'siteJump3−1−13'
      jumpEnergies(energyIndex+3) = 5
    elseif ( coordinationCalculation(boundaryConditionChecker(indexes(1,1) + 1),
        indexes(1,2)) == 4) then
      !!print *, 'siteJump3−1−14'
      jumpEnergies(energyIndex+3) = 4
    elseif ( coordinationCalculation(boundaryConditionChecker(indexes(1,1) +1),
        indexes(1,2)) == 5) then
      !!print *, 'siteJump3−1−15'
      jumpEnergies(energyIndex+3) = 2
    elseif ( coordinationCalculation(boundaryConditionChecker(indexes(1,1) +1),
        indexes(1,2)) == 2) then
      !!print *, 'siteJump3−1−16'
      jumpEnergies(energyIndex+5) = 7
    else
      !print *, '2−4 Coordination diffusion error, no data below' , jumpEnergies(
          energyIndex:energyIndex+5)
    endif
  !Two on left, only valued when the next location has coordination of 5
  elseif (grid(boundaryConditionChecker(indexes(1,1) −oddModifier), indexes(1,2)
      −1)%occupationNumber ==1 .and. &
  grid(boundaryConditionChecker(indexes(1,1)−oddModifier),indexes(1,2)+1)%
      occupationNumber ==1) then
    !!print *, 'siteJump3−3'
    if (coordinationCalculation(boundaryConditionChecker(indexes(1,1) −1), indexes
        (1,2)) == 6) then
      !!print *, '2−5−1'
```

```
      jumpEnergies(energyIndex+2) = 1
    else
      !print *, '2-5 coordination Jump error  left', jumpEnergies(energyIndex:
          energyIndex+5)
    endif
  !Two on Right, only valued when next location has coordination of 5
  elseif (grid(boundaryConditionChecker(indexes(1,1) + 1 -oddModifier), indexes(1,2
      ) -1)%occupationNumber == 1 .and. &
  grid(boundaryConditionChecker(indexes(1,1) + 1 -oddModifier), indexes(1,2) + 1)%
      occupationNumber ==1) then
    if (coordinationCalculation(boundaryConditionChecker(indexes(1,1) + 1), indexes
        (1,2)) == 6) then
      !!print *,'2-5-2'
      jumpEnergies(energyIndex+3) = 1
    else
      !print *, '2-5-1 coordination jump error  right', jumpEnergies(energyIndex:
          energyIndex+5)
    endif
  else
  ! !print*, '2-6 Coordination diffusion  error, configuration not in database',
      jumpEnergies(energyIndex:energyIndex+5),&
!   movieIndex, indexes(1,:) ,grid(boundaryConditionChecker(indexes(1,1) -oddModifier)
  , indexes(1,2) -1)%occupationNumber,&
!   grid(boundaryConditionChecker(indexes(1,1)-oddModifier),indexes(1,2)+1)%
  occupationNumber,&
!   grid(boundaryConditionChecker(indexes(1,1) + 1 -oddModifier), indexes(1,2) -1)%
  occupationNumber,&
```

```
!      grid(boundaryConditionChecker(indexes(1,1) + 1 -oddModifier), indexes(1,2)  + 1)%occupationNumber,&
!      grid(boundaryConditionChecker(indexes(1,1)-1), indexes(1,2))%occupationNumber, &
!      grid(boundaryConditionChecker(indexes(1,1)+1), indexes(1,2))%occupationNumber, &
!      coordinationCalculation(indexes(1,1),indexes(1,2))
      return
    endif

  !Coordination 3 has 5 possible moves 3->2, 3->3, 3->4, 3->5, 3->2S
  case (3)
    !!print *, 'siteJump4'
    !Two below, one next to and left
    if(grid(boundaryConditionChecker(indexes(1,1) - 1), indexes(1,2))%occupationNumber == 1 .and. &
    grid(boundaryConditionChecker(indexes(1,1) -oddModifier), indexes(1,2) -1)%occupationNumber == 1 .and. &
    grid(boundaryConditionChecker(indexes(1,1) + 1 -oddModifier), indexes(1,2) - 1)%occupationNumber ==1) then
      !!print*, 'siteJump4-1'
      if(coordinationCalculation(boundaryConditionChecker(indexes(1,1) + 1), indexes(1,2)) == 3) then
        jumpEnergies(energyIndex+3) = 12
      elseif(coordinationCalculation(boundaryConditionChecker(indexes(1,1) + 1), indexes(1,2)) == 4) then
        jumpEnergies(energyIndex+3) = 11
```

```
      elseif (coordinationCalculation(boundaryConditionChecker(indexes(1,1) + 1),
          indexes(1,2)) == 5) then
        jumpEnergies(energyIndex+3) = 9
      elseif (coordinationCalculation(boundaryConditionChecker(indexes(1,1) + 1),
          indexes(1,2)) == 6) then
        jumpEnergies(energyIndex+3) = 3
      endif
      !Schwoebel jumps, the indexing is a little off
      if (coordinationCalculation(boundaryConditionChecker(indexes(1,1) −1 −
          oddModifier), indexes(1,2) + 1) == 2 &
      .and. grid(boundaryConditionChecker(indexes(1,1) −1 −oddModifier), indexes(1,2
          ) + 1)%occupationNumber == 0) then
        jumpEnergies(energyIndex+4) = 15
      endif
    !Two below, one next to and right
    elseif (grid(boundaryConditionChecker(indexes(1,1) +1),indexes(1,2))%
        occupationNumber == 1 .and. &
    grid (boundaryConditionChecker(indexes(1,1) −oddModifier),indexes(1,2)−1)%
        occupationNumber ==1 .and. &
    grid(boundaryConditionChecker(indexes(1,1) +1 −oddModifier), indexes(1,2) −1)%
        occupationNumber ==1) then
      !!print*, 'siteJump4−2'
      if (coordinationCalculation(boundaryConditionChecker(indexes(1,1) − 1), indexes
          (1,2)) == 3) then
        jumpEnergies(energyIndex+2) = 12
      elseif (coordinationCalculation(boundaryConditionChecker(indexes(1,1) − 1),
          indexes(1,2)) == 4) then
```

```
        jumpEnergies(energyIndex+2) = 11
      elseif (coordinationCalculation(boundaryConditionChecker(indexes(1,1) - 1), indexes(1,2)) == 5) then
        jumpEnergies(energyIndex+2) = 9
      elseif (coordinationCalculation(boundaryConditionChecker(indexes(1,1) - 1), indexes(1,2)) == 6) then
        jumpEnergies(energyIndex+2) = 3
      endif
      !Schwoebel jumps, the indexing is a little off
      if (coordinationCalculation(boundaryConditionChecker(indexes(1,1) + 2 - oddModifier), indexes(1,2) + 1) == 2 &
      .and. grid(boundaryConditionChecker(indexes(1,1) + 2 - oddModifier), indexes(1,2) + 1)%occupationNumber == 0) then
        jumpEnergies(energyIndex+5) = 15
      endif
    !Two above, one next to and left
    elseif (grid(boundaryConditionChecker(indexes(1,1) - 1), indexes(1,2))%occupationNumber == 1 .and. &
    grid(boundaryConditionChecker(indexes(1,1) -oddModifier), indexes(1,2) +1)%occupationNumber == 1 .and. &
    grid(boundaryConditionChecker(indexes(1,1) + 1 -oddModifier), indexes(1,2) +1)%occupationNumber ==1) then
      !!print*, 'siteJump4-3'
      if (coordinationCalculation(boundaryConditionChecker(indexes(1,1) + 1), indexes(1,2)) == 3) then
        jumpEnergies(energyIndex+3) = 12
```

```
    elseif (coordinationCalculation(boundaryConditionChecker(indexes(1,1) + 1),
        indexes(1,2)) == 4) then
      jumpEnergies(energyIndex+3) = 11
    elseif (coordinationCalculation(boundaryConditionChecker(indexes(1,1) + 1),
        indexes(1,2)) == 5) then
      jumpEnergies(energyIndex+3) = 9
    elseif (coordinationCalculation(boundaryConditionChecker(indexes(1,1) + 1),
        indexes(1,2)) == 6) then
      jumpEnergies(energyIndex+3) = 3
    endif
    !Schwoebel jumps, the indexing is a little off
    if (coordinationCalculation(boundaryConditionChecker(indexes(1,1) -1 -
        oddModifier), indexes(1,2) - 1) == 2 &
    .and. grid(boundaryConditionChecker(indexes(1,1)-1 -oddModifier), indexes(1,2)
         -1)%occupationNumber == 0) then
      jumpEnergies(energyIndex) = 15
    endif
  !Two above, one next to and right
  elseif (grid(boundaryConditionChecker(indexes(1,1) +1),indexes(1,2))%
      occupationNumber == 1 .and. &
  grid(boundaryConditionChecker(indexes(1,1) -oddModifier), indexes(1,2)+1)%
      occupationNumber ==1 &
  .and. grid(boundaryConditionChecker(indexes(1,1) + 1 -oddModifier), indexes(1,2)
      +1)%occupationNumber ==1) then
    !!print*, 'siteJump4-4'
    if (coordinationCalculation(boundaryConditionChecker(indexes(1,1) - 1), indexes
        (1,2)) == 3) then
```

```
    jumpEnergies(energyIndex+2) = 12
  elseif (coordinationCalculation(boundaryConditionChecker(indexes(1,1) - 1),
      indexes(1,2)) == 4) then
    jumpEnergies(energyIndex+2) = 11
  elseif (coordinationCalculation(boundaryConditionChecker(indexes(1,1) - 1),
      indexes(1,2)) == 5) then
    jumpEnergies(energyIndex+2) = 9
  elseif (coordinationCalculation(boundaryConditionChecker(indexes(1,1) - 1),
      indexes(1,2)) == 6) then
    jumpEnergies(energyIndex+2) = 3
  endif
  !Schwoebel jumps, the indexing is a little off
  if (coordinationCalculation(boundaryConditionChecker(indexes(1,1) + 2 -
      oddModifier), indexes(1,2) - 1) == 2 &
  .and. grid(boundaryConditionChecker(indexes(1,1)+2 - oddModifier), indexes(1,2
      ) - 1)%occupationNumber == 0) then
    jumpEnergies(energyIndex+1) = 15
  endif
!Two below, one above and left
elseif (grid(boundaryConditionChecker(indexes(1,1) -oddModifier), indexes(1,2)
      -1)%occupationNumber == 1 .and. &
grid(boundaryConditionChecker(indexes(1,1) -oddModifier),indexes(1,2) + 1)%
    occupationNumber == 1 .and. &
grid(boundaryConditionChecker(indexes(1,1) + 1 - oddModifier), indexes(1,2) -1)%
    occupationNumber == 1) then
  !!print*, 'siteJump4-5'
```

```
  if (coordinationCalculation(boundaryConditionChecker(indexes(1,1) −1), indexes
      (1,2)) ==6) then
    jumpEnergies(energyIndex+2) = 3
  endif
!Two above, one below and left
elseif (grid(boundaryConditionChecker(indexes(1,1) −oddModifier), indexes(1,2)
    −1)%occupationNumber == 1 .and. &
grid(boundaryConditionChecker(indexes(1,1) −oddModifier),indexes(1,2) + 1)%
    occupationNumber == 1 &
.and. grid(boundaryConditionChecker(indexes(1,1) + 1 −oddModifier), indexes(1,2)
    +1)%occupationNumber == 1) then
  !!print*, 'siteJump4−6'
  if (coordinationCalculation(boundaryConditionChecker(indexes(1,1) −1), indexes
      (1,2)) ==6) then
    jumpEnergies(energyIndex+2) = 3
  endif
!Two below, one above and right
elseif (grid(boundaryConditionChecker(indexes(1,1) −oddModifier), indexes(1,2)
    −1)%occupationNumber == 1 .and. &
grid(boundaryConditionChecker(indexes(1,1) +1 −oddModifier),indexes(1,2) + 1)%
    occupationNumber == 1 &
.and. grid(boundaryConditionChecker(indexes(1,1) + 1 −oddModifier), indexes(1,2)
    −1)%occupationNumber == 1) then
  !!print*, 'siteJump4−7'
  if (coordinationCalculation(boundaryConditionChecker(indexes(1,1) +1), indexes
      (1,2)) ==6) then
    jumpEnergies(energyIndex+3) = 3
```

```
    endif
   !Two above, one above and right
   elseif (grid(boundaryConditionChecker(indexes(1,1) + 1 −oddModifier), indexes(1,2
       ) −1)%occupationNumber == 1 .and. &
   grid(boundaryConditionChecker(indexes(1,1) −oddModifier),indexes(1,2) + 1)%
       occupationNumber == 1 &
   .and. grid(boundaryConditionChecker(indexes(1,1) + 1 −oddModifier), indexes(1,2)
       +1)%occupationNumber == 1) then
    !!print*, 'siteJump4−8'
    if (coordinationCalculation(boundaryConditionChecker(indexes(1,1) +1), indexes
         (1,2)) ==6) then
       jumpEnergies(energyIndex+3) = 3
    endif
   else
    !!print *, '3 coordination diffusion error, configuration not in database'
   endif

 !Coordination of 4 has 4 possible moves 4−>2, 4−>3, 4−>4, 4−>5
 case (4)
   !!print *, 'siteJump5'
   !Two Below, one left, and above left
   if (grid(boundaryConditionChecker(indexes(1,1) − oddModifier), indexes(1,2) −1)%
       occupationNumber == 1 .and. &
   grid (boundaryConditionChecker(indexes(1,1) + 1 − oddModifier), indexes(1,2) −1)
       %occupationNumber == 1 &
   .and. grid(boundaryConditionChecker(indexes(1,1)− 1), indexes(1,2))%
       occupationNumber == 1 .and. &
```

```
grid(boundaryConditionChecker(indexes(1,1) - oddModifier), indexes(1,2) + 1)%
    occupationNumber == 1) then
  if (coordinationCalculation(boundaryConditionChecker(indexes(1,1) + 1),indexes
      (1,2)) == 3) then
    jumpEnergies(energyIndex+3) = 17
  elseif (coordinationCalculation(boundaryConditionChecker(indexes(1,1) + 1),
      indexes(1,2)) == 5) then
    jumpEnergies(energyIndex+3) = 10
  elseif (coordinationCalculation(boundaryConditionChecker(indexes(1,1) + 1),
      indexes(1,2)) == 4) then
    jumpEnergies(energyIndex+3) = 19
  endif
!Two below, one  right,  and above  right
elseif (grid(boundaryConditionChecker(indexes(1,1) - oddModifier), indexes(1,2)
    -1)%occupationNumber == 1 .and. &
grid(boundaryConditionChecker(indexes(1,1) + 1 -oddModifier), indexes(1,2) -1)%
    occupationNumber == 1 &
.and. grid(boundaryConditionChecker(indexes(1,1) +1), indexes(1,2))%
    occupationNumber == 1 .and. &
grid(boundaryConditionChecker(indexes(1,1) +1 -oddModifier), indexes(1,2) + 1)%
    occupationNumber == 1) then
  if (coordinationCalculation(boundaryConditionChecker(indexes(1,1) - 1),indexes
      (1,2)) == 3) then
    jumpEnergies(energyIndex+2) = 17
  elseif (coordinationCalculation(boundaryConditionChecker(indexes(1,1) - 1),
      indexes(1,2)) == 5) then
    jumpEnergies(energyIndex+2) = 10
```

```
    elseif (coordinationCalculation(boundaryConditionChecker(indexes(1,1) - 1),
        indexes(1,2)) == 4) then
      jumpEnergies(energyIndex+2) = 19
    endif
  !Two below, one  right,  and above  left
  elseif (grid(boundaryConditionChecker(indexes(1,1) - oddModifier), indexes(1,2)
      -1)%occupationNumber ==1 .and. &
  grid(boundaryConditionChecker(indexes(1,1) +1 -oddModifier), indexes(1,2) -1)%
      occupationNumber ==1 .and. &
  grid(boundaryConditionChecker(indexes(1,1) +1), indexes(1,2))%
      occupationNumber ==1 .and. &
  grid(boundaryConditionChecker(indexes(1,1) -oddModifier), indexes(1,2)+1)%
      occupationNumber ==1) then
    if (coordinationCalculation(boundaryConditionChecker(indexes(1,1) -1), indexes
        (1,2)) == 5) then
      jumpEnergies(energyIndex+2) = 6
    endif
  !Two below, one  left,  and above  right
  elseif (grid(boundaryConditionChecker(indexes(1,1) - oddModifier), indexes(1,2)
      -1)%occupationNumber ==1 .and. &
  grid(boundaryConditionChecker(indexes(1,1) +1 -oddModifier), indexes(1,2) -1)%
      occupationNumber ==1 .and. &
  grid(boundaryConditionChecker(indexes(1,1) -1), indexes(1,2))%occupationNumber
       ==1 .and. &
  grid(boundaryConditionChecker(indexes(1,1) +1 -oddModifier), indexes(1,2)+1)%
      occupationNumber ==1) then
```

```
    if (coordinationCalculation(boundaryConditionChecker(indexes(1,1) −1), indexes
        (1,2)) == 5) then
      jumpEnergies(energyIndex+3) = 6
    endif
  !Two above, one  left,  and below  left
  elseif (grid(boundaryConditionChecker(indexes(1,1) − oddModifier), indexes(1,2)
      +1)%occupationNumber == 1 .and. &
  grid  (boundaryConditionChecker(indexes(1,1) + 1 −oddModifier), indexes(1,2) +1)%
      occupationNumber == 1 &
  .and. grid(boundaryConditionChecker(indexes(1,1)−1), indexes(1,2))%
      occupationNumber == 1 .and. &
  grid(boundaryConditionChecker(indexes(1,1)−oddModifier), indexes(1,2) − 1)%
      occupationNumber == 1) then
    if (coordinationCalculation(boundaryConditionChecker(indexes(1,1) + 1),indexes
        (1,2)) == 3) then
      jumpEnergies(energyIndex+3) = 17
    elseif (coordinationCalculation(boundaryConditionChecker(indexes(1,1) + 1),
        indexes(1,2)) == 5) then
      jumpEnergies(energyIndex+3) = 10
    elseif (coordinationCalculation(boundaryConditionChecker(indexes(1,1) + 1),
        indexes(1,2)) == 4) then
      jumpEnergies(energyIndex+3) = 19
    endif
  !Two above, one  right  and below  right
  elseif (grid(boundaryConditionChecker(indexes(1,1) − oddModifier), indexes(1,2)
      +1)%occupationNumber == 1 .and. &
```

```
grid (boundaryConditionChecker(indexes(1,1) + 1 −oddModifier), indexes(1,2) +1)%
    occupationNumber == 1 &
.and. grid(boundaryConditionChecker(indexes(1,1)+1), indexes(1,2) )%
    occupationNumber == 1 .and. &
grid(boundaryConditionChecker(indexes(1,1) +1 −oddModifier), indexes(1,2) − 1)%
    occupationNumber == 1) then
  if (coordinationCalculation(boundaryConditionChecker(indexes(1,1) − 1),indexes
      (1,2)) == 3) then
    jumpEnergies(energyIndex+2) = 17
  elseif (coordinationCalculation(boundaryConditionChecker(indexes(1,1) − 1),
      indexes(1,2)) == 5) then
    jumpEnergies(energyIndex+2) = 10
  elseif (coordinationCalculation(boundaryConditionChecker(indexes(1,1) − 1),
      indexes(1,2)) == 4) then
    jumpEnergies(energyIndex+2) = 19
  endif
!Two below, one right, and above left
elseif (grid(boundaryConditionChecker(indexes(1,1) − oddModifier), indexes(1,2)
    +1)%occupationNumber ==1 .and. &
grid(boundaryConditionChecker(indexes(1,1) +1 −oddModifier), indexes(1,2) +1)%
    occupationNumber ==1 .and. &
grid(boundaryConditionChecker(indexes(1,1) +1), indexes(1,2))%
    occupationNumber ==1 .and. &
grid(boundaryConditionChecker(indexes(1,1) −oddModifier), indexes(1,2)−1)%
    occupationNumber ==1) then
  if (coordinationCalculation(boundaryConditionChecker(indexes(1,1) −1), indexes
      (1,2)) == 5) then
```

```
      jumpEnergies(energyIndex+2) = 6
    endif
  !Two below, one  left,   and above  right
  elseif (grid(boundaryConditionChecker(indexes(1,1) − oddModifier), indexes(1,2)
      +1)%occupationNumber ==1 .and. &
  grid(boundaryConditionChecker(indexes(1,1) +1 −oddModifier), indexes(1,2) +1)%
      occupationNumber ==1 .and. &
  grid(boundaryConditionChecker(indexes(1,1) −1), indexes(1,2))%occupationNumber
       ==1 .and. &
  grid(boundaryConditionChecker(indexes(1,1) +1 −oddModifier), indexes(1,2)−1)%
      occupationNumber ==1) then
    if (coordinationCalculation(boundaryConditionChecker(indexes(1,1) −1), indexes
        (1,2)) == 5) then
      jumpEnergies(energyIndex+3) = 6
    endif
  !Two below, one  left,   and one  right
  elseif (grid(boundaryConditionChecker(indexes(1,1) − oddModifier), indexes(1,2)
      −1)%occupationNumber ==1 .and. &
  grid(boundaryConditionChecker(indexes(1,1) +1 −oddModifier), indexes(1,2) −1)%
      occupationNumber ==1 .and. &
  grid(boundaryConditionChecker(indexes(1,1) −1), indexes(1,2))%occupationNumber
       ==1 .and. &
  grid(boundaryConditionChecker(indexes(1,1) +1), indexes(1,2))%
      occupationNumber ==1) then
      jumpEnergies(energyIndex:energyIndex+5) = 20
  !Two above, one  left,   and one  right
```

```
  elseif (grid(boundaryConditionChecker(indexes(1,1) − oddModifier), indexes(1,2)
      +1)%occupationNumber ==1 .and. &
  grid(boundaryConditionChecker(indexes(1,1) +1 −oddModifier), indexes(1,2) +1)%
      occupationNumber ==1 .and. &
  grid(boundaryConditionChecker(indexes(1,1) −1), indexes(1,2))%occupationNumber
      ==1 .and. &
  grid(boundaryConditionChecker(indexes(1,1) +1), indexes(1,2))%
      occupationNumber ==1) then
      jumpEnergies(energyIndex:energyIndex+5) = 20
  else
!   !print *, '4 coordination diffusion error, configuration not in database',
    jumpEnergies(energyindex:energyIndex+5)
  ! coordinationCalculation (boundaryConditionChecker(indexes(1,1)),indexes(1,2)),
      indexes(1,1),indexes(1,2), movieIndex
  endif

!Coordination of 5 has 5 possible moves 5−>2, 5−>3, 5−>4, 5−>5, 5−>5V
case (5)
  !!print *, 'siteJump6'
  !Two below and above, and one left
  if (grid(boundaryConditionChecker(indexes(1,1) −oddModifier), indexes(1,2) −1)%
      occupationNumber == 1 .and. &
  grid(boundaryConditionChecker(indexes(1,1) +1 −oddModifier), indexes(1,2) − 1)%
      occupationNumber == 1 &
  .and. grid(boundaryConditionChecker(indexes(1,1) −1), indexes(1,2))%
      occupationNumber == 1 .and. &
```

```
grid(boundaryConditionChecker(indexes(1,1)−oddModifier), indexes(1,2)+1)%
    occupationNumber == 1 &
.and. grid(boundaryConditionChecker(indexes(1,1) +1 −oddModifier), indexes(1,2)
    +1)%occupationNumber == 1) then
  if (coordinationCalculation(boundaryConditionChecker(indexes(1,1) + 1), indexes
      (1,2)) == 6) then
    !Check for bulk vacancy diffusion
    !I don't think even/oddness will modify this, as the layers are similar type
    if (grid(boundaryConditionChecker(indexes(1,1) + 1), indexes(1,2) + 2)%
        occupationNumber== 1 &
    .and. grid(boundaryConditionChecker(indexes(1,1) + 1), indexes(1,2)−2)%
        occupationNumber ==1) then
      jumpEnergies(energyIndex+3) =18
    else
      jumpEnergies(energyIndex+3) = 8
    endif
  elseif (coordinationCalculation(boundaryConditionChecker(indexes(1,1) + 1),
      indexes(1,2)) == 3) then
    jumpEnergies(energyIndex+3) = 14
  elseif (coordinationCalculation(boundaryConditionChecker(indexes(1,1) + 1),
      indexes(1,2)) == 4) then
    jumpEnergies(energyIndex+3) = 16
  elseif (coordinationCalculation(boundaryConditionChecker(indexes(1,1) + 1),
      indexes(1,2)) == 5) then
    jumpEnergies(energyIndex+3) = 13
  endif
!Two below and above, and one right
```

```
elseif (grid(boundaryConditionChecker(indexes(1,1) −oddModifier), indexes(1,2)
    −1)%occupationNumber == 1 .and. &
grid(boundaryConditionChecker(indexes(1,1) +1 −oddModifier), indexes(1,2) − 1)%
    occupationNumber == 1 &
.and. grid(boundaryConditionChecker(indexes(1,1) +1), indexes(1,2))%
    occupationNumber == 1 .and. &
grid(boundaryConditionChecker(indexes(1,1)−oddModifier), indexes(1,2)+1)%
    occupationNumber == 1 &
.and. grid(boundaryConditionChecker(indexes(1,1) +1 −oddModifier), indexes(1,2)
    +1)%occupationNumber == 1) then
  if (coordinationCalculation(boundaryConditionChecker(indexes(1,1) − 1), indexes
      (1,2)) == 6) then
    !Check for bulk vacancy diffusion
    !I don't think even/oddness will modify this, as the layers are similar type
    if (grid(boundaryConditionChecker(indexes(1,1) − 1), indexes(1,2) + 2)%
        occupationNumber== 1 &
    .and. grid(boundaryConditionChecker(indexes(1,1) − 1), indexes(1,2)−2)%
        occupationNumber ==1) then
      jumpEnergies(energyIndex+2) =18
    else
      jumpEnergies(energyIndex+2) = 8
    endif
  elseif (coordinationCalculation(boundaryConditionChecker(indexes(1,1) − 1),
      indexes(1,2)) == 3) then
    jumpEnergies(energyIndex+2) = 14
  elseif (coordinationCalculation(boundaryConditionChecker(indexes(1,1) − 1),
      indexes(1,2)) == 4) then
```

```
      jumpEnergies(energyIndex+2) = 16
    elseif (coordinationCalculation(boundaryConditionChecker(indexes(1,1) - 1),
        indexes(1,2)) == 5) then
      jumpEnergies(energyIndex+2) = 13
    endif
  else
    !!print *, '5 coordination diffusion error, configuration not in database',
        jumpEnergies(energyIndex:energyIndex+5)
  endif
!The atom is surrounded
case (6)
  !!print *, 'siteJump7'
  !!print *, 'Atom is immobile, this should not be selected'
  jumpEnergies(energyIndex:energyIndex+5) = 20
!This case could happen during deposition, depending on the order of reading the
    positions
case default
  !!print *, 'siteJump8'
  if (grid(indexes(1,1),indexes(1,2))%occupationNumber == 1) then
    !print *, 'Incorrect coordination number during diffusion', &
    !coordinationCalculation(boundaryConditionChecker(indexes(1,1)), indexes(1,2)) &
    !, indexes(1,:), leafIndex, oddModifier
  endif
  !Exit this iteration of the subroutine
  return
end select
```

```
 !Update the energy sum
 jumpTree(leafIndex) = 0.0
 do i = 0,5
   jumpTree(leafIndex) = jumpTree(leafIndex) + probabilities(jumpEnergies(
       energyIndex + i))
 enddo
 !!print *, 'New site energy', jumpTree(leafIndex)
 leafIndexOld = leafIndex
 !Move one rung up the tree
 leafIndexOld = FLOOR((leafIndexOld -1)/2.0)
 !Update the binary tree
 do i = 2, leafN
   jumpTree(leafIndexOld) = jumpTree(2*leafIndexOld + 1) + jumpTree(2*
       leafIndexOld +2)
 ! print *, jumpTree(leafIndexOld)
   leafIndexOld = FLOOR((leafIndexOld -1)/2.0)
 enddo

 ! if (jumpTree(leafIndex) > 1.0) then
   !!print *, 'Bad energies', jumpEnergies(energyIndex:energyIndex+5),
       coordinationCalculation(&
   !boundaryConditionChecker(indexes(1,1) - 1), indexes(1,2))
 !endif
 !!print *, 'siteJump10'
end subroutine siteJumpInfo
```

```
! ------------------------------------------------------------------------------------

!Determine the exact location to deposit the vapor atom.
!Need to account for situations where the atom would be deposited above or below the site with a coordination of 1
!This doesn't work, and we should deposit to whichever side has the higher coordination.
subroutine stickSiteFinder(vaporCoords, siteCoords)

  use globalVariables
  use indexConversion
  use coordinationHelpers

  real, dimension(2), intent(in) :: siteCoords
  real, dimension(2), intent(in) :: vaporCoords
  integer, dimension(2) :: intSiteCoords

  !Don't know if oddModifier will be an integer or real here.
  integer :: oddModifier, xDeposit, yDeposit
  real :: evenModifier

  !print *, 'starting stickSiteFinder', vaporCoords, siteCoords
  ! First check if the vapor atom is left or right of the site.
  !Need to add boundary compliance, which we do through multiBCC
  !NEED to account for even/odd rows, which we do through oddModifier
  if (mod(NINT(siteCoords(2)),2) > 0) then
```

```
    oddModifier = 1
    evenModifier = 0
  else
    oddModifier = 0
    evenModifier = .5
endif


intSiteCoords(1) = NINT(siteCoords(1) - evenModifier)
intSiteCoords(2) = NINT(siteCoords(2))
!print *, 'intSiteCoords', intSiteCoords


xDeposit = 0
yDeposit = 0


!Check if vapor atom is to left or right of the site's center
!Need to also account for the coordination of the same-row sites left & right of the
    siteCoords
!The sites a row above or below should always be valid locations, but the next one
    may not
!Need to account for when the site is on the edge with only 2 neighbor atoms, we
    should try
!to deposit above and left
if (vaporCoords(1)-siteCoords(1)<0) then
  !print *, 'vapor < siteCoords x'
  !Check if the atom is above or below the y-midpoint at clashtime
  if (vaporCoords(2) - siteCoords(2) > 0) then
    !print *, 'vapor > siteCoords y'
```

```
!Check if the site next too the deposition one is not occupied, and not on its
    own.
if (grid(multiBCC((intSiteCoords(1)−1)),intSiteCoords(2))&
%occupationNumber /= 1 .and. coordinationCalculation(multiBCC((&
intSiteCoords(1)−1)),intSiteCoords(2)) > 1) then
  xDeposit = multiBCC(intSiteCoords(1)−1)
  yDeposit = intSiteCoords(2)
  !print *, 'Deposit 1'
elseif (grid(multiBCC(intSiteCoords(1)−oddModifier),intSiteCoords(2)+1)&
%occupationNumber/= 1 .and. coordinationCalculation(multiBCC((intSiteCoords
    &
(1)−oddModifier)),intSiteCoords(2)+1) > 1) then
  !Deposit above lefts
  xDeposit = multiBCC((intSiteCoords(1)−oddModifier))
  yDeposit = intSiteCoords(2) +1
  !print *, 'Deposit 2'
elseif (grid(multiBCC(intSiteCoords(1) + 1 − oddModifier),intSiteCoords(2) + &
1)%occupationNumber /= 1 .and. coordinationCalculation(multiBCC(
    intSiteCoords(1) + 1 − oddModifier)&
,intSiteCoords(2) + 1) > 1) then
  !Deposit above right
  xDeposit = multiBCC((intSiteCoords(1) + 1 − oddModifier))
  yDeposit = intSiteCoords(2) + 1
  !print *, 'Deposit 2−1'
else
  print *, 'Error Deposit 2', grid(multiBCC((intSiteCoords(1)−oddModifier)&
  ),intSiteCoords(2)+1)%occupationNumber, coordinationCalculation&
```

```
        (multiBCC((intSiteCoords(1)-oddModifier)),intSiteCoords(2)+1)
        print *, multiBCC((intSiteCoords(1)-oddModifier))
        print *, intSiteCoords(2) + 1
        print *, coordinationCalculation(intSiteCoords(1), intSiteCoords(2))
        print *, grid(intSiteCoords(1), intSiteCoords(2))%occupationNumber
        print *, REAL(depositionFlux(atomCount,2))
      endif
    else
      !print *, 'vapor < siteCoords y'
      if (grid(multiBCC((intSiteCoords(1)-1)),&
      intSiteCoords(2))%occupationNumber /= 1 .and. coordinationCalculation(
          multiBCC&
      ((intSiteCoords(1)-1)),intSiteCoords(2)) > 1) then
        xDeposit = multiBCC((intSiteCoords(1)-1))
        yDeposit = intSiteCoords(2)
        !print *, 'Deposit 3'
      elseif (grid(multiBCC((intSiteCoords(1)-oddModifier)),intSiteCoords(2)-1)&
      %occupationNumber/= 1 .and. coordinationCalculation(multiBCC((intSiteCoords
          (1)-oddModifier)&
      ),intSiteCoords(2)-1) >1) then
        !Deposit below left
        xDeposit = multiBCC((intSiteCoords(1)-oddModifier))
        yDeposit = intSiteCoords(2)-1
        !print *, 'Deposit 4'
      elseif (grid(multiBCC(intSiteCoords(1)+1-oddModifier), intSiteCoords(2)-1)%
          occupationNumber&
```

```
    /= 1 .and. coordinationCalculation(multiBCC(intSiteCoords(1)+1-oddModifier)
        ,intSiteCoords(2)-1)>1) then
      !Deposit below right
      xDeposit = multiBCC((intSiteCoords(1) +1 -oddModifier))
      yDeposit = intSiteCoords(2) -1
      !print *, 'Deposit 4-1'
    else
      print *, 'Error Deposit 4', grid(multiBCC((intSiteCoords(1)-oddModifier))&
      ,intSiteCoords(2)-1)%occupationNumber, coordinationCalculation(multiBCC&
      ((intSiteCoords(1)-oddModifier)),intSiteCoords(2)-1)
      print *, multiBCC((intSiteCoords(1)-oddModifier))
      print *, intSiteCoords(2) - 1
      print *, grid(multiBCC(intSiteCoords(1)),intSiteCoords(2))%occupationNumber
      print *, coordinationCalculation(multiBCC(intSiteCoords(1)),intSiteCoords(2))
      print *, grid(multiBCC(intSiteCoords(1)-1),intSiteCoords(2))%
          occupationNumber
      print *, coordinationCalculation(multiBCC(intSiteCoords(1)-1),intSiteCoords
          (2))
      print *, REAL(depositionFlux(atomCount,2))
    endif
  endif
!Deposit atom to the right
else
  !print *, 'vapor > siteCoords x'
  !Check if the atom is above or below the y-midpoint at clashtime
  if (vaporCoords(2) - siteCoords(2) > 0) then
    !print *, 'vapor > siteCoords y'
```

```
!Check if the site next too the deposition one is occupied.  If it is, deposit
    above.
if (grid(multiBCC((intSiteCoords(1)+1))&
,intSiteCoords(2))%occupationNumber /= 1 .and. coordinationCalculation(
    multiBCC&
((intSiteCoords(1)+1)),intSiteCoords(2)) > 1) then

  xDeposit = multiBCC((intSiteCoords(1) +1))
  yDeposit = intSiteCoords(2)
! print *, 'Deposit 5'
elseif (grid(multiBCC(intSiteCoords(1) + 1 − oddModifier),intSiteCoords(2) + &
1)%occupationNumber /= 1 .and. coordinationCalculation(multiBCC(
    intSiteCoords(1) + 1 − oddModifier)&
,intSiteCoords(2) + 1) > 1) then
  !Deposit above right
  xDeposit = multiBCC((intSiteCoords(1) + 1 − oddModifier))
  yDeposit = intSiteCoords(2) + 1
! print *, 'Deposit 6'
elseif (grid(multiBCC(intSiteCoords(1)−oddModifier),intSiteCoords(2)+1)&
%occupationNumber/= 1 .and. coordinationCalculation(multiBCC((intSiteCoords
    &
(1)−oddModifier)),intSiteCoords(2)+1) > 1) then
  !Deposit above lefts
  xDeposit = multiBCC((intSiteCoords(1)−oddModifier))
  yDeposit = intSiteCoords(2) +1
! print *, 'Deposit 6−1'
else
```

```
        print *, 'Error Deposit 6', grid(multiBCC((intSiteCoords(1) + 1 − oddModifier)
            )&
        ,intSiteCoords(2)  + 1)%occupationNumber , coordinationCalculation(multiBCC
            &
        ((intSiteCoords(1) + 1  − oddModifier)),intSiteCoords(2) + 1)

        print *, multiBCC((intSiteCoords(1) + 1 − oddModifier))
        print *, intSiteCoords(2) + 1
        print *, grid(multiBCC(intSiteCoords(1) + 1), intSiteCoords(2))%
            occupationNumber
        print *, coordinationCalculation(multiBCC(intSiteCoords(1)+1),intSiteCoords
            (2))
        print *, REAL(depositionFlux(atomCount,2))
      endif
    else
      !print *, 'vapor < intSiteCoords y'
      if (grid(multiBCC((intSiteCoords(1)+1)),intSiteCoords(2))%occupationNumber
          /= 1&
      .and. coordinationCalculation(multiBCC((intSiteCoords(1)+1)),intSiteCoords(2)) >
           1) then
        xDeposit = multiBCC((intSiteCoords(1) +1))
        yDeposit = intSiteCoords(2)
    !   print *, 'Deposit 7'
      elseif (grid(multiBCC(intSiteCoords(1)+1−oddModifier), intSiteCoords(2)−1)%
          occupationNumber&
      /= 1  .and. coordinationCalculation(multiBCC(intSiteCoords(1)+1−oddModifier)
          ,intSiteCoords(2)−1)>1) then
```

```
        !Deposit below right
        xDeposit = multiBCC((intSiteCoords(1) +1 -oddModifier))
        yDeposit = intSiteCoords(2) -1
!       print *, 'Deposit 8'
      elseif (grid(multiBCC((intSiteCoords(1)-oddModifier)),intSiteCoords(2)-1)&
      %occupationNumber/= 1 .and. coordinationCalculation(multiBCC((intSiteCoords(1)-oddModifier)&
      ),intSiteCoords(2)-1) >1) then
        !Deposit below left
        xDeposit = multiBCC((intSiteCoords(1)-oddModifier))
        yDeposit = intSiteCoords(2)-1
!       print *, 'Deposit 8-1'
      else
        print *, 'Error Deposit 8'
        print *, multiBCC(intSiteCoords(1) +1), intSiteCoords(2)
      endif
    endif
  endif

  grid(xDeposit,yDeposit)%occupationNumber = 1
  call depositionUpdate(xDeposit,yDeposit)
! print *, 'Atom deposited at', xDeposit, yDeposit, coordinationCalculation(xDeposit,yDeposit)

  if (yDeposit > gridMaxHeight) then
    gridMaxHeight = yDeposit
    gridMaxXValue = xDeposit
```

```
    print *, 'new Max ', gridMaxHeight
  endif

end subroutine stickSiteFinder



!----------------------------------------------------------------------------------------
!Subroutine to update the jumpTree when an atom is deposited.  Need to zero the values out for covered atoms
!and calculate values for the newly deposited atom
!
!I don't think we need a matrix for the leafIndex variable, since we call siteJumpInfo everytime
!We need to account for boundary conditions in this subroutine
subroutine depositionUpdate(depositedXIndex, depositedYIndex)

  use indexConversion
  use globalVariables

  integer :: oddModifier, xIndexLocal, i
   integer, intent(in) :: depositedXIndex, depositedYIndex
   integer, dimension(11) :: leafIndex, leafEnergyIndex
   integer, dimension(2, 11) :: movieCoordinates
! integer, dimension(6,6) :: treeIntersection = 0 sdf
```

```
 !Determine the evenness of the lattice site
 if (mod(depositedYIndex,2) > 0) then
   oddModifier = 1
 else
   oddModifier = 0
 endif

 xIndexLocal = boundaryConditionChecker(depositedXIndex)

 !Advance the movie index
 if (movieIndex < movieIndexMax) then
   movieIndex = movieIndex +1
   !Update the movie grid
   movieCoordinates = movieCoordinateFinder(xIndexLocal, depositedYIndex)
!  print *, movieCoordinates, 'DepositionUpdate'
!  print*, 'xIndex', xIndexLocal, 'yIndex', depositedYIndex
   movieGrid(movieCoordinates(1,1),movieCoordinates(2,1), movieIndex) = 2
   movieGrid(movieCoordinates(1,2:5),movieCoordinates(2,2:5), movieIndex) = 5
   movieGrid(movieCoordinates(1,6:9),movieCoordinates(2,6:9), movieIndex) = 4
   movieGrid(movieCoordinates(1,10:11),movieCoordinates(2,10:11), movieIndex) = 5
 endif

 !update jump energies.
 !Set energies to zero if atom is now totally surrounded
 !Although the atom cannot move to the two spots below/above it, it can influence its
     jump ability
```

```
 !by changing its coordination number
 !We don't need to call the coordinationCalculation or anything, we can just do siteJumpInfo for all cases

 !Udpdate the deposited location
 leafIndex(11) = gridToJump(xIndexLocal, depositedYIndex)
 leafEnergyIndex(11) = jumpToEnergy(leafIndex(11))




 do i = 0, 1
   !Check the above and below sites, will modify their coordination and jump values
!  print *, 'oddModifier', oddModifier
   leafIndex(i+1) = gridToJump(boundaryConditionChecker(xIndexLocal +i −oddModifier), depositedYIndex −1)
   leafEnergyIndex(i+1) = jumpToEnergy(leafIndex(i+1))
!   call siteJumpInfo(leafIndex(i+1))
   leafIndex(i+3) = gridToJump(boundaryConditionChecker(xIndexLocal +i −oddModifier), depositedYIndex +1)
   leafEnergyIndex(i+3) = jumpToEnergy(leafIndex(i+3))
!   call siteJumpInfo(leafIndex(i+3))
 enddo

 !Modify the Schowebel jumps above and below
 leafIndex(7) = gridToJump(boundaryConditionChecker(xIndexLocal −1 −oddModifier), depositedYIndex −1)
 leafEnergyIndex(7) = jumpToEnergy(leafIndex(7))
```

```
! call siteJumpInfo(leafIndex(7))
  leafIndex(8) = gridToJump(boundaryConditionChecker(xIndexLocal +2 -oddModifier), depositedYIndex -1)
  leafEnergyIndex(8) = jumpToEnergy(leafIndex(8))
! call siteJumpInfo(leafIndex(8))
  leafIndex(9) = gridToJump(boundaryConditionChecker(xIndexLocal -1 -oddModifier), depositedYIndex +1)
  leafEnergyIndex(9) = jumpToEnergy(leafIndex(9))
! call siteJumpInfo(leafIndex(9))
  leafIndex(10) = gridToJump(boundaryConditionChecker(xIndexLocal +2 -oddModifier), depositedYIndex +1)
  leafEnergyIndex(10) = jumpToEnergy(leafIndex(10))
! call siteJumpInfo(leafIndex(10))

  !Update the sites to the immediate left and right
  leafIndex(5) = gridToJump(boundaryConditionChecker(xIndexLocal -1), depositedYIndex)
  leafEnergyIndex(5) = jumpToEnergy(leafIndex(5))
! call siteJumpInfo(leafIndex(5))
  leafIndex(6) = gridToJump(boundaryConditionChecker(xIndexLocal +1), depositedYIndex)
  leafEnergyIndex(6) = jumpToEnergy(leafIndex(6))
! call siteJumpInfo(leafIndex(6))

  !Go through all the leafIndices and update their jump parameters
  do i = 1, 11
    !print *, 'Updating siteJumpInfo'
```

```
    !Check for the odd/even index of the lattice site
    if (i /= 5 .and. i /= 6 .and. i /=11) then
      if (oddModifier == 1) then
        call siteJumpInfo(leafIndex(i), leafEnergyIndex(i), 0)
      else
        call siteJumpInfo(leafIndex(i), leafEnergyIndex(i), 1)
      endif
    else
      call siteJumpInfo(leafIndex(i), leafEnergyIndex(i), oddModifier)
    endif
!   print *, 'New site energy', jumpTree(leafIndex(i))
    if (jumpTree(leafIndex(i)) > 1.0) then
!     print *, 'Coordinates', jumpToGrid(leafIndex(i))
    endif
  enddo

end subroutine depositionUpdate
```

Bibliography

[1] J E Greene. Tracing the 5000-year recorded history of inorganic thin films from 3000 BC to the early 1900s AD. *Applied Physics Reviews*, 1(4):041302, December 2014.

[2] D D Hass and Haydn N G Wadley. Gas jet assisted vapor deposition of yttria stabilized zirconia. *Journal of Vacuum Science & Technology A: Vacuum, Surfaces, and Films*, 27(2):404–414, 2009.

[3] DJ Frurip and SH Bauer. Homogeneous Nucleation In Metal Vapors. 4. Cluster Growth-Rates From Light-Scattering. *Journal Of Physical Chemistry*, 81(10): 1007–1015, 1977.

[4] T S Cale, G B Raupp, and T H Gandy. Free molecular transport and deposition in long rectangular trenches. *Journal of Applied Physics (ISSN 0021-8979)*, 68 (7):3645, 1990.

[5] YG Yang, XW Zhou, RA Johnson, and Haydn N G Wadley. Atomistic simulations of deep submicron interconnect metallization. *Journal Of Vacuum Science & Technology B*, 20(2):622–630, 2002.

[6] María Vallet-Regí and Eduardo Ruiz-Hernández. Bioceramics: From Bone

Regeneration to Cancer Nanomedicine. *Advanced Materials*, pages 1–42, October 2011.

[7] S M Best, A E Porter, E S Thian, and J Huang. Bioceramics: Past, present and for the future. *Journal Of The European Ceramic Society*, 28(7):1319–1327, January 2008.

[8] David R Clarke, Matthias Oechsner, and Nitin P Padture. Thermal-barrier coatings for more efficient gas-turbine engines. *MRS Bulletin*, 37(10):891–898, October 2012.

[9] U Schulz, SG Terry, and CG Levi. Microstructure and texture of EB-PVD TBCs grown under different rotation modes. *Materials Science And Engineering A-Structural Materials Properties Microstructure And Processing*, 360(1-2):319–329, 2003.

[10] J Singh and DE Wolfe. Nano and macro-structured component fabrication by electron beam-physical vapor deposition (EB-PVD). *Journal Of Materials Science*, 40(1):1–26, 2005.

[11] D J Broer and W Luijks. Penetration of p-xylylene Vapor into Small Channels Prior to Polymerization. *Journal of Applied Polymer Science*, 26(7):2415–2422, 1981.

[12] H O Pierson. *Handbook of chemical vapor deposition: principles, technology and applications*. William Andrew, 1 edition, 1999.

[13] Milton Ohring. *Materials Science of Thin Films*. Academic Press, 2 edition, January 2001.

[14] K Wasa, editor. *Handbook of Sputter Deposition Technology*. William Andrew, Oxford, 2 edition, December 2012.

[15] Aric Sanders, Paul Blanchard, Kris Bertness, Matthew Brubaker, Christopher Dodson, Todd Harvey, Andrew Herrero, Devin Rourke, John Schlager, Norman Sanford, Ann N Chiaramonti, Albert Davydov, Abhishek Motayed, and Denis Tsvetkov. Homoepitaxial n-core: p-shell gallium nitride nanowires: HVPE overgrowth on MBE nanowires. *Nanotechnology*, 22(46):465703, October 2011.

[16] Kris A Bertness, Norman A Sanford, and Albert V Davydov. GaN Nanowires Grown by Molecular Beam Epitaxy. *IEEE Journal of Selected Topics in Quantum Electronics*, 17(4):847–858, August 2011.

[17] R F Bunshah. High-Rate Evaporation-Deposition Processes of Metals, Alloys, and Ceramics for Vacuum Metallurgical Applications. *Journal Of Vacuum Science & Technology*, 11(4):814–819, 1974.

[18] R F Bunshah and C V Deshpandey. Evaporation processes. *MRS Bulletin*, December 1988.

[19] B L Halpern, J J Schmitt, J W Golz, and D L Johnson. Gas jet deposition of thin films. *Applied Surface Science*, 48:19–26, June 1991.

[20] E B Graper. Evaporation Characteristics of Materials From an Electron-Beam Gun. *Journal Of Vacuum Science & Technology*, 8(1):333–&, 1971.

[21] E B Graper. Evaporation Characteristics of Materials From an Electron-Beam

Gun II. *Journal of Vacuum Science & Technology A: Vacuum, Surfaces, and Films*, 5(4):2718–2723, 1987.

[22] G K Hubler. Pulsed Laser Deposition. *MRS Bulletin*, 17:26–29, 1992.

[23] YG Yang, D D Hass, and Haydn N G Wadley. Porosity control in zig-zag vapor-deposited films. *Thin Solid Films*, 471(1-2):1–11, 2005.

[24] DA Murdick, XW Zhou, and Haydn N G Wadley. Low-temperature atomic assembly of stoichiometric gallium arsenide from equiatomic vapor. *Journal Of Crystal Growth*, 286(1):197–204, 2006.

[25] DD Hass, AJ Slifka, and Haydn N G Wadley. Low thermal conductivity vapor deposited zirconia microstructures. *Acta Mater.*, 49(6):973–983, 2001.

[26] R Darolia. Thermal barrier coatings technology: critical review, progress update, remaining challenges and prospects. *International Materials Reviews*, 58(6):315–348, August 2013.

[27] Sanjay Sampath, Uwe Schulz, Maria Ophelia Jarligo, and Seiji Kuroda. Processing science of advanced thermal-barrier systems. *MRS Bulletin*, 37(10): 903–910, October 2012.

[28] Hengbei Zhao, Fengling Yu, Ted D Bennett, and Haydn N G Wadley. Morphology and thermal conductivity of yttria-stabilized zirconia coatings. *Acta Mater.*, 54(19):5195–5207, 2006.

[29] CG Levi. Emerging materials and processes for thermal barrier systems. *Current Opinion In Solid State & Materials Science*, 8(1):77–91, 2004.

[30] Hengbei Zhao, Carlos G Levi, and Haydn N G Wadley. Vapor deposited samarium zirconate thermal barrier coatings. *Surface and Coatings Technology*, 203(20-21):3157–3167, 2009.

[31] Carlos G Levi, John W Hutchinson, Marie-Hélène Vidal-Sétif, and Curtis A Johnson. Environmental degradation of thermal-barrier coatings by molten deposits. *MRS Bulletin*, 37(10):932–941, October 2012.

[32] German S Fox-Rabinovich, Kenji Yamamoto, Ben D Beake, Iosif S Gershman, Anatoly I Kovalev, Stephen C Veldhuis, Myriam H Aguirre, Goulnara Dosbaeva, and Jose L Endrino. Hierarchical adaptive nanostructured PVD coatings for extreme tribological applications: the quest for nonequilibrium states and emergent behavior. *Science and Technology of Advanced Materials*, 13(4):043001, July 2012.

[33] Steven M George. Atomic Layer Deposition: An Overview. *Chemical Reviews*, 110(1):111–131, January 2010.

[34] Nikolaos Cheimarios, George Kokkoris, and Andreas G Boudouvis. Multiscale modeling in chemical vapor deposition processes: Coupling reactor scale with feature scale computations. *Chemical Engineering Science*, 65(17):5018–5028, September 2010.

[35] D D Hass, Y Marciano, and Haydn N G Wadley. Physical vapor deposition on cylindrical substrates. *Surface and Coatings Technology*, 185(2-3):283–291, 2004.

[36] K von Niessen and M Gindrat. Plasma Spray-PVD: A new thermal spray

process to deposit out of the vapor phase. *Journal Of Thermal Spray Technology*, 20(4):736, 2011.

[37] Haydn N G Wadley, AX Zhou, RA Johnson, and M Neurock. Mechanisms, models and methods of vapor deposition. *Progress In Materials Science*, 46 (3-4):329–377, 2001.

[38] Raymond A Adomaitis. The Nearest Uniformity Producing Profile (NUPP) optimization criterion for thin-film processing applications. *Journal of Process Control*, 18(10):9–9, December 2008.

[39] K L Choy. Chemical vapour deposition of coatings. *Progress In Materials Science*, 48(2):57–170, November 2002.

[40] Seungyup Baek and Vittaldas Prabhu. Computational Model for Substrate Motion in EB-PVD Process. *Materials and Manufacturing Processes*, 24(12): 1331–1336, 2009.

[41] E Reinhold, P Botzler, and C Deus. EB-PVD process management for highly productive zirconia thermal barrier coating of turbine blades. *Surface and Coatings Technology*, 120:77–83, 1999.

[42] S Cho, I Fuke, and V Prabhu. Motion planning for coating process optimisation in electron beam physical vapour deposition. *Surface Engineering*, 21(4): 279–289, August 2005.

[43] J Webb, B Casaday, B Barker, J P Bons, A D Gledhill, and N P Padture. Coal Ash Deposition on Nozzle Guide Vanes—Part I: Experimental Characteristics

of Four Coal Ash Types. *Journal Of Turbomachinery-Transactions Of The Asme*, 135(2):021033, March 2013.

[44] SA Slater, AD Leeming, and JB Young. Particle deposition from two-dimensional turbulent gas flows. *International Journal Of Multiphase Flow*, 29 (5):721–750, 2003.

[45] S Chapman and T G Cowling. *The Mathematical Theory of Non-Uniform Gases*. Cambridge University Press, 3 edition, 1970.

[46] Bojan Mitrovic, Alex Gurary, and William Quinn. Process conditions optimization for the maximum deposition rate and uniformity in vertical rotating disc MOCVD reactors based on CFD modeling. *Journal Of Crystal Growth*, 303(1):323–329, May 2007.

[47] Alain Dollet. Multiscale modeling of CVD film growth—a review of recent works. *Surface and Coatings Technology*, 177-178:245–251, January 2004.

[48] R A Adomaitis. A Ballistic Transport and Surface Reaction Model for Simulating Atomic Layer Deposition Processes in HighAspectRatio Nanopores. *Chemical Vapor Deposition*, 2011.

[49] Douglas T Queheillalt, Derek D Hass, David J Sypeck, and Haydn N G Wadley. Synthesis of open-cell metal foams by templated directed vapor deposition. *Journal of Materials Research*, 16(4):1028–1036, April 2001.

[50] T M Rodgers, H Zhao, and Haydn N G Wadley. Thermal barrier coating deposition by rarefied gas jet assisted processes: Simulations of deposition

on a stationary airfoil. *Journal of Vacuum Science & Technology A: Vacuum, Surfaces, and Films*, 31(6):0651509, November 2013.

[51] Stanley Tang and Uwe Schulz. Gas flow sputtering - An approach to coat complex geometries and Non Line of Sight areas. *Surface and Coatings Technology*, 204(6-7):1087–1091, 2009.

[52] Konstantin von Niessen and Malko Gindrat. Vapor Phase Deposition Using a Plasma Spray Process. *Journal of Engineering for Gas Turbines and Power*, 133 (6):061301, 2011.

[53] Andreas Hospach, Georg Mauer, Robert Vassen, and Detlev Stöver. Columnar-Structured Thermal Barrier Coatings (TBCs) by Thin Film Low-Pressure Plasma Spraying (LPPS-TF). *Journal Of Thermal Spray Technology*, 20(1-2): 116–120, January 2011.

[54] B L Halpern and J J Schmitt. Multiple jets and moving substrates: Jet Vapor Deposition of multicomponent thin films. *Journal of Vacuum Science & Technology A: Vacuum, Surfaces, and Films*, 12(4), February 1994.

[55] John H Perepezko. The Hotter the Engine, the Better. *Science*, 326(5956): 1068–1069, 2009.

[56] Matthew R Begley and Haydn N G Wadley. Delamination of Ceramic Coatings with Embedded Metal Layers. *Journal Of The American Ceramic Society*, 94: S96–S103, 2011.

[57] Matthew R Begley and Haydn N G Wadley. Delamination resistance of

thermal barrier coatings containing embedded ductile layers. *Acta Mater.*, 60 (6-7):2497–2508, 2012.

[58] Mark S Majewski, Colin Kelley, Jerod Lake, Michael W Renfro, Waled Hassan, William Brindley, and Eric H Jordan. Stress measurements via photoluminescence piezospectroscopy on engine run thermal barrier coatings. *Surface and Coatings Technology*, 206(11-12):2751–2758, 2012.

[59] Wei Pan, Simon R Phillpot, Chunlei Wan, Aleksandr Chernatynskiy, and Zhixue Qu. Low thermal conductivity oxides. *MRS Bulletin*, 37(10):917–922, October 2012.

[60] J Rosler, M Baker, and M Volgmann. Stress state and failure mechanisms of thermal barrier coatings: Role of creep in thermally grown oxide. *Acta Mater.*, 49(18):3659–3670, 2001.

[61] R W Steinbrech, V Postolenko, J Mönch, J Malzbender, and L Singheiser. Testing method to assess lifetime of EB-PVD thermal barrier coatings on tubular specimens in static and cyclic oxidation tests. *Ceramics International*, 37(1):363–368, January 2011.

[62] S Kumar and A C F Cocks. Journal of the Mechanics and Physics of Solids. *Journal of the Mechanics and Physics of Solids*, 60(4):723–749, April 2012.

[63] Hengbei Zhao, Matthew R Begley, Arthur Heuer, Reza Sharghi-Moshtaghin, and Haydn N G Wadley. Reaction, transformation and delamination of samarium zirconate thermal barrier coatings. *Surface and Coatings Technology*, 205(19):4355–4365, 2011.

[64] Sebastian Mihm, Thomas Duda, Heiko Gruner, Georg Thomas, and Birger Dzur. Method and Process Development of Advanced Atmospheric Plasma Spraying for Thermal Barrier Coatings. *Journal Of Thermal Spray Technology*, 21(3):400–408, June 2012.

[65] B J Harder and D Zhu. Plasma SprayPhysical Vapor Deposition (PSPVD) of Ceramics for Protective Coatings. *Advanced Ceramic Coatings and Materials for Extreme Environments: Ceramic Engineering and Science Proceedings, Volume 32*, 32, 2011.

[66] James Frederick Groves, S H Jones, T Globus, L M Hsiung, and Haydn N G Wadley. Directed Vapor-Deposition Of Amorphous And Polycrystalline Electronic Materials-Nonhydrogenated A-Si. *Journal Of The Electrochemical Society*, 142(10):L173–L175, 1995.

[67] DD Hass, James Frederick Groves, and Haydn N G Wadley. Reactive vapor deposition of metal oxide coatings. *Surface and Coatings Technology*, 146: 85–93, 2001.

[68] DD Hass, PA Parrish, and Haydn N G Wadley. Electron beam directed vapor deposition of thermal barrier coatings. *Journal of Vacuum Science & Technology A: Vacuum, Surfaces, and Films*, 16(6):3396–3401, 1998.

[69] James Frederick Groves and Haydn N G Wadley. Functionally graded materials synthesis via low vacuum directed vapor deposition. *Composites Part B-Engineering*, 28(1-2):57–69, 1997.

[70] R G Wellman and J R Nicholls. Erosion, corrosion and erosion–corrosion of

EB PVD thermal barrier coatings. *Tribology International*, 41(7):657–662, July 2008.

[71] Vanni Lughi, Vladimir K Tolpygo, and David R Clarke. Microstructural aspects of the sintering of thermal barrier coatings. *Materials Science and Engineering: A*, 368(1-2):212–221, March 2004.

[72] Siegfried Schiller, Ullrich Heisig, and Siegfried Panzer. *Electron Beam Technology*. John Wiley & Sons, New York, 1982.

[73] M Matsumoto, K Wada, N Yamaguchi, and T Kato. Effects of substrate rotation speed during deposition on the thermal cycle life of thermal barrier coatings fabricated by electron beam physical vapor deposition. *Surface and Coatings Technology*, 202:3507–3512, 2008.

[74] James Frederick Groves. *Directed Vapor Deposition*. PhD thesis, University of Virginia, Charlottesville, April 1999.

[75] S Jin and Haydn N G Wadley. Lithium manganese oxide films fabricated by electron beam directed vapor deposition. *Journal of Vacuum Science & Technology A: Vacuum, Surfaces, and Films*, 26(1):114–122, 2008.

[76] Yoon Gu Kim and Haydn N G Wadley. Lithium phosphorous oxynitride films synthesized by a plasma-assisted directed vapor deposition approach. *Journal of Vacuum Science & Technology A: Vacuum, Surfaces, and Films*, 26(1):174–183, 2008.

[77] Yoon Gu Kim and Haydn N G Wadley. Plasma-assisted deposition of lithium

phosphorus oxynitride films: Substrate bias effects. *Journal Of Power Sources*, 187(2):591–598, 2009.

[78] Zhuo Yu, Hengbei Zhao, and Haydn N G Wadley. The Vapor Deposition and Oxidation of Platinum- and Yttria-Stabilized Zirconia Multilayers. *Journal Of The American Ceramic Society*, 94(8):2671–2679, March 2011.

[79] Z Yu, D D Hass, and Haydn N G Wadley. NiAl bond coats made by a directed vapor deposition approach. *Materials Science And Engineering A-Structural Materials Properties Microstructure And Processing*, 394(1-2):43–52, 2005.

[80] Z Yu, K P Dharmasena, D D Hass, and Haydn N G Wadley. Vapor deposition of platinum alloyed nickel aluminide coatings. *Surface and Coatings Technology*, 201(6):2326–2334, 2006.

[81] D D Hass, Y Y Yang, and Haydn N G Wadley. Pore evolution during high pressure atomic vapor deposition. *Journal of Porous Materials*, 17(1):27–38, 2010.

[82] J Cho, SG Terry, R LeSar, and CG Levi. A kinetic Monte Carlo simulation of film growth by physical vapor deposition on rotating substrates. *Materials Science And Engineering A-Structural Materials Properties Microstructure And Processing*, 391(1-2):390–401, 2005.

[83] X W Zhou, R A Johnson, and Haydn N G Wadley. Vacancy formation during vapor deposition. *Acta Mater.*, 1997.

[84] J J Quan, X W Zhou, and Haydn N G Wadley. Atomic assembly of metal surfaces and interfaces. *Surface Science*, 600(19):4537–4547, 2006.

[85] X W Zhou, R A Johnson, and Haydn N G Wadley. A molecular dynamics study of nickel vapor deposition: Temperature, incident angle, and adatom energy effects. *Acta Mater.*, 45(4):1513–1524, 1997.

[86] S Baek and V Prabhu. Simulation model for an EB-PVD coating structure using the level set method. *Journal of Manufacturing Processes*, 11:1–7, 2009.

[87] K Bobzin, E Lugscheider, and R Nickel. Modeling and simulation in the production process control and material property calculation of complex structured EB-PVD TBCs. *Computational Materials Science*, 39:600–610, 2007.

[88] M Gupta, N Curry, N Markocsan, and R Vaßen. Design of Next Generation Thermal Barrier Coatings-Experiments and Modelling. *Surface and Coatings Technology*, 220:20–36, 2012.

[89] Gangshi Hu, Jianqiao Huang, Gerassimos Orkoulas, and Panagiotis D Christofides. Investigation of film surface roughness and porosity dependence on lattice size in a porous thin film deposition process. *Physical Review E*, 80(4):041122, 2009.

[90] Gangshi Hu, Gerassimos Orkoulas, and Panagiotis D Christofides. Regulation of film thickness, surface roughness and porosity in thin film growth using deposition rate. *Chemical Engineering Science*, 64(17):3903–3913, September 2009.

[91] T P Schulze and P Smereka. Kinetic Monte Carlo simulation of heteroepitaxial growth: Wetting layers, quantum dots, capping, and nanorings. *Physical Review B*, 86(23):235313, December 2012.

[92] Chi-Hang Lam. Kinetic Monte Carlo simulation of shape transition of strained quantum dots. *Journal of Applied Physics (ISSN 0021-8979)*, 108(6):064328, 2010.

[93] Corbett C Battaile. The kinetic Monte Carlo method: Foundation, implementation, and application. *Computer Methods In Applied Mechanics And Engineering*, 197(41-42):3386–3398, 2008.

[94] G A Bird. *Molecular Gas Dynamics and the Direct Simulation of Gas Flows* . Oxford Engineering Science. Oxford University Press, Oxford, 2 edition, June 1994.

[95] YG Yang, RA Johnson, and Haydn N G Wadley. A Monte Carlo simulation of the physical vapor deposition of nickel. *Acta Mater.*, 45(4):1455–1468, 1997.

[96] Yougen Yang. *The Monte Carlo Simulation of Physical Vapor Deposition*. PhD thesis, University of Virginia, Charlottesville, October 2000.

[97] J Balakrishnan, ID Boyd, and DG Braun. Monte Carlo simulation of vapor transport in physical vapor deposition of titanium. *Journal of Vacuum Science & Technology A: Vacuum, Surfaces, and Films*, 18(3):907–916, 2000.

[98] J Fan, ID Boyd, and C Shelton. Monte Carlo modeling of electron beam physical vapor deposition of yttrium. *Journal of Vacuum Science & Technology A: Vacuum, Surfaces, and Films*, 18(6):2937–2945, 2000.

[99] A Venkattraman and A A Alexeenko. Direct simulation Monte Carlo modeling of e-beam metal deposition. *Journal of Vacuum Science & Technology A: Vacuum, Surfaces, and Films*, 28(4):916–924, 2010.

[100] Ayyaswamy Venkattraman and Alina A Alexeenko. Direct simulation Monte Carlo modeling of metal vapor flows in application to thin film deposition. *Vacuum*, 86:1748–1758, May 2012.

[101] H A Al-Mohssen and N G Hadjiconstantinou. Arbitrary-pressure chemical vapor deposition modeling using direct simulation Monte Carlo with non-linear surface chemistry. *Journal Of Computational Physics*, 198(2):617–627, 2004.

[102] R Botha, T Novikova, and P Bulkin. Capillary jet injection of SiH4 in the high density plasma chemical vapor deposition of SiO2. *Journal of Vacuum Science & Technology A: Vacuum, Surfaces, and Films*, 27(4):849–854, 2009.

[103] Hadley M Cave, Susan P Krumdieck, and Mark C Jermy. Development of a model for high precursor conversion efficiency pulsed-pressure chemical vapor deposition (PP-CVD) processing. *Chemical Engineering Journal*, 135 (1-2):120–128, 2008.

[104] Daniel G Coronell and K F Jensen. Analysis of Transition Regime Flows in Low Pressure Chemical Vapor Deposition Reactors Using the Direct Simulation Monte Carlo Method. *Journal Of The Electrochemical Society*, 139(8):2264–2273, 1992.

[105] TJ Bartel, SJ Plimpton, and M A Gallis. Icarus: A 2-D Direct Simulation Monte Carlo (DSMC) Code for Multi-Processor Computers. *Sandia Report*, 2001.

[106] Jonathan D Madison, Veena Tikare, and Elizabeth A Holm. Journal of Nuclear Materials. *Journal of Nuclear Materials*, 425(1-3):173–180, June 2012.

[107] J Kelling, G Ódor, M F Nagy, H Schulz, and K H Heinig. Comparison of different parallel implementations of the 2+1-dimensional KPZ model and the 3-dimensional KMC model. *The European Physical Journal Special Topics*, 210(1):175–187, September 2012.

[108] D Srinivasa Rao, Krishna Valleti, S V Joshi, and G Ranga Janardhan. Processing-structure-property relationships in electron beam physical vapor deposited yttria stabilized zirconia coatings. *Journal of Vacuum Science & Technology A: Vacuum, Surfaces, and Films*, 29(3):031501, 2011.

[109] G Mauer, A Hospach, and R Vaßen. Process Development and Coating Characteristics of Plasma Spray-PVD. *Surface and Coatings Technology*, 220: 219–224, 2013.

[110] YongQing Wang and G Sayre. Surface & Coatings Technology. *Surface and Coatings Technology*, 203(16):2186–2192, May 2009.

[111] R Herzog, N Warnken, I Steinbach, B Hallstedt, C Walter, J Mueller, D Hajas, E Muenstermann, J M Schneider, R Nickel, D Parkot, K Bobzin, E Lugscheider, P Bednarz, O Trunova, and L Singheiser. Integrated approach for the development of advanced, coated gas turbine blades. *Advanced Engineering Materials*, 8(6):535–562, 2006.

[112] J M Nieuwenhuizen and H B Haanstra. Microfractography of Thin Films. *Philips Technical Review*, 27(3):87–91, June 1966.

[113] A G Dirks and H J Leamy. Columnar Microstructure In Vapor-Deposited Thin-Films. *Thin Solid Films*, 47(3):219–233, 1977.

[114] KC Kannenberg and ID Boyd. Strategies for efficient particle resolution in the direct simulation Monte Carlo method. *Journal Of Computational Physics*, 157(2):727–745, 2000.

[115] TJ Bartel and S Plimpton. DSMC simulations of low-density fluid flow on MIMD supercomputers. *Computing Systems in Engineering*, 3(1-4):333–336, 1992.

[116] James Frederick Groves and Haydn N G Wadley. Monte Carlo Modeling of Atom Transport During Directed Vapor Deposition. *MRS 2000*, pages 1–8, June 2000.

[117] Sang-Wan Jin. *Directed Vapor Deposition of Lithium Manganese Oxide Films*. PhD thesis, University of Virginia, Charlottesville, July 2008.

[118] HIH Saravanamutto, GFC Rogers, Henry Cohen, and Paul Straznicky. *Gas Turbine Theory*. Pearson Education Limited, Harlow, 6 edition, September 2008.

[119] T M Rodgers, Hengbei Zhao, and Haydn N G Wadley. Microstructure of Vapor Deposited Coatings on Curved Substrates. *Journal of Vacuum Science & Technology A: Vacuum, Surfaces, and Films*, 2015.

[120] DD Hass. *Thermal Barrier Coatings Via Directed Vapor Deposition*. PhD thesis, University of Virginia, Charlottesville, 2001.

[121] R A Johnson. Analytic nearest-neighbor model for fcc metals. *Physical Review B*, 37(8):3924, 1988.

[122] Matthew Pelliccione. *Evolution of Thin Film Morphology: modeling and simulations*. Springer series in materials science. Springer, 1 edition, 2008.

[123] Hengbei Zhao, Carlos G Levi, and Haydn N G Wadley. Molten silicate interactions with thermal barrier coatings. *Surface and Coatings Technology*, pages 1–13, April 2014.

[124] R O Duda and P E Hart. Use of the Hough transformation to detect lines and curves in pictures. *Communications of the ACM*, 1972.

[125] B Tanto, G Ten Eyck, and T M Lu. A model for column angle evolution during oblique angle deposition. *Journal of Applied Physics (ISSN 0021-8979)*, 108(2): 026107, 2010.

[126] T Smy, D Vick, Michael J Brett, SK Dew, AT Wu, JC Sit, and KD Harris. Three-dimensional simulation of film microstructure produced by glancing angle deposition. *Journal of Vacuum Science & Technology A: Vacuum, Surfaces, and Films*, 18(5):2507–2512, 2000.

[127] K Robbie and M J Brett. Sculptured thin films and glancing angle deposition: Growth mechanics and applications. *Journal of Vacuum Science & Technology A: Vacuum, Surfaces, and Films*, 15(3):1460–1465, 1997.

[128] R N Tait, T Smy, and M J Brett. Modelling and characterization of columnar growth in evaporated films. *Thin Solid Films*, 226:196–201, April 1993.

[129] S Lichter and J Chen. Model for columnar microstructure of thin solid films. *Physical Review Letters*, 56(13):1396–1399, March 1986.

[130] P Meakin. The growth of rough surfaces and interfaces. *Physics Reports*, 235 (4):189–289, 1993.

[131] M M Hawkeye and M J Brett. Glancing angle deposition: Fabrication, properties, and applications of micro-and nanostructured thin films. *Journal of Vacuum Science & Technology A: Vacuum, Surfaces, and Films*, 2007.

[132] T M Rodgers, Hengbei Zhao, and Haydn N G Wadley. Physical Vapor Deposition on Doublet Airfoil Substrates: Factors Controlling the Coating Thickness. *In preparation*, 2015.

[133] T M Rodgers, Hengbei Zhao, and Haydn N G Wadley. Microstructure of Vapor Deposited Coatings on Curved Substrates with Interior Channels. *In preparation*, 2015.